



Technische Universität München

Fakultät für Maschinenwesen

Lehrstuhl für Nukleartechnik

Mechanical Analysis of the Bow Deformation of Fuel Assemblies in a Pressurized Water Reactor Core

Andreas Wanninger

Vollständiger Abdruck der von der Fakultät für Maschinenwesen der Technischen Universität München zur
Erlangung des akademischen Grades eines

Doktor-Ingenieurs (Dr.-Ing.)

genehmigten Dissertation.

Vorsitzender: Univ.-Prof. Dr.-Ing. Michael Gee

Prüfer der Dissertation: 1. Univ.-Prof. Rafael Macián-Juan, Ph.D.
2. Univ.-Prof. Olivier Doaré, Ph.D., ENSTA ParisTech

Die Dissertation wurde am 11.01.2018 bei der Technischen Universität München eingereicht und durch die
Fakultät für Maschinenwesen am 12.07.2018 angenommen.

Acknowledgments

First, I would like to express my sincere gratitude to my advisor and first examiner Prof. Dr. Rafael Macián-Juan for giving me the opportunity to conduct my PhD research at the Chair of Nuclear Technology and for the continuous support he offered me over the years. I very much appreciated his accessibility, his always open ear, and his support in attending conferences and other events worldwide.

My very deep gratitude goes to my mentor Dr. Marcus Seidl, who is the principal initiator of the present project, for the guidance provided throughout the course of my research, his constructive criticism, many valuable suggestions and continuous support. Without his help, this work would not have been possible. I wholeheartedly wish him great success in his future endeavors.

Moreover, I would like to thank Prof. Dr. Olivier Doaré for assuming the function of the second examiner. It was him who awoke my initial interest in fluid-structure interaction problems in the framework of his course at my second Alma Mater ENSTA ParisTech.

I am, as well, very grateful to the current and former members of the Chair of Nuclear Technology, who I had the pleasure working with. They made my time at the chair very pleasant and supported me wherever possible. Special thanks go to Dr. Martin Ohlerich, the co-initiator of the project, for constantly raising profound questions about the applied modeling methods, thus inciting new ideas; to Dr. Clotaire Geffray for providing me important background knowledge about sensitivity and uncertainty analysis; to Dr. Sabin Ceuca who introduced me into applied CFD modeling during my diploma thesis which served as a valuable basis for my PhD work; and to the staff of the secretary's office, Margitta Franke and Petra Popp, who were always very supportive in bureaucratic matters.

I am also very grateful to PreussenElektra GmbH, respectively the former e.on Kernkraft GmbH, for providing significant funding which allowed me to undertake this research. Moreover, I thank all the members of the nuclear fuel group for their trust, their precious feedback, and their support with data.

In addition, I would like to give special thanks to David Schrire, Vattenfall SE, for providing experimental creep data and valuable feedback at the TopFuel conferences. Besides, I thank Petter Gabriellsson for offering new perspectives for the continuation of this work.

Finally, I would like to take the opportunity to thank all the people that have helped me getting to this point: my family, particularly my parents Claudia and Helmut and my grandparents, for their love, their permanent moral and financial support, and their continuous encouragement; my fiancée Marian for her love,

patience, and the personal support she offered me also in difficult times; as well as all my remaining family and my friends, who have been there for me over the years. Without all them, this work would hardly have been possible.

Abstract

The permanent bow deformation of fuel assemblies (FAs) in the core of pressurized water reactors (PWRs) during irradiation may cause both safety and handling problems. The evolution of the FA bow deformation is considered to be a complex process with a large number of influencing mechanisms and several unknowns due to the limited knowledge about the boundary conditions and processes inside an operating nuclear reactor core. Since the first occurrence of strongly bowed cores, computational tools to predict the FA deformation have been developed to optimize the FA design and the FA loading pattern in the core. However, significant prediction errors persist, both regarding the bow amplitude and direction. The objective of this work is therefore to approach the FA bow modeling from a novel point of view, namely setting the focus on sensitivity and uncertainty analysis to assess the predictability of the FA bow patterns. To perform these analyses, a finite-element FA structural model is built up and is finally extended to a coupled row model of 15 FAs in the reactor core. To estimate the distribution of lateral hydraulic forces within the core row, a two-dimensional CFD (Computational Fluid Dynamics) model is created with a porous-medium approach. In addition, creep, irradiation growth, and spring relaxation models are developed to predict the evolution of the FA deformation during irradiation. The obtained in-laboratory and in-reactor FA model response is in good qualitative agreement with what is observed for FAs deployed in nuclear reactors. The sensitivity and uncertainty analyses, performed for both single FAs and a row of FAs, demonstrate that the uncertainties about the creep rate and the hydraulic conditions have a considerable impact on the bow amplitudes and directions. They may therefore fundamentally modify the bow pattern predicted with best estimate methods. It is concluded that FA bow calculations should always be accompanied by an uncertainty analysis to estimate the variability of the model predictions. To improve the predictions in the future, a specific effort must be invested in decreasing the uncertainty range of the concerned parameters.

Contents

Acknowledgments	iii
Abstract	v
List of Figures	xi
List of Tables	xvii
List of Acronyms	xix
1 Introduction	1
1.1 FA bow in PWR power plants	1
1.2 Problems related to FA bow	5
1.3 Bow influencing mechanisms	6
1.4 Literature review of the modeling of FA deformations and of related phenomena	10
1.5 Motivation and objectives of this work	13
1.6 Outline of the thesis: modeling and simulation steps	15
2 Modeling Theory	17
2.1 Structural mechanics	17
2.1.1 Linear isotropic elasticity	17
2.1.2 Creep – a type of rate-dependent plasticity	19
2.1.3 Engineering structural mechanics of FA tubes and rods	26
2.2 Computational Structural Mechanics (CSM) and Finite Element Method (FEM)	31
2.2.1 Fundamentals of the FEM	31
2.2.2 Finite elements for FA structural analysis	33
2.2.3 Solution methods	37
2.3 Fluid mechanics	40
2.3.1 Navier-Stokes equations	40
2.3.2 Internal channel flow	40
2.3.3 Porous medium approach	43
2.4 Zirconium alloys - metallurgy, in-reactor behavior, and modeling	46
2.4.1 Generations of Zirconium alloys	46
2.4.2 Crystallography and texture of Zirconium alloys	47

2.4.3	Irradiation damage processes in microstructure	48
2.4.4	In-reactor creep	50
2.4.5	In-reactor growth	51
2.4.6	Modeling of the in-reactor creep of Zirconium alloys	53
3	Fuel Assembly Structural Model	57
3.1	General properties	57
3.1.1	Reference FA design	57
3.1.2	Set-up of the model	57
3.2	FA structural elements	60
3.2.1	Guide tubes (GTs) and Fuel rods (FRs)	60
3.2.2	Spacer grids	63
3.2.3	FA foot and head structures	64
3.2.4	Inter-assembly gaps	64
3.2.5	Guide tube (GT) connections	65
3.2.6	Fuel rod (FR) support	67
3.2.7	Holddown (HD) device	73
3.3	Structural constraint boundary conditions (BCs)	75
3.3.1	Displacement BCs	75
3.3.2	Rotational BCs	76
3.4	Model reduction	76
3.4.1	FR reduction method	76
3.4.2	Reduced 3D Model	79
3.4.3	Reduced 2D Model	80
3.4.4	Performance of reduced models	81
3.5	Laboratory deflection tests	81
3.5.1	Deflection test set-up and description	82
3.5.2	Axial deflection test	83
3.5.3	Lateral deflection test	85
3.6	Model calibration	86
3.6.1	Axial response	87
3.6.2	Lateral response	87
4	In-Reactor Model	91
4.1	Modeling of reactor cycle: start-up, operation and shutdown	91
4.1.1	General description of reactor cycle	91
4.1.2	Load steps and BCs for reactor cycle runs	92
4.2	Creep of structures	94
4.2.1	GT creep	95

4.2.2	FR creep	100
4.3	Growth of Structures	102
4.3.1	FA or GT growth	102
4.3.2	FR growth	104
4.4	Reactor operating conditions	105
4.4.1	Power distribution	105
4.4.2	Burnup (BU) pattern	107
4.4.3	Temperature distribution in structures	108
4.4.4	Fast neutron flux	109
4.5	Spring relaxation models	109
4.5.1	Grid spring relaxation	109
4.5.2	Holddown (HD) spring compression and relaxation	111
5	Hydraulic Model	113
5.1	Derivation of the loss coefficients for the porous model	114
5.1.1	Axial loss coefficients	114
5.1.2	Lateral loss coefficients	115
5.2	Model pre- and postprocessing	120
5.2.1	Mesh and flow model	120
5.2.2	Boundary conditions (BCs)	121
5.2.3	Postprocessing	123
5.3	Analysis of model results	126
5.3.1	Uniform inlet and outlet profiles	126
5.3.2	Symmetric inlet and outlet profiles	128
5.3.3	Asymmetric inlet and symmetric outlet profiles	131
5.4	Fluid-structure interaction (FSI)	133
6	In-Reactor Simulation Results and Sensitivity Analyses	135
6.1	Single-FA deflection tests	135
6.1.1	Definition of operation and burnup (BU) states	135
6.1.2	Investigation of axial stress states	136
6.1.3	In-reactor lateral deflection tests	138
6.1.4	Sensitivity Analysis of FA lateral stiffness increase with structural parameters	140
6.2	Single-FA creep deformation analysis	142
6.2.1	Creep deformation due to lateral hydraulic forces	142
6.2.2	Deformation of peripheral FAs due to differential creep and growth	146
6.2.3	Sensitivity analysis of FA creep deformation with uncertainty parameters	148
6.3	In-reactor creep deformation of FA rows over one cycle	151

6.3.1	Preliminary analysis: effect of thermal and neutron flux gradients without hydraulic forces	153
6.3.2	Reference case: symmetric hydraulic forces with best estimate (BE) creep and growth	155
6.3.3	First parameter change: asymmetric hydraulic forces with best estimate (BE) creep and growth	158
6.3.4	Second parameter change: creep and growth uncertainties	160
6.3.5	Analysis with initially bowed elements	162
6.3.6	The effect of fluid-structure interaction (FSI)	166
7	Conclusions and Outlook	169
7.1	Summary of achievements	169
7.1.1	Development of a computational FA bow model	169
7.1.2	Analysis of the FA bow model sensitivities and uncertainties	170
7.1.3	Final conclusions	172
7.2	Towards a validated full-core FA bow model	172
A	Derivation of the Euler-Bernoulli beam equations	177
B	Modeling of the anisotropic creep of Zirconium alloy FRs	181
C	Equivalence of the FR internal energy for the full and reduced models	185
D	Pressure drop correlations to determine axial hydraulic forces	187
E	Screening sensitivity analysis	193
	Bibliography	195

List of Figures

1.1	Schematic of PWR reactor pressure vessel (RPV) and internals (USNRC, 2012).	2
1.2	Schematic of PWR FA and rod control cluster assembly (RCCA) (USNRC, 2012).	2
1.3	Schematic of the drag forces acting on a control rod traveling through a bowed GT (Aulló and Rabenstein, 2005).	3
1.4	Examples of FA bow measurements at Ringhals power plant (Andersson et al., 2005).	3
1.5	Spacer grid corner fretting.	6
1.6	Graphical representation of in-reactor FA bow influencing mechanisms. Background drawing from USNRC (2012).	7
1.7	Examples for FA bow predictions by computational tools.	11
1.8	Example outputs for CFD calculations over partial core sections.	12
1.9	Examples for recent bow predictions versus measurements (Lascar et al., 2015).	13
1.10	Schematic of the modeling steps done in this thesis based on Figure 1.6. The black dashed line encloses the modeled domain.	15
2.1	Notation for stress components on an infinitesimal volume element (Szabó and Babuška, 2011).	18
2.2	Schematic of a creep curve.	22
2.3	Evolution of stress and strain during creep relaxation (Rust, 2011).	25
2.4	Schematic views of a beam element (Gross et al., 2012).	26
2.5	Schematic of grid coupling effects.	28
2.6	Schematic of the spring element (Merkel and Öchsner, 2010).	34
2.7	Schematic of the finite bar element (Merkel and Öchsner, 2010).	34
2.8	Gap-contact element with normal spring.	36
2.9	Friction element with spring representing stick stiffness.	37
2.10	Graphic representation of the angle of attack θ for the case of straight FAs or deformable FAs when considering two-way fluid-structure interaction (FSI).	46
2.11	The hexagonal close-packed (hcp) crystal structure (Franklin et al., 1983).	48
2.12	Typical texture of Zirconium tubing (Franklin et al., 1983).	48
2.13	Schematic of different stages of irradiation damage.	49
2.14	Schematic drawings of dislocation loops (Franklin et al., 1983).	50
2.15	Schematic drawings of microstructural creep mechanisms (Franklin et al., 1983).	50

2.16	Arrhenius plot of in-reactor creep of stress-relieved annealed (SRA) cladding (Garzarolli et al., 1996).	51
2.17	Schematic of texture-related irradiation growth (Stehle et al., 1975).	52
2.18	Irradiation growth of Zircaloy at 300 °C (Garzarolli et al., 1996).	52
2.19	Dimensional changes of ZIRLO and Zircaloy-4 tubing and strip as a function of hydrogen content (King et al., 2002).	53
2.20	Time dependence of creep strain for Zircaloy-2 obeying the strain-hardening rule at increasing variable stress as compared to data with constant stress (Lucas and Pelloux, 1981).	54
2.21	Linear versus power-law relationship for the development of a creep correlation (Wood, 1975).	54
2.22	Relationship between saturated primary creep strain and secondary creep rate (Limbäck and Andersson, 1996).	55
3.1	16x16 KWU-type FA (Garzarolli et al., 2000).	58
3.2	Schematic of the wireframe structure of the FA structural model.	58
3.3	Top views of the FR and GT bundle.	61
3.4	FA front view. Schematic drawing (Ziegler, 1984) and ANSYS model.	61
3.5	Actual shape of spacer grid versus modeled configuration.	63
3.6	Example schematics of the spot-weld connections between GTs and spacer grids (Mattos Schettino et al., 2014).	65
3.7	Cross-sectional cuts through the guide tube connections with the nozzles.	66
3.8	Views of a 5×5 section cut of the inner part of a spacer grid (Lee et al., 2014). 11: Fuel rod. 15: Grid strap. 25: Grid cell. 28: Grid spring. 29: Grid dimple.	67
3.9	Schematics of FR support.	68
3.10	Representation of the loading and unloading phases of the grid-to-rod joint. Black continuous line: spring is loading or unloading; grey continuous line: spring is at rest; black dotted line: rod slides over perpendicular spring/dimple.	69
3.11	Modeled configuration of FR support.	70
3.12	Measured grid spring characteristic (Kim, 1993).	70
3.13	Experimental record of a fuel rod supported by a spacer grid and laterally loaded by a force F in distance L (Stabel and Hübsch, 1995).	72
3.14	FR support rotational loading test.	72
3.15	Spring and dimple force variation ΔF as a function of rotation during the FR support loading test with $\mu = 0.55$ in Figure 3.14. $\Delta F > 0$ means positive contribution to grid-to-rod moment and vice versa.	72
3.16	Schematic drawings of FA head with holddown springs (Steinke, 1981).	74
3.17	Schematics of the mechanical holddown system.	74
3.18	Top view of the FR and GT bundles for reduced models.	80
3.19	FA deflection test schematics.	82
3.20	Axial deflection test: qualitative comparison of simulation results versus measurements.	84
3.21	Axial force transmitted per grid cell at grid levels 1 to 9 during the axial deflection test.	84

3.22	Lateral deflection test: qualitative comparison of simulation results versus measurements.	85
3.23	Normalized grid-to-rod moment at grid levels 1 to 9 during the lateral deflection test.	86
3.24	Lateral deflection shape.	86
3.25	Lateral deflection plot before the final calibration step compared to experimental record.	88
3.26	Calibration of FA lateral response.	89
4.1	Flow chart of the FA bow calculation procedure.	94
4.2	Irradiation creep rates for ZIRLO depending on the final heat treatment (Foster et al., 2015).	95
4.3	GT axial creep strain as a function of fluence for conventional or low-tin RZA Zry-4 for different experimental data by Yvon et al. (1998), Pettersson (2002), McGrath and Yagnik (2011), and Seibold et al. (2000).	97
4.4	Axial creep strain as a function of fluence obtained from bending creep tests with two widely used GT alloys in fresh material (FM) and pre-irradiated material (IM) condition tested in pile (IP) and out of pile (OP). Data kindly provided by Vattenfall originating from bending tests financed by SKI and the Swedish nuclear industry research co-operation (BFUK).	98
4.5	BE creep curve with lower and upper bounds developed based on the GT bending creep test data given in Figure 4.4.	98
4.6	FR cladding hoop creep strain as a function of fluence for low-tin SRA Zry-4 and new Zirconium alloys with Niobium content.	100
4.7	Derived laws for the modeling of best estimate (BE) and upper bound (UB) GT growth of Zircaloy-4 and advanced alloys with underlying FA growth performance data by Wikmark et al. (2009).	102
4.8	FR growth for different cladding materials (Gilbon et al., 2000).	104
4.9	Typical power distribution in an operating KWU-type PWR (Fabry, 2014).	106
4.10	Example of a FA core loading plan (USNRC, 2012).	106
4.11	Lateral and axial distribution of the boundary conditions.	107
4.12	Relaxation of mid-grid spring (Billerey, 2005).	110
4.13	Linear least-squares regression to define creep relaxation law.	111
5.1	As-fabricated FA (MHI, 2016) and corresponding schematic of porous model regions with loss coefficients.	114
5.2	Picture of EOLE test section (Peybernès, 2005).	116
5.3	MISTRAL test section (Peybernès, 2005).	118
5.4	Comparison of CFX simulation results using the EOLE correlation with the experimental results with the MISTRAL test section.	118
5.5	Streamlines for a Large Eddy Simulation (LES) analysis over a FA section (Bieder, 2015).	120
5.6	Isometric view of meshed domain. Black arrows indicate the mass flow inlet and outlet BCs and red arrows the symmetry BC.	120
5.7	Different core inlet velocity profiles established by measurements or calculations.	122
5.8	Defined relative mass flow profiles over one FA row at inlet and outlet.	123

5.9	Schematic of the loading of a doubly-clamped beam with a force F (Wittenburg and Richard, 2012).	125
5.10	Axial velocity for uniform inlet and outlet profiles.	126
5.11	Pressure gradient plots for uniform inlet and outlet conditions.	127
5.12	Axial velocity for non-uniform symmetric inlet and outlet profiles.	128
5.13	Flow solution for non-uniform symmetric inlet and outlet profiles.	129
5.14	Hydraulic forces on FAs for non-uniform symmetric inlet and outlet profiles.	130
5.15	Flow solution for shifted, asymmetric inlet profile and symmetric outlet profile.	132
5.16	Hydraulic forces on FAs for shifted, asymmetric inlet profile and symmetric outlet profile.	133
5.17	Flow chart of implemented explicit two-way fluid-structure coupling procedure.	134
6.1	Axial stress σ_z [Pa] in GTs (inner tubes) and FRs (outer tubes).	137
6.2	In-Reactor lateral deflection test for the cases in Table 6.1.	139
6.3	Morris' $ \mu $ and σ measures for the input parameters in Table 6.2.	142
6.4	Single-FA creep test over one cycle with hydraulic load of FA 12 in Figure 5.14.	143
6.5	Normalized grid spring forces at the different grid levels over the reactor cycle during the single-FA creep test with FA 12.	143
6.6	Distribution of selected distributed variables in selected GTs and FRs for the single-FA creep deflection test.	144
6.7	Single-FA creep test over one cycle of FA 1 and FA 2 in Figure 4.11a under the effect of power gradients without lateral hydraulic forces.	147
6.8	Lateral strain gradients $\Delta\epsilon/\Delta x$ at grid 5 over the peripheral FAs 1 and 2.	147
6.9	Evolution over BU of the monitored output variable (lateral FA deflection u_{lat}) for the simulation experiment with BE parameters.	149
6.10	Example for predicted versus measured secondary creep strain (Limbäck and Andersson, 1996)	149
6.11	Literature values (Billerey, 2005, in blue) and deduced model nominal (nom.), minimum (min.) and maximum (max.) values for the normalized spring force and gap size of Zry-4 mid grids.	150
6.12	Morris' $ \mu $ and σ measures for the last time step of the FA creep deformation simulation experiment for the input parameters in Table 6.3.	150
6.13	BU-dependent evolution of the normalized Morris measures for the input parameters in Table 6.3.	151
6.14	Considered system of a row of 15 FAs in the reactor core.	152
6.15	FA deformations for different operation states under the effect of thermal and flux gradients without hydraulic forces. FAs 1 to 8 consist of Zry-4 materials and FAs 9 to 15 of advanced Zirconium alloys.	154
6.16	Lateral strain gradients $\Delta\epsilon/\Delta x$ at grid 5 over the GTs of FA 1 for BE and upper bound (UB) GT growth.	155
6.17	FA deformations for different operation states with symmetric hydraulic forces. FAs 1 to 8 consist of Zry-4 materials and FAs 9 to 15 of advanced Zirconium alloys.	156

6.18	FA deformations for different cold end of cycle (EOC) states after operation with symmetric hydraulic forces. FAs 1 to 8 consist of Zry-4 materials and FAs 9 to 15 of advanced Zirconium alloys.	157
6.19	Evolution of maximum and RMS displacements for the reference case.	157
6.20	FA deformations for different operation states with asymmetric hydraulic forces using advanced Zirconium alloys.	159
6.21	FA deformations for the two extremal cases defined in Table 6.4 with asymmetric hydraulic forces using advanced Zirconium alloys.	161
6.22	Deviation of ex-core lateral displacements u_x at EOC between the reference case and the case with extremal parameter changes.	162
6.23	Preparation runs to create a core configuration consisting of both undeformed FAs and FAs presenting initial bow.	164
6.24	FA deformations when introducing FAs with initial bow.	165
6.25	Flow forces and FA deformations accounting for two-way FSI with uniform core inlet and outlet profiles.	167
A.1	Infinitesimal beam cross-section forming circular arc with opening angle $d\psi$ (Gross et al., 2012).	178
A.2	Schematic of Bernoulli's normality assumption (Gross et al., 2012). $w = u_z$ stands for the beam deflection and $w' = \frac{\partial u_z}{\partial x} = -\theta$ stands for the slope of the bending curve.	178
A.3	Infinitesimal beam elements (Gross et al., 2012).	179
A.4	Deformed infinitesimal beam element with cutting forces (Gross et al., 2012).	180
B.1	Axial strain as a result of anisotropic creep of Zirconium alloys under a biaxial stress state (Soniak et al., 2002).	183

List of Tables

2.1	Typical composition of Zirconium alloys for LWRs in wt.% (Murty and Charit, 2006). Only selected components are given.	47
3.1	FA reference data.	62
3.2	Description of the loading and unloading phases of the grid-to-rod joint which are represented in Figure 3.10.	69
3.3	FR support parameter values.	71
3.4	Holddown (HD) device parameter values.	75
3.5	Comparison of elapsed simulation times on a single central processing unit (CPU) and errors for different tests with the reduced models.	81
4.1	Processes over the reactor cycle (based on Salaün et al., 1993).	92
4.2	Constraints and loads for different simulation steps.	93
4.3	Coefficients for the GT creep law by Yvon et al. (1998).	96
4.4	Creep coefficients for equation 4.2 derived from linear regression.	99
4.5	Parameters for the advanced-alloy GT creep law in equation 4.2.	99
4.6	Parameters for the SRA Zry-4 FR creep law based on Soniak et al. (2002).	101
4.7	Parameters for the M5 FR creep law representative for all advanced alloys.	102
4.8	Parameters defined for the BE GT growth model based on equation 4.5 and for the linear UB growth.	104
4.9	Reference reactor data.	105
4.10	Initial Parameters for different BU conditions.	107
5.1	Geometric dimensions used for meshing the MISTRAL test section.	117
6.1	Simulation cases with constant parameters for different BU conditions.	136
6.2	Sensitivity analysis input parameters for the FA stiffness test.	141
6.3	Sensitivity analysis input parameters for the FA creep deformation test.	149
6.4	Creep and growth models used for the different FAs in the core row for the two extremal cases: lower bound (LB), best estimate (BE), or upper bound (UB).	160
B.1	Anisotropy Factors F , G , and H for cold-worked Zircaloy-2 (Zry-2) or Zircaloy-4 (Zry-4) in α -phase published by different authors.	181

List of Acronyms

BC	Boundary condition	IP	In pile
bcc	Body-centered cubic	IRI	Incomplete rod insertion
BE	Best estimate	KWU	Kraftwerk Union
BOC	Beginning of cycle	LB	Lower bound
BOL	Beginning of life	LES	Large Eddy Simulation
BU	Burnup	LWR	Light water reactor
BWR	Boiling water reactor	MOC	Middle of cycle
CC	Cold condition	NRMSE	Normalized root mean square error
CFD	Computational Fluid Dynamics	OP	Out of pile
CPU	Central processing unit	PKA	Primary knock-on atom
CSM	Computational Structural Mechanics	pRXA	Partially recrystallization-annealed
DOF	Degree of freedom	PWR	Pressurized water reactor
EOC	End of cycle	RCCA	Rod control cluster assembly
EOL	End of life	RMS	Root mean square
FA	Fuel assembly	RPV	Reactor pressure vessel
FEM	Finite Element Method	RXA	Recrystallization-annealed
FM	Fresh material	SIA	Self-interstitial atom
FR	Fuel rod	SIPA	Stress-induced preferred absorption
FSI	Fluid-structure interaction	SIPN	Stress-induced preferred nucleation
GT	Guide tube	SRA	Stress-relieved annealed
GUI	Graphical User Interface	UB	Upper bound
HC	Hot condition	Zry-4	Zircaloy-4
hcp	Hexagonal close-packed	Zry-2	Zircaloy-2
HD	Holddown		
IM	Pre-irradiated material		

Chapter 1

Introduction

1.1 Fuel assembly (FA) bow in pressurized water reactor (PWR) power plants

FAs essentially form the core of any nuclear light water reactor (LWR). Figure 1.1 illustrates the position of the FAs in the reactor pressure vessel (RPV) of a PWR. The FAs, Figure 1.2, consist of the FA structure and a bundle of fuel rods (FRs), in which the nuclear fuel is enclosed. In addition to the FRs, the FAs contain a number of control rod guide thimble tubes, or short, guide tubes (GTs). On the one hand, the GTs are an essential part of the FA structure because they carry, by means of the spacer grids, the FR bundle and connect the bottom and top nozzles, also denominated FA foot and head. On the other hand, the GTs are designed to guide the single control rods of the rod control cluster assembly (RCCA). These obtain neutron-absorbing materials to contain the fission reaction in the reactor core. Therefore, the design of the GTs must ensure that the RCCA can be inserted or dropped into the core during operation. To slow down the RCCA once it is nearly completely inserted, the bottom part of the GTs is designed to serve as a hydraulic dashpot, see the dashpot region in Figure 1.2. The correct and quick insertion of the RCCA is of crucial importance for safety since it serves to decrease the reactor power or to shut it down quickly, thereby guaranteeing the control of the reactivity, which is one of the fundamental safety functions in operational state. Since the 1990s several incomplete rod insertion (IRI) events have occurred which potentially put this safety function at risk. The first event occurred in 1994 in the Ringhals 4 reactor (Andersson et al., 2005), when one control rod failed to insert completely after a reactor scram and several others presented increased drop times. In the following fuel inspection, FA bow was determined to be the reason for these events. In particular, the FA causing the IRI exhibited an S-shaped bow with an amplitude of 20 mm. Figure 1.3 illustrates that, due to the deformed GTs, increased friction drag forces act on the single rods of the dropping RCCA, causing them to decelerate or to get stuck. In the following years, several other IRIs and increased control rod drop times were detected in different Western reactors (Roudier and Béraha, 1996). In the German LWR plants, increased permanent FA deformations have been observed since the year 2000 (RSK, 2015). Both the magnitude of the deformations and the frequency of occurrence had increased

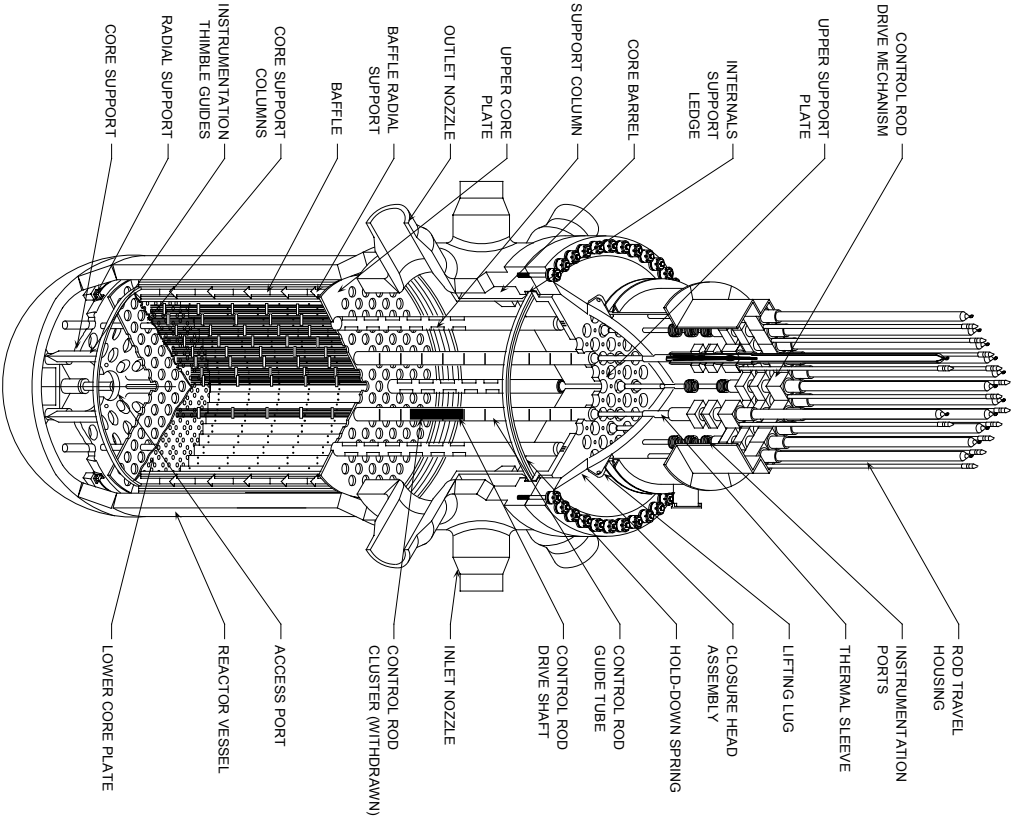


Figure 1.1: Schematic of PWR RPV and internals (USNRC, 2012).

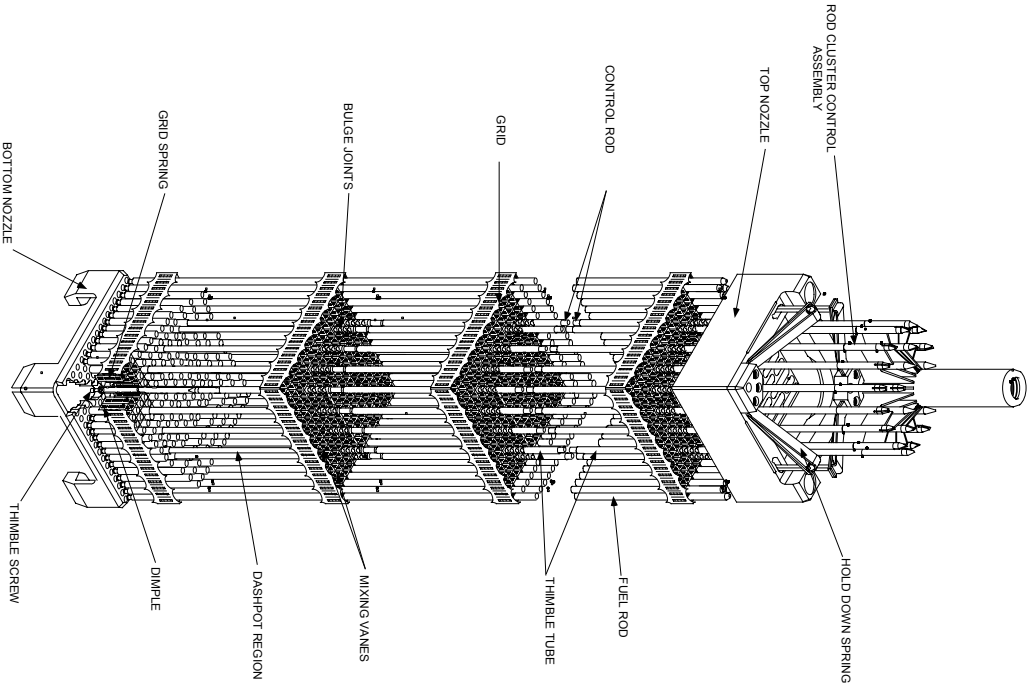


Figure 1.2: Schematic of PWR FA and RCCA (USNRC, 2012).

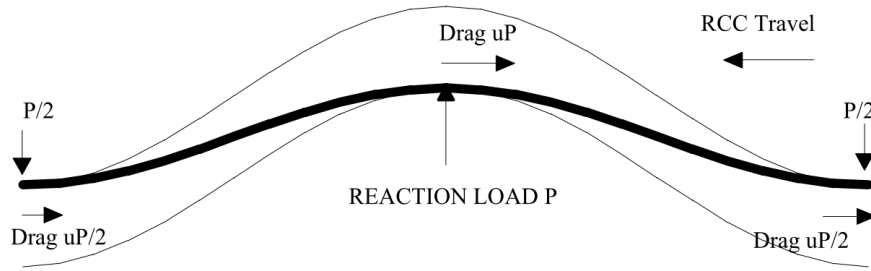
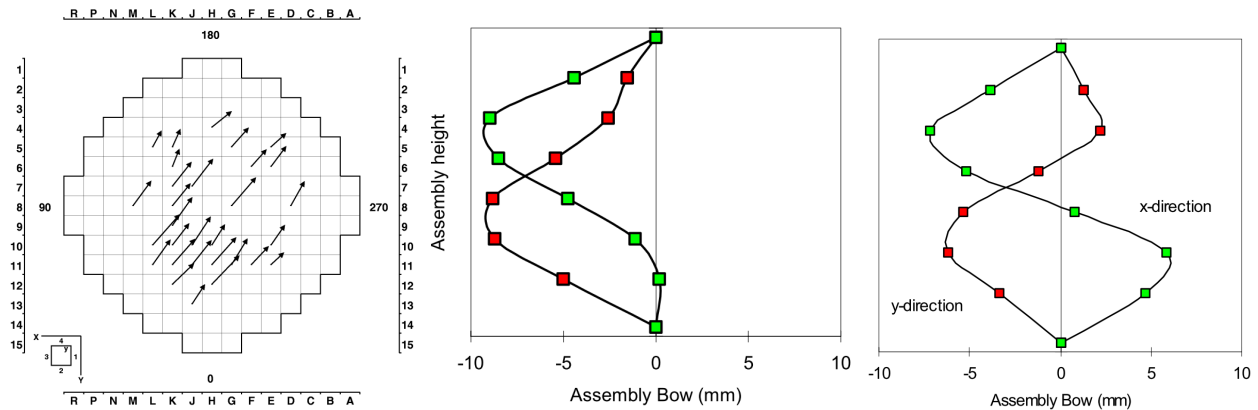


Figure 1.3: Schematic of the drag forces acting on a control rod traveling through a bowed GT (Aulló and Rabenstein, 2005).

since then until the beginning of 2010s when several events related to FA bow were reported in different power plants. In one single case, an IRI event occurred. In several other cases, increased RCCA drop times were measured, which partly exceeded the specified maximum values. In most of the above cases, collective assembly bow over the whole core was observed. The single FAs may exhibit bow amplitudes up to 25 mm and are usually deformed in one of the first three characteristic modes, that is, in a C-shape, S-shape, or W-shape. The bow shape might differ in each of the two lateral dimensions. The occurrence of collective bow over the entire core points out that FA bow cannot be analyzed individually for each FA. Instead, the FAs are coupled mechanically over the entire core, leading to seemingly random bow patterns. Often, the symmetry in the core is clearly broken, which corroborates that FA bow must be considered as a 3D problem and therefore has a multitude of degrees of freedom (DOFs). Figure 1.4 gives examples of FA bow measurements performed at the Ringhals power plant.



(a) Collective FA bow pattern measured at Ringhals 2. (b) C-shape bow measured at Ringhals 3. (c) S-shape bow measured at Ringhals 4.

Figure 1.4: Examples of FA bow measurements at Ringhals power plant (Andersson et al., 2005).

To understand the causes for the occurrence of bowed FAs since the 1990s, we need to consider the evolution process of the design and management of nuclear fuel since the first deployment in PWRs. Initially, FAs were deployed in the reactor core for a residence time of three cycles with a length of 12 months each. The degree to which the fissile material in the fuel is depleted, or “burnt”, is measured with the burnup

(BU), which expresses the energy produced per mass of heavy metal in the fuel. At the same time, this variable also represents a measure to which degree the fuel and the carrying structure have been damaged by material degradation mechanisms due to irradiation. In the initial phase in the history of PWR operation, FAs reached discharge BUs in the range of 30 GWd/t_{HM}, depending on the specific power history. Over the years, the economic incentive for optimizing core design lead to an extension of the residence time in the reactor, that is, higher maximum discharge BUs. But not only the total residence time was increased, but also the length of the single reactor cycles was often extended to 18 months to increase availability of the plants and reduce the maintenance costs associated with the refueling shutdowns. Both evolutions place increasing demands on the design performance of fuel. In particular, they require the consideration of new phenomena which occur only for high BUs, that is, in the range from 40 GWd/t_{HM} up to more than 60 GWd/t_{HM}. In conjunction with the introduction of a competitive market for the supply of fuel, operators and fuel vendors reached a substantial improvement and diversification of nuclear fuel and operational strategies in order to obtain a safe and efficient high-BU performance. To gain these advantages, several minor design changes have been introduced in FAs. Although the adverse effect on fuel stability of these changes is usually judged negligible, their cumulative impact might still destabilize the fuel structure. One of the many effects of higher discharge BU and longer cycles, is the bowing of the GTs in PWR FAs. A general understanding of the bow mechanisms appears often difficult since due to the diversification of management strategies and reactor-specific modifications the issues have become more and more plant-specific. Distortions are reported to be limited to certain power plants or reactors, for example high-temperature plants, and to FAs with certain characteristics, for example certain power histories or design features. Often not only high-BU FAs are concerned, but also FAs after the first reactor cycle. This can be explained by the fact that FA bow propagates over several cycles and that the bowed FAs with higher BUs induce bow of the fresh FAs in their first reactor cycle due to the core-wide mechanical coupling.

Since the occurrence of FA bow, operators and fuel suppliers have taken several measures to counteract the problem. On the one hand, FAs with new features have been designed to prevent the occurrence of the FA bow already at the design stage. New more creep-resistant materials were deployed for the GTs and stress-reducing measures for the FA structure were taken in order to decrease the creep deformation rates during operation. Stresses in the structures can mainly be reduced by decreasing external loads, such as the holddown (HD) forces, and by increasing the FA stiffness, by maximizing the GT wall thickness or stiffening the connection between GTs and spacer grids, for example. On the other hand, operators attempted to account for the bow at the core planning stage, placing the bowed FAs so as to prevent a further propagation of bow, or even to promote a reduction of bow. However, only simple measures can be taken as long as no computational tool is available which reliably integrates the consideration of FA bow into core planning. For example, bowed FAs can be set next to FAs which are not concerned or placed at positions or angles, at which further bowing is judged the least probable to occur.

Thanks to these measures, FA deformations could be reduced in many instances (Gentet et al., 2012; Aulló et al., 2012; RSK, 2015) and no new IRIs due to bowed assemblies have been reported in the most recent past. Still, the bow amplitudes could not be decreased to the level before the occurrence of the difficulties and FA bow continues to be observed. The bow problems can hence not be considered completely resolved, especially as the joint effect of the multitude of influencing mechanisms is still not fully understood. Therefore, the analysis of the causes of FA bow and the development of bow modeling approaches remains an important

field of research. This is particularly relevant in the light of future developments or design changes to further extend FA BU since these may bring out new safety concerns. After the introduction of new types of FAs, the modifications might be in a sort of “latent state” (Roudier and Béraha, 1996) for a time and be revealed only a few years after the changes have been made. It is hence primordial to procure that future design changes, material choice and operating strategies be in accordance with the objective to limit FA deformations.

1.2 Problems related to FA bow

FA bow causes both safety-related problems during operation and FA handling issues during outage. Safety-related problems mean that the FA bow potentially interferes, directly or indirectly, with one or several of the three fundamental safety functions, which need to be ensured during operation, namely:

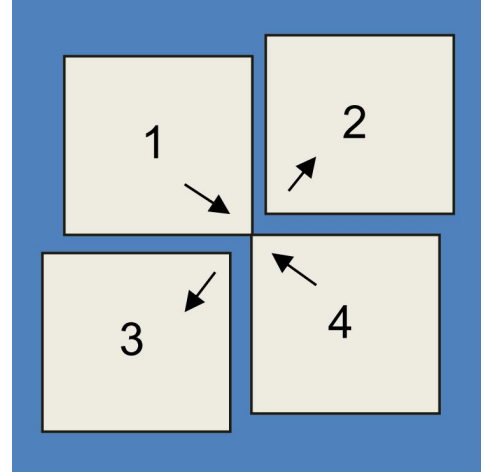
1. the control of the reactivity;
2. the heat removal from the core and, in particular, from the FRs; and
3. the confinement of radioactive materials.

One direct effect concerns the control of the reactivity due to the previously discussed increased RCCA drop times or IRIs. Other indirect effects of the FA deformations concern the thermohydraulics and the neutronics of the reactor core. For straight FAs, a water gap of about 1.6 mm exists between two neighboring FAs during operation, through which a certain amount of coolant bypasses the FAs. Due to the relative deformation of FAs as a result of FA bow, the gap width changes locally. Increased water gaps may lead to an increase in local power density due to a more effective moderation. Besides, modified gaps size may cause a different coolant flow distribution, potentially harming the heat transfer from the FRs. Moreover, in certain instances operators detected a relationship between FA bow and increased amplitudes of the neutron flux fluctuations in the reactor core, which might also cause locally increased power or decreased heat transfer. For this reason, the second fundamental function, the heat removal from the core, can also be affected by FA bow. Finally, FA bow is a factor in the third safety function by facilitating FR failure, that is, by causing damages to the FR cladding in a manner that radioactive materials are released into the coolant circuit. With the increase of FA bow, a larger number of FAs damaged by spacer grid corner fretting, depicted in Figure 1.5a, has been reported. Figure 1.5b illustrates a scenario in which contact of the spacer grid corners of two diagonally opposite FAs is possible, increasing the risk of fretting wear. As an immediate cause of the corner fretting, the FRs in the FA corner have been damaged in some cases. FR failure might also occur due to the debris released due to fretting wear at the spacer grid corners. Finally, the deformed FA structure might provoke different vibration characteristics of the FAs, thus promoting fretting wear of the FR cladding.

FA damage due to FA bow is not only an issue during operation, but also forms part of the FA handling problems during outage. When loading or unloading the reactor core, the probability of causing damage to spacer grids or FR cladding is increased due to friction forces between the bowed FAs. To avoid damages, special care or additional measures must be taken when loading or unloading deformed FAs, for example, by following a specific loading strategy or inserting dummy FAs next to strongly deformed FAs. These handling issues have a practical and economical relevance for the operator because such measures potentially increase outage times. This means a decreased availability of the reactor, thus reducing its profitability.



(a) Photograph of grid corner fretting damage (Spykman and Pattberg, 2014).



(b) Configuration of four FAs with increased risk for grid corner fretting (RSK, 2015).

Figure 1.5: Spacer grid corner fretting.

1.3 Bow influencing mechanisms

Over the years, a multitude of mechanisms have been discussed to be at the origin of FA bow or to promote it. In general, two different kinds of influencing mechanisms must be distinguished, bow-inducing mechanisms and bow-enhancing mechanisms. Bow-inducing mechanisms are those which are at the origin of bow by creating bending moments in the structure. Bow-enhancing mechanisms are those which cannot trigger the bow by themselves, but have an important influence on how and how fast it is promoted. The final bow patterns are probably the result of the interaction between the various mechanisms so that it is difficult to determine and quantify the contribution of each single effect. This coupling between several mechanisms, in addition to the mechanical coupling of the FAs in the core, can potentially have counter-intuitive and self-amplifying effects and could explain the occurrences of strongly deformed cores with asymmetric bow patterns. The coupling effect between a multitude of influencing factors and DOFs represents one of the largest challenges in the modeling of FA bow. The following paragraphs present the different influencing mechanisms that have been identified as potentially bow-inducing or bow-enhancing. On the one hand, they cover material degradation mechanisms, which are physically speaking at the origin of the permanent FA deformations by means of microstructural changes in the material. On the other hand, they discuss certain reactor boundary conditions (BCs) on the FAs, which cause this material degradation to happen and might therefore induce the bow. Figure 1.6 summarizes graphically the different bow-influencing mechanisms.

Holddown (HD) force The FAs in the reactor core are compressed from the top by the upper core plate to prevent the FA to lift off from the lower core plate due to the effect of the upward coolant flow. For this purpose, the FA top nozzle is provided with HD springs, which are in contact with the upper core plate and generate a compressive HD force on the FA. When higher than expected FA bow was first observed in Ringhals in 1994, the occurrence of bow was ascribed to excessive HD force. GT buckling due to excessive axial loads can, however, be excluded as root cause for the deformation since the GTs are designed to

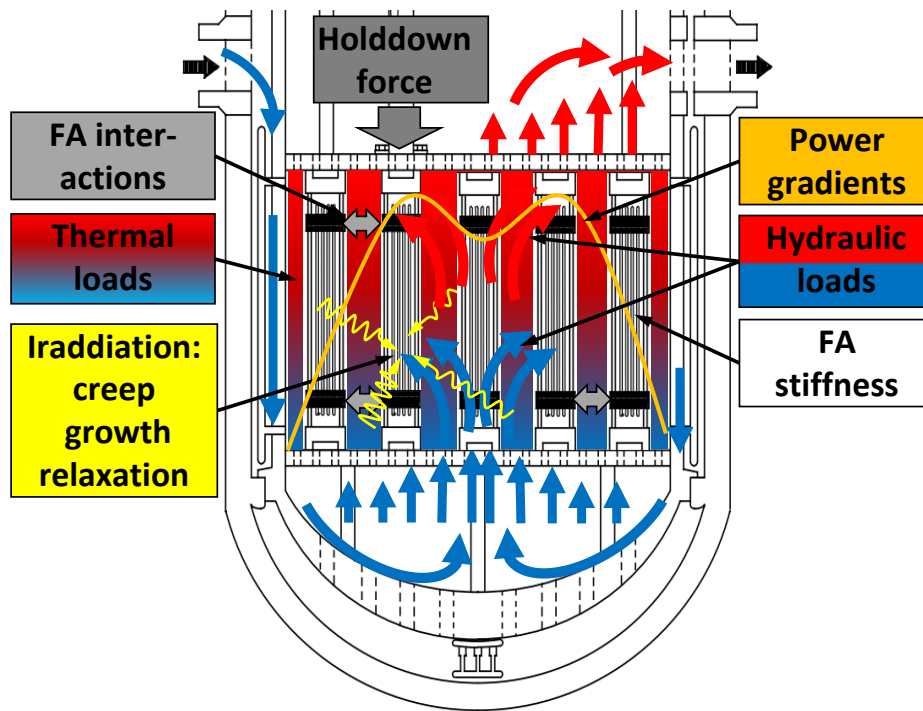


Figure 1.6: Graphical representation of in-reactor FA bow influencing mechanisms. Background drawing from USNRC (2012).

offer sufficient margin against buckling in highly demanding situations, such as design-basis accidents. The maximum GT compressive load under normal operation is hence by far below the critical buckling load. Nevertheless, the HD force can contribute to the occurrence of FA bow by means of the structural softening effect of normal compressive stresses in slender structures. That is, the higher the axial compressive load on the FA, the lower is the effective lateral stiffness. High HD forces consequently enhance the FA elastic lateral deformation due to external loads, and by this means also the lateral creep deformation rate, which is one of the causes of the permanent FA deformation, see section 1.3.

Structural growth Structural irradiation growth is the root cause for increasing HD forces during operation. Due to the fast neutron irradiation in the reactor, the Zirconium-alloy GTs undergo a length increase as a result of their anisotropic crystal lattice. This lengthening leads to an axial growth of the FA structure, thus compressing the HD springs and potentially increasing the HD forces. By this means, irradiation growth may indirectly enhance FA bow. In addition, structural growth may also directly induce FA bow by means of the differential elongation of the single GTs. Each single GT might undergo a different length increase due to the effect of lateral gradients of the fast neutron flux over the FA, thus creating bending moments in the FA structure.

Structural creep The permanent deformation of the FAs is associated with the formation of plastic strains in the FA structure. The materials of the FA structure are selected such that they offer sufficient margin between the mechanical stresses occurring during operation and the yield stress beyond which an instantaneous plastic deformation occurs. The plastic strains causing FA bow must hence derive from long-

term time-dependent plasticity effects without stress threshold such as creep or growth. In nuclear reactors, creep is induced and enhanced by microscopic effects of the fast neutron irradiation on the crystal lattice of the material, leading to plastic strain in the direction of the applied stress. Creep exists only in the presence of internal material stresses, which are the result of external loads. The creep deformation is hence an important contributor to FA bow; however, driving forces are required to induce this deformation.

FA stiffness The lateral stiffness of the FA determines the elastic deformation and therefore the stresses in the FA structure. The higher the elastic deformation is under an external load, the higher will be the creep deformation rate. Therefore, the susceptibility of the FA structure to lateral bow can be reduced by increasing its stiffness. Important influencing parameters on the FA stiffness are: on the one hand, the bending stiffness and axial stiffness of the single GTs and FRs; on the other hand, the structural coupling between all GTs and FRs at the spacer grid levels, which provides an additional stiffening effect to the FA structure. The strength of the coupling effect is mostly determined by two factors; first, the stiffness of the connections between the spacer grids and the GTs and FRs; second, the cross-sectional positions of the FRs and GTs, an effect known from Steiner's theorem.

Structural relaxation The lateral FA stiffness does not remain constant during the operational life of the FA. Before operation, the spacer grid springs are pre-stressed to maintain the FRs in position under all transport and handling conditions. For fresh FAs, the FRs hence contribute strongly to the overall FA stiffness. During operation, the spring preload relaxes, thus reducing the coupling between the FR bundle and the FA structure and therefore the overall FA stiffness. The reduced stiffness naturally leads to higher stresses for a given load condition. This effect increases the creep deformation rate and, hence, promotes the FA bow. The structural relaxation of the FA springs can therefore be regarded as a bow-enhancing mechanism. In contrast, the relaxation of the HD spring decreases the HD force and therefore can reduce the bow-enhancing effect of the HD force.

Thermal loads (Temperature) Like the fast neutron flux, the material temperature is an important parameter for the creep deformation of materials under mechanical stresses. As a result of lateral thermal gradients, thermal loads might also induce permanent FA deformations by means of a laterally variable build-up of creep strains. Important lateral temperature differences contributing to this effect are mostly expected for the FRs, due to lateral power gradients over the FA. The FA structure, in turn, is well cooled by the coolant flow so that mainly axial temperature differences exist. Besides their influence on creep, lateral thermal gradients over the FA can also induce FA deformations as an independent mechanism. This is due to the differential thermal expansion of the FA components leading to internal bending moments. Although this is a reversible process, which loses its effect when the gradient vanishes, it might introduce perturbations into the system of coupled FAs. Finally, the axially variable coolant temperature along the FA may also lead to axial differences in the grid spring relaxation. This may modify the axial center of rigidity of the FA, leading to potentially different deformation shapes.

Fast neutron irradiation The fast neutron irradiation plays a fundamental role for the permanent deformation of the FA structure in the reactor core. Fast neutrons are capable of creating damage to the crystal lattice of the metallic alloys, thereby inducing irradiation creep and growth. Moreover, fast neutron

irradiation enhances thermal creep mechanisms. Without the contribution of the fast neutron irradiation, the creep and relaxation effects would be strongly reduced and practically no growth would occur. The distribution of the fast neutron flux in the reactor depends on the power profile and plays an important role for the FA deformations. Depending on the position of the FA in the core, the magnitude of the flux will be different, thus accelerating or decelerating the creep rate when compared to the average flux. The maximum-to-minimum flux ratio can reach values up to 3, particularly for core loading patterns with low neutron leakage at the core periphery. The power gradients in the core can lead to lateral fast flux gradients over single FAs, thus causing differential creep and growth in the FA structure. These induce internal bending moments in the FA structure, which add up to the bending produced by external loads.

Lateral mechanical coupling When the relative lateral deformation between two neighboring FAs is larger than the initial gap between them, the gap is closed and inter-FA contact is established. In this manner, the two FAs are coupled mechanically in the lateral translational DOF. In practice, most FAs in the core are getting in contact to each other during operation at different axial levels, creating a coupled nonlinear mechanical system with a multitude of DOFs. That is, the bow deformation of single FAs may propagate over the entire core, thus creating collective bow patterns. On the other hand, the mechanical coupling also sets a limit to the deformation. When a deformed FA is coupled laterally to an undeformed FA, the reaction force acting on the deformed FA at the point of contact might decrease its permanent deformation over time. Moreover, the lateral coupling of the peripheral FAs with the core baffle limits the maximum deformation of the FAs in the reactor core. Within one FA row, the deformation is limited to the cumulative gap size between the FAs of this row. Since the nominal gap size in hot condition between the Zirconium alloy grids of two neighboring FAs is about 1.6 mm, the maximum deformation is limited to a maximum of about 26 mm. This value is possibly decreased by the growth of the spacer grids during reactor operation.

Lateral hydraulic loads Figures 1.6 illustrates that the coolant flow follows a specific path through the RPV: from the inlet nozzles down the downcomer to the lower plenum and then through the reactor core and the upper plenum to the outlet nozzles. Due to the direction change of the flow in the lower and upper plena, a uniform flow profile at the inlet and the outlet of the core cannot be guaranteed. Ulrych and Weber (1983) offered a detailed description of the specific flow conditions in the plena: The lower plenum consists of the hemispherical bottom of the RPV and the internal structures installed for homogenizing the flow distribution, for example, a so-called flow skirt. The flow conditions in the lower plenum are complex and depend on how the flow developed in the downcomer. One influencing factor might be the start-up order of the main coolant pumps, for example. Without the internal structures, the coolant flows along the RPV wall due to its inertia. A high-pressure region develops at the bottom of the lower plenum with flow stagnation in the lowest point. Due to this, the coolant is diverted and flows upwards with a maximum in the center of the core. At the same time, large eddies in the peripheral regions of the core would drag the flow downwards at the sides so that the peak-to-average velocity at the core inlet would become excessive without internal structures. The purpose of these internal structures is therefore to force the coolant upwards already in the peripheral regions, thus homogenizing the flow. Still, a characteristic flow profile with a maximum in the core center develops in most cases. The exact profile shape depends on the design of the lower plenum structures, which differ significantly among the different PWR types. In the upper plenum, the suction effect

of the coolant outlet nozzles produces a non-uniform lateral pressure distribution with increased pressures in the central region and low pressure in the periphery close to the nozzles. The pressure distribution is additionally influenced by the support structures in the upper plenum. Due to these specific conditions in the upper plenum, a non-uniform flow profile with increased velocities at the periphery develops also at the core outlet.

Due to the non-uniform coolant flow inlet and outlet profiles at the lower and upper core plates, cross-flow is induced in the core as a result of lateral pressure gradients. In general, a certain amount of cross-flow may be desired to achieve improved heat transfer between hotter and colder areas in the reactor core. For this purpose, the FA spacer grids are also equipped with mixing vanes to induce flow swirls, thus increasing cross-flow and local heat transfer. At the FA scale, this local cross-flow has normally no preferential direction since the generated eddies are of the length scale of the FR pitch. In contrast, the cross-flow generated by the non-uniform distribution of the flow at the core inlet and outlet induces cross-flow over several FAs. In this manner, unidirectional hydraulic loads on the single FAs are generated, thus creating bending moments on the FA structures. Over short time scales, this transverse flow may induce FA or FR vibrations whereas over long time scales – such as an entire operating cycle – the hydraulic loads may induce permanent FA deformations as a result of creep. These hydraulic loads are believed to be one of the major driving mechanisms of FA bow.

1.4 Literature review of the modeling of FA deformations and of related phenomena

This review is divided into three parts. The first part introduces the development of FA structural models, the second part presents the efforts in modeling the core-wide flow distribution, and finally recent approaches which couple both the FA structures and coolant flow are described.

FA structural models Since the first deployment of FAs in PWR cores, structural models have been developed to evaluate the FA structural response. Barinka (1971) was one of the first to publish a theoretical description of the general structural behavior of FAs, considering it as a particular case of a coupled tubular structure. In this description, the spacer grids are so-called coupling stations, which are considered rigid and to which the GTs and FRs are connected by means of nonlinear translational and rotational springs. Based hereupon, Barinka developed an analytical computer model, consisting of linear Euler-Bernoulli beams coupled with nonlinear springs. This allows to calculate the nonlinear deflection response of the FA structure due to mechanical loads. Since models of this type consider only the structural behavior of fresh FAs with zero BU, they can easily be validated with experimental data from in-laboratory structural deflection tests. In this early stage, the modeling of the in-reactor FA material degradation effects – such as creep, growth, and spring relaxation – was mostly of interest for the FR mechanical response. With this type of analysis, operators predict the permanent diametral deformation of the FR cladding, referred to as creep-down, the permanent axial elongation, referred to as growth, as well as the change of the vibration behavior of the FR due to the relaxation of the grid springs which form the FR support. Before the occurrence of FA bow, the relevance of the material degradation effects on the FA structural response was mostly limited to the prediction of the axial FA growth. These calculations serve to guarantee sufficient HD force on the FA to prevent lift-off and to maintain sufficient margin for the FRs to elongate freely (Salaün et al., 1993, for

example).

With the increasing relevance of FA bow to safety in the 1990s, several models to predict the lateral FA deformation during operation have been created. These models were the first step to develop computational tools to ultimately predict the FA bow deformation in the core in order to optimize the FA design and core planning. Stabel and Hübsch (1995) and Salaün et al. (1997), for example, presented FA deformation models based on an analytical approach. At the same time, FA structural models based on the Finite Element Method (FEM) were also established (Levasseur et al., 2009; Aleshin et al., 2009; Morales et al., 2012). These models use a completely numerical approach, which allows a higher flexibility in the implementation and the use of widely available modular FEM software. By coupling the single FA models next to each other, calculations over FA rows or the entire core became possible. Such models were described, for example, by Marin et al. (2001). Figure 1.7 gives two examples for the typical output produced by such tools.

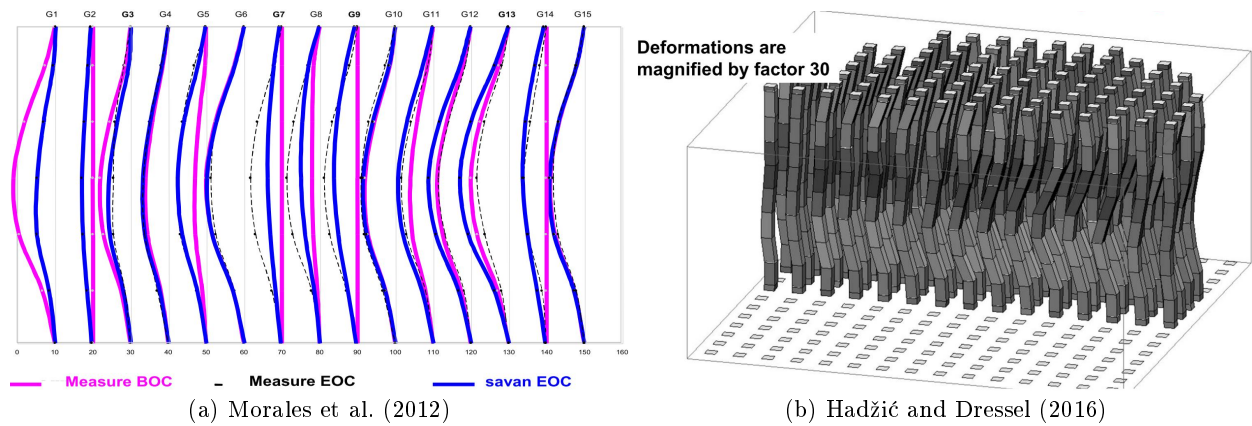


Figure 1.7: Examples for FA bow predictions by computational tools.

Core-wide lateral hydraulic flow models In the initial phase of bow code development, researchers concentrated on the thermal and neutron flux loads to calculate the structural behavior of the FAs. It became, however, clear that the bow could not be explained without an additional driving force. The lateral hydraulic forces due to cross-flow in the reactor core was hence judged to be a very important parameter for FA bow. However, an accurate prediction of the flow distribution in the core is difficult to achieve. This is both due to the large size of the resulting computational models and the lack of validation possibilities because it is not realistic to perform reliable measurements of the flow distribution inside the reactor core. As a first approach, results from thermohydraulic codes were integrated into the bow models as constant BC (Levasseur et al., 2009). Stabel et al. (2011) presented a hydraulic model developed specifically for FA bow calculations which consists of a network of pipes with different hydraulic parameters.

Using simplified thermohydraulic models to predict the lateral loads presents, however, several weaknesses. First, the hydraulic parameters necessary for the implementation of local pressure losses are difficult to obtain due to the small and complex geometry of the spacer grids and other relevant structures as well as due to the strong dependence of the lateral drag forces on the angle of attack. Second, the flow upstream and downstream of the core can have an important influence on the flow distribution inside the core, which is why the core inlet and outlet BCs must be well known to reliably predict the hydraulic forces. Computational Fluid Dynamics (CFD) simulations with resolved structures predicting the flow evolution in the entire RPV

– or at least from the lower to the upper plenum – would be necessary for this purpose. The length scales of the flow of the coolant through the reactor core extend over several orders of magnitude, from the core size of several meters down to tenths of millimeters when considering the details of the spacer grids or the FR deformations. When resolving the structure with a discretization grid, the resulting large model size requires significant computational resources and modeling effort. Although resolved CFD calculations over the entire flow path of the coolant in the RPV remain still out of reach, calculations over parts of the flow path of the coolant in the RPV have become possible with the quick evolution of computational performance. CFD calculations with a resolved structure have recently been performed over specific core and plenum regions, see the publications of Fournier et al. (2007), Karoutas et al. (2010), or Xu et al. (2012), for example. To verify the validity of the prediction results, the authors mostly refer to experimental investigations on simplified and downscaled mock-ups, mostly operated with air as flow medium.

Fournier et al. (2007) calculated the flow in the lower plenum and the lower core region of a PWR using a CFD model with resolved structures. The results confirmed the non-uniform core inlet velocity distribution observed with experimental flow loops. Figure 1.8a gives an example output of the axial velocity distribution under the first spacer grid. The CFD calculations by Karoutas et al. (2010) over one quarter of a PWR core also predicted a non-uniform velocity profile in the lower portion of the core. The distribution of the obtained core inlet velocities was in reasonable agreement with experimental data. Finally, Xu et al. (2012) gave results of resolved CFD simulations over the upper plenum including the top of the reactor core and the outlet nozzles and detected a clear influence of the outlet nozzles on the lateral flows in the reactor core. Figure 1.8b gives an example output of the pressure distribution in the upper core plate. Nonetheless, it must be remembered that the coolant flow in nuclear reactor cores is highly turbulent. Therefore, Large Eddy Simulation (LES) techniques might be required to obtain reliable results. However, with the current computational performance only LES simulations over a fraction of a single FA are feasible (Bieder, 2015).

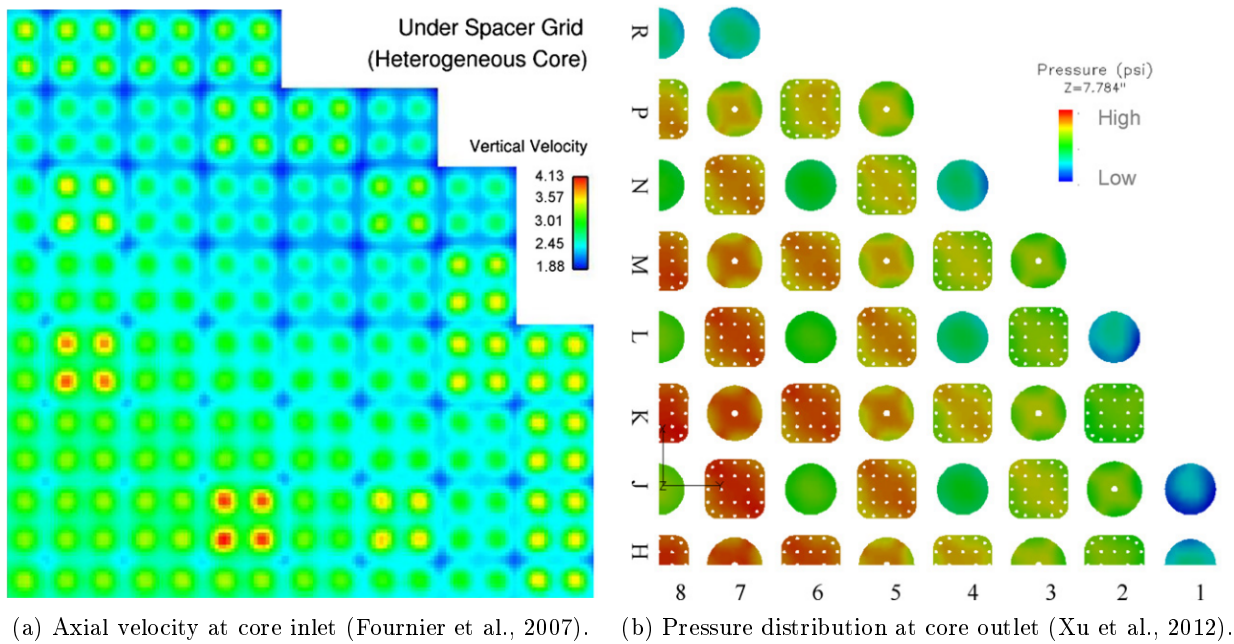


Figure 1.8: Example outputs for CFD calculations over partial core sections.

Recent approaches including fluid-structure interaction (FSI) Experimental results published by Stabel et al. (2011) have demonstrated the importance of flow-induced FA bow due to FSI effects acting between neighboring FAs. The experiments showed that bow may be induced on straight FAs due to the flow displacement effects caused by the deformation of neighboring FAs. Moreover, the specific FA and spacer grid design proved to have an influence on the elastic deformation shape. Along with the experimental results, Stabel et al. (2011) presented a FA bow model which offers a two-way coupling between the FA structure and a simplified hydraulic model. Horvath and Dressel (2013) undertook a first attempt to model a two-way coupling between CFD calculations and a FA structural bowing code, considering one row of FAs in the reactor core. Coupled CFD and structural simulations over the entire core require still a tremendous computational expense and have not been realized so far. Lascar et al. (2015) published the most recent description of bow modeling over the entire core, which uses simplified hydraulic models validated with local CFD simulations. When compared to end of cycle (EOC) bow measurements, the obtained results are promising but underline, at the same time, that considerable prediction uncertainties remain, both regarding the deformation amplitude and direction, see Figure 1.9.

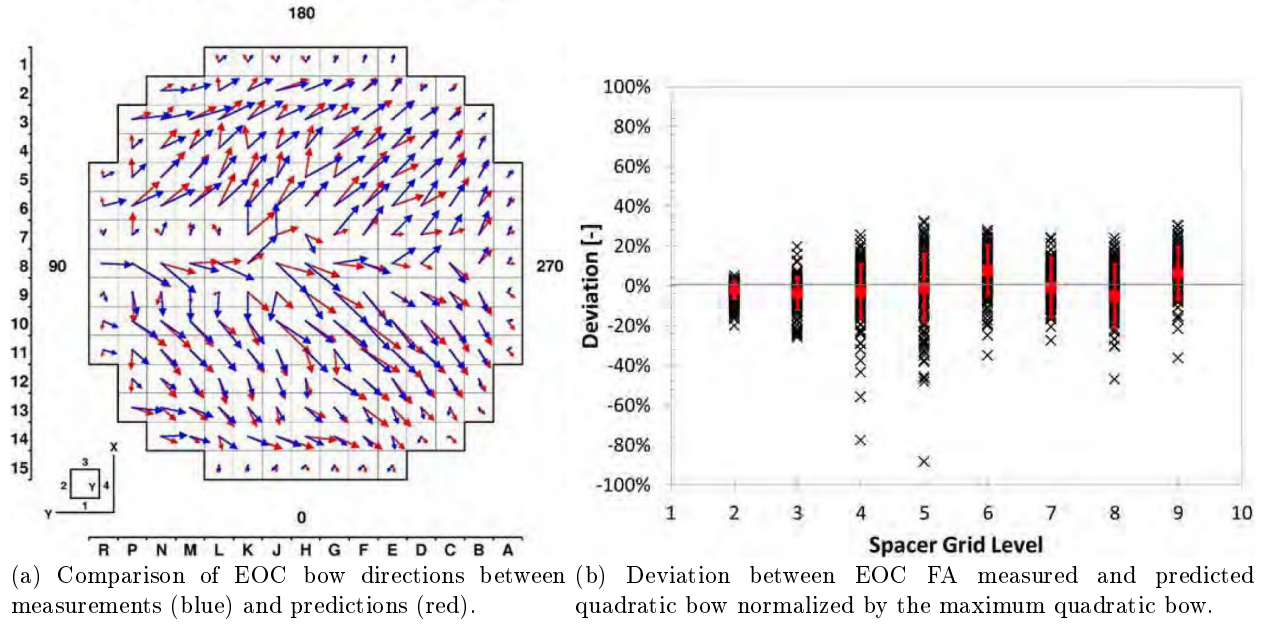


Figure 1.9: Examples for recent bow predictions versus measurements (Lascar et al., 2015).

1.5 Motivation and objectives of this work

The so far presented bow modeling results show that still larger deviations exist between theory and the final measurements of the free bow shapes at EOC despite the large modeling effort invested in making reliable predictions. This raises the fundamental question about how reliable the prediction of the FA bow shapes and amplitudes can be with the available modeling methods. There might be a more fundamental reason for these discrepancies which cannot be solved by ever more refining the model, at least not with the currently available computational methods and means for code validation. When considering most of the presented influencing mechanisms, there is an important uncertainty about their actual value in the reactor.

The only parameters that can be measured reliably are the out of pile (OP) stiffness and deformation of the fresh FA and the neutron flux at certain positions in the reactor. The online measurement of other parameters, such as the coolant cross-flow velocity or the in-core deformation of the FAs, would require the costly development of new measurement techniques and retrofittings in the reactor to install the devices. Moreover, the informative value of punctual flow measurements is questionable since the global cross-flow can be overlaid by other effects such as local eddies. There is hence a fundamental epistemic uncertainty about these parameters. To still obtain the required parameter values to feed the models, researchers have created simplified and down-sized experimental set-ups, which allow to estimate the probable parameter values during operation. Examples are hydraulic flow tests in RPV mock-ups or creep tests of specific FA components performed in test or power reactors. However, the resulting irradiation test data often exhibit an important scatter among several samples. While there may be deterministic reasons for this spread, they can be described as aleatoric uncertainties since they often cannot be controlled by the experimentalist. Possible reasons are differences in the microstructure or imperfections inherent to the manufacturing process.

To summarize, the intrinsic difficulty of bow modeling is that there are significant epistemic and aleatoric uncertainties about the BCs and material models. The uncertainties might even systematically add up due to the multitude of influencing mechanisms. An additional detrimental effect may be caused by the core-wide coupling of the mechanical system and the resulting large number of DOFs. Due to this, the uncertainties might propagate over time and space, leading to unexpected results. Under these circumstances, it can be very challenging to find a best estimate (BE) solution with a sufficiently small uncertainty width to obtain meaningful predictions about the bow patterns to expect after one reactor cycle.

The objective of this work is therefore to approach the FA bow modeling from a novel point of view, namely setting the focus on sensitivity and uncertainty analysis. For this purpose, a computer model needs to be created as a first step to perform the analyses of the FA bow phenomena. The majority of the work on FA bow and its modeling has been performed in the context of industrial research. Therefore, most of the models are proprietary so that the possibilities to investigate specific model features and to verify their performance are limited. By constructing a completely new model, a first step to the treatment of the highly complex FA bow modeling problem in the framework of academic research shall be done. The objective is to build up a generic model which is capable of reproducing the typical in-reactor structural behavior of PWR FAs. The structural and hydraulic submodels are to be generated in such a flexible way that the most common PWR FA designs can be simulated. Although several choices about the specific FA design must be made in this thesis, the model should be adaptable to other designs by simply modifying the concerned parameters. In this present work, the ANSYS software suite is used for the Computational Structural Mechanics (CSM) and CFD applications. Despite the use of this specific software package, the modeling strategy of the single features shall be described comprehensively from a general point of view. This guarantees the reproducibility of the model for the purpose of further academic research using any software that offers an interface for the implementation of the required model features.

The computer model is to be created as a modular tool, featuring all the influencing mechanisms which have been identified as possibly significant for the FA bow, see section 1.3. With this tool sensitivity analyses shall be performed to investigate the sensitivity of the modeled system to the different influencing factors. This serves to identify, on the one hand, the most important structural parameters of the FA model and, on the other hand, the dominant mechanisms leading to the permanent FA bow. An important part of this

sensitivity analysis will be the estimation of the uncertainty range of the different model input parameters based on the available data sources and the acquired knowledge about the system. After identifying the most significant uncertainty factors, the final objective is to evaluate the total effect of these uncertainties on the outcome of the simulations. That is, we want to observe the variability of the bow predictions based on the uncertainty about the most important influencing parameters. By this means, we can evaluate the predictive power and reliability of bow prediction models and draw conclusions about the predictability of a single FA bow pattern for a specific reactor cycle.

1.6 Outline of the thesis: modeling and simulation steps

The main part of this thesis can be subdivided into three blocks: theory, model description, and results. Chapter 2 gives the theoretical basis for the modeling concepts used in this work. It describes the analytical and numerical concepts necessary for the modeling of the structural and fluid mechanical problems. The next block describes the set-up of the model and its BCs and is subdivided into three chapters. Chapter 3 describes the set-up of the FA structural model and justifies the modeling choices that are made. The FA structural model represents the first modeling step on the path to modeling the FA behavior in the reactor:

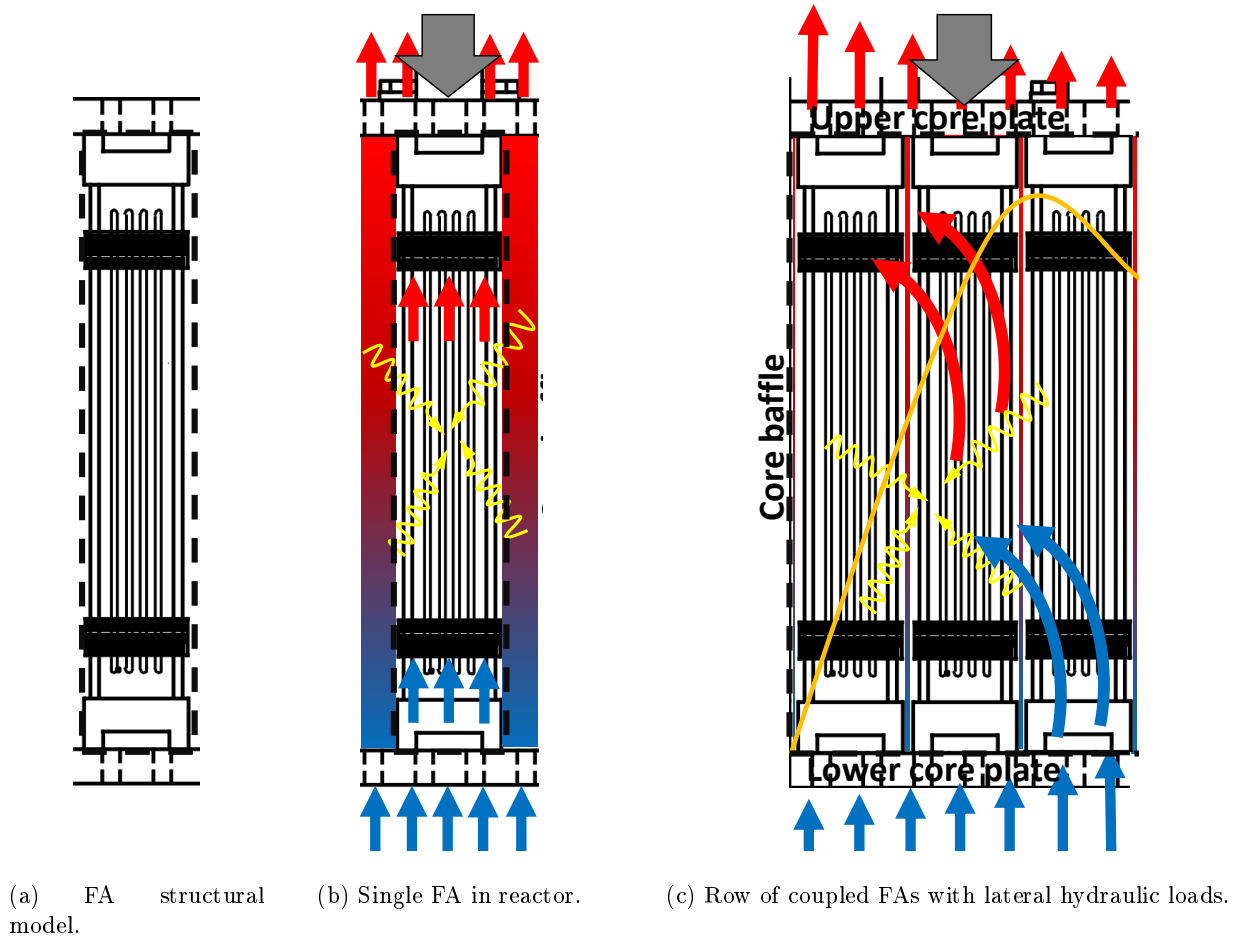


Figure 1.10: Schematic of the modeling steps done in this thesis based on Figure 1.6. The black dashed line encloses the modeled domain.

the modeling and simulation of the structural response of an isolated FA in laboratory conditions, see Figure 1.10a. Chapter 4 covers the modeling of all mechanisms influencing the deformation of FAs during reactor operation except for the hydraulic loads, which are treated in a separate chapter. In particular, the modeling of the material degradation mechanisms creep, growth, and relaxation is considered. Moreover, the temperature and neutron flux BCs are defined, which are essential for the calculation of the material degradation. Chapter 5 then describes the hydraulic model, which is used to produce the distribution of hydraulic forces on the FAs in the core, that is, the hydraulic load BC.

The last block, chapter 6, gives the entirety of the results for the simulations of the FA deformation during one reactor cycle obtained with the presented model and of the associated sensitivity analyses. For this purpose, several scenarios are described. First, only a single isolated FA in the reactor is considered, simulating its response to all axial reactor loads as well as discrete lateral test loads, see Figure 1.10b. This represents an intermediate modeling step since the realistic reactor loads and model components inducing lateral bow are not yet accounted for. These loads are integrated in the last modeling step, illustrated in Figure 1.10c. The FAs are set in a row and are coupled mechanically to each other. Then, an estimated distribution of lateral hydraulic loads and power gradients are imposed on the model. For each of the modeling scenarios, reference results are described based on the BE model parameters defined in the model description. Then, different sensitivity and uncertainty analyses are performed to investigate the sensitivity of the model to different influencing mechanisms based on the assumed uncertainty range for the concerned model parameters.

The final chapter 7 gives the conclusions obtained from the modeling process and the observed results. It discusses further aspects and gives an outlook on future work.

Chapter 2

Modeling Theory

2.1 Structural mechanics

2.1.1 Linear isotropic elasticity

The time scales of the permanent fuel assembly (FA) creep and growth deformation effects are very long compared to the characteristic FA vibration frequencies. We can therefore limit this introduction to the theory of elastostatic problems. Elastostatic problems are based on three fundamental relationships, the strain-displacement equations, the stress-strain relationships, and the equilibrium equations (Szabó and Babuška, 2011). The unknowns of any mechanical problem are the components of the displacement vector u_i at any position x_i in the Euclidean space. Strain is a relative measure of the deformation at a certain point of the continuum in relation to a reference length. For arbitrarily large displacements and strains, a multitude of stress-strain relationships can be constructed, one of which is the Almansi strain tensor e_{ij} :

$$e_{ij} = \frac{1}{2} \left(\frac{\partial u_i}{\partial x_j} + \frac{\partial u_j}{\partial x_i} - \frac{\partial u_k}{\partial x_j} \frac{\partial u_k}{\partial x_i} \right) \quad (2.1)$$

Since the bow deformations are small compared to the FA length scale, we can use the infinitesimal strain theory which assumes small displacements and rotations, $\|u_i\| \ll 1$, as well as small strains, $\|\frac{\partial u_i}{\partial x_j}\| \ll 1$. This allows us to neglect the nonlinear term in equation 2.1, which results in the linear infinitesimal strain tensor ε_{ij} :

$$\varepsilon_{ij} = \frac{1}{2} \left(\frac{\partial u_i}{\partial x_j} + \frac{\partial u_j}{\partial x_i} \right) \quad (2.2)$$

The mechanical stress σ is defined as force per unit area. In any externally loaded material there exists a three-dimensional internal stress field, see Figure 2.1. The single components form together the stress tensor

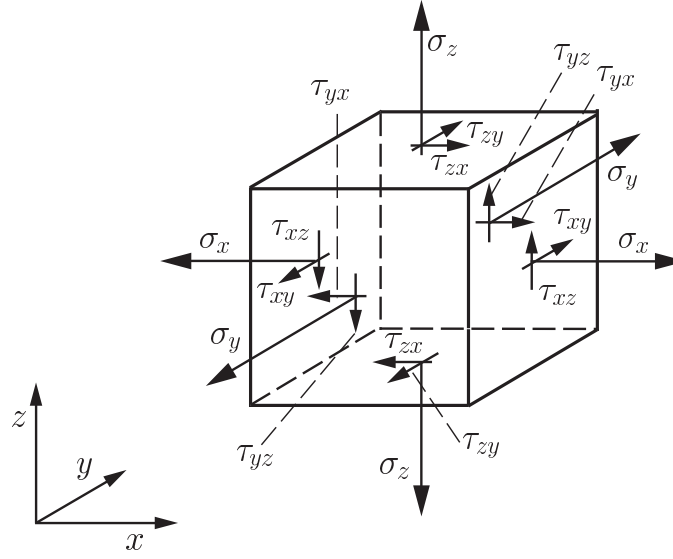


Figure 2.1: Notation for stress components on an infinitesimal volume element (Szabó and Babuška, 2011).

σ_{ij} , in which σ denominates normal stresses and τ denominates shear stresses:

$$\boldsymbol{\sigma} = \begin{bmatrix} \sigma_x & \tau_{xy} & \tau_{xz} \\ \tau_{yx} & \sigma_y & \tau_{yz} \\ \tau_{zx} & \tau_{zy} & \sigma_z \end{bmatrix} \quad (2.3)$$

Assuming that the material is not loaded by distributed moments, the stress tensor is symmetric, that is, $\sigma_{ij} = \sigma_{ji}$. The stress tensor can be related to the strain tensor by the following constitutive equation:

$$\sigma_{ij} = C_{ijkl} \varepsilon_{ij} \quad (2.4)$$

where C_{ijkl} is the elasticity tensor of 4th order which consists of 81 components. For a linear, isotropic, and elastic continuum, equation 2.4 can be reduced to a relationship between stress and elastic strain ε^{el} with only two constants by introducing the Lamé coefficients λ and μ :

$$\sigma_{ij} = \lambda \varepsilon_{kk}^{\text{el}} \delta_{ij} + 2\mu \varepsilon_{ij}^{\text{el}} \quad (2.5)$$

Equation 2.5 can be reshaped into Hooke's law, introducing the experimentally established Young's modulus E and Poisson's ratio ν as constants:

$$\varepsilon_{ij}^{\text{el}} = \frac{1+\nu}{E} \sigma_{ij} - \frac{\nu}{E} \sigma_{kk} \delta_{ij} \quad (2.6)$$

Due to the thermal expansion of the material, a thermal strain ε^{th} is introduced into the stress-strain relationship. The thermal strain is defined as the relative shape change of the material when heating or cooling it from a reference temperature T_{ref} to temperature T so that $\Delta T = T - T_{\text{ref}}$.

$$\varepsilon^{\text{th}} = \int_{T_{\text{ref}}}^T \alpha_{\text{tan}}(\hat{T}) d\hat{T} = \alpha_{\text{sec}}(\Delta T) \Delta T \quad (2.7)$$

In equation 2.7, α_{tan} is the tangent, or instantaneous, coefficient of thermal expansion and α_{sec} is the secant, or integrated, coefficient of thermal expansion. For thermoelastic materials, the total strain ε^{tot} is the sum of the elastic strain and the thermal strain.

$$\varepsilon^{\text{tot}} = \varepsilon^{\text{el}} + \varepsilon^{\text{th}} \quad (2.8)$$

The thermoelastic constitutive equations are obtained by expanding Hooke's law:

$$\varepsilon_{ij}^{\text{tot}} = \frac{1+\nu}{E}\sigma_{ij} - \frac{\nu}{E}\sigma_{kk}\delta_{ij} + \alpha\Delta T \quad (2.9)$$

The final set of equations necessary for solving an elastostatic problem are the equilibrium equations. Considering the volume element in Figure 2.1, the elastostatic equilibrium of the internal stresses with an external body force $f_{B,i}$ in the three spatial dimensions is given by the following equation:

$$\frac{\partial \sigma_{ij}}{\partial x_j} + f_{B,i} = 0 \quad (2.10)$$

The internal strain energy associated to the internal stresses and strains is obtained by integration over the entire continuous domain Ω , see the first term in equation 2.11. The total internal energy $U(u_i)$ for a kinematically admissible displacement field u_i is composed of the internal strain energy of the continuum and the energy of the translational and rotational springs with stiffness k_u and k_θ :

$$U(u_i) = \frac{1}{2} \int_{\Omega} \sigma_{ij} \varepsilon_{ij} dV + \frac{1}{2} \sum_j k_{u,j} u_j^2 + \frac{1}{2} \sum_j k_{\theta,j} \theta_j^2 \quad (2.11)$$

The work $W(u_i)$ of the external forces, composed of the body force $f_{B,i}$ applied over Ω and the surface force $f_{S,i}$ applied at the domain boundary $\partial\Omega$, is given in equation 2.12:

$$W(u_i) = \int_{\Omega} f_{B,i} u_i dV + \int_{\partial\Omega} f_{S,i} u_i dS \quad (2.12)$$

The potential energy Π is defined as:

$$\Pi = U - W \quad (2.13)$$

2.1.2 Creep – a type of rate-dependent plasticity

The classical concept of plasticity describes time-independent inelastic deformations, assuming that the deformation occurs instantaneously with the load application as soon as the stress in the material reaches a specific yield stress σ_Y . However, plastic flow can also develop as time-dependent inelastic strain which may occur for stresses below the yield stress. This phenomenon is referred to as creep and implies progressing inelastic strains, leading potentially to creep rupture. Since the materials and structures in nuclear reactors are designed to provide sufficient margin to yielding under normal operation, the only possible stress-induced mechanism to permanently deform the structures is creep. The mathematical theory of the modeling of creep is, for example, discussed by Kojić and Bathe (2005) and Naumenko and Altenbach (2007) and is introduced in the following subsections. First, the general theory of plasticity models is introduced. The subsequent

section describes more in detail the evolution of creep under specific loading conditions and the associated creep laws.

2.1.2.1 Plasticity modeling

An important step in the theory of plasticity modeling is the definition of a yield criterion $f_Y(\sigma_{ij}) = 0$, which defines for which three-dimensional stress states yielding of the material occurs. As a 3×3 tensor of second degree, the stress tensor possesses three invariants J_i , which are independent of any base transformation:

$$J_1 = \sigma_{kk} \quad (2.14)$$

$$J_2 = \frac{1}{2} (\sigma_{ii}\sigma_{jj} - \sigma_{ij}\sigma_{ji}) \quad (2.15)$$

$$J_3 = \frac{1}{3} \sigma_{ij}\sigma_{jk}\sigma_{ki} \quad (2.16)$$

Supposing that the material is isotropic, plastic yielding can depend only on the magnitudes of the principal stresses and not on their directions. Hence, any yield criterion must be expressible as a function f_Y of the invariants of the stress tensor.

$$f_Y(J_1, J_2, J_3) = 0 \quad (2.17)$$

It is experimentally proven that the yielding of a metal is to a first approximation unaffected by a moderate hydrostatic pressure or tension. The hydrostatic component of the stress tensor has the following form:

$$\sigma_{ij}^{\text{hyd}} = \delta_{ij} \frac{J_1}{3} \quad (2.18)$$

Based hereupon, also a non-hydrostatic component of the stress tensor can be constructed, the so-called deviatoric stress tensor σ'_{ij} .

$$\sigma'_{ij} = \sigma_{ij} - \sigma_{ij}^{\text{hyd}} \quad (2.19)$$

It follows that the yield function depends only on the deviatoric stress tensor σ'_{ij} and the associated invariants $J'_i = J_i(\sigma'_{ij})$:

$$J'_1 = 0 \quad (2.20)$$

$$J'_2 = \frac{1}{2} \sigma'_{ij} \sigma'_{ij} \quad (2.21)$$

$$J'_3 = \frac{1}{3} \sigma'_{ij} \sigma'_{jk} \sigma'_{ki} \quad (2.22)$$

Assuming that yielding does not involve J'_3 , von Mises (1913) proposed the following yield criterion:

$$f_{Y, \text{von Mises}}(J'_2) = J'_2 - k^2 = 0 \quad (2.23)$$

Defining the effective stress of a material as

$$\sigma_{\text{eff}} = \sqrt{3J'_2} = \sqrt{\frac{3}{2} \sigma'_{ij} \sigma'_{ij}} = \sqrt{\frac{1}{2} \left((\sigma_x - \sigma_y)^2 + (\sigma_y - \sigma_z)^2 + (\sigma_z - \sigma_x)^2 + 6(\tau_{yz}^2 + \tau_{zx}^2 + \tau_{xy}^2) \right)} \quad (2.24)$$

the yield criterion in equation 2.23 reduces to

$$f_{Y,\text{von Mises}}(\sigma_{\text{eff}}) = \sigma_{\text{eff}} - \sigma_Y = 0 \quad (2.25)$$

with σ_Y being the yield stress which can be obtained from uniaxial tensile testing. Once the yield criterion is met for a specific stress state in the material, the evolution of plastic strains must be modeled. In analogy to the constitutive equation 2.4, the relationship between the plastic strain increment $d\varepsilon^{\text{pl}}$ and stress is established, based on experimental evidence, by the Prandtl-Reuss equations:

$$d\varepsilon_{ij}^{\text{pl}} = d\lambda \sigma'_{ij} \quad (2.26)$$

where $d\lambda$ is a scalar factor of proportionality, denominated the plastic multiplier, which is to be determined for a specific case. Equation 2.26 states that the direction of plastic flow is in the direction of the stress state or normal to the yield surface, which is called the normality principle. The Prandtl-Reuss equations can be generalized to the associated flow rule, equation 2.27, in which the yield criterion $f_Y(\sigma_{ij})$ represents the plastic potential.

$$d\varepsilon_{ij}^{\text{pl}} = d\lambda \frac{\partial f_Y(\sigma_{ij})}{\partial \sigma_{ij}} \quad (2.27)$$

For $d\lambda$ we obtain by virtue of the hypothesis of the equivalence of plastic work under general and uniaxial loading conditions:

$$d\lambda = \frac{3}{2} \frac{d\varepsilon_{\text{eff}}^{\text{pl}}}{\sigma_Y} \quad (2.28)$$

with $d\varepsilon_{\text{eff}}^{\text{pl}}$ being the increment of effective plastic strain defined as:

$$d\varepsilon_{\text{eff}}^{\text{pl}} = \sqrt{\frac{2}{3} d\varepsilon_{ij}^{\text{pl}} d\varepsilon_{ij}^{\text{pl}}} \quad (2.29)$$

Since Zirconium alloys are anisotropic materials, the modeling of anisotropic plastic behavior is relevant for the present work. The theory of plastic anisotropy is based on the work of Hill (1948) and is presented more vastly in Hill (1983). For simplicity, Hill considers only states of anisotropy which possess three mutually orthogonal planes of symmetry. Hill's approach is to create a yield criterion $f_{Y,\text{Hill}}$ for anisotropic materials as a generalization of the von Mises yield criterion for isotropic materials:

$$f_{Y,\text{Hill}} = F(\sigma_y - \sigma_z)^2 + G(\sigma_z - \sigma_x)^2 + H(\sigma_x - \sigma_y)^2 + 2L\tau_{yz}^2 + 2M\tau_{zx}^2 + 2N\tau_{xy}^2 - \sigma_Y^2 = 0 \quad (2.30)$$

where F, G , and H are anisotropy factors, which are to be determined for the specific anisotropic material. For an isotropic material we have $F = G = H = L/3 = M/3 = N/3 = 0.5$ so that the anisotropy criterion hence to von Mises' yield criterion, equation 2.25, when the anisotropy vanishes. By analogy with isotropic materials, it is supposed that $f_{Y,\text{Hill}}$ in equation 2.30 is the plastic potential. The strain-increment relations are then given by inserting the yield criterion into the associated flow rule, see also section 2.1.2.3.

2.1.2.2 Creep evolution and laws

Under the effect of an initial strain ε_0 and a constant stress and temperature, the creep strain increases with time in three different stages and adds up to the initial strain, see Figure 2.2. The total strain for a problem including creep is then given as:

$$\varepsilon^{\text{tot}} = \varepsilon^{\text{el}} + \varepsilon^{\text{th}} + \varepsilon^{\text{cr}} \quad (2.31)$$

In the primary stage, the creep strain rate is high and then decreases to a constant value in the secondary stage. In this stage, stationary or steady-state creep is present. In the tertiary stage, the creep strain increases again until the material bursts due to creep rupture. The length of each stage in the creep curve depends on the material. For Zirconium alloys under normal reactor operation, generally only the secondary creep stage is approached, and the tertiary stage is not reached.

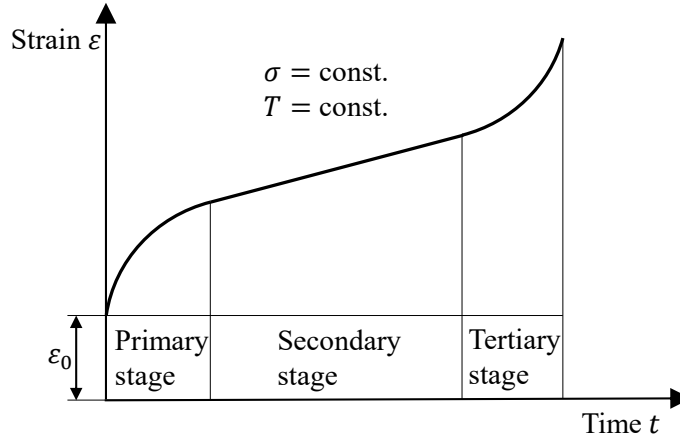


Figure 2.2: Schematic of a creep curve.

The creep curves are strongly dependent on the stress level and the temperature. Under the common assumption that the influencing variables are mutually independent, we obtain the following general equation for the description of creep, the so-called creep law.

$$\varepsilon^{\text{cr}} = f_{\sigma}(\sigma)f_t(t)f_T(T) \quad (2.32)$$

Over the years, a large array of creep laws has been proposed for various materials and applications. General theory on creep laws for conventional applications can, for example, be found in Penny and Marriott (1995). In the following paragraph, the most important conventional creep correlations for non-nuclear applications are presented. These serve as a basis for the Zirconium alloy creep laws used for in-reactor applications, which are discussed in section 2.4.6.

Most creep laws go back to Norton's (1929) law for high-temperature creep of steels which relates the secondary creep rate to the stress by means of a power-law relationship with stress exponent n_{σ} , also called Norton's exponent, and the Norton constant $C_{\text{Norton}}(T)$ which depends on temperature.

$$\dot{\varepsilon}^{\text{cr}} = C_{\text{Norton}}(T)\sigma^{n_{\sigma}} \quad (2.33)$$

The effect of temperature is usually accounted for by introducing an Arrhenius term into equation 2.33:

$$C_{\text{Norton}}(T) = C_{\text{Arrh}} e^{-\frac{Q_{\text{cr}}}{RT}} = C_{\text{Arrh}} e^{-\frac{Q_T}{T}} \quad (2.34)$$

where Q_{cr} is the activation energy of creep deformation and R is the ideal gas constant. Both are often merged to the activation temperature Q_T .

Sophisticated systems such as nuclear reactors require close dimensional tolerances on many components so that also the small creep deformations in the primary stage are of interest. A time-dependent component needs to be introduced to account for the effect of this primary creep component. Based on Bailey (1935), a common approach is to approximate the combined integrated effect of primary and secondary creep by a power-law relationship with time exponent n_t . The resulting model is often referred to as Norton-Bailey model. This model is particularly useful when the primary creep rate is dominant for a specific alloy and considered span of time.

$$\varepsilon^{\text{cr}} = C_{\text{cr}} \sigma^{n_\sigma} t^{n_t} \quad (2.35)$$

Another approach is to account for the effects of primary and secondary creep separately by adding up their contributions. The primary creep component is assumed to approximate asymptotically a saturated value $\varepsilon^{\text{cr,pri,sat}}$ expressed by an exponential decrease of the transient creep rate with an exhaustion rate of p_{cr} , which is to be defined for the specific case.

$$\varepsilon^{\text{cr}} = \varepsilon^{\text{cr,pri,sat}} (1 - e^{-p_{\text{cr}} t}) + \dot{\varepsilon}^{\text{cr,sec}} t \quad (2.36)$$

Another common description of the asymptotic saturation of the primary creep is the use of a rational-polynomial time behavior, see the report by Booker (1977), for example:

$$\varepsilon^{\text{cr}} = \varepsilon^{\text{cr,pri,sat}} \frac{p_{\text{cr}} t}{1 + p_{\text{cr}} t} + \dot{\varepsilon}^{\text{cr,sec}} t \quad (2.37)$$

In both cases, p_{cr} describes the slope of the time-dependent creep curve at $t = 0$, but the rational-polynomial function converges significantly slower than the exponential function.

Under a variable stress over time, there are two approaches to determine the creep strain, the time hardening and the strain hardening approach. For the time hardening approach, there is assumed no influence of the loading history on the creep strain. The creep strain rate is calculated by simply deriving the time function f_t .

$$\dot{\varepsilon}^{\text{cr}} = f_\sigma(\sigma) \dot{f}_t(t) f_T(T) \quad (2.38)$$

From a mechanistic point of view, it is more plausible that the instantaneous creep rate is not a function of time itself, but of the creep strain accumulated so far. In the strain hardening approach, the creep rate is determined as a function of the cumulative creep strain ε^{cr} .

$$\dot{\varepsilon}^{\text{cr}} = f_\sigma(\sigma) f_\varepsilon(\varepsilon^{\text{cr}}) f_T(T) \quad (2.39)$$

To derive a strain hardening creep law from the general time-dependent form in equation 2.38, the so-called hardening time $t_h(\varepsilon^{\text{cr}})$ must be determined by solving equation 2.32 for t . Inserting the result into the differentiated form, equation 2.38, yields the strain hardening law as in equation 2.39. For the example of a Norton-Bailey creep law, the strain hardening law reads as:

$$\dot{\varepsilon}^{\text{cr}} = C_{\text{cr}}^{\frac{1}{n_t}} n_t \sigma^{\frac{n_\sigma}{n_t}} (\varepsilon^{\text{cr}})^{\frac{n_t-1}{n_t}} \quad (2.40)$$

2.1.2.3 Multiaxial creep modeling

The laws for isotropic and anisotropic multiaxial creep can be derived in analogy to the laws for instantaneous plasticity, considering the creep strain rate $\dot{\varepsilon}^{\text{cr}}$ as the derivative of the time-dependent plastic creep strain ε^{cr} .

$$\dot{\varepsilon}^{\text{cr}} = \frac{\partial \varepsilon^{\text{cr}}}{\partial t} \stackrel{!}{=} \frac{\partial \varepsilon^{\text{pl}}}{\partial t} \quad (2.41)$$

In analogy to the Prandtl-Reuss equations 2.26, we obtain the following creep constitutive relation for the isotropic case:

$$\dot{\varepsilon}_{ij}^{\text{cr}} = \dot{\lambda} \sigma'_{ij} = \frac{3}{2} \frac{\dot{\varepsilon}_{\text{eff}}^{\text{cr}}}{\sigma_{\text{eff}}} \sigma'_{ij} \quad (2.42)$$

where $\dot{\varepsilon}_{\text{eff}}^{\text{cr}}$ is the effective creep strain rate:

$$\dot{\varepsilon}_{\text{eff}}^{\text{cr}} = \sqrt{\frac{2}{3} \dot{\varepsilon}_{ij}^{\text{cr}} \dot{\varepsilon}_{ij}^{\text{cr}}} \quad (2.43)$$

Using, for example, an arbitrary strain hardening creep law as defined in equation 2.39, the effective creep strain rate is given as:

$$\dot{\varepsilon}_{\text{eff}}^{\text{cr}} = f_\sigma(\sigma_{\text{eff}}) f_\varepsilon(\varepsilon_{\text{eff}}^{\text{cr}}) f_T(T) \quad (2.44)$$

For the anisotropic case, Ross-Ross et al. (1972) derived the equations for the creep of Zirconium alloy tubes or rods with a cylindrical coordinate system based on Hill's general theory of anisotropic plasticity. Assuming that the axes of anisotropy of a Zirconium alloy pressure tube coincide with the axes of principal stresses, we obtain, based on equation 2.30, the following definition for the stress state in the cladding:

$$\sigma_{\text{eff}}^2 = F(\sigma_z - \sigma_\theta)^2 + G(\sigma_\theta - \sigma_r)^2 + H(\sigma_r - \sigma_z)^2 \quad (2.45)$$

where σ_r , σ_θ , and σ_z are the radial, transverse, and axial stresses. The corresponding relationship between stresses and creep strains was derived by Merkle (1967) based on the associated flow rule, equation 2.27, yielding the equations of the Prandtl-Reuss type for multiaxial creep:

$$\dot{\varepsilon}_r = \frac{\dot{\varepsilon}_{\text{eff}}^{\text{cr}}}{\sigma_{\text{eff}}} [H(\sigma_r - \sigma_z) - G(\sigma_\theta - \sigma_r)] \quad (2.46)$$

$$\dot{\varepsilon}_\theta = \frac{\dot{\varepsilon}_{\text{eff}}^{\text{cr}}}{\sigma_{\text{eff}}} [G(\sigma_\theta - \sigma_r) - F(\sigma_z - \sigma_\theta)] \quad (2.47)$$

$$\dot{\varepsilon}_z = \frac{\dot{\varepsilon}_{\text{eff}}^{\text{cr}}}{\sigma_{\text{eff}}} [F(\sigma_z - \sigma_\theta) - H(\sigma_r - \sigma_z)] \quad (2.48)$$

2.1.2.4 Relaxation as a case of creep

The creep relaxation denominates the occurrence of creep under the specific loading condition that the total strain is held constant. If, for example, a material is elastically strained by $\varepsilon^{\text{el}} = \varepsilon^{\text{tot}}$ in a certain direction, it undergoes an initial stress σ_0 corresponding to the elastic strain, see Figure 2.3. When holding the total strain constant for $t > t_0$, the contribution of creep strain to the total strain will increase, thus decreasing the elastic strain and stress. That is, the stress is being relaxed:

$$\sigma(t) = (\varepsilon^{\text{tot}} - \varepsilon^{\text{cr}}(t))E \quad (2.49)$$

Differentiating the stress-strain relationship in equation 2.49 with respect to time, the following differential equation is determined:

$$\dot{\sigma} = -\dot{\varepsilon}^{\text{cr}} E \quad (2.50)$$

With a known Norton-Bailey creep law, equation 2.50 becomes:

$$\dot{\sigma} = -C_{\text{cr}} \sigma^{n_\sigma} n_t t^{n_t-1} E \quad (2.51)$$

Solving the differential equation, for example, for the common case $n_\sigma = 1$ and an initial stress of σ_0 , we obtain:

$$\sigma(t) = \sigma_0 e^{-C_{\text{cr}} E t^{n_t}} \quad (2.52)$$

Creep relaxation plays an important role regarding the relaxation of pre-stressed springs. In terms of the force-displacement relationship commonly used for one-dimensional springs, equation 2.52 becomes:

$$F(t) = F_0 e^{-C_{\text{cr}} E t^{n_t}} \quad (2.53)$$

That is, the spring force decreases exponentially during the relaxation of a pre-stressed spring when $n_\sigma = 1$.

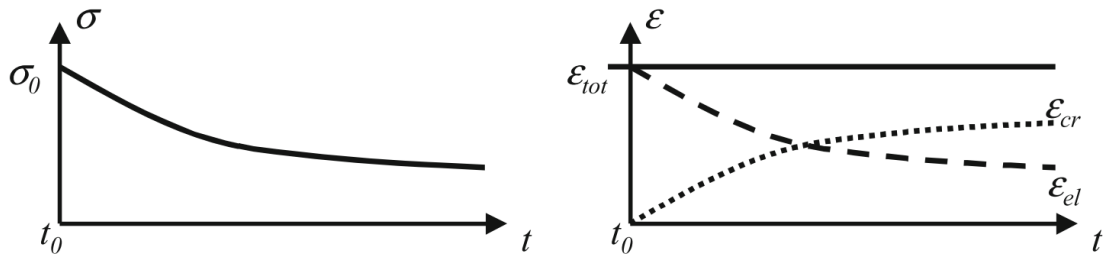


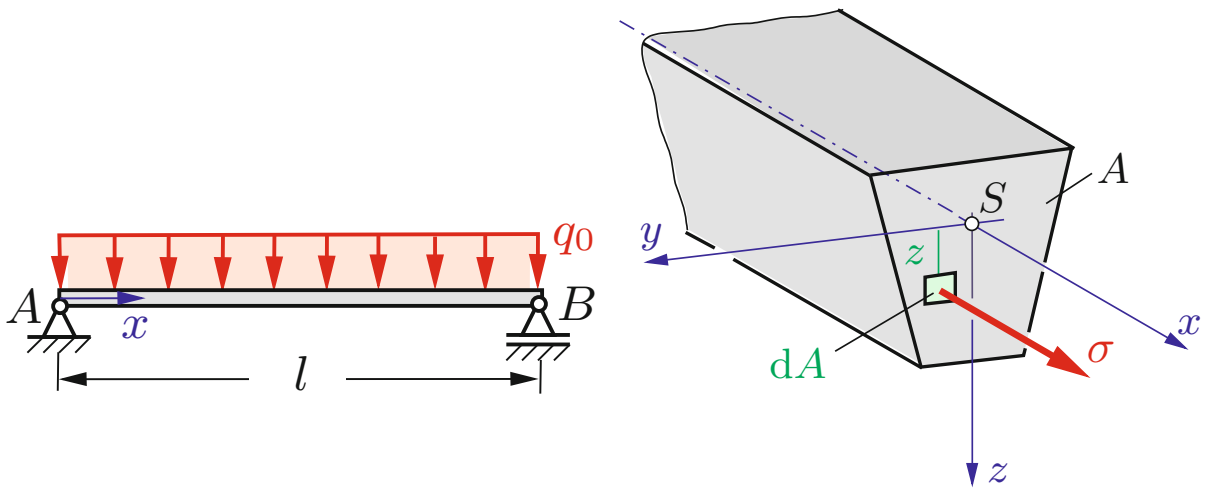
Figure 2.3: Evolution of stress and strain during creep relaxation (Rust, 2011).

2.1.3 Engineering structural mechanics of FA tubes and rods

Engineering structures often can be calculated by simplified methods because they usually possess a well-defined geometry which offers elastic resistance in specific directions according to the anticipated loading state. The general three-dimensional stress and strain state introduced in section 2.1.1 can be reduced to one- or two-dimensional problems composed of line or surface elements. The simplification to line elements is applicable to slender structures with a length greatly superior to its cross-sectional dimensions. A well-known example are trusses. These are an assembly of bar elements connected by pin-joints without moment transmission; that is, the bars only transmit axial forces. Likewise, nuclear fuel elements are assemblies composed of slender structures, namely the guide tubes (GTs) and fuel rods (FRs). Unlike for trusses, joints in FAs are designed to transmit moments in order to create a stiffer structure. The assumption of bars hence does not hold for the FA GTs and FRs. Beams, on the other hand, transmit moments, and are ideal to describe the FA GTs and FRs. In contrast to the GTs, FRs are actually slender closed pressure vessels that withstand a pressure difference between the internal and the external fluids. As such, they can be represented by pipe structures which combine the properties of beam structures and pressure vessels. The simplified modeling for both beams and pressure vessels will be introduced in this section. Moreover, the coupling effect of the joints connecting the single GTs and FRs is described.

2.1.3.1 Euler-Bernoulli beam equation and stress stiffening

The simplest description of beams goes back to the Euler-Bernoulli beam theory, which represents a fully linearized model. In the present context, a beam describes an arbitrarily supported and loaded slender structure with an axially uniform and homogeneous cross-section, Figure 2.4. The x -coordinate describes the axial direction and y and z the transverse directions. This section presents the differential equations to obtain the beam bending curve $u_z(x)$ as a result of the loading of the beam in the x - z plane by a distributed transverse load $q(x)$. A derivation of these equations is given in appendix A. Under the Euler-Bernoulli assumptions, the bending curve $u_z(x)$ is given by the solution of the following linear differential equation,



(a) Beam under a uniform distributed load $q(x) = q_0$.

(b) Perspective view of beam cross-sectional cut.

Figure 2.4: Schematic views of a beam element (Gross et al., 2012).

known as the Euler-Bernoulli beam equation:

$$EI \frac{d^4 u_z(x)}{dx^4} = q(x) \quad (2.54)$$

where I is the second moment of area defined in equation A.7.

If the magnitude of the axial loads, leading to the normal cutting force $N(x)$, is much higher than that of the transverse loads, an additional term must be added to equation 2.54, resulting in the following nonlinear differential equation:

$$EI \frac{d^4 u_z}{dx^4} - \frac{d}{dx} \left(N(x) \frac{du_z}{dx} \right) = q(x) \quad (2.55)$$

The new term leads to an effective stiffening of the structure if a normal tensile force is present, $N(x) > 0$. This effect is called stress stiffening. If a compressive load is applied, the stiffness of the beam decreases compared to the case without axial load, which is sometimes referred to as stress weakening. Due to the potentially high compressive holddown (HD) force on the FAs and the heavy fuel, it is important to account for this effect in the FA model to obtain conservative estimations.

2.1.3.2 Mechanical coupling of tube bundles

A FA consists of a bundle of GTs and FRs which can be modeled as beams. Without the spacer grids, the stiffness of the bundle would correspond to that of the sum of the single beams. The spacer grids couple the beams mechanically at certain axial levels, thus increasing stiffness. Barinka (1971) offered a theoretical description of the coupling effect in tubular structures such as FAs. Based hereupon, the principle of the FA stiffening due to the grid coupling is described in this section. This description also provides the theoretical basis for the model reduction in section 3.4. The following assumptions must be made for this theoretical analysis.

1. All forces attack in the neutral axis of the FA or are equally distributed over all like tubes, that is, the FRs or GTs.
2. All like tubes have an identical stiffness and are identically supported in the spacer grid.
3. All tubes are arranged symmetrically about the FA neutral axis. That is, for each tube at a certain position x_i there exists the same tube at $-x_i$.
4. All spacer grid coupling structures can be considered rigid relative to the stiffness of the tube bundle. Therefore, they rotate as plane sections. In addition, the stiffness of the lateral support of the tubes in the spacer grids is also much larger than the stiffness of the tubes.

To illustrate the working principle of the grid coupling, Figure 2.5 gives a minimum configuration with two equal tubes with a length of l , cross-sectional area A and flexural rigidity EI . The tubes with indexes j and k are positioned symmetrically about the perpendicular bending axis at $x_j = x_0$ and $x_k = -x_0$ and are coupled to each other at their top by means of a spacer grid. The connections (not visible) between the spacer grids and the tubes are elastic and given by an axial spring with stiffness k_z and a rotational spring with stiffness k_θ . If a lateral force F_x is applied centrally on the coupling structure, this force is equally distributed over both tubes according to assumption (1). From assumptions (2) and (3), it results that all

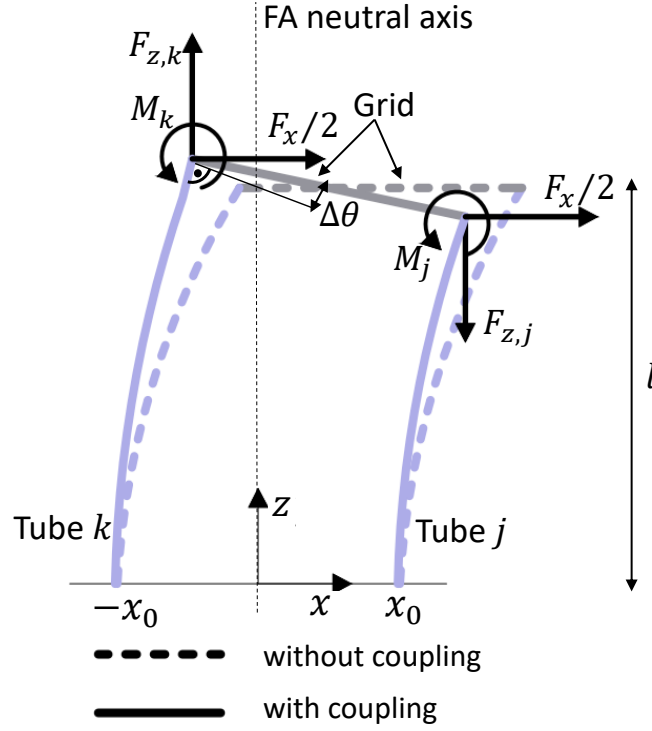


Figure 2.5: Schematic of grid coupling effects.

like tubes undergo the same lateral and rotational deformations, $u_{x,j} = u_{x,k}$ and $\theta_j = \theta_k$, according to the Euler-Bernoulli beam equations. If $k_\theta = k_z = 0$, no coupling is present and the tubes deform like single isolated tubes. Since for the present case either tube undergoes a lateral load of $F_x/2$, the tube deflection according to the Euler-Bernoulli beam theory is (Wittenburg and Richard, 2012):

$$u_x = \frac{F_x}{2} \frac{l^3}{3EI} \quad (2.56)$$

For the general case with n_{FR} FRs and n_{GT} GTs, the total flexural rigidity of the FA without grid coupling is given in equation 2.57. The Young's modulus E is omitted since it is constant for all tubes.

$$I_{\text{tot}} = n_{\text{FR}} I_{\text{FR}} + n_{\text{GT}} I_{\text{GT}} \quad (2.57)$$

If $k_\theta, k_z > 0$, the rotation θ of the tubes will create a counter-moment M at the connection with the grid, induced by the differential rotation $\Delta\theta$ between the coupling structure and the tube:

$$M = k_\theta \Delta\theta \quad (2.58)$$

At the same time, the reaction moment rotates the grid in the load direction. In this manner, the tube at $x > 0$ is compressed and the tube at $x < 0$ is under tension. The corresponding axial forces F_z on the tubes are induced by the differential axial displacement Δu_z between the grid and the tube:

$$F_z = k_z \Delta u_z \quad (2.59)$$

Due to the coupling with the rotational degree of freedom (DOF) of the grid, the bending moment in the tube is relieved by M , reducing the deflection in equation 2.56 to:

$$u_x = \frac{F_x}{2} \frac{l^3}{3EI} - \frac{Ml^2}{2EI} \quad (2.60)$$

Instead, this moment is transmitted axially through the tubes by means of the grid rotation θ . This becomes apparent when considering the equilibrium of moments at the grid.

$$\sum_i M_i = M_j + M_k - F_{z,j}x_j - F_{z,k}x_k = 2k_\theta\Delta\theta - k_z\Delta u_{z,j}x_j - k_z\Delta u_{z,k}x_k = 0 \quad (2.61)$$

For an arbitrary position i , the grid rotation is linked to the axial displacements by the following geometric compatibility condition.

$$\Delta u_{z,i} = \Delta\theta x_i \quad (2.62)$$

For the general case with n_{FR} FRs and n_{GT} GTs, equation 2.61 becomes:

$$\sum_i M_i = \sum_{i=1}^{n_{\text{FR}}+n_{\text{GT}}} (M_i - F_{z,i}x_i) = \sum_{i=1}^{n_{\text{FR}}+n_{\text{GT}}} (k_{\theta,i}\Delta\theta - k_{z,i}x_i^2\Delta\theta) = 0 \quad (2.63)$$

We can conclude that the higher the number n_{grid} of spacer grid coupling stations is along the bundle, the higher is the stiffening effect. The limiting case occurs when $k_z, k_\theta, n_{\text{grid}} \rightarrow \infty$. This means that the grid connections are rigid and there is an infinite number of coupling stations over the tube bundle. In this case, the flexural rigidity of the bundle is given by Steiner's theorem.

$$I_{\text{tot}} = n_{\text{FR}}I_{\text{FR}} + n_{\text{GT}}I_{\text{GT}} + \sum_{i=1}^{n_{\text{FR}}+n_{\text{GT}}} A_i x_i^2 \quad (2.64)$$

2.1.3.3 Pressure vessels

Pressure vessels store liquid or gas under pressure. Common shapes of pressure vessels are cylinders or spheres. In the case of long cylinders, one refers to pressure tubes. FRs pressurized with a filling gas are an example of pressure tubes. The stresses in pressure tubes are denoted in cylindrical coordinates $(\sigma_r, \sigma_\theta, \sigma_z)$, where σ_r is the radial stress and σ_z is the axial or longitudinal stress. σ_θ is the stress in circumferential direction, which is also referred to as hoop stress or membrane stress. Depending on the ratio of the tube wall thickness and the radius, approximations can be made to deduce simplified equations for calculating the stresses in the tube wall based on the tube inner and outer pressures p_i and p_o . Most authors in literature refer to a pressure tube as thin-walled if the ratio of wall thickness t_{tube} to inner radius r_i is not greater than 0.1, see Mubeen (2002), for example. For thin-walled pressure tubes, the circumferential stress can be assumed constant over the wall thickness and the difference between inner and outer radius can be neglected for the calculation of stresses, $r_i \approx r_o \approx r$. For thick-walled pressure tubes these assumptions do not hold and the stresses must be calculated as a function of the radius r . Larger differences over the radius are, however, only expected for ratios of thickness to radius greater than 0.2. pressurized water reactor (PWR) FRs usually present a ratio of cladding thickness to inner radius of 0.13 to 0.16. In general, the formulation

for thick-walled pressure tubes should be used, but the circumferential stress can still be assumed constant. That is, we can use the equations for thick-walled pressure tubes and evaluate them at the mean radius r_m . Still, for rough estimations it is common to use the thin-wall approximation, which is given in equations 2.65 to 2.67.

$$\sigma_\theta = \frac{(p_i - p_o)r_i}{t_{\text{tube}}} \quad (2.65)$$

$$\sigma_z = \frac{(p_i - p_o)r_i}{2t_{\text{tube}}} = \frac{\sigma_\theta}{2} \quad (2.66)$$

Due to the thin wall, the radial stress is small compared to σ_θ and σ_z and is therefore assumed zero.

$$\sigma_r = 0 \quad (2.67)$$

The stresses in a thick-walled pressure tube can be calculated using the so-called Lamé equations. The stress components can be represented as a function of two reference stress terms, σ_A and $\sigma_B(r)$.

$$\sigma_r = \sigma_A - \sigma_B \quad (2.68)$$

$$\sigma_\theta = \sigma_A + \sigma_B \quad (2.69)$$

$$\sigma_z = \sigma_A \quad (2.70)$$

with

$$\sigma_A = \frac{p_i r_i^2 - p_o r_o^2}{r_i^2 - r_o^2} \quad (2.71)$$

$$\sigma_B(r) = \frac{r_i^2 r_o^2 (p_i - p_o)}{r^2 (r_i^2 - r_o^2)} \quad (2.72)$$

Evaluating equation 2.72 at the mean radius r_m , provides a constant value for σ_B , which will be used in the present work:

$$\sigma_B = \frac{r_i^2 r_o^2 (p_i - p_o)}{r_m^2 (r_i^2 - r_o^2)} \quad (2.73)$$

2.1.3.4 Axial stress state in FRs and GTs

Due to their slender structure, the axial stress component σ_z in FRs and GTs is the most relevant to determine the structural deformation. In FAs, the GT and FR axial stress is composed of several terms originating from different loads. The axial stress $\sigma_{z,\text{unif}}$ is due to axial loads which have a laterally uniform distribution over the FA. These loads are produced, for example, by the HD force, gravity, or axial hydraulic loads. $\sigma_{z,\text{unif}}$ is associated to the normal cutting force in the tube, $N_{\text{unif}}(z)$, which is a function of the axial coordinate only and is independent of its lateral position in the FA, according to assumption (1) in section 2.1.3.2. It follows:

$$\sigma_{z,\text{unif}} = \frac{N_{\text{unif}}(z)}{A} \quad (2.74)$$

The second component is the axial stress $\sigma_{z,\text{cpl}}$ due to the axial force between grid and FRs resulting from the grid coupling due to the grid rotation θ , see equations 2.59 and 2.62. This reaction generates a normal cutting force $N_{\text{cpl}}(z, x_i)$ in the tubes which depends on the lateral position x_i of the considered tube i inside the spacer grid. For a linear system with a constant spring stiffness k_z , these forces are linearly proportional to x_i :

$$N_{\text{cpl}}(z, x_i) = N_{\text{cpl,ref}}(z) \frac{x_i}{x_{\text{ref}}} \quad (2.75)$$

where $N_{\text{cpl,ref}}$ is the normal cutting force for the reference tube positioned at x_{ref} . It follows:

$$\sigma_{z,\text{cpl}} = \frac{N_{\text{cpl,ref}}(z)}{A} \frac{x_i}{x_{\text{ref}}} \quad (2.76)$$

We can sum up $\sigma_{z,\text{unif}}$ and $\sigma_{z,\text{cpl}}$ to form a general uniaxial stress component $\sigma_{z,\text{uniax}}$ due to the total cutting force $N(z, x_i)$:

$$\sigma_{z,\text{uniax}} = \sigma_{z,\text{unif}} + \sigma_{z,\text{cpl}} = \frac{N_{\text{unif}}(z)}{A} + \frac{N_{\text{cpl,ref}}(z)}{A} \frac{x_i}{x_{\text{ref}}} = \frac{N(z, x_i)}{A} \quad (2.77)$$

The third component is the axial bending stress $\sigma_{z,\text{bend}}$ due to the bending moment $M_{\text{bend}}(z)$ produced by the lateral loads and the reactions between the grids and the tubes, see equation 2.63. Therefore, $\sigma_{z,\text{bend}}$ is independent of the lateral position of the tube, but according to equation A.9 has a linear profile over the tube cross-section. If $\hat{x}_i = x - x_i$ is the distance from the neutral axis of the considered tube positioned at x_i , the bending stress is expressed as:

$$\sigma_{z,\text{bend}} = \frac{M_{\text{bend}}}{I} \hat{x}_i \quad (2.78)$$

Finally, an additional stress component is added for the pressurized FRs, namely the axial stress due to the biaxial stress state $\sigma_{z,\text{biax}}$ resulting from the pressure difference between the inner and outer diameter, which was previously defined in equation 2.70:

$$\sigma_{z,\text{biax}} = \frac{p_i r_i^2 - p_o r_o^2}{r_i^2 - r_o^2} \quad (2.79)$$

2.2 Computational Structural Mechanics (CSM) and Finite Element Method (FEM)

2.2.1 Fundamentals of the FEM

The FEM is considered as a standard numerical method of solving field problems for many applications, in particular for structural analysis (Lemaitre and Chaboche, 1990; Szabó and Babuška, 2011). The FEM can be derived from generic principles in structural mechanics, one of which is the principle of virtual work. By multiplying the equilibrium equations 2.10 by a test function ν_i and integrating over the considered domain

Ω , we obtain, mathematically speaking, a weak form of these equations:

$$\int_{\Omega} \frac{\partial \sigma_{ij}}{\partial x_j} \nu_i dV + \int_{\Omega} f_i \nu_i dV = 0 \quad (2.80)$$

Using the divergence theorem, this weak formulation can be recast into the following form:

$$\int_{\Omega} \sigma_{ij} \frac{\partial \nu_i}{\partial x_j} dV = \int_{\Omega} f_{B,i} \nu_i dV + \int_{\partial\Omega} f_{S,i} \nu_i dS \quad (2.81)$$

The test function ν_i can be interpreted as an arbitrary “virtual” displacement δu_i , which is independent of the applied body force $f_{B,i}$ and surface force $f_{S,i}$ at the domain boundary $\partial\Omega$. With $\delta \varepsilon_{ij}$ being the virtual strain associated to the virtual displacement, we get:

$$\int_{\Omega} \sigma_{ij} \delta \varepsilon_{ij} dV = \int_{\Omega} f_{B,i} \delta u_i dV + \int_{\partial\Omega} f_{S,i} \delta u_i dS \quad (2.82)$$

In this case, the term at the left represents the work done by the internal stresses and the term at the right the work by the external forces due to any kinematically admissible virtual displacement. Equation 2.82 expresses the generic form of the principle of virtual work. By comparison with equation 2.13, the principle of virtual work can be interpreted physically that a body deforms so that the total potential energy is minimized, that is, $\delta \Pi = 0$.

For the application of the FEM, the structure is decomposed into individual finite elements to obtain a discretized solution. The FEM consists in calculating the potential energy Π as the sum of all elements and finding a class of fields for which the potential energy is minimized. The basic finite element shapes are line, surface, or volume elements, depending on the schematic representation of the structure. Before introducing individual element types, the general methodology to construct a finite-element model is presented. The vertices of any finite element are usually defined as the nodes of the discretization grid of the domain. The displacements of these nodes are the DOFs of the elements. For convenience, we abandon the index notation for this section and use matrix notation. All DOFs of a single element are included in the vector of nodal displacements \mathbf{u}_N . Within each finite element, the unknown displacement field $\mathbf{u}(\mathbf{x})$ is linearly related to the nodal displacements by means of shape functions which are included in the matrix \mathbf{N} :

$$\mathbf{u}(\mathbf{x}) = \mathbf{N} \mathbf{u}_N \quad (2.83)$$

Examples for different shape functions are given in the descriptions of the bar and beam elements in the next sections. As symmetric tensors, we can define the stress and strain tensors as vectors with six components each, $\boldsymbol{\sigma}$ and $\boldsymbol{\varepsilon}$. The linear strain-displacement relationship in equation 2.2 can then be expressed by means of the matrix of differential operators \mathbf{L} .

$$\boldsymbol{\varepsilon} = \mathbf{L} \mathbf{u} \quad (2.84)$$

The stress-strain relationship in equation 2.4 can be expressed defining the elasticity matrix \mathbf{D} .

$$\boldsymbol{\sigma} = \mathbf{D} \boldsymbol{\varepsilon} \quad (2.85)$$

The product of the matrix of shape functions \mathbf{N} and the matrix of differential operators \mathbf{L} is defined as \mathbf{B} .

$$\mathbf{B} = \mathbf{L}\mathbf{N} \quad (2.86)$$

The product of the stress and virtual strain tensor results in the following formulation:

$$\delta\boldsymbol{\varepsilon}^T \boldsymbol{\sigma} = \delta\boldsymbol{\varepsilon}^T \mathbf{D}\boldsymbol{\varepsilon} = \delta\mathbf{u}_N^T \mathbf{B}^T \mathbf{D}\mathbf{B}\mathbf{u}_N \quad (2.87)$$

Inserting equation 2.87 into the principle of virtual work in equation 2.82, we obtain:

$$\delta\mathbf{u}_N^T \left(\int_{\Omega} \mathbf{B}^T \mathbf{D}\mathbf{B}\mathbf{u}_N dV - \int_{\Omega} \mathbf{N}^T \mathbf{f}_B dV - \int_{\partial\Omega} \mathbf{N}^T \mathbf{f}_S dS \right) = 0 \quad (2.88)$$

Since this equation must be satisfied for arbitrary $\delta\mathbf{u}_N$, the term inside the parentheses must be equal zero. Defining the stiffness matrix

$$\mathbf{K} = \int_{\Omega} \mathbf{B}^T \mathbf{D}\mathbf{B} dV \quad (2.89)$$

and the external force vector \mathbf{f}^{ext} of externally applied nodal forces,

$$\mathbf{f}^{\text{ext}} = \int_{\Omega} \mathbf{N}^T \mathbf{f}_B dV + \int_{\partial\Omega} \mathbf{N}^T \mathbf{f}_S dS \quad (2.90)$$

we obtain an algebraic system of equations:

$$\mathbf{K}\mathbf{u}_N = \mathbf{f}^{\text{ext}} \quad (2.91)$$

The last step of the FEM is to assemble the algebraic equations of each single finite element to one large system of equations by imposing equal displacements for nodes common to neighboring elements. The initial problem which required the solution of a partial differential equation is hence replaced by a algebraic system of equations, which can be solved for the unknown nodal displacements and reaction forces using algebraic methods. After the solution step, the displacements within the elements can be calculated with equation 2.83 using the previously defined shape functions. Based on the displacement field, the stresses and strains can be calculated in any point of the domain using equations 2.84 and 2.85.

2.2.2 Finite elements for FA structural analysis

To solve the FA structural problems in this work, the FEM computer code ANSYS Mechanical APDL is used (ANSYS, 2013b). This code provides predefined finite elements based on which the user can build a FEM model. After the model implementation and definition of boundary conditions (BCs) by the user, the ANSYS code performs automatically the matrix assembly and solution steps as well as the calculation of the derived solution variables. This section presents the general properties of the finite elements used in the FA structural analysis.

2.2.2.1 Spring elements

Spring elements are the simplest class of elements used in this work. They present a simple relationship between the nodal displacements, u_1 and u_2 , and forces, F_1 and F_2 , of two nodes connected by a stiffness k

illustrated in Figure 2.6 and expressed in equation 2.92.

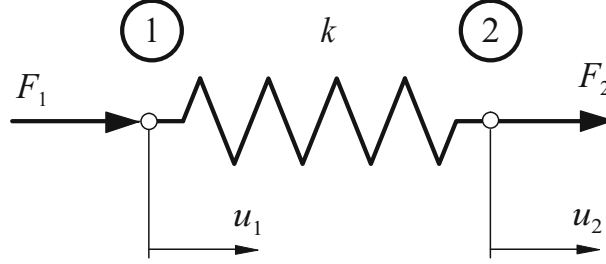


Figure 2.6: Schematic of the spring element (Merkel and Öchsner, 2010).

$$F_2 = k(u_2 - u_1) \text{ and } F_1 = k(u_1 - u_2) \quad (2.92)$$

The stiffness matrix and nodal displacement vector for this element are given as:

$$\mathbf{K} = \begin{bmatrix} k & -k \\ -k & k \end{bmatrix} \text{ and } \mathbf{u}_N = \begin{bmatrix} u_1 \\ u_2 \end{bmatrix} \quad (2.93)$$

This linear spring behavior can be modeled using the ANSYS element *COMBIN14*. To define a nonlinear spring response for which the stiffness changes with the spring displacement, $k = f(\Delta u)$, the ANSYS element *COMBIN39* can be used.

2.2.2.2 Bar element

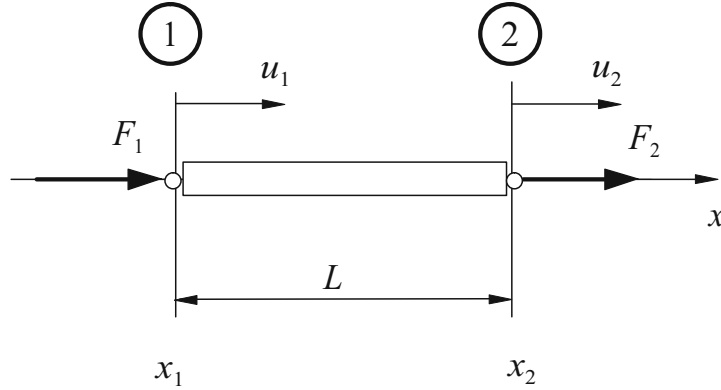


Figure 2.7: Schematic of the finite bar element (Merkel and Öchsner, 2010).

Although bar elements, Figure 2.7, are not explicitly used in the present FA model, its characteristics are relevant for this work since the bar element formulation provides the axial properties of the beam elements introduced in the next section. Assuming that the x -axis of the element local coordinate system is aligned with the axial direction, only the scalar displacement function $u(x)$ needs to be determined based on the nodal displacement vector.

$$\mathbf{u}_N = \begin{bmatrix} u_{x,1} \\ u_{x,2} \end{bmatrix} \quad (2.94)$$

A common approach is to use linear interpolation functions based on the Lagrangian polynomials as shape functions:

$$\mathbf{N}(x) = \begin{bmatrix} \frac{1}{L}(x_2 - x) & \frac{1}{L}(x - x_1) \end{bmatrix} \quad (2.95)$$

The matrix $\mathbf{B}(\mathbf{x})$ simplifies to the following vector:

$$\mathbf{B}(\mathbf{x}) = \mathbf{L}\mathbf{N}(x) = \frac{d\mathbf{N}(x)}{dx} = \begin{bmatrix} -\frac{1}{L} & \frac{1}{L} \end{bmatrix} \quad (2.96)$$

Using equation 2.96, the stiffness matrix is finally given as follows:

$$\mathbf{K}_x = \int_{\Omega} \mathbf{B}^T \mathbf{D} \mathbf{B} dV = EA \int_L \mathbf{B}^T \mathbf{B} dx = \frac{EA}{L} \begin{bmatrix} 1 & -1 \\ -1 & 1 \end{bmatrix} \quad (2.97)$$

The linear system for the bar element becomes:

$$\mathbf{K}_x \mathbf{u}_N = \mathbf{f}_x^{\text{ext}} \quad (2.98)$$

2.2.2.3 Beam elements

For beam elements, there are two unknowns per node and bending axis, namely the nodal displacement and the nodal rotation in perpendicular direction, for example, $u_{z,1}$ and $\theta_{y,1}$. Merkel and Öchsner (2010) give an overview about different approaches for shape functions and finite-element formulations for beam elements with and without shear deformation. Both separate and combined shape functions for displacements and rotations are possible. For Euler-Bernoulli beams without shear deformation, shape functions combining the displacements and rotations are often used. ANSYS provides the element *BEAM188* for beam modeling (ANSYS, 2013b), which models also the shear deformation based on the Timoshenko beam theory. For Timoshenko beams, separate shape functions for displacements and rotations, $N_{u,i}$ and $N_{\theta,j}$, are usually used:

$$u_z(x) = \sum_{i=1}^n N_{u,i} u_{y,i} \quad (2.99)$$

$$\theta_y(x) = \sum_{j=1}^m N_{\theta,j} \theta_{z,j} \quad (2.100)$$

According to the order $n - 1$ and $m - 1$ of the shape function polynomials, additional internal interpolation nodes are placed between the outer element nodes. For the present project, the use of quadratic interpolation functions, *BEAM188* key option *KEYOPT(3)=2*, was determined to offer a good compromise between accuracy and computational cost. The derivation of the beam structural stiffness matrix \mathbf{K} based on these shape functions is somewhat cumbersome and is not covered in this work but is described at length in the cited literature. If the stress stiffening effect is to be accounted for, a stress stiffness matrix \mathbf{S} is added to the structural stiffness matrix \mathbf{K} of the beam element (ANSYS, 2013b; Rust, 2011). The stress stiffness matrix is a function of the axial beam forces obtained from equation 2.98 and is therefore coupled to the nodal solution of the problem, $\mathbf{S} = \mathbf{S}(\mathbf{u}_N)$. The force-displacement relationship of the complete beam element is

summarized by the following nonlinear system of equations:

$$[K + S(u_N)]u_N = f^{\text{ext}} \quad (2.101)$$

In the ANSYS model, the stress stiffening term is invoked by including the option to model geometric nonlinearities: *LDGEOM,ON*.

2.2.2.4 Frictional gap-contact elements

Frictional gap-contacts elements are an elementary part of the FA structural model. With these elements, the frictional support of the FRs in the spacer grid and the inter-FA gaps can be modeled. ANSYS provides the element *CONTA178* for this purpose. These elements combine the properties of friction elements, gap-contact elements, and spring elements.

The gap-contact property is active along the axial direction of the element, the local x -direction. Figure 2.8a gives a schematic representation of the gap-contact element with normal spring. The force normal to the gap F_{norm} is determined by the relative axial displacement of the element nodes $u_{x,1}$ and $u_{x,2}$ and the initial gap size $b_{\text{gap,ini}}$, see equation 2.102.

$$F_{\text{norm}} = \begin{cases} 0, & \text{if } b_{\text{gap}} = b_{\text{gap,ini}} + u_{x,2} - u_{x,1} > 0 \\ k_{\text{norm}} b_{\text{gap}}, & \text{otherwise} \end{cases} \quad (2.102)$$

If the gap size $b_{\text{gap}} > 0$, the contact is open, and no force is transmitted. If $b_{\text{gap}} \leq 0$, the contact is closed and the contact force F_{norm} is established as a function of the normal contact stiffness k_{norm} and the gap interference b_{gap} . The force-displacement response is hence status-dependent (open/closed) and therefore nonlinear as illustrated in Figure 2.8b.

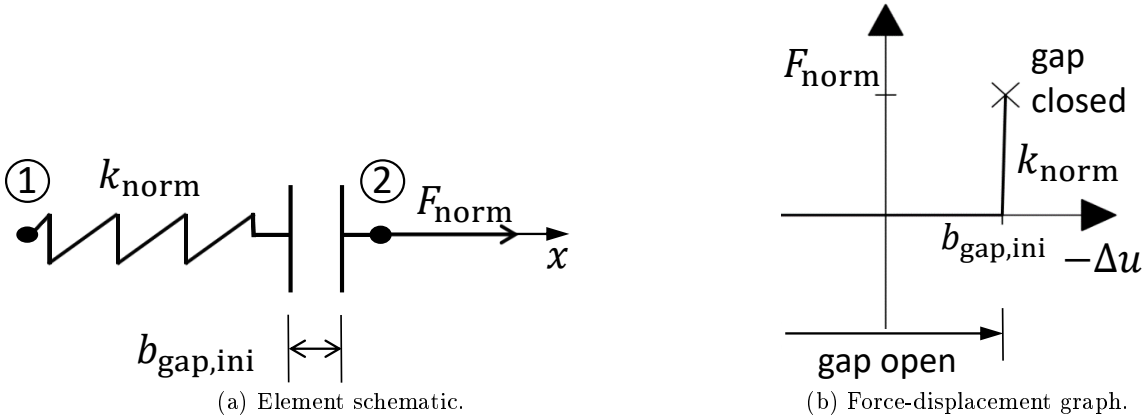


Figure 2.8: Gap-contact element with normal spring.

The frictional property of the element acts in the direction tangential to the gap and is activated as soon as the contact is closed. Figure 2.9a illustrates schematically the resulting friction element with a spring representing the stick stiffness. Equation 2.103 and Figure 2.9b represent the force-deflection response of the

element.

$$F_{\text{tang}} = \begin{cases} 0, & \text{if } b_{\text{gap}} > 0 \\ k_{\text{tang}} \Delta u_{\text{tang}}, & \text{if } b_{\text{gap}} < 0 \text{ and } k_{\text{tang}} \Delta u_{\text{tang}} < \mu F_{\text{norm}} \\ \mu F_{\text{norm}}, & \text{if } b_{\text{gap}} < 0 \text{ and } k_{\text{tang}} \Delta u_{\text{tang}} = \mu F_{\text{norm}} \end{cases} \quad (2.103)$$

The maximum tangential friction force is limited by the slip condition of the frictional contact which depends on the gap normal force F_{norm} and the friction coefficient μ . Before sliding, F_{tang} depends on the stick stiffness of the frictional contact k_{tang} and the contact slip distance Δu_{tang} after the contact was closed. Supposing no relative tangential displacement of the nodes when the contact is open, the contact slip distance is given as the norm of the relative displacement vector in tangential direction, $\Delta u_{\text{tang}} = \sqrt{(u_{y,2} - u_{y,1})^2 + (u_{z,2} - u_{z,1})^2}$. Equation 2.103 introduces an asymmetric element into the stiffness term of the nonlinear system of equations.

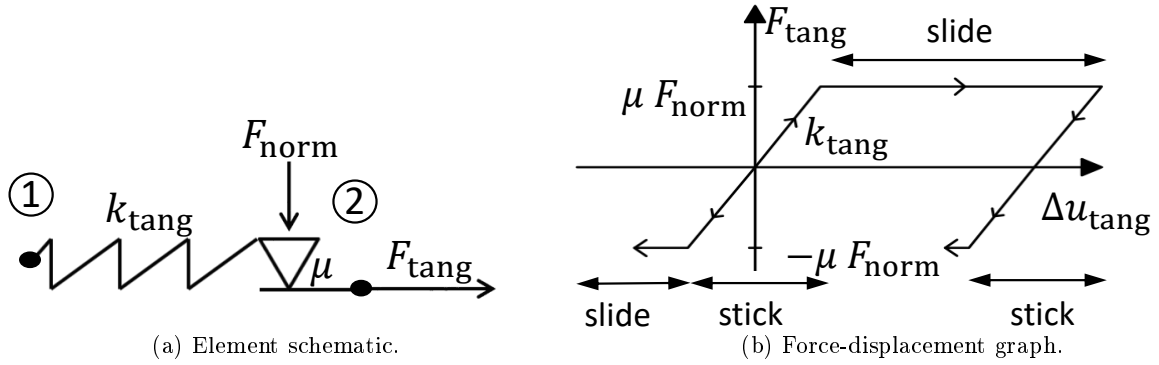


Figure 2.9: Friction element with spring representing stick stiffness.

2.2.3 Solution methods

For FA structural analysis, specific solution methods beyond the simple solution of the linear algebraic problem given in equation 2.91 are required due to the use of nonlinear elements and the need to calculate the time-dependent creep evolution. This section presents the applied methods for the creep algorithm and for the solution of the nonlinear system of equations.

2.2.3.1 Creep algorithm

One of the most important features of the FA bow analysis is the calculation of the in-reactor creep deformation. With the methods presented so far, only an elastostatic equilibrium of the structure can be calculated. The creep introduces a time component into the problem. Since creep is a slow process compared to the time scale of the inertial term, creep can be solved by a quasi-static simulation. That is, for each creep increment after a certain time step, a new elastostatic equilibrium must be found. The following paragraph presents the typical procedure for a creep algorithm over one time step (Boyle and Spence, 1983; Penny and Marriott, 1995; ANSYS, 2013b). In section 2.2.1, only elastic strains are considered to calculate the virtual work. Considering all strain effects, the total strain is:

$$\varepsilon^{\text{tot}} = \varepsilon^{\text{el}} + \varepsilon^{\text{th}} + \varepsilon^{\text{cr}} + \varepsilon^{\text{gr}} \quad (2.104)$$

where ε^{gr} is the growth strain. The modified constitutive relation is:

$$\boldsymbol{\sigma} = D\boldsymbol{\varepsilon}^{\text{el}} = D(\boldsymbol{\varepsilon}^{\text{tot}} - \boldsymbol{\varepsilon}^{\text{th}} - \boldsymbol{\varepsilon}^{\text{cr}} - \boldsymbol{\varepsilon}^{\text{gr}}) \quad (2.105)$$

When applying the principle of virtual work using this modified constitutive relation, additional artificial force terms appear in equation 2.88 and therefore in the linear system in equation 2.91. The new terms are the thermal force vector \mathbf{f}^{th} , the creep force vector \mathbf{f}^{cr} , and the growth force vector \mathbf{f}^{gr} :

$$\mathbf{f}^{\text{th}} = \int_{\Omega} \mathbf{B}^T D \boldsymbol{\varepsilon}^{\text{th}} dV, \mathbf{f}^{\text{cr}} = \int_{\Omega} \mathbf{B}^T D \boldsymbol{\varepsilon}^{\text{cr}} dV, \mathbf{f}^{\text{gr}} = \int_{\Omega} \mathbf{B}^T D \boldsymbol{\varepsilon}^{\text{gr}} dV \quad (2.106)$$

The linear system to be solved becomes

$$\mathbf{K} \mathbf{u}_N = \mathbf{f}^{\text{ext}} + \mathbf{f}^{\text{th}} + \mathbf{f}^{\text{cr}} + \mathbf{f}^{\text{gr}} = \mathbf{f}^{\text{tot}} \quad (2.107)$$

The thermal and growth force vectors are not dependent on the element solution and can therefore be calculated at the beginning of each time step using the nodal temperature and flux values. However, the creep strain increment for a certain time step, $\Delta \varepsilon^{\text{cr}}$ depends on the element stress during this time step. The stress is a derived solution variable so that 2.107 becomes an implicit system of equations. Furthermore, the stress in the element is a non-uniform distribution over the cross-section. To solve the integral in equation 2.106, the element cross-section at each node must be discretized into an arbitrary number n of integrating points with index j distributed over the element cross-section. At these integration points, the local stress $\boldsymbol{\sigma}_j$ needs to be determined, based on which the creep strain $\boldsymbol{\varepsilon}_j^{\text{cr}}$ is calculated. Depending on the covered area, each integrating point is associated to a weighting coefficient c_j . The creep force vector obtains the following form:

$$\mathbf{f}^{\text{cr}} = \sum_{j=1}^n c_j \mathbf{B}_j^T D \boldsymbol{\varepsilon}_j^{\text{cr}} \quad (2.108)$$

To solve the implicit system of equations, a numeric time step method needs to be defined. The following algorithm illustrates the sequence of necessary calculation steps for the creep algorithm, starting from a fully established nodal solution. That is, all nodal displacements \mathbf{u}_N and stresses $\boldsymbol{\sigma}_j$ at the integration points are defined.

1. Calculate the effective creep rate $\dot{\varepsilon}_{\text{eff}}^{\text{cr}}$ at each integration point according to equation 2.44, that is, based on the effective stress, equation 2.45, and the previously accumulated effective creep strain $\varepsilon_{\text{eff}}^{\text{cr}}$.
2. Calculate the components of the creep strain increments according to the Prandtl-Reuss equations applied to creep, equations 2.46 to 2.48.
3. Determine the time step size Δt . For the present work, the automatic time step algorithm provided by ANSYS is used, see the *AUTOTS* command in ANSYS (2013b). Additionally, a creep criterion is used if necessary, command *CRPLIM*, with which the size of the creep ratio C_S can be limited. The creep ratio relates the effective creep strain increment to the total effective strain.

$$C_S = \frac{\Delta \varepsilon_{\text{eff}}^{\text{cr}}}{\varepsilon_{\text{eff}}^{\text{tot}}} \quad (2.109)$$

4. Calculate the creep strain increments based on the time step size.

$$\Delta \epsilon^{\text{cr}} = \dot{\epsilon}^{\text{cr}} \Delta t \quad (2.110)$$

5. Form the creep force vector \mathbf{f}^{cr} according to equation 2.108.
6. Solve the system in equation 2.107 to obtain the updated nodal displacements and forces. Based on the nodal solution, the stresses at the integration points are to be updated.

The most straightforward method is the explicit Euler forward method, for which only information from the previous time step is used to calculate the solution of the current time step. For this reason, only one iteration over the presented calculation steps is required per time step, limiting the computing time per time step. For many problems, however, the time step size using the explicit algorithm must be chosen very small to obtain reasonable accuracy and a numerically stable solution. Implicit methods are inherently stable; therefore, no limit must be set on the time step size. Using an implicit Euler algorithm, the presented calculation steps must be repeated iteratively, updating each time the creep strain increment based on the previous solution. The algorithm is converged when the maximum change in the creep strain increment related to the previous iteration is smaller than some prescribed error tolerance ϵ . Implicit methods often provide higher accuracy for a given time step size since they use also the information of the current time step to obtain the creep strain increment in equation 2.110. Although implicit methods require several iterations per time step, they are often computationally more efficient because significantly larger time steps may be used. Therefore, an implicit creep algorithm is used in the present work to guarantee a computationally efficient solution while maintaining high accuracy and numeric stability.

2.2.3.2 Newton-Raphson method

The present finite-element problem generates a nonlinear system of equations which is to be solved for the unknown nodal displacements, see equation 2.111, where $\mathbf{f}(\mathbf{u}_N)$ is the vector of nonlinear functions of the nodal displacements \mathbf{u}_N .

$$\mathbf{f}(\mathbf{u}_N) = \mathbf{f}^{\text{tot}} \quad (2.111)$$

Unlike for linear system of equations, for which an exact solution is possible, nonlinear systems need to be solved with numeric methods, for example, the Newton-Raphson method. The Newton-Raphson method generates iteratively approximated linear systems of equations based on the Taylor series until the required accuracy is reached. The full Newton-Raphson procedure (ANSYS, 2013b), in which the stiffness matrix is updated at each equilibrium iteration, is used for all calculations performed in this work. Due to the important role of friction for the FA stiffness, the unsymmetric option is applied (ANSYS command *NROPT,UNSYM*), which uses unsymmetric matrices of elements where applicable. In this manner, we can guarantee a robust solution of the system of equations. To solve the linear systems of equations generated by the Newton-Raphson algorithm, both direct methods with an exact solution and iterative methods with approximated solutions are available. In general, the larger the linear system of equations, the more efficient are iterative solvers in terms of memory use and computational run time. The models in the present applications are still sufficiently small to be solved efficiently with a direct solver. For this purpose, a sparse

direct solver based on the Gaussian elimination method with LU decomposition is used, ANSYS command *EQSLV,SPARSE*.

2.3 Fluid mechanics

2.3.1 Navier-Stokes equations

For the simulation of the coolant flow in the reactor, a flow model based on a porous medium approach is used in this work. The simulation of any flow problem is based on the Navier-Stokes equations, which comprise the balance equations for mass, momentum, and energy for fluid flow. Equations 2.112 and 2.113 give the incompressible Navier-Stokes equations for adiabatic flow of Newtonian fluids in their differential form, which are derived in Todreas and Kazimi (2012), for example.

Balance of mass or continuity equation

$$\nabla \cdot \mathbf{v} = 0 \quad (2.112)$$

For incompressible flow, the continuity equation states that the mass of the flow entering a fluid volume must be equal to the mass leaving the volume. Using Gauss's divergence theorem, this is expressed by the fact that the divergence of the velocity \mathbf{v} is zero.

Balance of forces or momentum equation

$$\rho \frac{\partial \mathbf{v}}{\partial t} + \rho(\mathbf{v} \cdot \nabla)\mathbf{v} = -\nabla p + \mu \Delta \mathbf{v} + \mathbf{f}_B \quad (2.113)$$

The momentum equation represents Newton's second law applied to fluid flow. The first term accounts for the unsteady effects and is called the transient term. The second term accounts for the moment transport and is called the transport or convection term. The first two terms at the right are the pressure term and the viscous term. The latter accounts for the shear stresses in the fluid due to its dynamic viscosity μ . The last term describes the effect of distributed volumetric body forces \mathbf{f}_B which derive often from a potential, such as gravity. This momentum source term can also be used to impose additional momentum losses on a system when applying a porous medium approach, for example.

No general analytical solution has been discovered so far for the Navier-Stokes equations. Systems described by equations 2.112 and 2.113 must usually be solved with numerical methods using computers. This field of application is called CFD (Computational Fluid Dynamics).

2.3.2 Internal channel flow

The study of internal channel flow is a field of fluid mechanics referring to confined flow inside channels with specific geometries, for example, pipes, ducts, or tube bundles. By simplification of the Navier-Stokes equations and the use of correlations, the equations governing internal channel flow can usually be solved analytically. Due to the simple geometries under consideration, the flow is usually two-dimensional with a principal flow direction, the streamwise direction, and a perpendicular component, the transverse direction. In pipe flow, for example, the axial component is the streamwise direction and the radial component is the transverse direction. The transport equations established for pipe and duct flow are usually one-dimensional,

solving only for the streamwise direction, see the Bernoulli equations introduced in the next section. The effect of the transverse direction is mostly accounted for by previously established empiric correlations describing, for example, the effects of wall friction or the pressure loss due to obstructions to the flow. These correlations are usually derived from experimental tests with specific geometries and relate to dimensionless constants which are characteristic for the respective problem. Idel'čik (1994), Kast and Nirschl (2013), or Todreas and Kazimi (2012), for example, provide a multitude of correlations established experimentally by different authors for various applications.

Bernoulli equations for channel flow Bernoulli's principle states that an increase of the fluid pressure or potential energy along one streamline is accompanied by a decrease in fluid speed and vice versa. The Bernoulli equations are a class of equations which express this principle and are valid for inviscid flows. They can be derived from the Navier-Stokes equations by integration, see Todreas and Kazimi (2012). For the particular case of steady-state pipe flow, that is, incompressible flow in the gravitational field with a single flow direction, we obtain the following form of the Bernoulli equation:

$$\frac{\dot{m}^2}{2\rho A^2} + \rho g z + p = \text{constant} \quad (2.114)$$

where z is the coordinate in the direction opposed to gravity, \dot{m} is the mass flow rate in the channel, and A is the cross-sectional area perpendicular to the flow. Since the viscous term has been neglected for the integration, equation 2.114 is only applicable to inviscid flow. In real channel flow, however, the viscosity introduces shear forces within the fluid due to the friction of the flow with the confining wall, causing a loss of driving pressure. These shear effects can be accounted for in the Bernoulli equation by a pressure loss term. Equation 2.114, established between the points 1 and 2 along the flow path, can be rewritten as:

$$\frac{\dot{m}^2}{2\rho} \left(\frac{1}{A_2^2} - \frac{1}{A_1^2} \right) + \rho g(z_2 - z_1) + p_2 - p_1 + \Delta p_{\text{loss}} = 0 \quad (2.115)$$

where Δp_{loss} is the irrecoverable pressure loss, which is expressed by empirically established correlations. It is the sum of the form and friction losses along the flow path, Δp_{form} and Δp_{fric} . The total pressure drop along the flow path can be represented as the sum of the single pressure drops due to channel cross-section constriction or expansion, the gravitational head, and the viscous losses.

$$p_1 - p_2 = \Delta p_{\text{cross}} + \Delta p_{\text{grav}} + \Delta p_{\text{form}} + \Delta p_{\text{fric}} \quad (2.116)$$

The equations to determine the form and friction pressure losses are introduced in the following paragraphs. For this purpose, the concept of the hydraulic diameter is to be defined first. The confined flow inside a channel with arbitrary geometry can be approximated by considering the flow through a pipe with a diameter equal to the hydraulic diameter d_{hyd} of the channel given in equation 2.117, where A_{flow} is the area normal to the flow and P_{wet} is the wetted perimeter. The subchannel flow along the FA structure in the reactor core can also be considered as a type of channel flow.

$$d_{\text{hyd}} = \frac{A_{\text{flow}}}{P_{\text{wet}}} \quad (2.117)$$

Friction pressure losses The friction losses develop due to the formation of a boundary layer between the fluid bulk and the structural wall, at which the fluid velocity is zero. Frictional losses are dominant for the flow along structures parallel to the flow, for example, flow inside pipes or along the GT and FR walls. The corresponding pressure loss due to pipe wall friction along a pipe with length l is:

$$\Delta p_{\text{fric}} = \frac{f_D l}{d_{\text{hyd}}} \frac{\rho v^2}{2} = \frac{f_D l}{d_{\text{hyd}}} \frac{G^2}{2\rho} \quad (2.118)$$

The pressure loss is proportional to the dynamic pressure of the flow, $p_{\text{dyn}} = \frac{1}{2}\rho v^2$, where v is the average flow velocity in the pipe. In flow with a heat source, as in a nuclear reactor, it is often more convenient to refer to the mass flux, $G = \rho v$, instead. f_D is the Darcy friction factor which depends on several influencing factors, such as the flow regime and the surface roughness. The flow regime in a pipe is generally characterized by the non-dimensional Reynolds number Re :

$$Re = \frac{\rho v d_{\text{hyd}}}{\mu} = \frac{G d_{\text{hyd}}}{\mu} \quad (2.119)$$

The surface roughness is determined by the relative roughness $\frac{\lambda}{d_{\text{hyd}}}$. The values for $f_D(Re, \frac{\lambda}{d_{\text{hyd}}})$ are charted in the well-known Moody (1944) diagram. Based on the balance of forces in the momentum equation, the pressure loss in equation 2.118 causes the following friction force on the pipe wall:

$$F_{\text{fric}} = \Delta p_{\text{fric}} A_{\text{flow}} = \frac{f_D}{4} P_{\text{wet}} l \frac{G^2}{2\rho} = C_{\text{fric}} A_{\text{fric}} \frac{G^2}{2\rho} \quad (2.120)$$

where $C_{\text{fric}} = \frac{f_D}{4}$ is the friction coefficient and $A_{\text{fric}} = P_{\text{wet}} l$ is the surface friction area.

Form pressure losses The form losses in channel flow are usually due to inertial effects caused by obstacles to the flow path. In the reactor core, form losses are dominant for the flow across structures, such as the spacer grids and the orifice plates in the FA head and foot. These cause perturbations of the flow field in the wake after the obstacle, which generate a pressure difference between the upstream and downstream:

$$\Delta p_{\text{form}} = \zeta \frac{\rho v^2}{2} = \zeta \frac{G^2}{2\rho} \quad (2.121)$$

where ζ is the flow resistance coefficient. The pressure loss in equation 2.121 causes the following drag force on the structure:

$$F_{\text{form}} = \Delta p_{\text{form}} A_{\text{flow}} = \zeta A_{\text{flow}} \frac{G^2}{2\rho} \quad (2.122)$$

Form pressure loss in flow over tube bundles Most correlations provided in textbooks for the pressure loss in flow across tube bundles have been established for transversal flow with an angle of attack of $\theta = 90^\circ$. That is, they give the flow resistance coefficient for pure cross-flow, ζ_{90° , as a function of the Reynolds number in the narrow gap Re_{ng} :

$$Re_{\text{ng}} = \frac{\rho v_{\text{ng}} d_o}{\mu} \quad (2.123)$$

In equation 2.123, d_o is the outer diameter of the rods in the array and v_{ng} is the velocity in the narrow gap between two rods. The pressure drop over n rows of a rod bundle is then calculated as follows:

$$\Delta p = \zeta_{90^\circ} n \frac{\rho v_{ng}^2}{2} \quad (2.124)$$

Cross flow inside nuclear reactors, however, has an important axial component due to the high mass flow rate through the core. The flow corresponds to an oblique flow over a rod bundle with a small angle of attack $\theta \ll 90^\circ$. With decreasing values of θ , the contribution of pressure drag to the flow resistance decreases in favor of friction drag, thus reducing the flow resistance. To obtain the pressure drop of the oblique flow, a resistance reduction ratio $\psi(\theta)$ is applied to the flow resistance coefficient obtained from pure cross-flow (Idel'čik, 1994):

$$\psi(\theta) = \frac{\zeta(\theta)}{\zeta_{90^\circ}} < 1.0 \quad (2.125)$$

Experimental values determining the values of ψ for different angles θ are scarce in literature, particularly for small angles $\theta < 30^\circ$. In a first approach, one could assume that the flow components which are perpendicular and parallel to the rods are independent from each other, which is called the independence principle. This would result in a resistance reduction ratio of $\psi = \sin^2 \theta$. Groehn (1982, 1988) proved, however, by means of experiments in a flow channel with inclined rods that the independence principle is not applicable to turbulent flow over rod bundles and proposed a generalized relation $\psi = \sin^a \theta$, with a to be determined experimentally. He also demonstrated that general relations for ψ , which depend only on the angle of attack, are not reliable since ψ was detected to depend also on the flow Reynolds number and the pitch-to-diameter ratio. For a correlation to be reliable, a flow resistance factor must be established and validated for the flow conditions and bundle geometry of interest.

2.3.3 Porous medium approach

In its classical application, the porous medium approach is used to model flows inside porous solid media for which the geometry is too complex to be resolved with a grid or is unknown. This is the case for classical porous media, which consist of a solid with interconnected small interstitial pores which are random in size. These media usually occur in nature, for example, in porous rocks or sediments. As a result of the small scale of the pores, mostly laminar flow is present in these porous media and the pressure gradient in flow direction x follows Darcy's law:

$$\frac{\partial p}{\partial x} = -\frac{\mu}{\kappa} v_x \quad (2.126)$$

where κ is the permeability of the medium. Alternatively, porous medium modeling can be used to model large-scale flow in technical applications, passing through small-scale geometries with a regular repetitive pattern, such as rod bundles or perforated plates. In these applications, the flow is usually turbulent, and the pressure gradient is related to the dynamic pressure of the flow with a loss coefficient K , similar to equation 2.121:

$$\frac{\partial p}{\partial x} = -K \frac{\rho v_x^2}{2} \quad (2.127)$$

The flow of the coolant through the reactor core represents such a large-scale turbulent flow through a small-scale geometry. Therefore, we can model this flow by determining the loss coefficients for the different core regions. Those will be derived in section 5.1. For this purpose, the necessary quantities for the definition of the porous model are defined and different modeling concepts are discussed in the following paragraphs.

The elementary quantity for the definition of a porous medium is the volume porosity γ . It represents the ratio of the volume available to flow V_{flow} and the total available volume including the solid V_{total} .

$$\gamma = \frac{V_{\text{flow}}}{V_{\text{total}}} = \frac{A_{\text{flow}}}{A_{\text{total}}} \quad (2.128)$$

Flow in porous media in ANSYS CFX can be calculated in two manners (ANSYS, 2013a). The first method uses only so-called “fluid domains” in conjunction with a model for momentum loss. The effects of porosity are accounted for only through this loss term while all other terms in the governing equations are not modified. For the example of a single FA, the fluid domain covers the entire volume of the FA subchannel in the reactor core without subtracting the volume occupied by the FRs and other structures. The simulation is hence solved for the superficial velocity v_{sup} , that is, the velocity of the fluid if no solid structures, but only fluid, were present inside the reactor core. This method is called the “superficial velocity formulation”. In opposition to the superficial velocity, the actual velocity of the fluid accounting for the presence of the solid structures in the subchannel is called the “true velocity” v , represented without subscript. Both variables are interrelated by the porosity γ :

$$v_{\text{sup}} = \gamma v \quad (2.129)$$

For the second method, so-called “porous domains” are used instead of “fluid domains”. In this case, the governing equations will be solved for the true velocity by introducing the porosity γ in all terms of the equations. Porous domains also include dedicated models for the solid in the porous region. Models created with “porous domains” are called “full porous models” since the solid is accounted for physically in the governing equations. When modeling FAs in a reactor, however, using the full porous model complicates the treatment of the gaps between the FAs. Therefore, the superficial velocity formulation is chosen for the porous medium model in this work. Analogously to the superficial velocity, a superficial relative pressure must also be defined, which is the pressure solved for in the superficial velocity formulation:

$$p_{\text{sup}} = \gamma p_{\text{rel}} \quad (2.130)$$

where $p_{\text{rel}} = p_{\text{abs}} - p_{\text{ref}}$ is the “true” relative pressure, which is the difference between the absolute pressure p_{abs} and the reference pressure p_{ref} . The latter is defined to be the nominal operating pressure p_{sys} of the considered reactor.

Momentum losses in porous regions can be modeled in ANSYS CFX by implementing negative momentum sources. Momentum sources act as volumetric forces distributed over a defined domain. They are hence implemented as a part of the body force term of the momentum equation 2.113. The momentum losses in an isotropic porous region can be formulated using one linear term, representing the viscous losses according to Darcy’s law, equation 2.126, and one quadratic term, representing the inertial losses from equation 2.127.

$$\mathbf{S}_{\text{M}} = -\frac{\mu}{\kappa} \mathbf{v} - K \frac{\rho}{2} |\mathbf{v}| \mathbf{v} \quad (2.131)$$

In the case of rod bundles in a reactor core, viscous losses can be neglected since, unlike in a classical porous medium with interconnected pores, the pressure drop due to the turbulent flow in the reactor is based only on flow resistance coefficients which are to be multiplied with the dynamic pressure term. We assume therefore that $\kappa \rightarrow \infty$. If K is constant in all directions, the loss model is isotropic. In many applications, the loss coefficient of the porous medium depends on the spatial orientation. FR bundles represent a special case of anisotropic medium in which the loss properties differ in the stream directions parallel and transverse to the rod axis. The momentum sources in the parallel and transverse directions become:

$$S_{M,\parallel} = -K_{\parallel} \frac{\rho}{2} |\mathbf{v}| v_{\parallel} \quad (2.132)$$

$$S_{M,\perp} = -K_{\perp} \frac{\rho}{2} |\mathbf{v}| v_{\perp} \quad (2.133)$$

where K_{\parallel} and K_{\perp} are the pressure loss coefficients parallel and transverse to the rod bundle. v_{\parallel} and v_{\perp} are the flow velocity components parallel and transverse to the rod bundle.

According to section 2.3.2, the angle of attack θ is an important quantity in the modeling of the pressure loss over rod bundles inclined to the flow. It must therefore be defined for the framework of the porous model used in this work. For the sake of simplicity, the mathematical description for the definition of θ is limited to the 2D case, which is used exclusively within this work. The rules for the 3D case ensue analogously. Mathematically speaking, the angle of attack represents the rotation of the flow velocity vector \mathbf{v} with reference to the axial rod bundle direction \mathbf{e}_{\parallel} and can hence be derived as follows.

$$\cos \theta = \frac{\mathbf{v} \cdot \mathbf{e}_{\parallel}}{|\mathbf{v}|} = \frac{v_{\parallel}}{|\mathbf{v}|} \quad (2.134)$$

We can then stipulate the following relations for the previously defined velocity components.

$$v_{\parallel} = |\mathbf{v}| \cos \theta \quad (2.135)$$

$$v_{\perp} = |\mathbf{v}| \sin \theta \quad (2.136)$$

When defining a coordinate system (x, y, z) for the porous model in accordance with the orientation of the structural coordinate system, z is defined as the vertical upward direction and x and y are the cross-sectional components. As opposed to θ , the flow angle θ_f represents the rotation of the flow velocity with reference to the vertical direction \mathbf{e}_z . When assuming straight FAs and no two-way fluid-structure interaction (FSI), the rod bundle is aligned with the coordinate system (x, y, z) and $\theta = \theta_f$, see Figure 2.10a. For the more general case with deformed rod bundles and two-way FSI, the rod axis direction varies in space. For any point in the porous medium, we can then define a local coordinate system (x', y', z') , in which z' is the component parallel to the structure (\mathbf{e}_{\parallel}) and x' and y' are the transversal components, see Figure 2.10b. For the 2D case, the orientation of this coordinate system depends on the local rotations of the structure about the cross-sectional y -axis. The new system is hence obtained with the coordinate transformation in equation 2.137 using the structural rotation angle θ_y , which will be denoted as θ' following the notation for the rotated coordinate system.

$$\begin{bmatrix} x' \\ z' \end{bmatrix} = \begin{bmatrix} \cos \theta' & -\sin \theta' \\ \sin \theta' & \cos \theta' \end{bmatrix} \begin{bmatrix} x \\ z \end{bmatrix} \quad (2.137)$$

From equation 2.134, we obtain by virtue of equation 2.137 and of the angle addition theorems the following relationship for θ .

$$\cos \theta = \frac{\mathbf{v} \cdot \mathbf{e}_{\parallel}}{|\mathbf{v}|} = \frac{\mathbf{v} \cdot \mathbf{e}_z \cos \theta' - \mathbf{v} \cdot \mathbf{e}_x \sin \theta'}{|\mathbf{v}|} = \cos \theta' \cos \theta_f + \sin \theta' \sin \theta_f = \cos(\theta_f - \theta') \quad (2.138)$$

Explicitly speaking, the angle of attack becomes the difference between the flow angle and the structural rotation.

$$\theta = |\theta_f - \theta'| \quad (2.139)$$

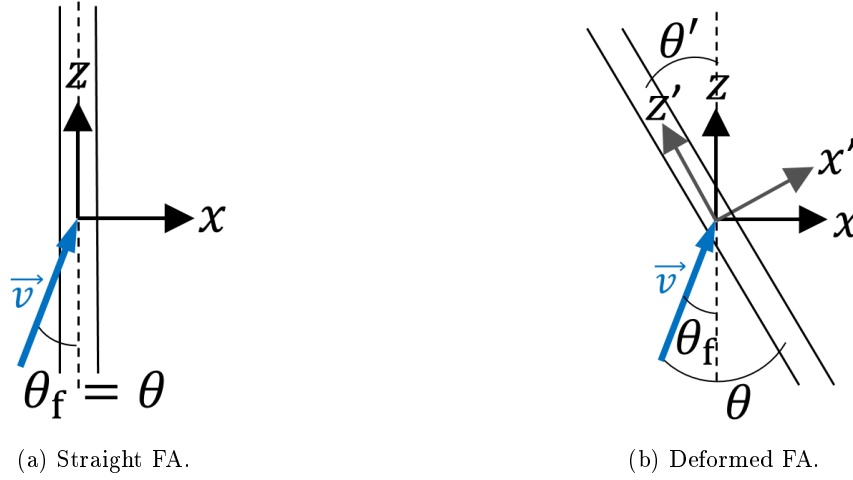


Figure 2.10: Graphic representation of the angle of attack θ for the case of straight FAs or deformable FAs when considering two-way FSI.

2.4 Zirconium alloys - metallurgy, in-reactor behavior, and modeling

2.4.1 Generations of Zirconium alloys

Murty and Charit (2006), and Murty (2013) offer good overviews of the history of the development and use of Zirconium alloys in thermal light and heavy water reactors. Zirconium alloys are extensively used in nuclear reactors primarily because of their unique combination of low neutron absorption cross-section and good corrosion resistance. Examples are the fuel cladding and spacer grids, channels in boiling water reactors (BWRs) or pressure and calandria tubes in heavy water reactors.

Table 2.1 lists the principal Zirconium alloys used in light water reactors (LWRs) and presents their alloying components and their typical content used. The first Zirconium alloy to be used extensively in LWRs was Zircaloy-2 (Zry-2) after Zircaloy-1 showed only poor corrosion resistance. To this date Zry-2 is widely used in BWRs. Since the Nickel content showed to promote hydrogen embrittlement of Zry-2 under PWR environment conditions, the development continued until with Zircaloy-4 (Zry-4) an alloy with almost as

Table 2.1: Typical composition of Zirconium alloys for LWRs in wt.% (Murty and Charit, 2006). Only selected components are given.

Alloy name	Sn	Fe	Cr	Ni	Nb	O
Zry-2	1.5	0.15	0.1	0.05	-	0.1
Zry-4	1.5	0.2	0.1	-	-	0.1
Low-Sn Zry-4	1.3	0.2	0.1	-	-	0.1
M5	-	-	-	-	1.0	0.1
MDA	0.8	0.2	0.1	-	0.5	-
ZIRLO	1.0	0.1	-	-	1.0	0.1
Opt. ZIRLO	0.7	0.1	-	-	1.0	0.1

good steam corrosion resistance as Zry-2 but with reduced hydrogen absorption was found, which became the standard for cladding fuel in PWRs. Zry-2 and Zry-4 have become widely used and accepted as the standard for structural materials in LWRs and are given different heat treatments depending on the application; recrystallization-annealed (RXA) Zry-2 cladding is used in BWRs, while cold worked and stress-relieved annealed (SRA) Zry-4 is used in PWRs. This is because the PWR FR cladding must resist higher pressure differences and therefore must present a higher yield stress, which is obtained by the cold-working process. Since PWR GTs are not internally pressurized, they undergo only smaller stresses so that RXA Zry-4 is usually used.

Since these developments dating to the 1950s, processing techniques as well as heat treatments have primarily been the only advances from the original design of the Zircaloy material for several decades. As FA burnup (BU) increased, it was found that the Zry-4 no longer met corrosion and hydriding needs in PWRs. Therefore, more recent developments include the use of low-tin Zry-4 with increased corrosion resistance and finally new alloys with added Niobium content. Amongst them figure the M5 alloy developed by Areva, the MDA alloy by Mitsubishi, and the ZIRLO and optimized ZIRLO alloys developed by Westinghouse.

2.4.2 Crystallography and texture of Zirconium alloys

This summary of the crystallography of Zirconium alloys is mainly based on Franklin et al. (1983), who gave an extensive review on creep and other deformation processes of Zirconium alloys in nuclear reactors. Two distinct crystal structures are known for pure Zirconium. For temperatures up to 862 °C, the equilibrium phase is called α -phase and exhibits a hexagonal close-packed (hcp) crystal structure. Figure 2.11 depicts the unit cell of the hcp crystal structure, pointing out the atom positions and the principal axes of the lattice. Above 862 °C up to the melting point, the equilibrium phase is called β -phase with a body-centered cubic (bcc) crystal structure. In the following, only the crystallography of α -Zirconium will be considered since it is the stable phase under PWR operating conditions. Any statements made in this thesis about Zirconium and its alloys refer to the α -phase.

Manufactured products from Zirconium alloys such as tubing are usually polycrystalline. That is, they consist of many individual crystals or grains. Hence, if the tube were composed of a large number of randomly oriented grains, the macroscopic properties could be expected to be isotropic despite the anisotropy of the individual crystals. However, Zirconium grains develop a preferred crystallographic orientation, or texture, with respect to the working directions in the thermomechanical fabrication process. As a result of this preferred alignment, a macroscopic anisotropy develops in the properties of the manufactured material. During deformation processing for tubing, the basal poles or c-directions of the individual hexagonal crystals

tend to align with the compressive fabrication stresses and the perpendicular directions with the tensile fabrication stresses, which corresponds to the axial direction in tubing. This distribution exhibits typically a maximum at a certain angle ϕ to the tube radial direction. Figure 2.12 gives a schematic illustration of this typical texture. To quantify this distribution, the Kearns factors f_a , f_r , and f_t are used, which describe the volume fraction of basal poles in the axial, radial and transverse directions. It follows that $f_a + f_r + f_t = 1$. Typical Kearns factors for cladding tubes are: $f_a = 0.05$, $f_r = 0.6$ to 0.8 , and $f_t = 0.2$ to 0.4 (Garzaroli et al., 1996).

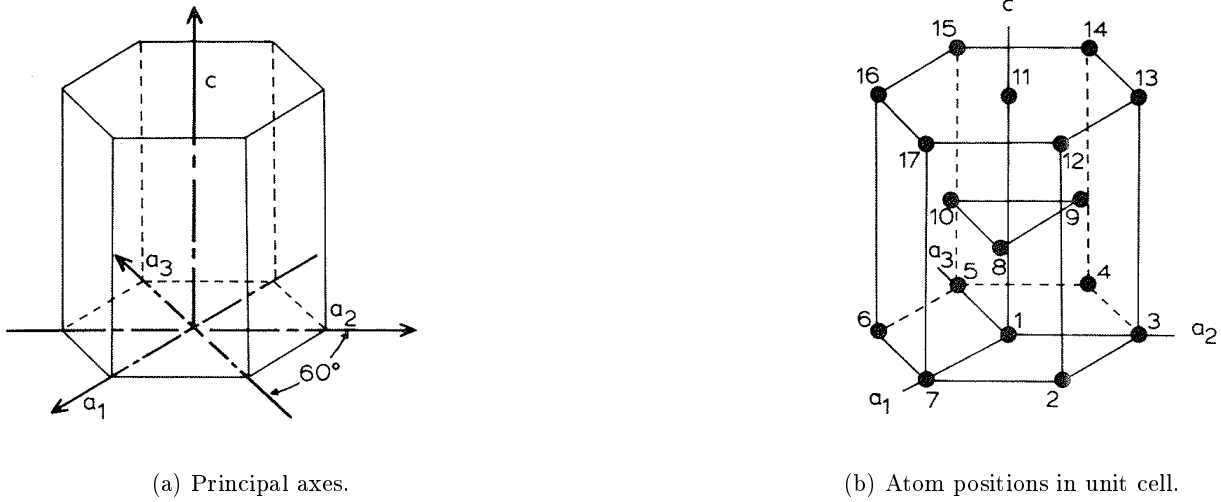


Figure 2.11: The hcp crystal structure (Franklin et al., 1983).

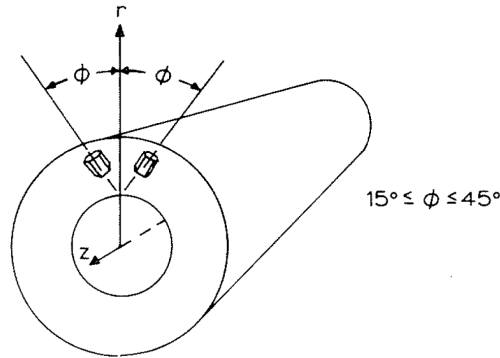


Figure 2.12: Typical texture of Zirconium tubing (Franklin et al., 1983).

2.4.3 Irradiation damage processes in microstructure

The degree of exposure of the material to fast neutron irradiation is essential in describing the irradiation creep and growth of Zirconium alloys. This is linked to the formation of an irradiation-induced microstructure, which exhibits a strong influence on the mechanical properties. The fast neutron irradiation in a nuclear reactor can be expressed in terms of the fast neutron flux $\phi(E_n > 1 \text{ MeV})$, that is, the number of fast neutrons with an neutron energy E_n greater than 1 MeV impinging on a certain area per unit time. The total exposure of a material to fast neutron irradiation can be determined by means of the fast neutron

fluence $\Phi(E_n > 1 \text{ MeV})$, which is the fast neutron flux integrated over the time of exposure:

$$\Phi(E_n > 1 \text{ MeV}) = \int_t \phi(E_n > 1 \text{ MeV}) dt \quad (2.140)$$

Since the thermal flux is of only minor importance for the calculations in this project, $\phi(E_n > 1 \text{ MeV})$ and $\Phi(E_n > 1 \text{ MeV})$ are henceforth referred to simply as ϕ and Φ .

Besides the fast neutron fluence, the microstructure is also affected by the material temperature, the stress state, the neutron energy spectrum, and the metallurgical conditions. Incident high-energy particle radiation can displace the regularly arranged atoms in a crystal lattice from their normal lattice position by means of various interactions. In the primary interaction, the initially displaced atom, the so-called primary knock-on atom (PKA), is given some initial kinetic energy. This energy is then transferred by the PKA to the surrounding atoms, which might pass it to others, resulting in a displacement cascade. Most secondary knock-on atoms come to rest within a short distance of their original lattice position. They are usually forced to take up an interstitial position in the lattice, designated self-interstitial atom (SIA), leaving behind a vacancy. SIAs and vacancies are types of point defects and a vacancy-interstitial pair is referred to as a Frenkel pair. The typical immediate effect of the interaction of a high-energy particle with the crystal structure is the creation of a displacement spike, see Figure 2.13a. This configuration is unstable and usually converts quickly into other patterns. First, a damage zone with a vacancy-rich core and an interstitial shell is created, see 2.13b. Then, the vacancies and SIAs tend to migrate to sinks, such as grain boundaries and dislocations, or combine together in planar arrays to form vacancy or interstitial dislocation loops, see Figure 2.14. These dislocation loops formed in irradiated materials represent an important type of lattice defect because they may propagate in preferential lattice directions according to the texture and stress state in the material.

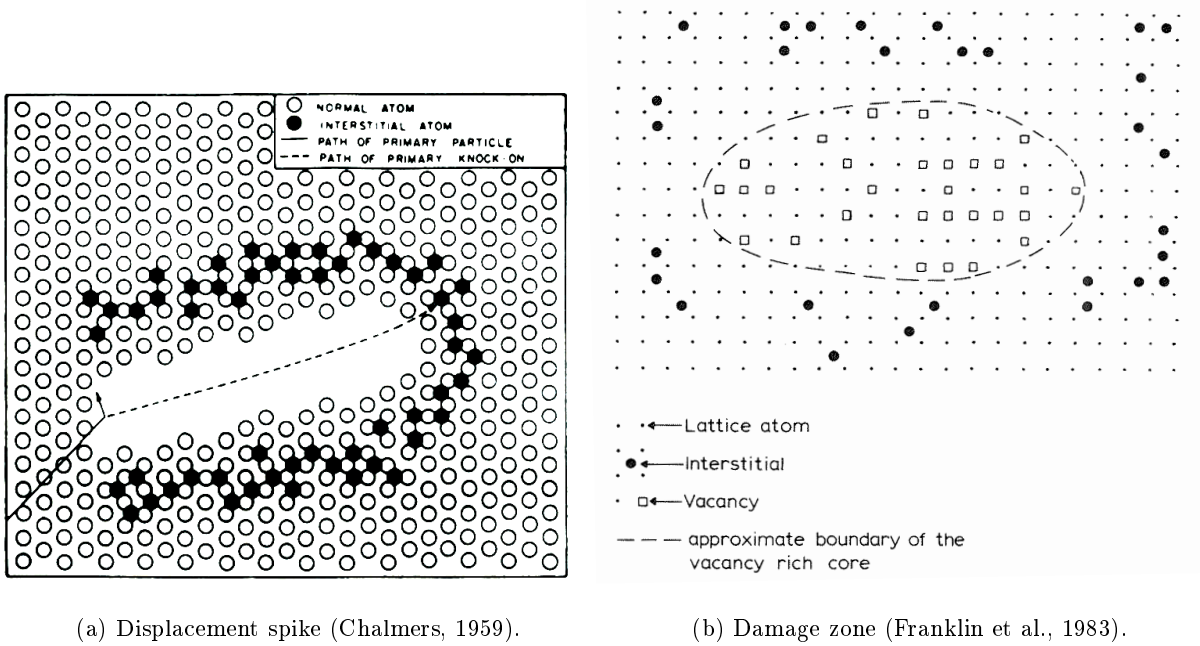


Figure 2.13: Schematic of different stages of irradiation damage.

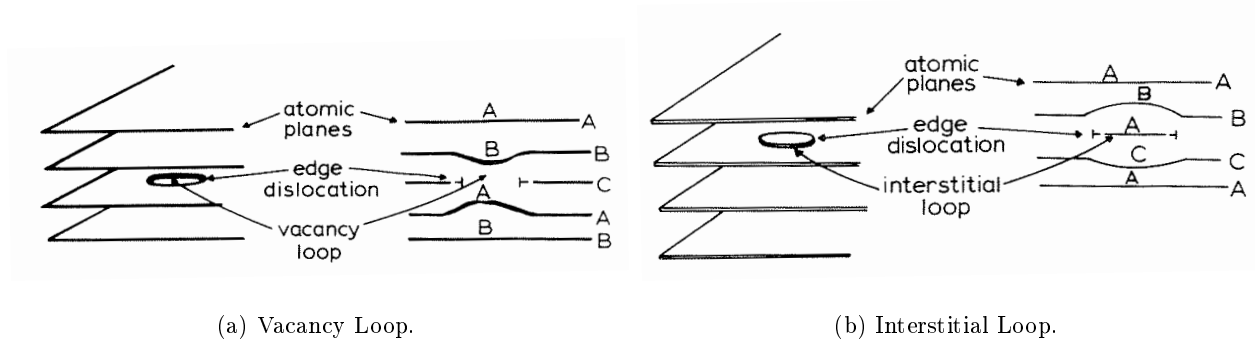


Figure 2.14: Schematic drawings of dislocation loops (Franklin et al., 1983).

2.4.4 In-reactor creep

The macroscopic effect of the preferential propagation of dislocations under the effect of stress can be observed as plastic creep strain. The permanent deformation induced directly by irradiation damages under the effect of stress is referred to as irradiation-induced creep. Two of the most-discussed propagation mechanisms for irradiation creep are stress-induced preferred nucleation (SIPN) and stress-induced preferred absorption (SIPA). The SIPN mechanism proposes the preferred nucleation of interstitial dislocation loops between atomic planes perpendicular to an applied tensile stress. Vacancy loops, in turn, may preferentially nucleate on planes parallel to the applied stress. In total, this leads to a net elongation of the material in the direction of the applied stress, as illustrated in Figure 2.15a. For the SIPA mechanism, it is not the nucleation but the growth of dislocation loops which is biased. SIAs are assumed to be preferentially absorbed at dislocation loops oriented perpendicular to the applied stress, leading to a material elongation in stress direction.

In addition to this irradiation-induced creep, thermally-activated creep exists in nuclear reactors. Thermal creep is based on microscopical mechanism completely different from those of irradiation-induced creep. One example is the climb-and glide mechanism. It is suggested that the creep deformation rate is controlled by

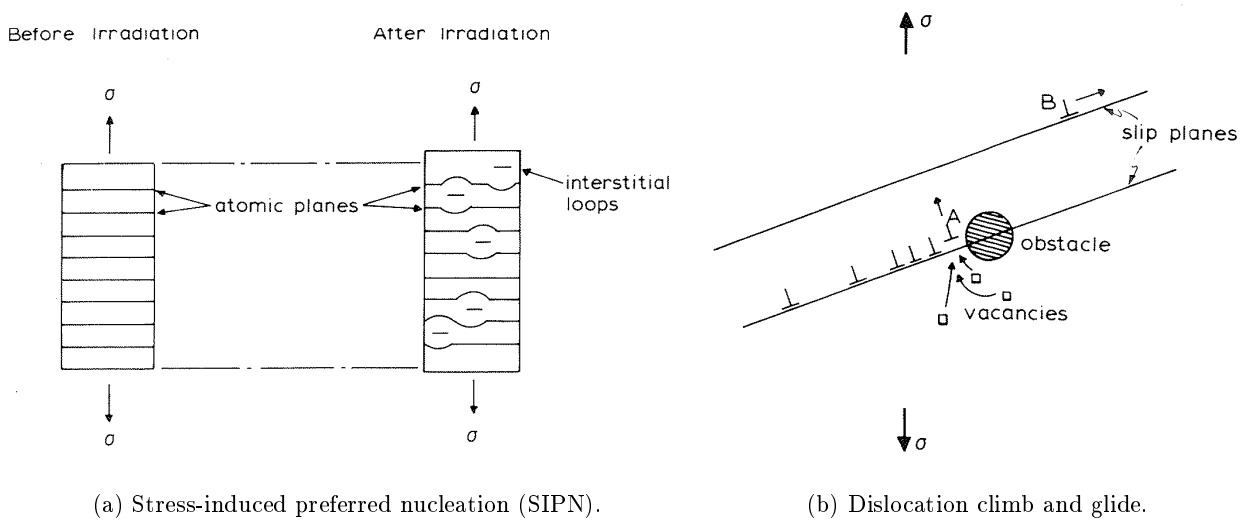


Figure 2.15: Schematic drawings of microstructural creep mechanisms (Franklin et al., 1983).

the rate at which dislocations climb to surmount obstacles in their slip plane. Figure 2.15b illustrates this process. Dislocations piled up at an obstacle in their slip plane may climb into a different slip plane by vacancy absorption, see dislocation A in the figure. After surmounting the obstacle, dislocation B may glide under the action of applied stress, providing an increment of plastic strain. While the thermal creep rate is relatively low for the temperatures encountered in thermal reactors, irradiation damages may enhance the thermal creep processes. One of the discussed mechanisms is an enhanced dislocation climb and glide, for which it is assumed that the dislocation climb is enhanced by the increased production of point defects, such as vacancies, during the irradiation.

Creep in nuclear reactors is hence the combined result of irradiation-induced creep and irradiation-enhanced thermal creep. The relative contribution of either mechanism depends strongly on operating temperature. Irradiation creep depends mainly on the fast neutron flux and exhibits only a weak temperature dependence. It is therefore often considered an athermal mechanism. Thermal creep, in turn, increases significantly with increasing temperature. In the low temperature region of thermal reactors, at about 300 °C, irradiation creep is the dominant mechanism. For high temperatures of about 350 °C, as found in the FR cladding, thermal creep becomes dominant, as illustrated in Figure 2.16.

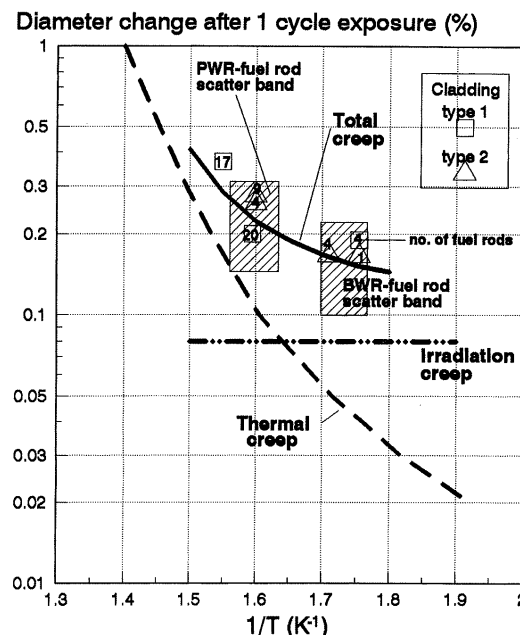


Figure 2.16: Arrhenius plot of in-reactor creep of SRA cladding (Garzarolli et al., 1996).

2.4.5 In-reactor growth

Zirconium alloys tend to undergo a length increase during reactor operation. This phenomenon is usually referred to as growth and is a result of different contributing mechanisms. Besides the fundamental mechanism of irradiation growth, these include corrosion, anisotropic creep-down and mechanical interaction between fuel and cladding. The last two are distinct features of FR growth since they occur only due to the biaxial stress state and the presence of the fuel pellets in the FR.

Irradiation growth The fundamental mechanism of material growth in nuclear reactors is the irradiation growth due to the material anisotropy of Zirconium alloys. Irradiation growth denominates the axial elongation of Zirconium alloy tubes due to fast neutron irradiation under absence of mechanical stresses. The exact mechanisms of irradiation growth are still a field of research but, in general, irradiation growth is attributed to differences in the distribution of sinks receiving a net flux of vacancies and sinks receiving a net flux of SIAs due to the anisotropy of the crystal lattice (Holt, 1988). In a simplistic view, SIAs are preferentially condensed on the prism planes and vacancies on the basal planes of the hcp crystal lattice. The individual crystal shrinks consequently in the direction normal to the basal plane and expands in the perpendicular directions, see Figure 2.17. Because of the typical texture of the Zirconium alloy tubes with a volume fraction of basal poles in axial direction of only about $f_a = 0.05$, a lengthening of the tubes occurs. Holt et al. (1996) elucidate that irradiation growth is a staged process, which can be subdivided in to three main stages. In the initial stage we observe rapid growth, which then saturates so that in the second stage growth is relatively slow. After a certain threshold, the growth rate accelerates again, and the growth strain increases quickly at nearly linear rates. This last stage is often referred to as breakaway growth. The length and importance of the different stages depends strongly on the degree of recrystallization. While for RXA materials the three stages are well defined over the irradiation time in the reactor, SRA materials grow in the third stage nearly from the beginning, see Figure 2.18.

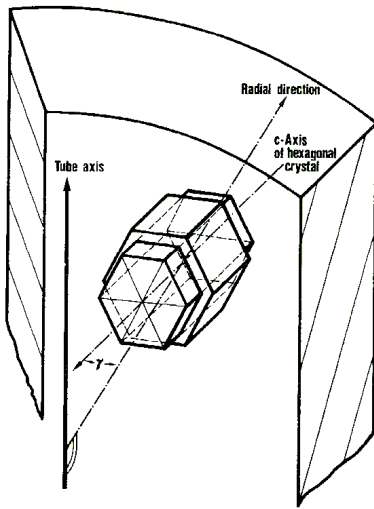


Figure 2.17: Schematic of texture-related irradiation growth (Stehle et al., 1975).

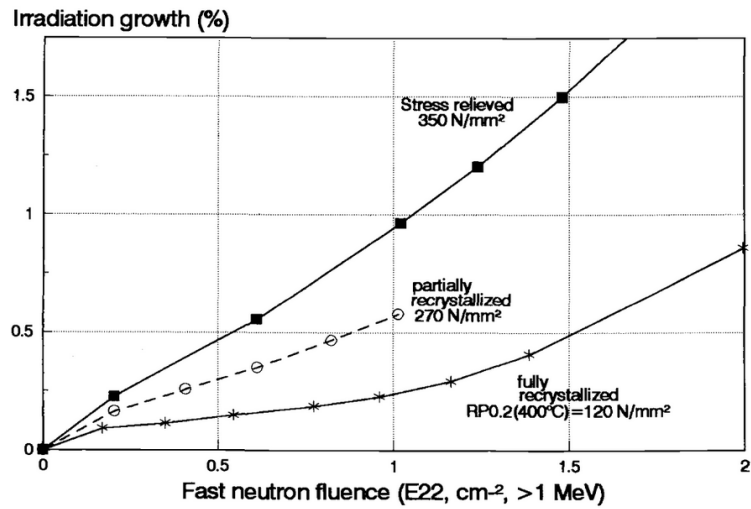


Figure 2.18: Irradiation growth of Zircaloy at 300°C (Garzarolli et al., 1996).

Corrosion One possible contributor to growth, which is mostly discussed in the context of GT growth, is corrosion (King et al., 2002). The related growth mechanisms are mainly the axial creep due to the formation of oxidation-induced stress due to build-up of the oxidation layer and the volumetric increase resulting from hydrogen pick-up due to the formation of a lower density hydride phase. Both King et al. (2002) and McGrath and Yagnik (2011) detected a strong dependence of growth rates of RXA GTs on the hydrogen uptake during irradiation, see Figure 2.19.

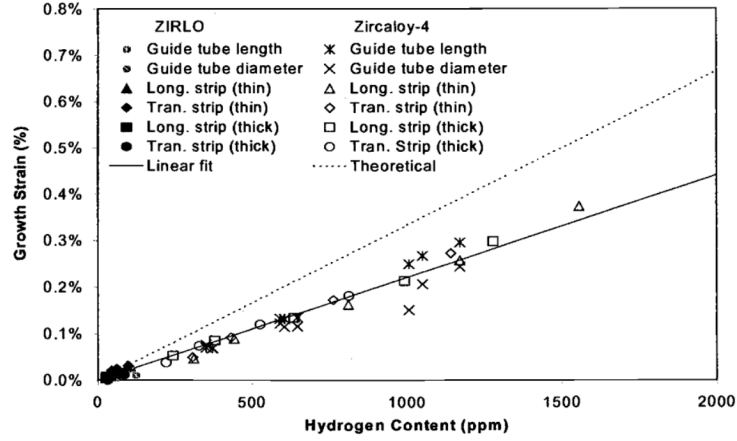


Figure 2.19: Dimensional changes of ZIRLO and Zircaloy-4 tubing and strip as a function of hydrogen content (King et al., 2002).

Anisotropic creep-down Anisotropic axial creep in the course of cladding creep-down, as discussed in appendix B, may also contribute to FR growth. Due to anisotropic creep-down, the axial strain may be increased or decreased, depending on the texture formation of the hexagonal crystal structure expressed by the Kearns factors. For f_r -to- f_t ratios larger than 1, anisotropic creep-down leads to an additional elongation of the FR and vice versa. Different directions of anisotropic creep can be appreciated in Figure B.1. For SRA Zry-4, a positive correlation exists between hoop strain and axial strain, causing a rod length reduction during creep-down. In contrast, for recrystallized materials such as the M5 alloy the correlation is negative, thus accelerating the FR growth during creep-down.

Mechanical interaction between pellet and cladding Finally, the mechanical interaction between the fuel pellet and the cladding influences FR growth. During operation, local contact points between fuel pellet and cladding develop as a result of cladding creep-down and fuel cracking and swelling. Due to the fuel expansion, axial tensile stress is produced locally in the cladding, increasing the rod length due to the resulting axial creep.

2.4.6 Modeling of the in-reactor creep of Zirconium alloys

The laws for thermal creep for conventional applications presented in section 2.1.2.2 also serve as a basis for Zirconium alloy creep laws for reactor applications. For these applications, Franklin et al. (1983), Murty (2013), or Was (2007) give a good overview. In creep laws for reactor applications, the influence of the fast neutron flux ϕ must be accounted for additionally to the stress, temperature, and time-dependent functions. The influence of different neutron flux levels is generally expressed by the neutron flux exponent n_ϕ . The most general formulation for an in-reactor creep law for Zirconium alloys is:

$$\dot{\epsilon}^{\text{cr,irr}} = C_{\text{cr,irr}} \sigma^{n_\sigma} e^{\frac{-Q_T}{T}} \phi^{n_\phi} [f_t(t) \text{ or } f_\epsilon(\epsilon^{\text{cr,irr}})] \quad (2.141)$$

According to whether a time or strain hardening formulation is used, $f_t(t)$ or $f_\epsilon(\epsilon^{\text{cr,irr}})$ must be defined. If $f(t) = g(\epsilon^{\text{cr,irr}}) = 1$, equation 2.141 becomes a steady-state or secondary creep law. Lucas and Pelloux (1981) stated that for Zircaloy the strain hardening formulation describes best the creep behavior for varying

stresses, see Figure 2.20. Still, most creep laws are based on experimental tests under constant stress and are hence expressed in a time hardening formulation. For this reason, all in-reactor creep laws in this document will be presented in their time hardening formulation, but will be implemented into the structural model in their strain hardening formulation. Which time function $f_t(t)$ to use depends on the considered alloy and application. Traditionally, in-reactor creep laws based on the Norton-Bailey equation 2.35 were used to describe the in-reactor creep of Zircalloys since due to the large primary creep strains of older alloys and shorter exposure to irradiation practically no secondary creep regime was exhibited (Franklin et al., 1983). The Norton-Bailey-type creep laws are still much used today to describe the creep behavior of a specific alloy experimentally tested under specific conditions of interest. For the in-reactor application, equation 2.35 becomes:

$$\varepsilon^{\text{cr}} = C_{\text{cr}} \sigma^{n_{\sigma}} e^{\frac{-Q_T}{T}} \Phi^{n_{\Phi}} \quad (2.142)$$

The fluence dependence with $n_{\Phi} = n_t$ is substituted for the time dependence in equation 2.35 to account for the integrated effect of irradiation. Note that n_{Φ} does not introduce any dependence on the neutron flux level under which the irradiation takes place. If such a dependence is observed, Φ must be decomposed into its components ϕ and t , using different exponents for each, $n_{\phi} \neq n_t$. In the differentiated notation equation 2.142 becomes:

$$\dot{\varepsilon}^{\text{cr}} = C_{\text{cr}} n_t \sigma^{n_{\sigma}} e^{\frac{-Q_T}{T}} \phi^{n_t-1+n_{\phi}} t^{n_t-1} \quad (2.143)$$

Figure 2.21 illustrates the development of two different creep correlations from the same data, one based on a Norton-Bailey creep law with a power relationship and one based on a steady-state secondary creep law. This second approach is, for example, used for the in-reactor creep models by Hoppe (1991) and Limbäck and Andersson (1996), which consider primary and secondary creep separately. The total creep strain ε^{cr} at a specific time t can then be expressed according to equations 2.36 or 2.37. The secondary irradiation creep

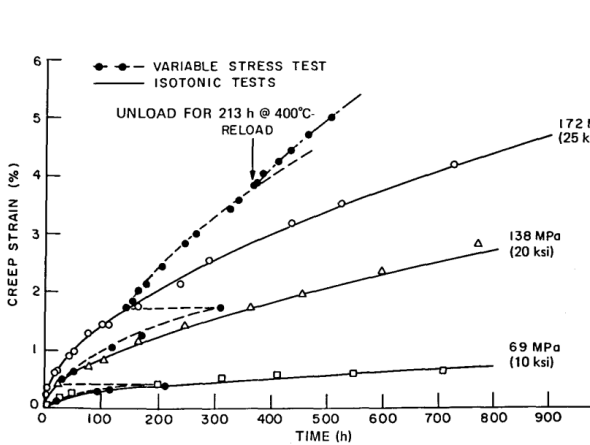


Figure 2.20: Time dependence of creep strain for Zircaloy-2 obeying the strain-hardening rule at increasing variable stress as compared to data with constant stress (Lucas and Pelloux, 1981).

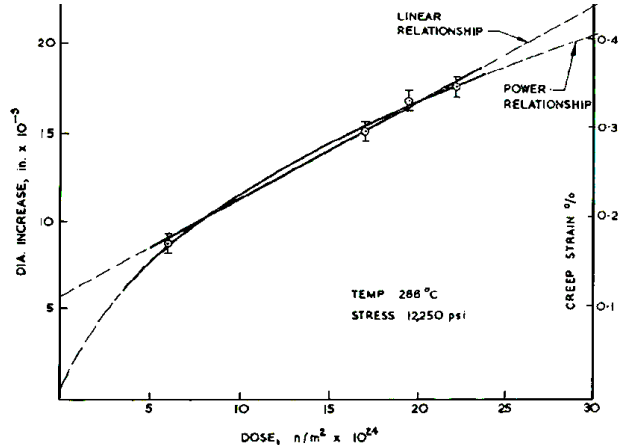


Figure 2.21: Linear versus power-law relationship for the development of a creep correlation (Wood, 1975).

rate is then given as:

$$\dot{\epsilon}^{\text{cr,sec}} = C^{\text{cr,sec}} \sigma^{n_\sigma} e^{\frac{-Q_T}{T}} \phi^{n_\phi} \quad (2.144)$$

The saturated primary creep strain $\epsilon_{\text{cr,pri,sat}}$ is sometimes indicated as a nonlinear function of the secondary creep rate. According to Limbäck and Andersson (1996), the saturated primary creep strain appears to be only weakly correlated to the secondary creep for small secondary creep rates, exhibiting small values with relatively large scattering. For higher secondary creep rates, the saturated primary creep strain increases strongly with increasing secondary creep rates. This behavior is represented in Figure 2.22.

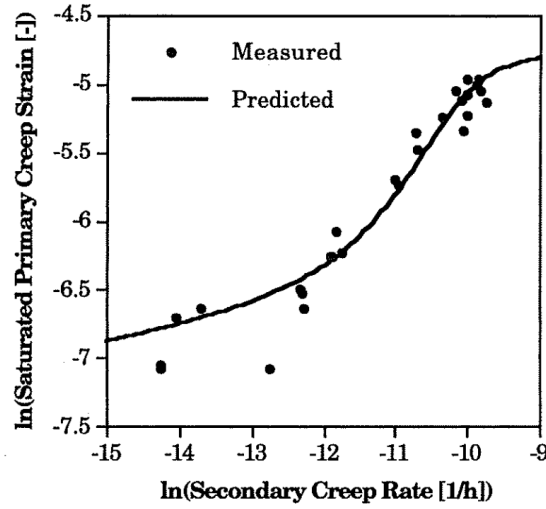


Figure 2.22: Relationship between saturated primary creep strain and secondary creep rate (Limbäck and Andersson, 1996).

Several authors have summarized, based on experimental evidence, typical reference values or value ranges for the different creep-law exponents for Zirconium alloys. As for the stress exponent n_σ , values of from 1 to 2 are often reported in literature. According to Fidleris (1988), the stress exponent has a value of $n_\sigma = 1$ at stresses below about $\frac{1}{3}\sigma_Y$. With increasing stress, n_σ gradually increases. For increasing temperatures, the stress exponent also increases due to a higher contribution of thermal creep which always yields values $n_\sigma > 1$. As Murty (2013) points out, an analysis of extensive creep data has shown that, as a general approximation, it can be assumed that the stress dependency of in-reactor creep is linear in the most relevant stress range of <10 MPa to 200 MPa and temperatures of 275 °C to 390 °C. For the activation temperature Q_T , Fidleris (1988) states that below about 300 °C the temperature dependence is weak and the Q_T has a value between 2000 K and 5000 K. At higher temperatures the dependence increases rapidly towards values of 25 000 K to 30 000 K. The temperature of transition from a weak to strong dependence varies, however, with alloying content, metallurgical condition and stress. For n_ϕ , pure irradiation-induced creep would predict a linear dependence on flux, but the inevitable contribution of thermal creep reduces n_ϕ below 1. This leads to an increase of creep strain in materials irradiated at lower neutron levels for the same fluence exposure. Data analysis for PWR neutron flux levels showed that typically $n_\phi = 0.85$, but might decrease down to $n_\phi = 0.25$ for low fluxes. Typical values for the fluence exponent are $0.4 < n_\phi < 0.8$.

Chapter 3

Fuel Assembly Structural Model

3.1 General properties

3.1.1 Reference fuel assembly (FA) design

Although the objective is to create a generic model, several choices about the specific FA design must be made. This concerns the general features of any FA structure, such as the number of fuel rods (FRs), the number and positions of guide tubes (GTs), or the number and positioning of the spacer grids. One of the incentives of this work is the FA bow problem observed in German Vor-Konvoi pressurized water reactors (PWRs) built by the former Kraftwerk Union (KWU). Therefore, the typical FA design for these reactors was used as the reference for the present model. Figure 3.1 depicts the characteristic FA design used in Vor-Konvoi plants. One distinctive feature of this FA type is the design of the bottom and top nozzles, elements 1 and 3 in Figure 3.1, usually referred to as FA foot and head. They consist of cuboidal stainless-steel frames, which are laterally open to five of the six faces. On the remaining face, they feature a perforated orifice plate (2 and 4), to which the control rod GTs are connected. The FA head also accommodates the holddown (HD) springs, for which coil-type springs are used, as opposed to leaf-type springs in various other designs. The spacer grids (7) provide a 16×16 lattice of positions, in which 20 positions are occupied by the GTs (6) and the remaining positions by the FRs (5). In total, there are nine spacer grids holding the FRs and providing additional structural stiffness. Reference data for this FA can be found in NEI (2012) or Ziegler (1984).

3.1.2 Set-up of the model

To obtain an as realistic as possible FA response, the stiffening effect of the FR bundle is modeled mechanistically. That is, the stiffness increase due to the grid coupling described in section 2.1.3.2 is an intrinsic result of the model configuration. This special feature distinguishes this model from many other FA structural models. Simplistic models often substitute one single central beam for the entirety of FRs or GTs. The stiffening effect of the grid coupling is added artificially by means of calibrated rotational springs between the single spacer grids. However, in this manner it is difficult to reproduce in detail the nonlinear features

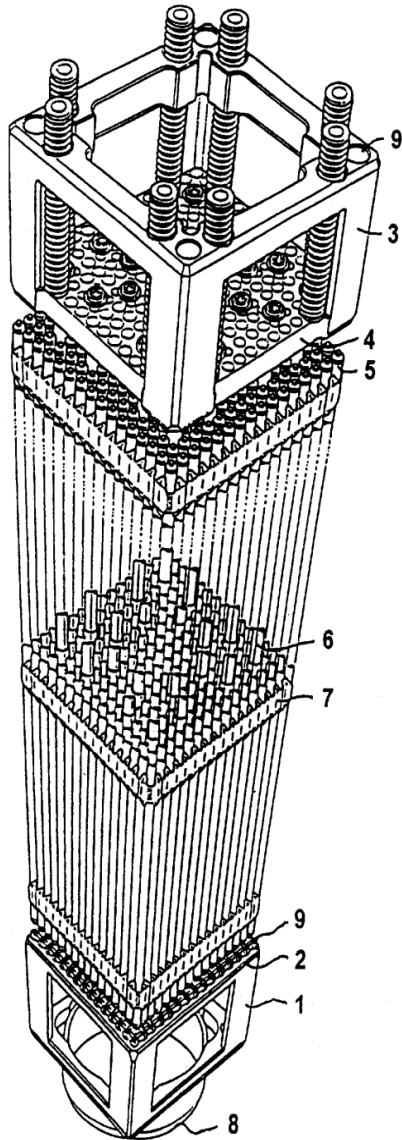


Figure 3.1: 16x16 KWU-type FA (Garzarolli et al., 2000).

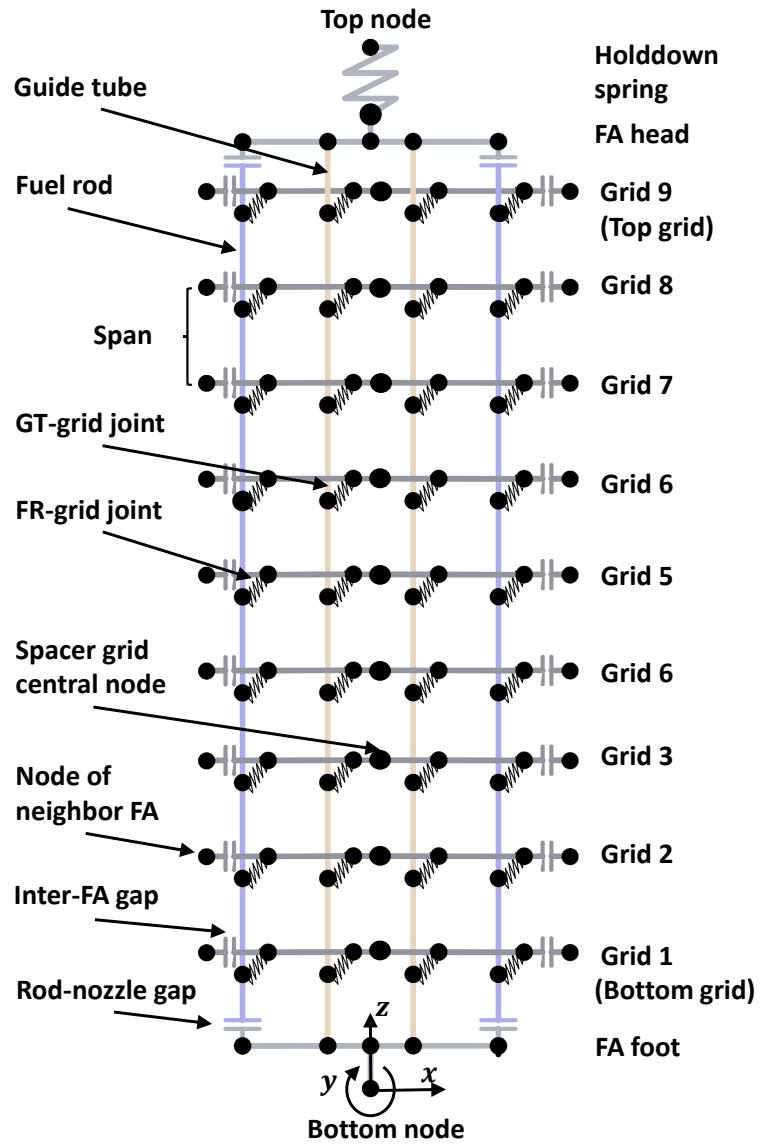


Figure 3.2: Schematic of the wireframe structure of the FA structural model.

of the coupling effect due to the nonlinear response of the FR support. To include the grid coupling effect, the fundamental configuration of the FA with four equal quarter sections must be maintained in order for the spacer grid to transmit the moments as in equation 2.63. Therefore, we start the modeling process with a full 3D FA model which considers each FR and GT individually. The 3D model takes automatically into account that the deformations in the cross-sectional directions are not independent of each other. For example, loading the FA simultaneously in both cross-sectional directions modifies the FA lateral stiffness due to the characteristics of the frictional FR support: rotationally loading the grid-to-rod connection about one axis affects the frictional behavior in the perpendicular direction. This behavior has been demonstrated by Alós Díez (2015) using the present model. Moreover, when two bending load states are superposed in the 3D model, different creep rates result than if independent 2D models for each direction were considered. This is due to the fact that the evolution of the creep rate is often nonlinear in the strain or stress dependence. After setting up the full 3D model, both a reduced 3D and a 2D model are developed in further steps, see section 3.4.

The specific design of a FA, consisting of only slender structures or very stiff structures, allows a modeling with 1D elements only. The real FA structure can hence be abstracted to a wireframe structure which is composed of interconnected 1D elements, see Figure 3.2. The connection points of the elements are the so-called nodes. The nodes are the degrees of freedom (DOFs) of the model, which are interrelated by the stiffness properties of the elements. The strategy for building up the FA model is to first define the finite elements which are appropriate for modeling the different structural elements in the FA, namely, the GTs, the FRs, the spacer grids, and the FA foot and head, see sections 3.2.1 to 3.2.3. The second step is to define the nodalization of the model, that is, the number and positions of the DOFs. It is clear that, in theory, the higher the number of nodes, the higher is the accuracy of the model, but also the longer is the computational run time. Nodes must be provided at least at the positions at which different structural elements are to be connected, for example, at the interface between GTs or FR and spacer grids, see the GT-grid and FR-grid joints in Figure 3.2. Between these nodes, the GTs and FRs may be subdivided into several individual elements, creating additional nodes; however, in general, it is sufficient to represent the GTs and FRs by one single 2-node or 3-node finite element per span between two grid levels. When defining the model, the nodes must be positioned at specific coordinates \mathbf{x}_0 in the Euclidean space; any nodal displacement during the simulation will be measured with respect to these coordinates: $\mathbf{u}_N(t) = \mathbf{x}(t) - \mathbf{x}_0$. The origin of the coordinate system is placed centrally at the bottom face of the FA foot, that is, the bottom node of the FA. The x - and y -axes form the cross-sectional or horizontal axes of the coordinate system. The z -axis indicates the axial or vertical direction.

The next step is to characterize the properties of the connections between the different structural elements, produced by welds, screw fixings, springs, or frictional contact. These connections usually cannot be considered stiff since they allow, to a certain degree, a relative movement between two structural components. Different structural components hence do not share the same nodes since this would mean that the concerning DOFs were fully coupled. Instead, two separate nodes are placed at the same position and their DOFs are connected to each other by spring elements or other DOF constraints. These connection elements have no dimensional length but represent a stiffness relationship between two nodes in a certain dimensional direction. If the model contains more than one FA, additional gap-contact elements between the individual FAs are necessary to model the inter-FA gaps. In this manner, we can account for a potential contact be-

tween the FAs when the gap closes. The modeling of the different connections is described in sections 3.2.4 to 3.2.7.

The last step is to define the boundary conditions (BCs), that is, to constrain the boundaries of the FA model in order to obtain a well-defined problem. Figure 1.1 illustrates that the FA foot stands on the lower core plate whereas the FA head is held down by the upper core plate. For the purpose of this model, the core structures, including the core plates, the core barrel, and the core baffle, are assumed to be stiff and to be rigidly connected among each other. Based on this assumption, the limits of the structural model can be drawn around the FAs, see the black dashed line in Figure 1.10c. That is, the core structures are considered as BCs, which are described in section 3.3. This assumption also implies that the upper and lower core plates remain horizontal, imposing the same constraint on all FAs. Likewise, the core baffle remains vertical, imposing the same BC on all outer FAs over their entire length. If a single FA is considered in a model simulation, the lateral DOFs are only constrained at the top and bottom nodes of the FA. If FA row or the entire core is considered, fixed nodes representing the core baffle constrain the movement of the outer FAs, see also section 3.2.4.

On the hardware side, serial runs using a single central processing unit (CPU) are usually used for performing calculation on a single FA whereas shared-memory parallel processing on four CPUs is used for the entire FA row.

3.2 FA structural elements

3.2.1 Guide tubes (GTs) and Fuel rods (FRs)

Thanks to their slender geometry the GTs and FRs can be modeled applying the Euler Bernoulli beam theory. For this purpose, we use the ANSYS element *BEAM188* (see section 2.2.2.3) with an annular cross-section, see the detail view at the top of Figure 3.3. In the dashpot region, the GT beam inner diameter is decreased by about 15%, see the cyan-colored part of the GT annulus. Figure 3.3 indicates also the cross-sectional arrangement of the GTs and the FRs in the square lattice with a FR pitch p_{FR} of 14.5 mm. The beam sections are defined by 8 cells with 4 integration points per cell, at which the constitutive calculations, such as the creep deformation, are performed (see section 2.2.3.1). All GT beams are spanned between two nodes, one at each spacer grid level, see Figure 3.4. The FR beams have three nodes per grid for the modeling of the FR support, see section 3.2.6. The creep and growth calculations are only performed in the active region of the core. No neutron flux is assumed outside this region. The top and the bottom of the active region are hence marked by additional nodes to separate the irradiated and the unirradiated beam elements. A further additional node separates the GT dashpot region from the rest of the GT. Due to the use of quadratic shape functions to ensure high accuracy, one additional node per beam element is generated internally by ANSYS. Table 3.1 introduces the most important structural parameters for this FA type and indicates the values used in this work.

Since the GTs are open to the surrounding fluid, the internal pressure is equal to the external pressure so that no hoop stresses are produced in the GT wall. The classical Euler Bernoulli theory with only axial, shear, and bending stresses is hence sufficient to describe the GT behavior. The magnitude of shear stresses can usually be neglected compared to the axial stresses. It is hence justified to define the GTs with an isotropic material, having the mechanical properties of the considered Zirconium alloy in the axial direction. In contrast, the FR cladding serves as a cylindrical pressure vessel. Due to the difference between

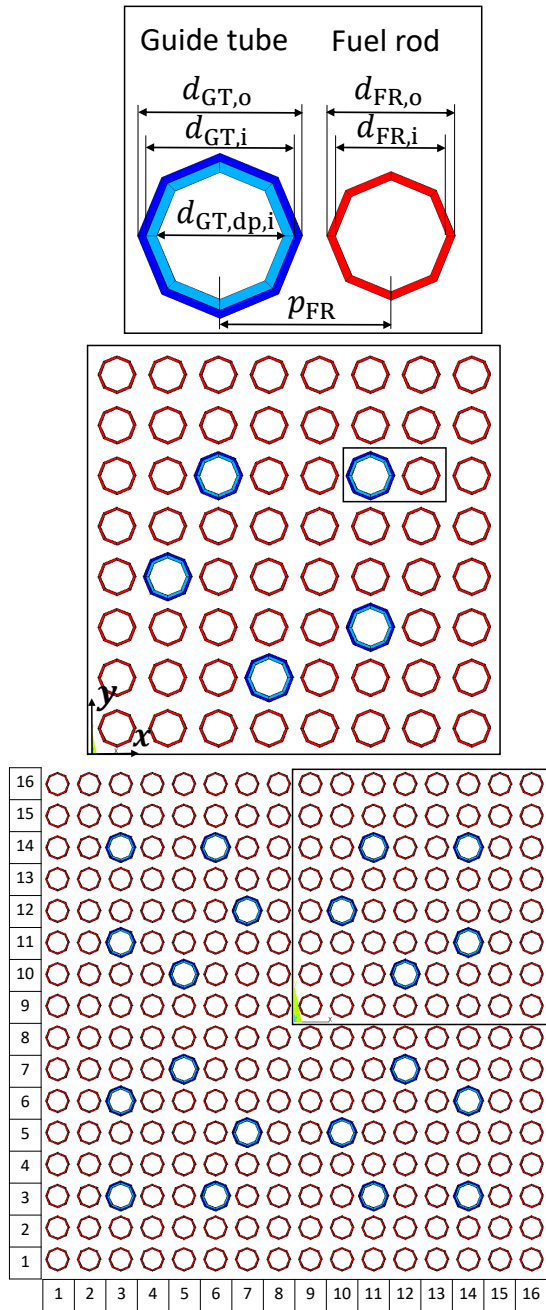


Figure 3.3: Top views of the FR and GT bundle.

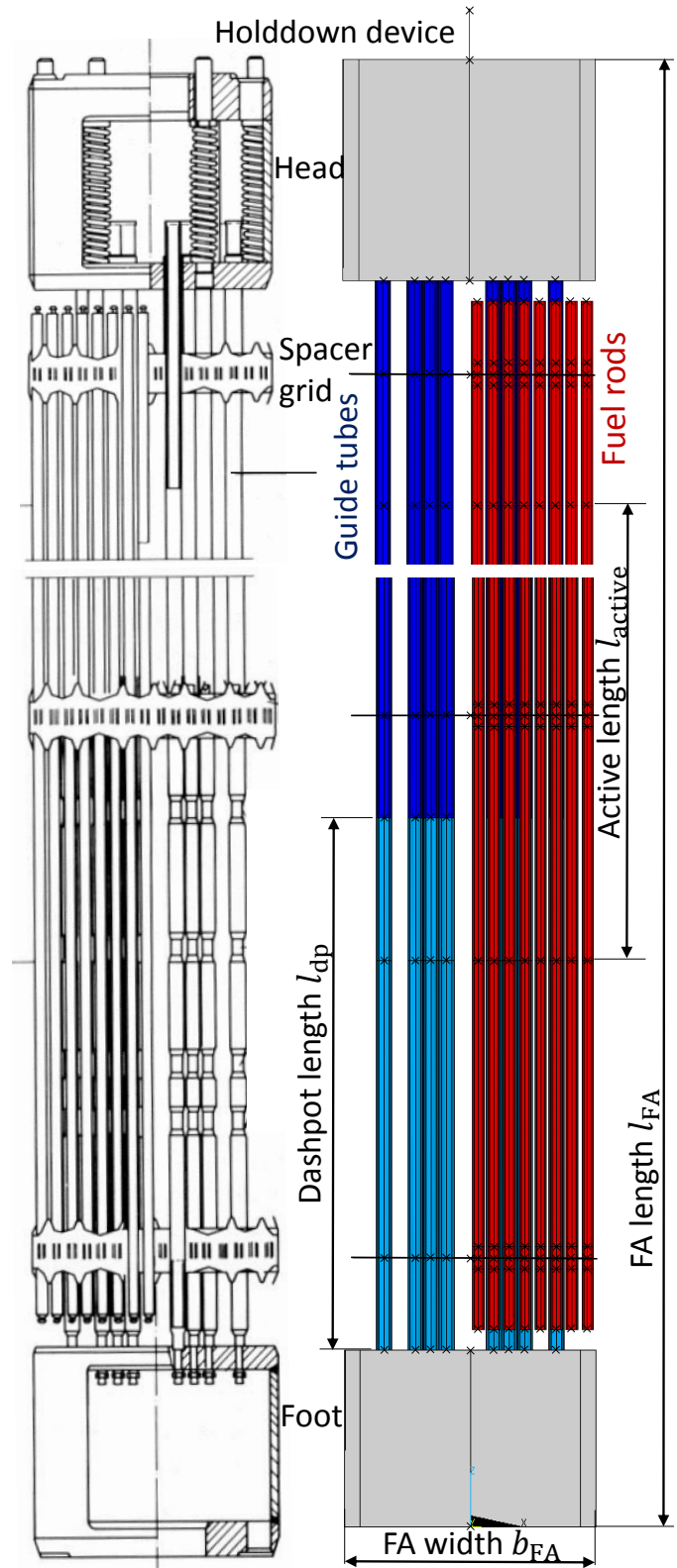


Figure 3.4: FA front view. Schematic drawing (Ziegler, 1984) and ANSYS model.

Table 3.1: FA reference data.

Variable	Symbol	Value
Assembly geometry	$n_{\text{pos}} \times n_{\text{pos}}$	16×16
Number FRs	n_{FR}	236
Number GTs	n_{GT}	20
FA width	b_{FA}	228.6 mm
FA pitch	p_{FA}	230 mm
FR outer diameter	$d_{\text{FR,o}}$	10.75 mm
FR inner diameter	$d_{\text{FR,i}}$	9.3 mm
Fuel pellet outer diameter	d_{pellet}	9.11 mm
FR pitch	p_{FR}	14.3 mm
FR length	l_{FR}	4425 mm
FA length	l_{FA}	4827 mm
GT length	l_{GT}	4850 mm
Active length	l_{active}	3900 mm
Dashpot length	l_{dp}	488 mm
GT outer diameter	$d_{\text{GT,o}}$	13.8 mm
GT inner diameter	$d_{\text{GT,i}}$	12.4 mm
GT dashpot inner diameter	$d_{\text{GT,dp,i}}$	10.59 mm

inner and outer pressure, membrane stresses appear in the FR cladding according to the equations given in section 2.1.3.3. For this type of application, ANSYS provides the so-called pipe elements, which behave like beam elements in their bending response but can evaluate hoop and radial stresses (σ_θ and σ_r) due to pressurization effects as well. The disadvantage of the pipe element is that it adds new DOFs to the model, as well as several new integration points for the creep calculations, slowing down the execution of the code. The calculation of the azimuthal and radial components is not of particular interest for the bow analysis since their effect on structural stiffness is fully included in the grid spring relaxation model presented in section 4.5.1. Therefore, the FRs are also modeled by *BEAM188* elements. However, the knowledge about the biaxial stress state, expressed by equations 2.68 to 2.70, is crucial for the calculation of the effective stress σ_{eff} , which is the basis for the FR creep calculations. To not harm the validity of the model for FA bow calculations, a particular strategy was developed to account implicitly for the biaxial stress state in the creep calculations. This strategy is presented in appendix B.

All values of the mechanical and thermophysical properties of Zirconium alloys and the nuclear fuel are based on Kim et al. (2006) and Whitmarsh (1962). The calculation of the structural mass of the GTs and FRs is done implicitly by the code based on the beam cross-sectional data and the indicated material density. The FR mass is composed of the FR structural mass and the fuel mass. The fuel pellet column inside the FR rests on a support tube which reaches from the lower end plug to the bottom of the active region. The mass of the fuel column is modeled by a lumped mass element, *MASS21*, applied at the FR bottom node and is calculated as

$$m_{\text{fuel,column}} = \gamma_{\text{UO}_2} \rho_{\text{UO}_2} l_{\text{active}} \frac{d_{\text{pellet}}^2 \pi}{4} \quad (3.1)$$

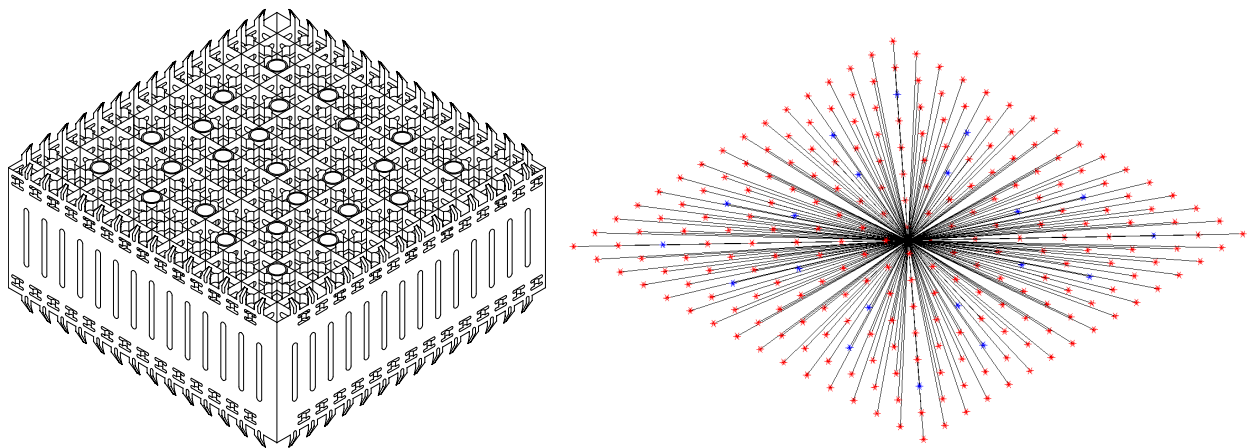
where ρ_{UO_2} is the theoretical density of the UO_2 fuel, γ_{UO_2} is the fuel porosity, l_{active} is the active length of the fuel column, and d_{pellet} is the pellet diameter. Note that for this approximation the pellets are assumed cylindrical; that is, the pellet chamfers and dishes are neglected. The plenum spring force on the fuel column

is also neglected.

3.2.2 Spacer grids

Spacer grids, Figure 3.5a, are lattice structures which are spaced along the FA at certain intervals to fulfill several functions. First, they support the FRs laterally and maintain the lateral spacing between them to ensure the coolability of the rods. Moreover, they provide a stiffening effect to the FA structure by mechanically coupling the individual GTs. Finally, the internal straps of the inner grids include mixing vanes which project into the coolant flow and promote the mixing of the coolant and, thereby, the heat transfer from the rods downstream of the vanes. The spacer grids usually consist of individual slotted straps that interlock to form a lattice in an “egg-crate” arrangement. The resulting square cells provide support for the FRs at six contact points by a combination of support dimples and springs in the two perpendicular planes. The modeling of the FR support in the spacer grid is treated separately in section 3.2.6. In the high flux region of the FAs Zirconium alloy straps are used as material due to its low neutron absorption properties. Outside of the active region, Inconel is often chosen as material because of its corrosion resistance and high strength. For the present FA design, only the bottom grid is made of Inconel while the top grid is also made of a Zirconium alloy.

In the present model, spacer grids are modeled as rigid structures due to their high stiffness compared to the adjacent elements. Figure 3.5b gives a plot of the modeled configuration of a single spacer grid in ANSYS. The grid consists of one independent central node placed at each grid level at the intersection of the vertical FA axis with the horizontal plane of the spacer grid. The number of dependent nodes depends on the number of modeled GTs and FRs. If no simplification is made, there is one dependent node placed in the center of each grid cell. These nodes coincide with the GT and FR element nodes and are connected to them by means of connection elements, see sections 3.2.5 and 3.2.6. Each dependent grid cell node is connected to the central node by means of a rigid beam, ANSYS element *MPC184*. This configuration creates the spacer grid as a stiff planar structure with three translational and three rotational DOFs. By using rigid beam elements,



(a) Schematic drawing of a bottom grid (USNRC, 2012). (b) Spacer grid model in ANSYS. Black lines mark rigid beams, blue and red stars mark GT and FR connection nodes. At the GT positions, the grid includes sleeves for the GT-grid connection.

Figure 3.5: Actual shape of spacer grid versus modeled configuration.

the dependent DOFs at the GT and FR positions are linked to the DOFs of the independent central grid node by means of kinematic constraint equations, which are created internally using the direct elimination method (ANSYS, 2013b). That is, the dependent nodes are eliminated from the solution matrix.

Since the *MPC184* rigid beams are massless elements, the spacer grid mass must be accounted for additionally. Therefore, a lumped mass element, *MASS21*, is placed at the central node of each spacer grid level. To calculate the spacer grid volume V_{grid} , it is assumed that the grid is only composed of massive grid straps without slots or protrusions so that $V_{\text{grid}} = A_{\text{grid}} l_{\text{grid}}$, with A_{grid} being the projected grid cross-section:

$$A_{\text{grid}} = (n_{\text{pos}}^2 (2p_{\text{FR}} - t_{\text{grid}}) + 2n_{\text{pos}} p_{\text{FR}} + t_{\text{grid}}) t_{\text{grid}} \quad (3.2)$$

This approximation yields a grid mass of roughly $m_{\text{grid}} = 1.5 \text{ kg}$ for a Zirconium alloy grid. For the Inconel grid, the same mass is assumed. Although the density of Inconel is higher, the grid straps can be fabricated with a reduced thickness since Young's modulus is higher as well.

3.2.3 FA foot and head structures

The modeled structural configurations of the FA foot and head are composed of two parts, the orifice plates and the structural frame. The orifice plates, that is the top plate of the FA foot and the bottom plate of the FA head, are the parts to which the GT extremities are connected. They are modeled analogously to the spacer grids. This means that for each GT additional nodes are placed coincident with the GT bottom and top nodes. Each of these nodes is connected to the central node of the respective orifice plate by means of rigid beam elements. The structural frames are modeled by single Euler-Bernoulli beams, creating the connection between the orifice plates and the opposite face, that is, the FA foot bottom face and the FA head top face. The beam is defined with a hollow rectangular cross-section out of type 304 stainless steel. This simplification is justified by the fact that the structural rigidity of the frame is very high compared to the rest of the FA. The mechanical and thermophysical properties of stainless steels are given, for example, in Davis (1994).

3.2.4 Inter-assembly gaps

The single FA models in the core are coupled to each other by gap-contact elements, ANSYS element *CONTA178*, which is described in section 2.2.2.4. Since inter-FA contact usually takes place between adjacent spacer grids, one contact element connects the neighboring spacer grid nodes at each axial grid level. If the relative FA displacement in lateral direction is larger than the indicated reference gap size $b_{\text{gap,ref}}$ (real constant *GAP* in ANSYS), then contact is established and the FAs are mechanically coupled in the lateral translational direction. Only lateral coupling forces are transmitted in the modeled contact elements. That is, only forces normal to the contact surface are considered, but no tangential forces due to friction are assumed. Based on the normal force-displacement relationship of the gap-contact element in equation 2.102, equation 3.3 expresses the lateral force $F_{x,\text{cont}}$ transmitted through the i -th gap in the FA row at the j -th grid level. $F_{x,\text{cont}}$ is determined by the relative lateral displacement u_x of the i -th and $(i - 1)$ -th FA at this axial level. For a row of 15 FAs, $i = 0$ and $i = 16$ represent the core baffle to the left and right of the FA

row. Since the core baffle is assumed stiff, we have $u_{x,0,j} = u_{x,16,j} = 0$.

$$F_{x,\text{cont},i,j} = \begin{cases} 0, & \text{if } b_{\text{gap},i,j} = b_{\text{gap,ref}} + u_{x,i,j} - u_{x,i-1,j} > 0 \\ k_{\text{cont}} b_{\text{gap},i,j}, & \text{otherwise} \end{cases} \quad (3.3)$$

For the inter-assembly gaps, k_{cont} is chosen very large compared to the remaining structure. This implies that the interference remains very small in relation to the displacements of the structure, that is, $b_{\text{gap},i,j} \approx 0$. $F_{x,\text{cont},i,j}$ is obtained based on the mechanical equilibrium of the coupled structure. The reference gap size reads as

$$b_{\text{gap,ref}} = b_{\text{gap,ini}} - \frac{\Delta b_{\text{grid},i,j} + \Delta b_{\text{grid},i-1,j}}{2} \quad (3.4)$$

where $\Delta b_{\text{grid},i,j}$ stands for the lateral growth of the grid j of the i -th FA and $b_{\text{gap,ini}}$ is the initial gap size under operation between two fresh and perfectly straight FAs. FA design criteria normally enforce $b_{\text{gap,ref}} > 0$. For the time being, the reference gap size is assumed not to be influenced by the grid growth during burnup (BU), that is, $\Delta b_{\text{grid},i,j} = 0$ and $b_{\text{gap,ref}} = b_{\text{gap,ini}}$. The nominal initial gap size under operating conditions is about $b_{\text{gap,ini}} = 1.6 \text{ mm}$ (RSK, 2015). In cold condition (CC), the gap size is somewhat lower due to the larger thermal expansion coefficient of the core support plate and FA nozzles as opposed to the Zircaloy grids. In the present model, $b_{\text{gap,ini}}$ is assumed constant for all inter-assembly gaps at all temperatures and fresh FAs are assumed to be initially perfectly straight. Gap-contact elements are also used to model the rod-nozzle gaps between the FR extremities and the foot and head in order to limit the axial movement of the FRs.

3.2.5 GT connections

GT to Zircaloy spacer grid The connection between the GTs and Zircaloy spacer grids is commonly realized by means of spot welds, sometimes with a sleeve as intermediate piece, depending on the FA design. Figure 3.6 shows a schematic of different spot-weld strategies for the GT-grid connection including the classical four-spot weld. These joints must provide an intact connection between the GTs and grids during operation, shipping, and handling in order to maintain the dimensional stability of the FA under all conditions. Due to the welds, the lateral translational connection can be considered as stiff, which means that the lateral DOF of the spacer grids and GTs are fully coupled in the model. The axial connection is also relatively stiff; however, to allow the model to be sufficiently flexible for a posterior calibration, the axial connection stiffness is modeled by a spring element with very high stiffness $k_{z,\text{GT-grid}}$. The rotational direction of the GT-grid connection

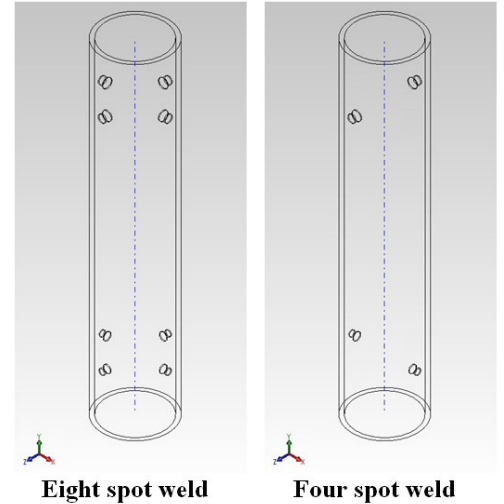


Figure 3.6: Example schematics of the spot-weld connections between GTs and spacer grids (Mattos Schettino et al., 2014).

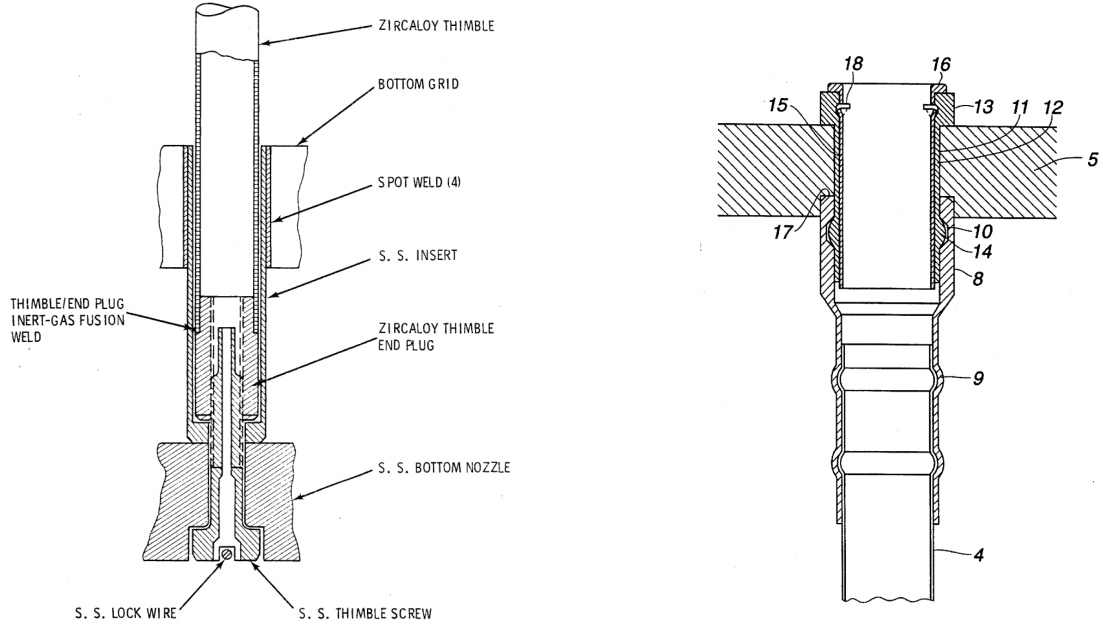
usually exhibits the lowest resilience to loading. Mattos Schettino et al. (2014), for example, presented a study on the important influence of the number of spot welds on the rotational stiffness of the GT-grid

connection. GTs and spacer grids being both essential parts of the FA skeleton, the rotational stiffness $k_{\theta, \text{GT-grid}}$ is hence a crucial parameter for the dimensional stability of the FA structure and consequently for the structural model.

Bottom spacer grid to bottom nozzle or foot For the reference FA design, the bottom grid is not attached to the GTs but is supported directly by the FA foot by means of insert sleeves. An example schematic drawing of this configuration is given in Figure 3.7a. By this means, a large fraction of the weight of the FRs is supported directly by the FA foot without loading the GTs. This implies that no moment can be transmitted by the bottom grid to the GTs; hence, no rotational springs are placed at these positions. The insert sleeves are modeled by linking the concerned grid nodes with the corresponding nodes of the FA foot by means of axial springs with a stiffness $k_{z, \text{sleeve}}$:

$$k_{z, \text{sleeve}} = \frac{E_{\text{Inc}}(p_{\text{FR}}^2 - d_{\text{gt,o}}^2)\pi}{4l_{\text{sleeve}}} \quad (3.5)$$

The inner diameter of the insert sleeve is hence assumed to be equal to the GT outer diameter and the sleeve outer diameter is assumed to be equal to the FR pitch. E_{Inc} is the Young's modulus of the sleeve material Inconel. Note that l_{sleeve} marks in this context the distance between the lower orifice plate and the axial center of the bottom grid, not the actual length of the sleeve.



(a) Screwed connection of a guide tube with the bottom nozzle of FA foot (Weihermiller and Allison, 1979). (b) Example for the guide tube (4) connection with the top nozzle (5) (Berglund, 1995).

Figure 3.7: Cross-sectional cuts through the guide tube connections with the nozzles.

GT to bottom nozzle or FA foot For the connection between the GTs and the FA foot, an internally threaded end plug is usually welded to the lower portion of the GTs. The GT is then connected to the orifice

plate of the FA foot by means of a GT screw inserted from the lower side of the plate and threaded into the GT end plug placed on the upper side of the plate. Figure 3.7a shows an example of the screwed GT connection at the FA foot. Due to the tight connection by means of screws, the lateral DOFs of the GTs and the FA foot are considered fully coupled. The axial and rotational connections can also be assumed nearly stiff. Therefore, axial and rotational linear spring elements with very high stiffness, $k_{z,\text{GT-nozzle}}$ and $k_{\theta,\text{GT-nozzle}}$, model the GT-foot connection. This allows a posterior calibration of the stiffness parameters.

GT to top nozzle or FA head The connection between the top nozzle and the GT is usually designed to allow separation of the top nozzle from the rest of the FA. The specific connection strategy depends strongly on the FA design, consisting in general of a system of interconnected sleeves with welding spots and a locking device to guarantee both a safe connection during handling, shipping, and operation and a quick disconnection and reinstallation when removal of the top nozzle is necessary. An example for the GT-head connection is given in Figure 3.7b. The connection is modeled in the same way as the GT-foot connection.

3.2.6 FR support

Analytical description The support of the FRs is provided due to frictional contact with the spacer grids. The frictional support allows the sliding of the FRs along the contact points. This feature is necessary due to their dimensional change as a result of the influence of temperature and neutron flux. Thanks to the absence of fixed supports, the risk of FR bow and high vibration amplitudes can be substantially diminished. A drawback of the frictional contact is, however, the possible occurrence of fretting wear at the FR to grid contacts, often as a result of flow-induced FR vibrations. The frictional support is typically provided by the spacer grids by means of a system of one spring and two dimples in each perpendicular direction of the grid. In conventional designs, the spring is placed in the axial center of the spacer grid cell and the dimples are

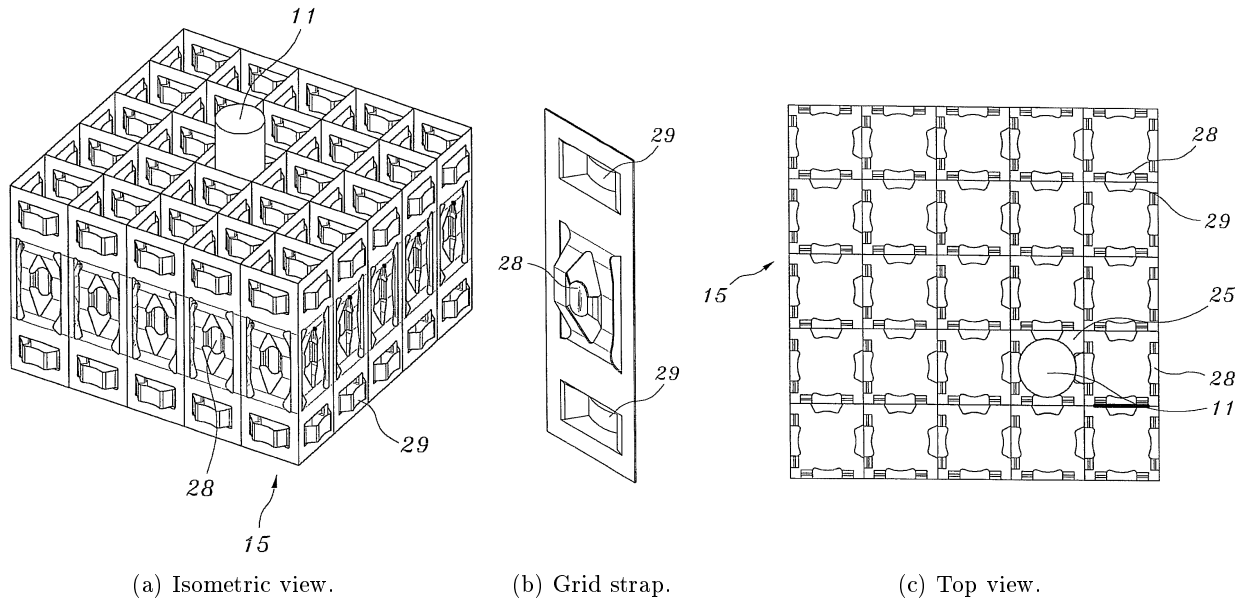


Figure 3.8: Views of a 5×5 section cut of the inner part of a spacer grid (Lee et al., 2014). 11: Fuel rod. 15: Grid strap. 25: Grid cell. 28: Grid spring. 29: Grid dimple.

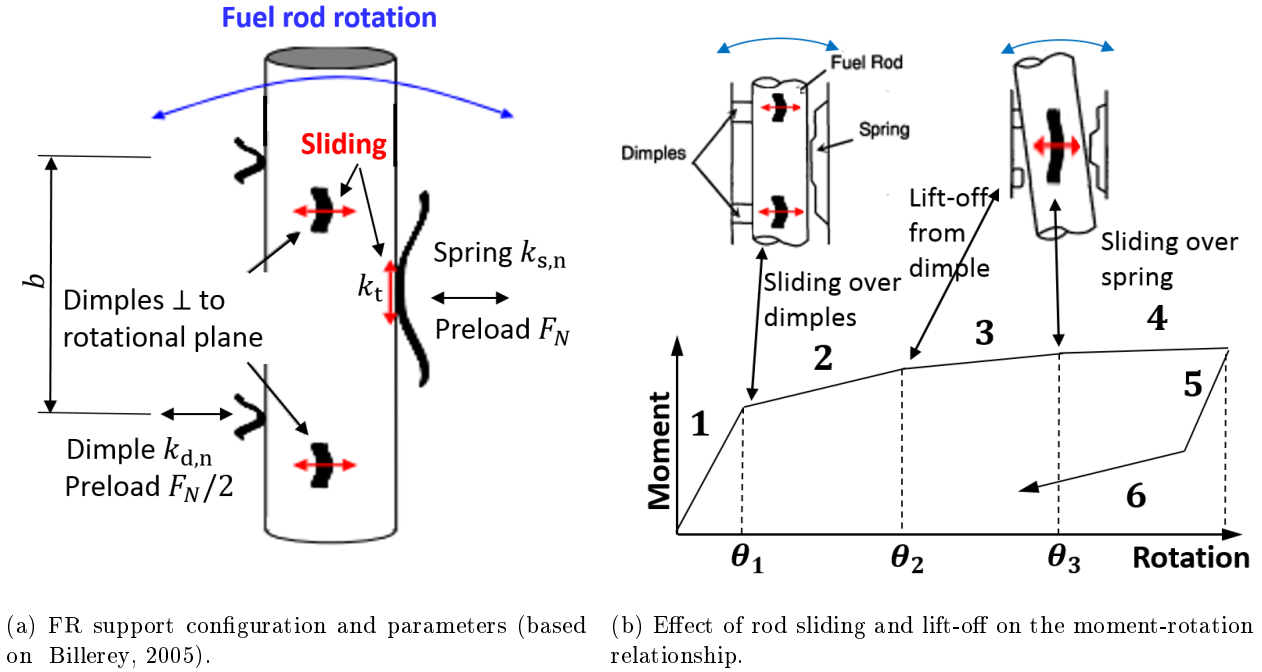
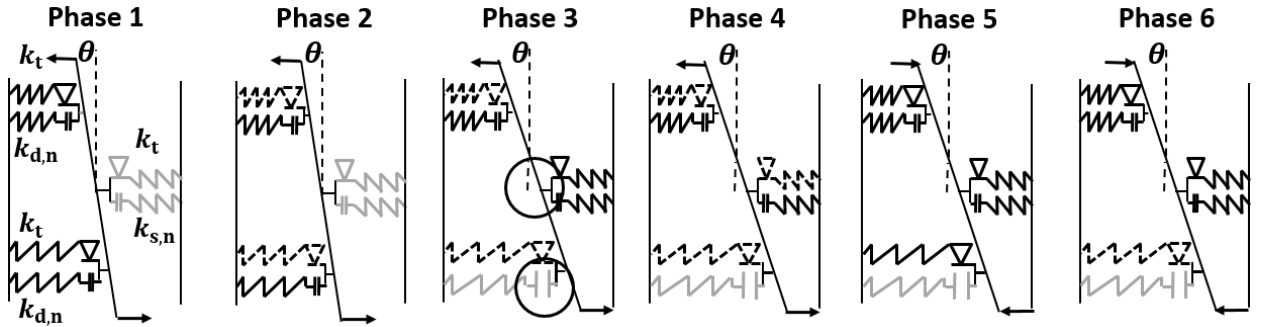


Figure 3.9: Schematics of FR support.

placed symmetrically above and below the spring, in a distance b from each other. For such designs, springs and dimples mostly provide point contacts, provoking fretting wear due to high contact pressures. More recent grid designs often provide line or area contacts, which makes them less prone to fretting wear due to decreased contact pressures. Figure 3.8 gives different views of a 5×5 section cut of a spacer grid illustrating how the FR is supported by the system of springs and dimples and how they are positioned. Figure 3.9a gives a more schematic illustration of the spring and dimples in one rotational plane of the FR and represents the most important parameters. Due to the constraints provided by the exact geometric position of the grid cell springs and dimples, the spring is compressed after insertion of the FR into its grid cell. As a result, the FR is braced against the two dimples in the same rotational plane as the corresponding spring. The magnitude of the lateral support force F_N is mainly controlled by the spring due to its significantly lower normal stiffness $k_{s,n}$ than that of the dimples, $k_{d,n}$. This normal preload determines, for a given Coulomb friction coefficient μ , the axial threshold force above which sliding occurs for a certain contact spot. Before sliding, the stick contact of the rod with the spring and dimples is characterized by a tangential stick stiffness k_t . When the FR support is loaded axially or rotationally under the effect of an external load, the load-deflection characteristics are determined by the different and stick and sliding processes and the different stiffness values of the spring and dimples. Figure 3.9b gives a schematic representation of the processes occurring in the FR support, as well as their implication on the moment-rotation curve when the FR support is loaded by rotating the FR about the perpendicular axis. According to Billerey (2005) four loading phases can be distinguished when applying an external moment on the grid-to-rod connection. Based on these four loading phases, we can add five unloading phases until the external moment is back to zero again. The loading and unloading phases are described in Table 3.2. Depending on the maximum deflection from which the FR is unloaded, several of the cited unloading phases may be omitted. Figure 3.10 illustrates the different

Table 3.2: Description of the loading and unloading phases of the grid-to-rod joint which are represented in Figure 3.10.

Loading:	
Phase 1	The FR is in sticking contact with the dimples and the spring which are sitting perpendicular to the plane of rotation. In the rotation plane, one dimple is compressed, the other one is decompressed from its preload. The loading is symmetric about the center of the grid cell.
Phase 2	The rod starts sliding over the two dimples in the perpendicular plane.
Phase 3	The rod has lifted off from the decompressed dimple, the symmetry of the configuration is broken as the FR compresses the grid spring. The rod remains in sticking contact with the perpendicular grid spring.
Phase 4	The FR starts sliding over the spring in the perpendicular plane.
Unloading:	
Phase 5	As unloading starts, the rod is in sticking contact with all dimples and springs in the perpendicular plane.
Phase 6	The rod starts sliding, in opposite direction, over the dimple which is perpendicular to the dimple from which it lifted off in phase 3.
Phase 7	The rod slides, in opposite direction, over both dimples. This phase is equivalent to the configuration of phase 3 in Figure 3.10.
Phase 8	The rod slides, in opposite direction, over the spring in the perpendicular plane. This phase is equivalent to phase 4.
Phase 9	The gap closes again between the FR and the dimple from which it lifted off in phase 3. This phase is equivalent to phase 2; however, the spring does not necessarily return to its initial position.

**Figure 3.10:** Representation of the loading and unloading phases of the grid-to-rod joint. Black continuous line: spring is loading or unloading; grey continuous line: spring is at rest; black dotted line: rod slides over perpendicular spring/dimple.

loading and unloading phases schematically. The dimples and springs in the rotation plane are represented by spring elements with a gap (lower elements). The dimples and springs perpendicular to the rotation plane are represented by a spring element with frictional slider (upper elements). The moment-rotation curve can be established analytically by solving for each phase the force and moment equilibria of the illustrated mechanical system. The resulting rotational stiffness $k_{\theta, \text{FR-grid}}$ has the general form given in equation 3.6.

$$k_{\theta, \text{FR-grid}} = \frac{b^2}{4} f(k_{s,n}, k_{d,n}, k_t) \quad (3.6)$$

Besides the slippage due to rotational loading, axial slippage of FRs is possible at higher BUs due to the relaxation of the FR support springs or under the effect of a very high HD force. The grid spring relaxation

is considered in the chapter about the BU-dependent modeling in section 4.5.1. If slippage occurs at all grid levels for a certain FR, it slides downwards axially through the grids. The bottom nozzle then provides a barrier to stop slippage and offers additional support.

FR support model Figure 3.11 gives a schematic representation of the modeled FR support. In the present model, the grid-to-rod connection is modeled by point contacts, represented by node-to-node contact elements. For this purpose, ANSYS provides the predefined finite element type *CONTA178*, see section 2.2.2.4. For a closed contact, the so-called penalty method (ANSYS, 2013b) is chosen for the element response in the normal direction. That is, the element behaves like a translational spring element: the element normal force is related to the relative displacement of the nodes by means of a normal stiffness k_n . The evident choice for k_n are the respective normal spring and dimple stiffness values, $k_{s,n}$ and $k_{d,n}$. Regarding the tangential response perpendicular to the closed contact, the contact element acts like a friction element. That is, one must distinguish between sticking and sliding contact. The sticking contact is characterized by a stick stiffness k_t relating the tangential forces and displacements. This value represents the elasticity of the frictional contact. The sliding contact occurs when the tangential forces reaches a value equal the product of the element's normal force and the Coulomb friction coefficient for sticking. The normal force is determined by the initial spring or dimple preload before operation (F_N or $F_N/2$), the current FR rotation, and the degree of relaxation during operation. For the present analysis, it is assumed that the spring's axial position is mid of the corresponding dimples and that the dimples and springs are positioned at the same axial levels for both rotational planes. Table 3.3 summarizes the values of the parameters related to the FR support used in this model based on a literature analysis. The values for the stiffness of the grid spring and dimples are based on Lee (1980). The grid spring usually exhibits a nonlinear force-deflection relationship. Figure 3.12 gives a representative example for the typical force-deflection curve of the grid

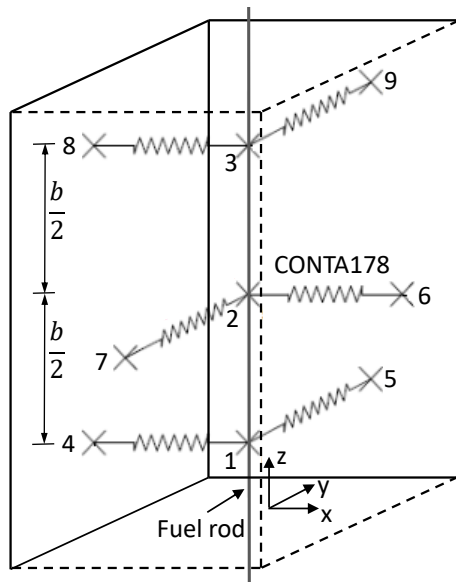


Figure 3.11: Modeled configuration of FR support.

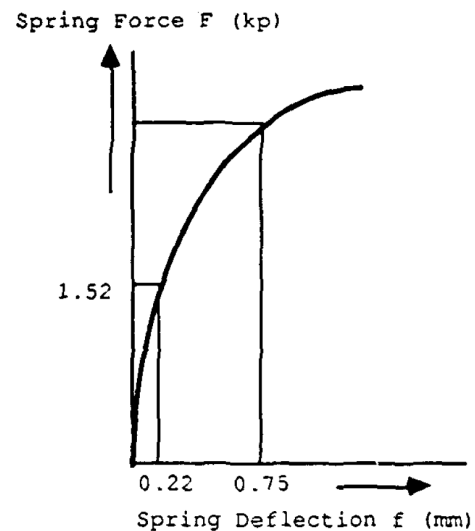


Figure 3.12: Measured grid spring characteristic (Kim, 1993).

Table 3.3: FR support parameter values.

Variable	Symbol	Value
Cold spring normal stiffness	$k_{s,n}$	35 N/mm
Cold dimple normal stiffness	$k_{d,n}$	546 N/mm
Cold spring and dimple tangential stiffness	k_t	1000 N/mm
Axial distance between dimples	b	20 mm
Initial cold spring preload	F_N	25 N
Friction coefficient	μ	0.55
Grid thickness	t_{grid}	0.6 mm
Grid length	l_{grid}	45 mm

spring. Modeling this nonlinear behavior would raise the model complexity and might have adverse effects on convergence. Therefore, we linearize the spring stiffness around the value of the initial spring preload. Lee (1980) gives a value of $k_{s,n} = 35 \text{ N/mm}$ for the spring normal stiffness at ambient temperature in this range. For the dimple normal stiffness, a value of $k_{d,n} = 546 \text{ N/mm}$ is given. The measurement of the static tangential stiffness value is very difficult to achieve. Therefore, Lee (1980) derived the tangential stiffness value using a semi-empirical method based on the measurement of the natural frequency and obtained a value of $k_t = 1000 \text{ N/mm}$. The grid spring is designed to provide sufficient preload to maintain the FRs axially in position under all transport and handling conditions before operation and to minimize possible fretting during operation. At the same time, the friction force must be low enough to not overstress the cladding at the points of contact between the grids and FRs and to allow growth of the FRs during operation with sufficient margin against buckling due to excessive compressive forces. Based on these requirements, the preload is usually adjusted to values of about $F_N = 25 \text{ N}$ (Park et al., 2003).

The value of the friction coefficient depends on several factors, like the mating materials (Zirconium alloy or Inconel), the surface condition (polished or oxidated), and temperature. Makarov et al. (2011) published several reference values that are specific to Zirconium alloys for FR cladding. They indicate an average friction coefficient of $\mu = 0.55$ for polished Zirconium alloy cladding as delivered from the manufacturing plant for sliding contact with spacer grid springs of the same mating material. This value will be used for all frictional contacts in the present model for the sake of simplicity. However, it must be kept in mind that this value might be substantially decreased in the case of oxidized surfaces.

Figure 3.13a depicts a schematic of an experimental set-up to test the moment-rotation behavior of the FR support. A lateral force is applied on a stiff rod at some distance from its support in the grid and the resulting deflection is measured. Figure 3.13b gives the resulting normalized force deflection curve. We perform now a similar test with the FR support model from Figure 3.11 to guarantee a realistic response of the model when compared qualitatively to the results of the experiment. For this purpose, we apply a stepwise increasing moment at the rod in the grid cell until the minimum stiffness is reached. Then the moment is reduced again until it is back to zero. Figure 3.14 gives the resulting moment-rotation curve for this test using friction coefficients of 0.55 and 0.35. Figure 3.15 shows for the case with $\mu = 0.55$ the tangential and normal dimple and spring forces which determine the moment on the FR. The plotted forces represent the variation of the spring and dimple forces ΔF with respect to the initial values when the FR support is not loaded by an external force or moment, that is, $\Delta F = F - F_0$. The sign of the forces in the plots is chosen such that positive forces have a moment-increasing effect. The different loading and unloading phases described in Table

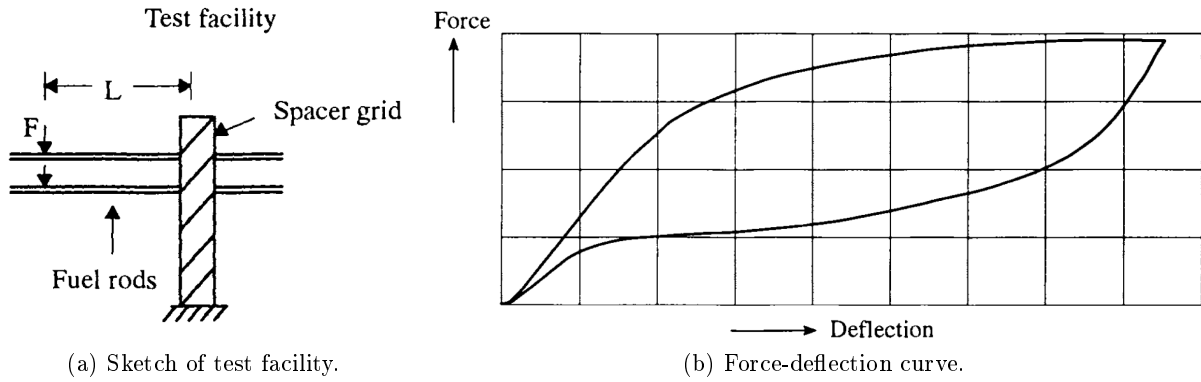


Figure 3.13: Experimental record of a fuel rod supported by a spacer grid and laterally loaded by a force F in distance L (Stabel and Hübsch, 1995).

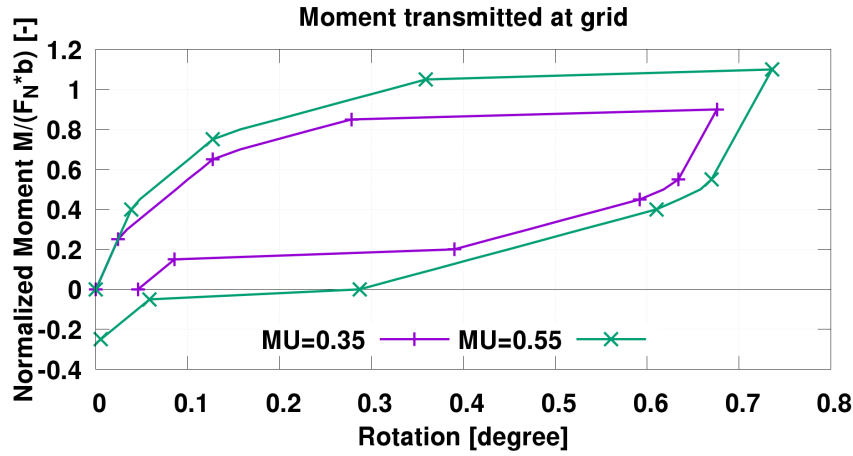


Figure 3.14: FR support rotational loading test.

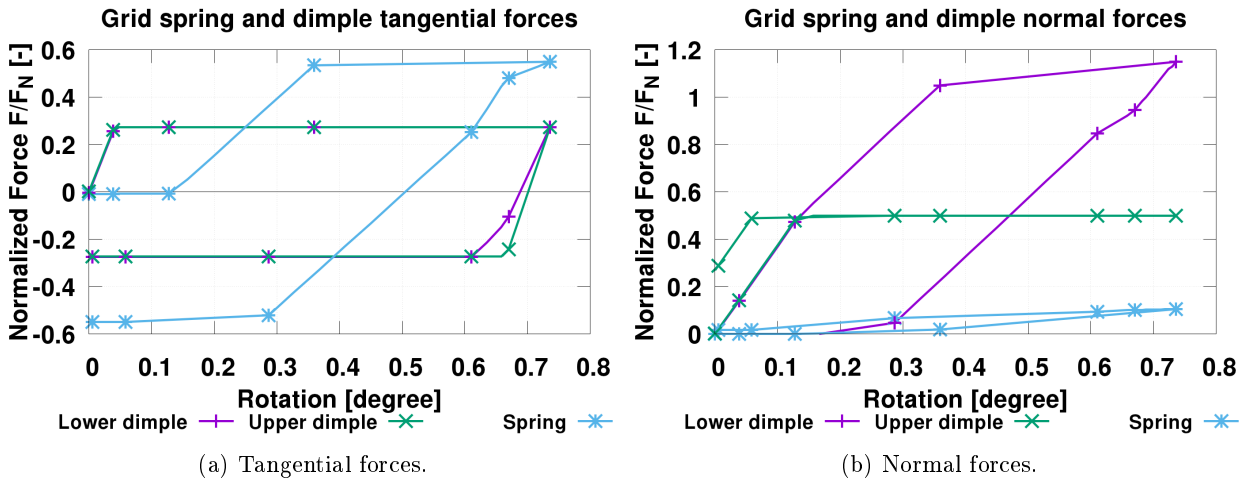


Figure 3.15: Spring and dimple force variation ΔF as a function of rotation during the FR support loading test with $\mu = 0.55$ in Figure 3.14. $\Delta F > 0$ means positive contribution to grid-to-rod moment and vice versa.

3.2 are well appreciable in the plots. Markers in all figures highlight the transitions between the different phases. Phase 1 of the FR support loading ends when both dimples reach the maximum tangential friction force, see particularly the first marker in Figure 3.15a. At the same time, the stiffness of the FR support decreases. Phase 2 ends when the upper dimple is decompressed, $\Delta F = 0.5F_N$, see the second marker in Figure 3.15b. The FR support stiffness continues to decrease accordingly. As phase 3 starts, the grid springs are loaded in normal and tangential directions. The third marker highlights the start of phase 4, when the FR slides over the grid spring. From this point, the stiffness would remain constant if the loading continued. Therefore, the loading is stopped, marker 5, and the unloading phase is started. Since sticking contact sets in again, the total FA stiffness is significantly higher than when loading stopped so that a load hysteresis develops. The next three markers show the end of phases 5, 6, and 7, when the rods slide over the springs and dimples with their negative maximum friction force. The FR support stiffness decreases accordingly. Phase 8 starts when the FR starts compressing dimple 2 again at a rotation close to zero so that the stiffness increases again.

Comparing the model results in Figure 3.14 with the experimental record in Figure 3.13b, a good qualitative agreement can be observed. The general curve evolution for both loading and unloading phases is well fit. It is remarkable that for the experimental test the curve evolution is much smoother and no pronounced phases are distinguishable. We can associate this to several effects which occur in the real experiment but have been neglected in the model. First, the real grid spring stiffness evolution is nonlinear with gradually decreasing values for high deformations, see Figure 3.12. Furthermore, the frictional contacts have been modeled with simple stick/slip point contact elements with a constant stick stiffness when the slip condition has not been reached yet. That is, we obtain a linear elastic response when the loading is initiated, and a break-away when the load reaches a critical value. In more realistic systems, partial slip occurs due to the presence of an elasto-plastic shear layer at the contact surface (Menq et al., 1986). This means that one part of the surface still sticks while the rest has already slipped, causing a much smoother curve evolution.

3.2.7 Holddown (HD) device

The HD device provides a nonlinear relationship between the axial FA deflection and the HD force. This guarantees sufficiently high HD forces to prevent the FA from lift-off while being able to accommodate dimensional changes of the FAs due to irradiation growth or thermal expansion without generating considerable reaction forces and moments. The HD device of the considered FA design is described, for example, in Steinke (1981) and is depicted in Figure 3.16. This HD device is composed of in total eight spring elements, which protrude from the frame of the FA head on both sides of each corner of the upper face, see the elements marked with the number 4 in Figure 3.16a. Figure 3.16b shows a cut illustrating one spring element in detail. Each spring element of the HD device contains a coil-type spring or spring package, marked with number 41. The spring is mounted around a pin, number 4, which is slidably inserted in the bores marked with the numbers 11 and 12. The lower part of the spring is braced against the bottom of the FA head while the top is braced against a stop, number 42, which is connected to the pin. In this manner, the pin is forced upwards, bracing the stop against the upper bar of the FA head. The left side of Figure 3.17 gives a schematic drawing of the mechanical HD system with one representative spring.

Based on this configuration, the working principle of the HD device can be deduced. Let the variables $k_{z,HD}$ be the stiffness of the represented spring, F_{spring} the compressive spring force, and l_{HD} the current

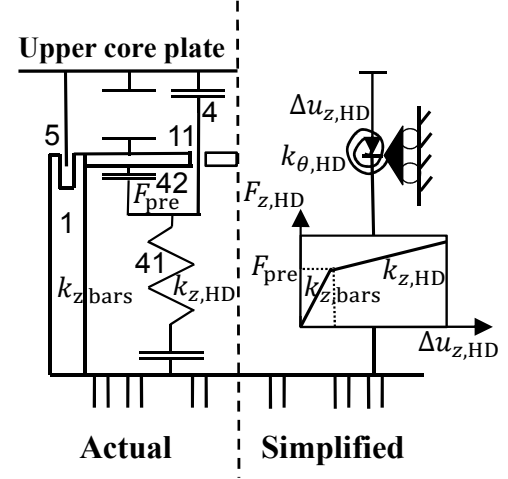
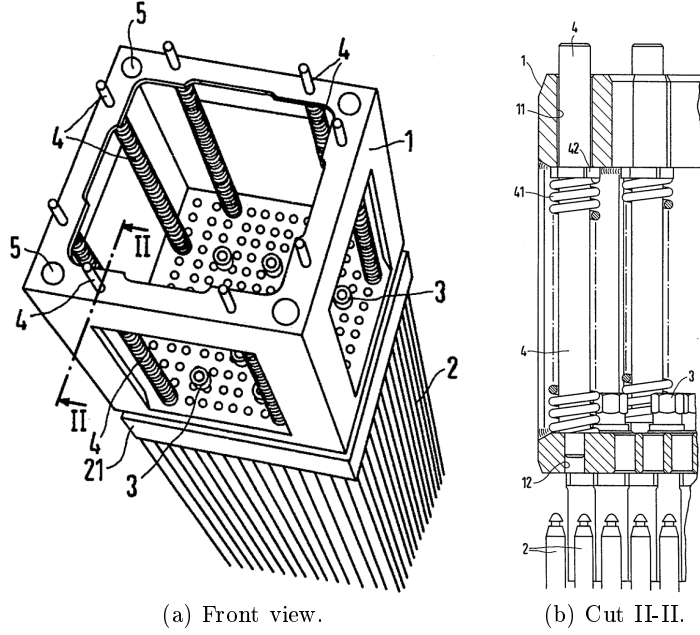


Figure 3.16: Schematic drawings of FA head with holddown springs (Steinke, 1981). **Figure 3.17:** Schematics of the mechanical holddown system.

spring length. $l_{HD,0}$ is the spring's length in the unloaded state while $l_{HD,1}$ stands for its length when it is compressed between the lower and upper bar of the FA head frame. The spring preload corresponding to this compression is given as:

$$F_{pre} = k_{z,HD}(l_{HD,0} - l_{HD,1}) \quad (3.7)$$

The reaction of this preload is a tensile load in the vertical bar of the FA head frame. No external HD force is exerted on the pin so far so that the effective HD force F_{HD} , that is, the axial downward force exerted by the FA head on the fuel element, is zero. Let now the top of the pin be gradually loaded by an external downward axial force, for example, due to the upper core plate. In a first phase, the spring force will remain constant, $F_{spring} = F_{pre}$ since the pin force must be greater than the spring preload for the spring to be pushed further down by the pin. Instead, the tensile reaction load in the vertical bars of the FA head frame will be gradually relieved. Effectively, the HD force is not transmitted through the spring element but through the FA head frame. The effective stiffness of the HD device in this phase corresponds to the axial stiffness of the vertical bars, which is substantially higher than the stiffness of the HD springs, $k_{z,bars} > k_{z,HD}$. Once the HD force is equal to the spring preload, $F_{HD} = F_{pre}$, the tensile load in the vertical bars vanishes and the spring preload is exclusively counteracted by the HD force. When the HD force is increased further, the pin will start to compress the spring beyond its preload reducing its length, $l_{HD} < l_{HD,1}$. The additional HD force is now transmitted through the spring with stiffness $k_{z,HD}$. In total, an bilinear relationship between the axial FA deflection and the HD force is produced due to the described configuration, see the graph at the right in Figure 3.17. The deflection after which the second phase is reached is $u_{z,pre} = F_{pre}/k_{z,bars}$. Hypothetically, a third phase exists, in which the pin is pushed down so much that the upper core plate touches the FA head. In this phase, the compression of the HD spring would stop and the force would be transmitted again

Table 3.4: HD device parameter values.

Variable	Symbol	Value
Number of HD spring packages	n_{HD}	8
HD spring package stiffness	$k_{z,\text{HD}}$	20 N/mm
HD spring package preload	F_{pre}	500 N

through the vertical bars of the FA head frame. This case is not considered in the presented model since the length of the pins is designed long enough to accommodate FA growth during normal operation within the second phase. To reduce the complexity of the model, the HD device is not modeled with contact elements as represented on the left side of Figure 3.17. Instead, a simplified configuration is used as illustrated on the right side of Figure 3.17. The simplified mechanical system consists of two single spring elements placed at the central FA axis, one for the axial response and one for the rotational response. The axial response of the HD device is modeled by a nonlinear spring element, ANSYS element *COMBIN39*. For the definition of the element, the bilinear curve given in Figure 3.17 is specified.

To calculate the rotational stiffness of the HD device for the rotational spring element, the distance of the single spring packages from the rotational axis must be known. The spring packages are arranged in pairs of two in two rows at each side of the rotational axes, with a distance of $x_{\text{HD},1}$ and $x_{\text{HD},2}$ from the axis. The rotational stiffness of the HD device $k_{\theta,\text{HD}}$ in both x and y directions is given by equation 3.8, where θ is the rotation of the FA top and M_i are the single moments developed at the FA top due to each spring package.

$$k_{\theta,\text{HD}} = \sum_{i=1}^{n_{\text{HD}}} \frac{M_i}{\theta} = 4 k_{z,\text{HD}} (x_{\text{HD},1}^2 + x_{\text{HD},2}^2) \quad (3.8)$$

Table 3.4 indicates the parameter values assumed for the modeled HD device. For each of the HD spring packages of the presented device, a stiffness of $k_{z,\text{HD}} = 20 \text{ N/mm}$ is assumed. The preload of the spring packages should be high enough to present enough margin for decreasing forces within the second phase; hence, a value of $F_{\text{pre}} = 500 \text{ N}$ is assumed, which gives a preload of $F_{\text{HD,pre}} = 8 \times 500 \text{ N} = 4000 \text{ N}$ for the entire HD device. For the spring package positions, the following rough estimation is made based on Figure 3.16a. The radial distance to the rotation axis of the springs closer to the axis is $x_{\text{HD},1} = 5.5 b_{\text{FA}}$ and the radial distance of the springs further away is $x_{\text{HD},2} = 7.5 b_{\text{FA}}$.

3.3 Structural constraint boundary conditions (BCs)

3.3.1 Displacement BCs

Axial support Neither the FA foot nor the FA head are fastened to the core structures. Ideally, the axial connection is to be modeled by contact elements because theoretically the contact can open, for example, in the case of a FA lift-off if upward forces are greater than the sum of HD and gravitational forces. Since design guidelines prevent such events during normal operation, the bottom and top of the FAs are assumed to be connected to the lower and upper core plates. This is realized by axial displacement constraints. The lower core plate is used as axial reference so that for the bottom node the axial displacement is imposed as zero, $u_z = 0$. The top node represents the connection between the upper core plate and the pins of the HD device. The displacement constraint on this node will be adjusted according to the initial compression

of the HD device in CC, the thermal expansion of the core structures, and the HD spring relaxation. The displacement constraint is hence variable over simulation time. Its calculation is presented in section 4.5.2.

Lateral support Bores are provided in each corner of the bottom face of the FA foot and the top face of the FA head. The FA head bores are marked with the number 9 in Figure 3.1. The FAs are horizontally aligned by adjustment pins which extrude from the lower and upper grid plates and are inserted into the bores at the bottom and top of the FA, offering lateral support. This horizontal alignment and support is modeled by displacement constraints of the bottom and top nodes in the cross-sectional x and y directions, $u_x = 0$ and $u_y = 0$. In the particular case of a 2D model in the x - z plane, the displacement DOFs of all FA nodes are fully constrained in y -direction, $u_y = 0$.

3.3.2 Rotational BCs

Torsion Moments can be transmitted from the FA to the core plates about all three dimensions. In the model, the FA is always loaded centrally, that is, in a manner that the resultant force vector acts on the central axis of the FA. This implies that no torsional moments, that is, moments about the vertical z -axis, appear in the FA. Therefore, the torsional degree of freedom is constrained for all nodes, $\theta_z = 0$.

Bending angle The lower face of the FA foot is pressed against the lower core plate by the HD force and the FA weight. In accordance with the assumption that the lower core plate is rigid and horizontal, the rotation of the lower face of the FA foot about the cross-sectional axes must be zero since overlapping is not possible. The imposed rotation angles for the FA bottom nodes are $\theta_x = 0$ and $\theta_y = 0$, which corresponds to a clamped connection. In contrast to the lower core plate, the upper core plate is not in contact with the upper face of the FA head during normal operation. Instead, lateral forces are transmitted through the alignment pins and axial forces through the HD spring element pins. The upper face of the FA may hence have a rotation angle different from zero. However, this rotational DOF is not free as for a simple support, but is constrained by the moment transmitted to the upper core plate through the HD springs. Section 3.2.7 specifies the properties of the rotational spring element implemented in the model to this end.

3.4 Model reduction

The FA structural model has initially been designed as a full 3D model composed of all individual FRs and GTs. In this section, a model reduction shall be performed with the objective of accelerating the run execution without substantially impairing the quality of the results. To reduce the model size, we substitute equivalent rods for groups of FRs, taking special care of maintaining the mechanistic features of the model. Both a reduced 3D model and reduced 2D model are developed. The reduced 3D model maintains all features of the full 3D model. That is, it is able to model simultaneous bowing of the FA in both cross-sectional directions. The 2D model, in turn, serves only for the calculation of FA bow in a single cross-sectional direction, assuming that no loading occurs in the third dimension.

3.4.1 FR reduction method

The largest potential in model reduction lies in diminishing the number of modeled FRs, for several reasons:

- The number of FRs is more than ten times larger than the number of GTs.

- Each FR consists of three independent nodes at each grid level as opposed to one node for the GTs.
- The FR grid cell consists of nonlinear gap elements which may require more iterations to converge.
- FA bow is mainly associated to the creep deformation of the FA skeleton while the grid cell springs relax over BU so that the influence of the FRs on the FA skeleton is reduced.

It is hence reasonable to reduce the model size by replacing the totality of n_{FR} FRs by a reduced number of n_{eq} equivalent rods. That is, each equivalent rod substitutes n_{subst} FRs:

$$n_{\text{subst}} = \frac{n_{\text{FR}}}{n_{\text{eq}}} \quad (3.9)$$

These rods are designed and positioned in such a manner that a mechanical system is created as if all single FRs were present. To maintain the mechanistic modeling of the coupling between FA skeleton and FR bundle, there must be at least one equivalent rod per FA quadrant. In this manner, the fundamental modeling configuration with four symmetry axes is maintained. This reduction method would also be applicable to the GTs; however, due to the low number of GTs per FA the reduction potential is limited. Moreover, it is preferable to model every single GT since their creep response is crucial for the FA bow.

To realize a model reduction, we need to develop a criterion which is able to verify if the reduced model is equivalent to the full model, regarding the deformations due to both thermoelastic and inelastic strains. For this purpose, an energy criterion is proposed that stipulates that the potential energy Π in the structure, defined in equation 2.13, remain equal for the reduced model. Hence also its components, the internal elastic strain energy U and the external work W must remain equal. For the criterion of the equivalence of external work it must be reminded that all external loads are assumed to attack in the neutral axis of the FA at a certain axial level k , such as the forces on the grids and the nozzles, or are distributed equally over all rods and tubes with index i , such as the hydraulic loads. If we assume only discrete forces \mathbf{F} , the total increment of work done by the external loads reads as:

$$\Delta W_{\text{FA}} = \sum_k \left(\sum_{i=1}^{n_{\text{FR}}+n_{\text{GT}}} (\mathbf{F}_{i,k} \Delta \mathbf{u}_{i,k}) + \mathbf{F}_k \Delta \mathbf{u}_{i,k} \right) \quad (3.10)$$

The work increment in the equivalent configuration, ΔW_{eq} must be equal to the original value, that is:

$$\Delta W_{\text{eq}} \stackrel{!}{=} \Delta W_{\text{FA}} \quad (3.11)$$

This condition must hold for each FA quadrant to maintain the characteristic features of the FA structure. The external work on the spacer grids and GTs remains equal in the equivalent configuration; hence, equation 3.11 can be reduced to equation 3.12, which must be valid for any axial force attacking point k .

$$\sum_{i=1}^{n_{\text{FR}}/4} \mathbf{F}_{i,\text{FR}} \Delta \mathbf{u}_{i,\text{FR}} = \sum_{i=1}^{n_{\text{eq}}/4} \mathbf{F}_{i,\text{eq}} \Delta \mathbf{u}_{i,\text{eq}} \quad (3.12)$$

To obtain equivalent deformations, it is required that the displacements be equal for both configurations at each point of the displacement field inside the FA; hence, we can reduce equation 3.12 to:

$$\mathbf{F}_{\text{eq,tot}} = \frac{n_{\text{FR}}}{n_{\text{eq}}} \mathbf{F}_{\text{FR,tot}} = n_{\text{subst}} \mathbf{F}_{\text{FR,tot}} \quad (3.13)$$

This expresses the trivial condition that when substituting one equivalent rod for n_{subst} FRs, the equivalent rod must bear n_{subst} times the load of a single FR. Therefore, also the stiffness of the equivalent rods and the adjacent spring elements must be increased n_{subst} times to produce equivalent displacements, which is expressed in equation 3.14. For the beam elements, this condition determines the geometry of the equivalent cross-section, equations 3.15 and 3.16. The axial dimensions and the modulus of elasticity of the equivalent rods remain unchanged.

$$n_{\text{subst}} k_{\text{FR}} = k_{\text{eq}} \quad (3.14)$$

$$n_{\text{subst}} A_{\text{FR}} = A_{\text{eq}} \quad (3.15)$$

$$n_{\text{subst}} I_{\text{FR}} = I_{\text{eq}} \quad (3.16)$$

With equations 3.13 to 3.16, the distribution of the equivalent loads and the stiffness of the equivalent rods and the adjacent spring elements are fully defined. Due to the grid coupling, the lateral positions $x_{i,\text{eq}}$ of the equivalent rods also play an important role to obtain an equivalent FA stiffness. To determine $x_{i,\text{eq}}$, the condition of the equivalence of internal strain energies in equation 3.17 can be exploited.

$$U_{\text{eq}} \stackrel{!}{=} U_{\text{FA}} \quad (3.17)$$

The internal energy of the GT bundle and the nozzles does not need to be considered since their configuration remains unchanged. Therefore, only the equivalence of the strain energy of the rods and of the spacer grids, including the FR support, need to be established to obtain $x_{i,\text{eq}}$. The spacer grid being a rigid structure, it stores strain energy only through the springs in the FR support. The internal strain energy of the grid in one FA quadrant after a rotation θ and an axial translation $u_{z,\text{grid}}$ at the neutral axis is:

$$U_{\text{grid,quadrant}} = \frac{1}{2} \sum_{i=1}^{n_{\text{FR}}/4} (F_{z,i,\text{FR}} u_{z,i} + M_{i,\text{FR}} \theta) \quad (3.18)$$

with $u_{z,i}$ being the axial translation at the lateral position x_i . Based on the geometric compatibility condition in equation 2.62, we have $u_{z,i} = u_{z,\text{grid}} + x_i \theta$. The condition for the equivalent internal strain energy of the reduced system is then:

$$\frac{1}{2} \sum_{i=1}^{n_{\text{FR}}/4} \left(k_{z,i,\text{FR}} (u_{z,\text{grid}} + x_{i,\text{FR}} \theta)^2 + k_{\theta,i,\text{FR}} \theta^2 \right) = \frac{1}{2} \sum_{i=1}^{n_{\text{eq}}/4} \left(k_{z,i,\text{eq}} (u_{z,\text{grid}} + x_{i,\text{eq}} \theta)^2 + k_{\theta,i,\text{eq}} \theta^2 \right) \quad (3.19)$$

Equation 3.19 can be reduced to equations 3.20 and 3.21, making use of equation 3.14 and under the assumption that k_z and k_θ are equal for all positions. This represents an approximation since the instantaneous

spring stiffness may slightly differ between the lateral positions due to the nonlinearity of the FR support.

$$n_{\text{subst}} \sum_{i=1}^{n_{\text{eq}}/4} x_{i,\text{eq}} = \sum_{i=1}^{n_{\text{FR}}/4} x_{i,\text{FR}} \quad (3.20)$$

$$n_{\text{subst}} \sum_{i=1}^{n_{\text{eq}}/4} x_{i,\text{eq}}^2 = \sum_{i=1}^{n_{\text{FR}}/4} x_{i,\text{FR}}^2 \quad (3.21)$$

That is, to obtain an equivalent grid strain energy in each FA quadrant, the linear sum and the sum of squares of the lateral positions x_i must remain constant between the full model and the reduced model. The equivalence of the sum of squares represents the stronger criterion for the equivalence of both models. It can be considered as a specific form of Steiner's theorem which guarantees the equivalence of the FA stiffness. As the final step, the equivalence of the internal strain energy of the FR bundle quarter sections $U_{\text{FR,tot}}$ needs to be ensured.

$$U_{\text{rods,quadrant}} = \sum_{i=1}^{n_{\text{FR}}/4} U_{i,\text{FR}} \stackrel{!}{=} \sum_{i=1}^{n_{\text{eq}}/4} U_{i,\text{eq}} \quad (3.22)$$

The theoretical derivation of the resulting condition for this equivalence is somewhat lengthy and is described in appendix C. It results that to fulfill the energy criterion in equation 3.22, the conditions in equations 3.20 and 3.21 must be complemented with a third condition for the equivalence of the sum of cubes of x_i .

$$n_{\text{subst}} \sum_{i=1}^{n_{\text{eq}}/4} x_{i,\text{eq}}^3 = \sum_{i=1}^{n_{\text{FR}}/4} x_{i,\text{FR}}^3 \quad (3.23)$$

The general equivalence of the reduced model has hence been proved theoretically under the given conditions and is confirmed with a test simulation in section 3.4.4. First, the specific set-up of different reduced models with equivalent rods is described.

3.4.2 Reduced 3D Model

For the 3D reduced FA model, the symmetry axes of the FAs must be maintained so that the bending stiffness of the FA I_{FA} remains constant for the bending about all symmetry axes. Therefore, the equivalent rods should be arranged in an array pattern and have an annular cross-section, that is, I_{eq} is constant in all cross-sectional directions. Equations 3.15 and 3.16 become:

$$n_{\text{subst}} A_{\text{FR}} = A_{\text{eq}} = (r_{\text{eq,o}}^2 - r_{\text{eq,i}}^2) \pi \quad (3.24)$$

$$n_{\text{subst}} I_{\text{FR}} = I_{\text{eq}} = (r_{\text{eq,o}}^4 - r_{\text{eq,i}}^4) \pi \quad (3.25)$$

The solution to the system of equations is:

$$r_{\text{eq,o}} = \sqrt{\frac{2I_{\text{FR}}}{A_{\text{FR}}} + \frac{n_{\text{subst}} A_{\text{FR}}}{2\pi}} \quad (3.26)$$

$$r_{\text{eq,i}} = \sqrt{r_{\text{eq,o}}^2 - n_{\text{subst}} A_{\text{FR}}} \quad (3.27)$$

Due to the root term in equation 3.27, a real solution can only be obtained if the number of equivalent rods is above the limit given in equation 3.28.

$$n_{\text{eq}} > n_{\text{FR}} \frac{r_{\text{FR,o}}^2 + r_{\text{FR,i}}^2}{r_{\text{FR,o}}^2 - r_{\text{FR,i}}^2} \quad (3.28)$$

Moreover, n_{eq} must be a multiple of 4 to have the same number of equivalent rods in each quadrant. For the present FA design, a minimum of nine equivalent rods per quadrant is necessary, that is, $n_{\text{eq}} = 4 \times 9$. To meet the criteria established in section 3.4.1, the system composed of equations 3.20, 3.21, and 3.23 must be solved for $x_{1,\text{eq}}$ to $x_{3,\text{eq}}$. In this manner, the equivalent rod array in each FA quadrant is fully defined for the 3D case because $y_{i,j} = x_{j,i}$, with j being the index for the lateral positions in the y -direction. Figure 3.18a illustrates the cross-sectional cut of the reduced 3D model. The cross-sections of the equivalent rods and GTs overlap in the graphics but are not in actual physical contact.

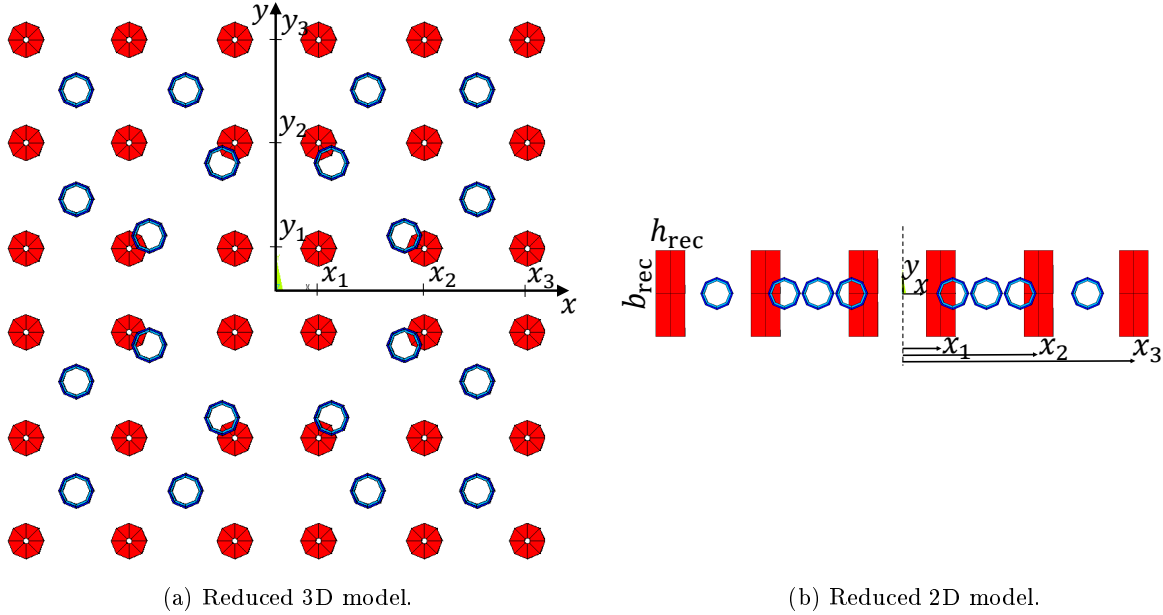


Figure 3.18: Top view of the FR and GT bundles for reduced models.

3.4.3 Reduced 2D Model

The studies in this work are limited to the analysis of FA rows. Therefore, a further reduction to a 2D-only model is possible since only the solution in the axial direction and in one lateral direction is required. If, for example, only the lateral deformations in x -direction are to be solved, we can cut the FA in two along the x -axis, not considering all structures at $y > 0$. For the solution, the displacements and rotations in the third dimension are blocked, $u_y = 0$ and $\theta_x = 0$, to remove these DOFs from the solution matrix. For the 2D case, all external loads acting on the entire FA must be reduced by one half in the preprocessing before the solution step. After solving, the concerned reaction forces are doubled again to obtain the results for an entire FA. An additional advantage of the 2D calculations is that the number of equivalent rods can be further reduced since I_{eq} does not need to be constant in all directions since no bending is considered in the third dimension. Therefore, a rectangular cross-section with $I_{y,\text{eq}} = n_{\text{subst}} I_{y,\text{FR}}$ and an arbitrary I_x can

be used. For each lateral position x_i of the FA quarter section, the three equivalent annular rods can be combined to one rectangular beam so that only six beams need to be modeled in total, $n_{\text{eq}} = 2 \times 3$. The following equations determine the side length of the rectangle, where b_{rec} is the length parallel to the bending axis and h_{rec} is the length in perpendicular direction, see Figure 3.18b.

$$n_{\text{subst}} = \frac{n_{\text{FR}}}{2n_{\text{eq}}} \quad (3.29)$$

$$h_{\text{rec}} = \sqrt{\frac{12I_{y,\text{FR}}}{A_{\text{FR}}}} \quad (3.30)$$

$$b_{\text{rec}} = \frac{n_{\text{subst}} A_{\text{FR}}}{h_{\text{rec}}} \quad (3.31)$$

3.4.4 Performance of reduced models

Table 3.5 compares the performance of the reduced models and the full model in terms of the modeling error and in terms of the memory requirements and the elapsed simulation run time for a serial run including the pre- and postprocessing procedures. As test case, the single-FA creep deflection test described in section 6.2.1 is used; however, the duration of the run is limited to the reactor operating cycle and an additional power gradient is imposed on the structure. In this manner, the simulation contains all relevant model features, that is, elastic, thermal, creep, and growth deformations, as well as the effect of gradients over the FA. The FA mid-grid deflection under operation at end of cycle (EOC) is used as reference output. The maximum modeling error is close to 1% and is therefore negligible in view of the large uncertainties about the creep rate and the lateral hydraulic loads. For the 3D case, the model reduction with equivalent rods decreases the elapsed run time to about one fifth of the original value. The memory expenses decrease almost to the same degree. For the 2D cases, the reduction potential is even larger. With the full model, more than half the computational time can be saved by exploiting the symmetry of the model. When reducing the model further by using six rectangular equivalent rods, the run time is reduced by 91% compared to the full model. This model is used as the standard model for all 2D calculations performed in this work for both single FAs and for an entire FA row.

Table 3.5: Comparison of elapsed simulation times on a single CPU and errors for different tests with the reduced models.

Model	FA deflection	Run time		Memory used	
	Error [%]	[s]	Decrease [%]	[MB]	Decrease [%]
3D Full	-	2245	-	1430	-
3D $n_{\text{eq}} = 4 \times 9$	0.93	469	79	476	67
2D Full	0.11	1040	54	633	56
2D $n_{\text{eq}} = 2 \times 9$	1.04	238	89	242	83
2D $n_{\text{eq}} = 2 \times 3$	1.04	195	91	185	87

3.5 Laboratory deflection tests

To verify the axial and lateral stiffness of any FA design before being deployed in the reactor, fuel suppliers perform experimental deflection tests in a laboratory environment. In general, the experiments take place at ambient temperature with air as ambient medium. These tests are performed to characterize the static

axial and lateral structural response of the FA. Furthermore, the deflection tests are useful to verify the performance of computational FA structural models. For the modeling of FA bow, this represents one of the only means of verification besides the measurements of the of bow shapes at EOC because it is very difficult to realize an experimental set-up measuring the FA deformation under reactor conditions. Therefore, it is of preliminary importance to compare the mechanical response of the created FA structural model to the results of in-laboratory FA deflection tests.

3.5.1 Deflection test set-up and description

Figure 3.19a gives an example for a typical experimental set-up for the mechanical testing of FAs. Figure 3.19b gives a schematic representation of the recorded variables during the deflection tests. In the experiment, the same constraints as exerted by the lower and upper core plates on the FA foot and head are recreated. The axial compression test is performed by loading the FA head with an axial compressive force F_{ax} while recording the downward axial displacement response u_{ax} . No lateral force F_{lat} is applied.

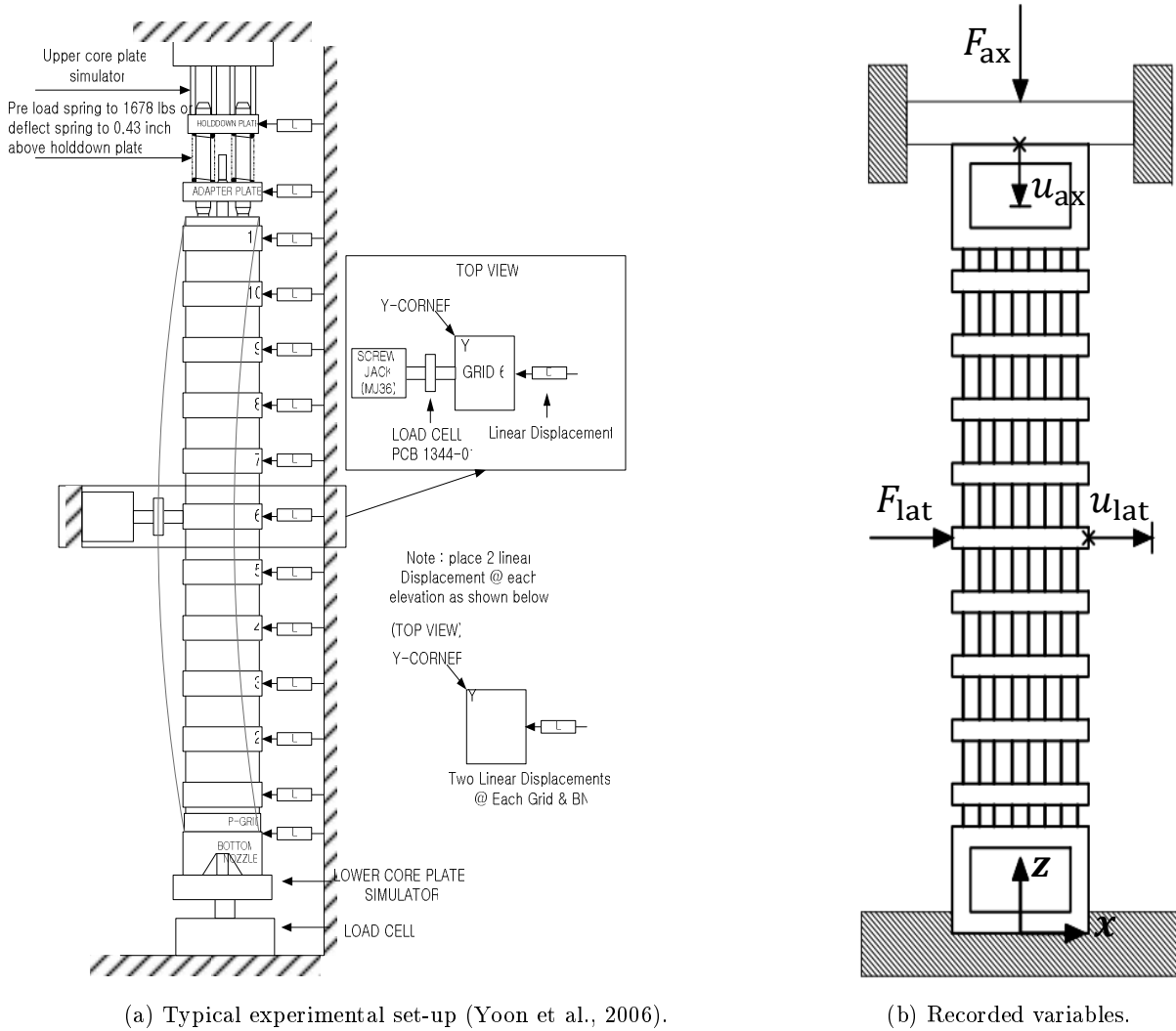


Figure 3.19: FA deflection test schematics.

For the lateral deflection test, the FA is laterally deflected along one axis to a displacement u_{lat} at the mid grid of the FA. At the same time, a constant HD force F_{ax} is applied at the top of the FA. The lateral force F_{lat} required to deflect the FA is measured continuously to obtain the evolution of the relationship between force and deflection. Due to slippage processes in the FR support, this relationship exhibits usually nonlinearities and a hysteresis for both axial and lateral deflection tests. Therefore, the unloading phase is recorded as well. In many experiments, the cycles are repeated several times, increasing the maximum force after each cycle. All loading and unloading processes are performed slowly to rule out dynamic effects and ensure the quasi-static behavior of the FA structure. The measurement data obtained from FA deflection tests are specific to a certain FA design by a FA vendor and are usually proprietary and not disclosed. However, the generic behavior of PWR FAs is vastly discussed in literature and normalized curves describing the force-deflection relationship have been published on several occasions (Salaün et al., 1997; Yoon et al., 2007; Levasseur et al., 2009; Morales et al., 2012).

In the next sections, we will first perform computational axial and lateral deflection tests with the generated FA structural model. In this manner, we can investigate the performance of the model compared to the general response of PWR FAs observed in experimental tests. Since an overall good qualitative agreement is found, the created model can be used as a generic model for the purpose of the analyses in this work, that is, to assess the effect of parameter changes. If a good fit to a specific set of data is required, the model can be calibrated by adjusting specific stiffness parameters. Such a calibration is performed in the last section of this chapter. This demonstrates the flexibility of the model to be calibrated to measurement data obtained with a specific design although not all features have been modeled meticulously, for example, the details of the FR support.

3.5.2 Axial deflection test

Figure 3.20a gives an example of the typical force-deflection response in a FA axial compression test experiment. The axial compression test represents an important validation step for the present FA structural model since it demonstrates the ability of the model to reproduce the sliding processes in the FR support. This test highlights the nonlinear and dissipative properties of the model. For the test, the FA head frame will be loaded with an axial compressive force. The force is applied directly on the FA head to better illustrate the FA structural behavior without the influence of the HD springs, whose stiffness is significantly lower than that of the remaining FA structure. To activate the axial sliding processes in pure axial loading, the applied compressive force must be substantially higher than during normal reactor operation. Therefore, the FA is axially loaded up to $F_{\text{ax,max}} = 60 \text{ kN}$. The test procedure consists in loading the FA gradually with a compressive axial force in load steps of $\Delta F_{\text{ax}} = 5 \text{ kN}$ until the maximum force is reached, solving for the static equilibrium after each load step. Then, the FA is unloaded completely using the same load step size. Figure 3.20b gives the results of the axial deflection test simulated with the FA structural model and, for comparison, the linear curve obtained when loading the FA skeleton only, which illustrates the influence of the FRs on the results. Comparing the FA axial deflection curve with the normalized experimental measurement data in Figure 3.20a, a good qualitative agreement is found. Both the nonlinear evolution in the loading phase and the development of a hysteresis when unloading are well matched.

To better understand the represented curve evolution, the single sliding processes occurring in the FR supports during loading and unloading will be described. For this purpose, the axial force transmitted per grid

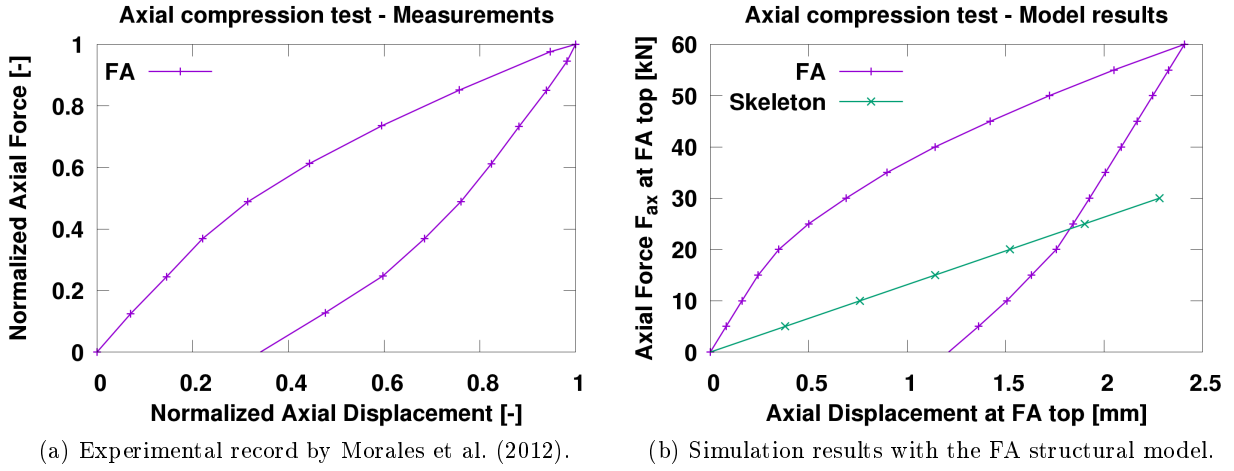


Figure 3.20: Axial deflection test: qualitative comparison of simulation results versus measurements.

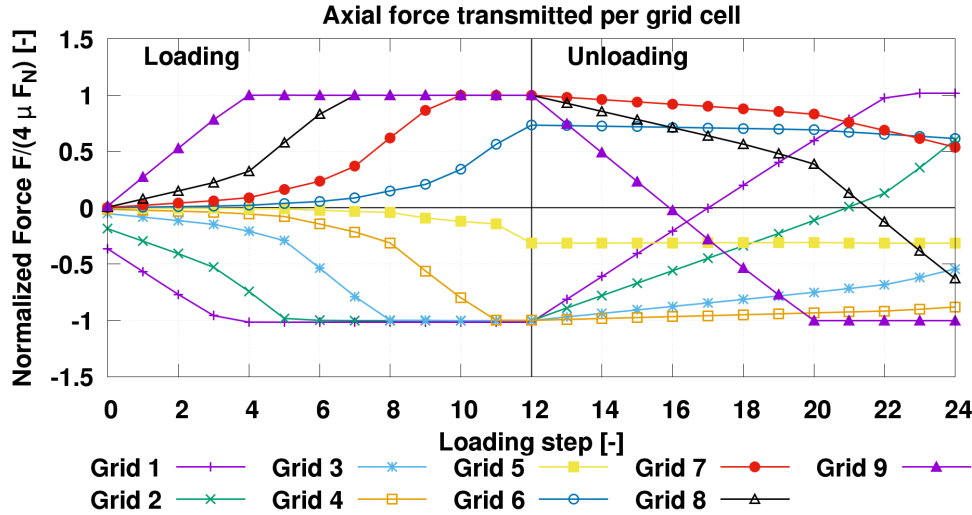


Figure 3.21: Axial force transmitted per grid cell at grid levels 1 to 9 during the axial deflection test.

cell through the FR support is plotted over the single load steps in Figure 3.21. The force is normalized by the maximum transmissible friction force per grid cell $4\mu F_N$. At the beginning of the simulation, an initial state is calculated including only the effect of gravity without any additional axial load. This state is represented as load step 0. The initial axial displacement of the FA top node due to the FA weight $u_{ax,grav}$ has a value of about 1 mm. This deformation is intrinsic to the real FA after inserting the FRs during the manufacturing process. To not bias the results, it is automatically subtracted from the code output during the postprocessing. Figure 3.21 indicates that the FR weight is mostly carried by grids 1 and 2 which are the only grids that transmit an appreciable axial force for load step 0. After this initial load step, a linear relationship between axial force and deflection is observed in the initial loading phase with a FA stiffness significantly superior to that of the skeleton. Between the top and the bottom grid, a certain fraction of the axial load is hence redistributed from the GTs to the FR bundle via the spacer grids, compressing the FRs. In the initial linear phase, all grid-to-rod contact elements are in sticking contact and are loaded continuously.

Between 15 kN and 20 kN, the instantaneous FA axial stiffness, that is, the slope of the deflection curve, decreases. This is because the FR supports at the extremities, spacer grids 1 and 9, reach the maximum friction force $4\mu F_N$. That is, only sliding contact exists between the FRs and the springs and dimples of these grids. Consequently, the FR bundle will continue to be loaded only between grids 2 to 8. No additional force is transmitted through grids 1 and 9 and therefore the lower and upper FR bundle spans. The total FA stiffness decreases accordingly. In the further course of the loading process, the contact elements of the other grids start to slide one after another, decreasing gradually the FA axial stiffness. When the maximum force is reached, the instantaneous FA axial stiffness approaches the FA skeleton stiffness since the contribution of the FRs to the FA stiffness has nearly vanished. In the unloading phase, the loading direction of the frictional elements is reversed so that stick contact is restored. Therefore, the axial stiffness is increased again to the initial value and the evolution is nearly linear until slippage starts in opposite direction at load step 20. From this point, the FA axial stiffness decreases again. When the FA is completely unloaded, a permanent axial displacement of about half the maximum deflection remains.

3.5.3 Lateral deflection test

Figure 3.22a gives an example of the typical force-deflection response in a FA lateral deflection test experiment. Figure 3.22b gives the results of the lateral deflection test simulated with the FA structural model and, for comparison, the linear curve obtained when loading the FA skeleton only. The test starts with an undeformed FA which is then laterally deflected by steps of $u_{\text{lat}} = 1$ mm until reaching a lateral displacement of $u_{\text{lat}} = 10$ mm. The lateral deflection test is performed with a constant axial preload of $F_{\text{ax}} = 7470$ N, which is a typical value for the initial HD force in CC. Again, we see a good qualitative agreement between the model results and the experimental record concerning the particular features of the FA load-deflection curve, that is, the nonlinearity and the hysteresis. Like for the axial deflection test, the nonlinear force-deflection relationship with hysteresis can be explained by the processes occurring in the FR support when loading and unloading the FA. Figure 3.23 gives the normalized moment transmitted per grid cell by the FR support as a function of the lateral deflection for all grid levels. It can be observed that the slippage and gap-opening behavior of the grid-to-rod connection plays an important role for the lateral response of the FA. When

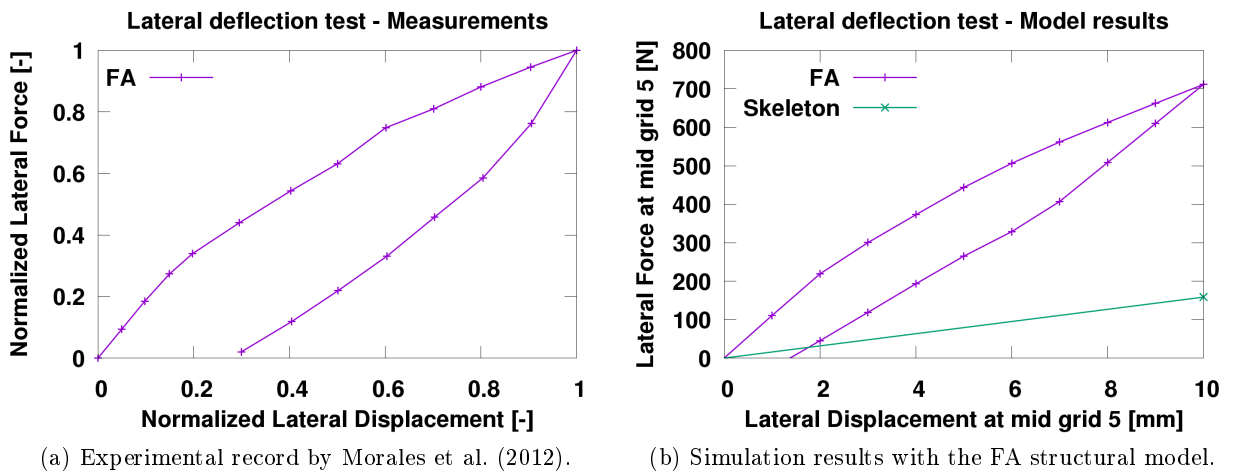


Figure 3.22: Lateral deflection test: qualitative comparison of simulation results versus measurements.

deflecting the FA, the evolution of the FR support follows the loading and unloading phases described in section 3.2.6. The lateral FA response is directly linked to the moment evolution at the grid levels 2 to 4 and 6 to 8. At these levels the highest rotations of the tubes about the perpendicular axis occur as a result of the lateral deflection, see also Figure 3.24, which depicts the lateral deformation shape for the state of maximum deflection. The curve is slightly asymmetric since the displacements are higher in the upper part of the FA than in the lower part. This is due to the higher stiffness in the lower part because of the clamped condition at the bottom end and the thicker GT walls in the dashpot region. A more detailed description of the effect of the FR support on the evolution of the lateral deflection curve is given in Wanninger et al. (2016a,c). In conclusion, the nonlinear curve evolution with a decreasing stiffness during loading and a hysteresis is well reproduced for both axial and lateral deflection tests. The generated model can hence be employed as a generic model to assess the effect of parameter changes and will be used for the analyses in the present work.

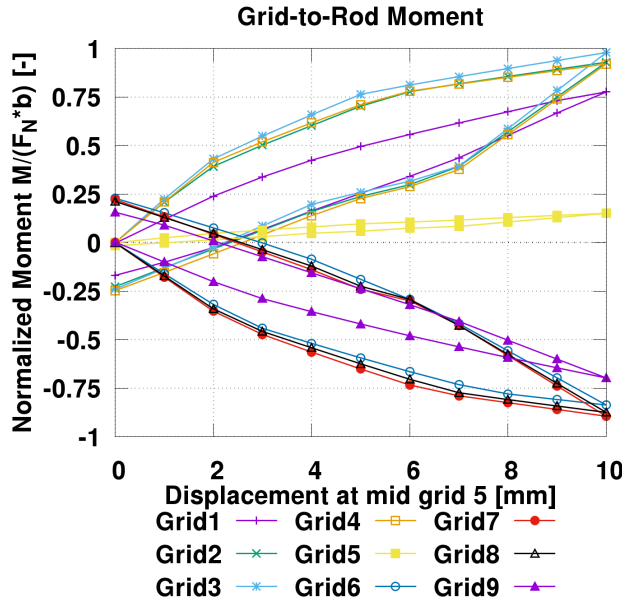


Figure 3.23: Normalized grid-to-rod moment at grid levels 1 to 9 during the lateral deflection test.

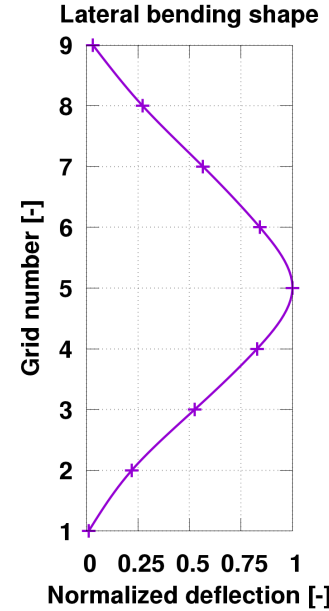


Figure 3.24: Lateral deflection shape.

3.6 Model calibration

In this section, we perform a calibration of the structural model to a set of reference data typical for the modeled FA design. Based on the knowledge acquired about the FA model mechanical response in the previous section, certain model parameters influencing the FA stiffness must be defined as calibration parameters. The stiffness of the GTs and FRs in the model is fixed by their known geometric dimensions and material choice and is therefore not useful for a calibration process. In contrast, the stiffness values for the connection spring elements used for the generic model were mostly based on values obtained from literature for different FA designs. Therefore, it is appropriate to use the stiffness of these spring elements as calibration parameters.

The applied calibration procedure is a stepwise process based on different reference data for the axial and lateral response of the FA and the skeleton. For each reference value, a different spring element stiffness will be defined as calibration parameter.

3.6.1 Axial response

In a first step, the axial response of the model is calibrated. For the considered FA design, approximate reference values for the initial linear axial stiffness are $k_{\text{ax,skel}} = 10\,000\text{ N/mm}$ for the FA skeleton and $k_{\text{ax,FA}} = 30\,000\text{ N/mm}$ for the FA with FRs. The results of the axial deflection test presented in Figure 3.20b exhibit a higher FA stiffness than given by these reference values. This is probably related to the fact that several components are assumed rigid in the generic model although they exhibit a certain elasticity. The cumulative effect of these simplifications can lead to a non-negligible stiffening of the modeled structure. Therefore, the stiffness values of certain axial spring elements must be selected as calibration parameters in order to adjust the model response to the reference values. For the calibration of the FA skeleton axial stiffness, the axial spring stiffness parameter $k_{z,\text{GT-nozzle}}$ is used, which models the connection between GTs and the top and bottom nozzles. For the purpose of the calibration, these springs are assumed to cover the joint effect of all unaccounted axial elasticities. The skeleton model is linear and the additional springs are connected in series with the stiffness of the uncalibrated model, $k_{\text{ax,skel},0}$. Therefore, the calibrated $k_{z,\text{GT-nozzle}}$ can be calculated analytically as a function of the targeted skeleton axial stiffness $k_{\text{ax,skel}}$, see equation 3.32.

$$k_{z,\text{GT-nozzle}} = \frac{2k_{\text{ax,skel},0}k_{\text{ax,skel}}}{n_{\text{GT}}(k_{\text{ax,skel},0} - k_{\text{ax,skel}})} = 5954 \frac{\text{N}}{\text{mm}} \quad (3.32)$$

Regarding the axial response of the complete FA, the initial linear FA stiffness before the first FR slippage can be calibrated. For this calibration, the axial spring stiffness parameter $k_{z,\text{GT-grid}}$ is used, which models the connection between GTs and spacer grids. To obtain the calibrated value, the root-finding problem $f(k_{z,\text{GT-grid}}) - k_{\text{ax,FA}} = 0$ must be solved iteratively, using the secant method, for example. $k_{z,\text{GT-nozzle}}$ is used as initial guess for the first iteration. Already after two iterations the true relative error drops below 0.1% and we obtain a value of $k_{z,\text{GT-grid}} = 4531\text{ N/mm}$ as result.

3.6.2 Lateral response

The next step is the calibration of the model lateral response. Again, first the skeleton response and then the FA response is calibrated. For the skeleton lateral stiffness, we can identify the rotational stiffness of the connection between GTs and grids, $k_{\theta,\text{GT-grid}}$, as the most relevant parameter, which is therefore ideal for the calibration of the linear model. The used reference value for the lateral stiffness of the FA skeleton is $k_{\text{lat,skel}} = 20\text{ N/mm}$. Again, the iterative secant method is applied. As an initial guess, the rotational stiffness values established experimentally by Mattos Schettino et al. (2014) for the four- and eight-spot-weld configuration are chosen, with values of 2950 N/mm and 8150 N/mm . The numerical calibration algorithm estimates a calibrated value of $k_{\theta,\text{GT-grid}} = 3852\text{ N/mm}$ after 4 iterations with an error below 0.1%.

For the full FA, for which the lateral stiffness decreases with increasing deflection, a systematic calibration is more complex than for the FA skeleton only. For a thorough calibration, a good fit to the reference set of data must be found, minimizing the sum of the squares of the residuals. We can hence use the normalized root mean square error (NRMSE) to determine the goodness-of-fit. Usually, regression methods are used

to find the minimum of this measure. For the present nonlinear model, a nonlinear regression would be necessary, which consists in iteratively finding the best fit. However, it is more time-efficient to rely on the model user's expert judgment to calibrate the model based on the knowledge about the influence of the FR grid cell parameters on the FA stiffness.

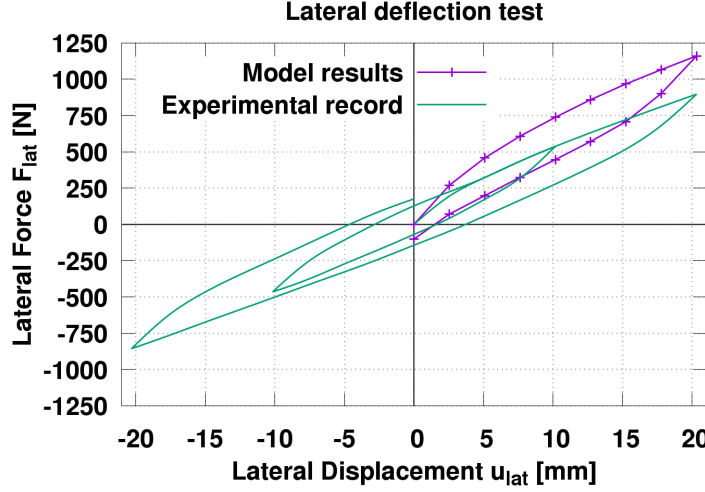
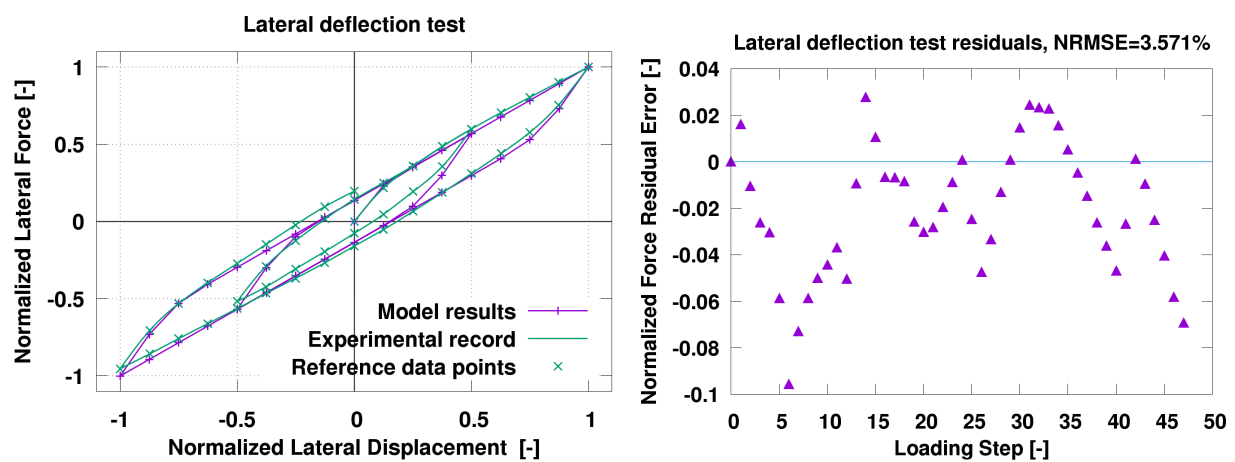


Figure 3.25: Lateral deflection plot before the final calibration step compared to experimental record.

Figure 3.25 gives the calculated force-deflection curve using the generic model including the previous calibration steps, as well as a experimental data record of a lateral FA deflection test to which the calibration is performed. This experimental test consists of two hysteresis cycles. Starting with an initially straight FA, the FA is deflected up to half the maximum deflection in the first loading phase. Then, it is unloaded and deflected up to the same displacement in the opposite direction and finally the first cycle is finished. Subsequently, a second cycle is started in which the FA is deflected up to the maximum deflection in both positive and negative directions. Since the nonlinear behavior is mainly due to the FR slippage in the grid cell, the FR support parameters in Table 3.3 are considered for the calibration. Different parameters are dominant in different phases of the rotation of the FR in the grid cell. It is apparent that a good agreement exists between measurement and model prediction for the shape and width of the hysteresis loop, which represents the dissipated energy during the hysteresis. This behavior is governed by the frictional parameters of the grid cell, namely the stick stiffness k_t and the maximum friction force $\mu F_{\text{norm,ini}}$. It can hence be assumed that these parameters are well estimated in the first approximation. Therefore, we can concentrate on the normal spring stiffness values of the grid spring and dimples for the calibration. Considering the different phases when loading the FR support, we determine that the dimple normal stiffness $k_{d,n}$ plays a significant role for all loading phases and is hence selected as main calibration parameter. From Figure 3.25 it is clear that the model results overpredict the FA stiffness. It can be deduced that by a substantial decrease of the normal dimple stiffness $k_{d,n}$, we can decrease the FA stiffness in all phases. Therefore, we try to find a good model fit by gradually decreasing $k_{d,n}$, down to a value of 10% of the original value. Figure 3.26 demonstrates that a good fit is established with the applied calibration method. The NRMSE of the lateral forces takes a value of under 4%. This modeling error is acceptable for the present application since the estimated uncertainties about other influencing parameters on FA bow during reactor operation are substantially higher. Figure 3.26b gives the distribution of the residuals and shows that the highest deviations

can be expected after the initially applied load is reversed. A possible scenario for this to happen in the reactor is, for example, that before operation a FA is bent into one certain direction by its neighboring FAs. When operation starts, the FA is bent into the opposite direction due to lateral hydraulic forces. Due to the high uncertainty about the lateral hydraulic forces, also the maximum normalized error of 10% can be judged acceptable. If an optimized fit with this model were required, a nonlinear calibration based on the Gauss-Newton method could be performed to minimize the modeling error. However, to better reproduce the particularities of the nonlinear curve evolution, a more detailed modeling of the spacer grid cell is required, which accounts for specific features of the considered spacer grid.



(a) Predictions with the calibrated model versus reference data. (b) Residual plot of model results versus measurement data.

Figure 3.26: Calibration of FA lateral response.

Chapter 4

In-Reactor Model

To run a in-reactor simulation of one or several fuel assemblies (FAs), the in-reactor boundary conditions (BCs) must be defined. We can distinguish between structural BCs and power-related BCs. The structural BCs are those necessary to fully define any structural mechanics problem, that is, the structural constraints and load BCs. The power-related BCs are indispensable for the modeling of the material degradation effects under irradiation, which were introduced in chapter 2: creep, growth, and spring relaxation.

In the first part of this chapter, the typical reactor cycle is described and the general properties of the BCs in the different simulation steps are introduced. The remaining sections concentrate on the description of the power-related BCs and material degradation models. The structural constraint BCs have been described previously in section 3.3.1. The load BC is due to the coolant flow in the reactor and is treated separately in chapter 5.

4.1 Modeling of reactor cycle: start-up, operation and shutdown

4.1.1 General description of reactor cycle

Table 4.1 illustrates the loads and physical phenomena affecting the FAs in the reactor over one reactor cycle, including the start-up and shut-down. After the insertion into the reactor, the weight load on the FAs is somewhat relieved by the buoyancy in the water coolant. The first step of any reactor cycle is closing the reactor pressure vessel (RPV) in cold condition (CC) at about $T = 50^\circ\text{C}$. By closing the RPV, the FAs are constrained in all translational and rotational degrees of freedom (DOFs) as described in section 3.3.1. In particular, the upper core plate is resiliently braced onto the holddown (HD) springs of the individual FAs, thus creating compressive HD forces. As the next step, the pumps are started, thus gradually increasing pressure and temperature until the hot condition (HC) with a temperature of about $T = 300^\circ\text{C}$ and an operating pressure of about 15.8 MPa is reached. The temperature increase has two effects on the structure, namely the thermal expansion and a change in the mechanical properties. Since different materials are involved, thermal strains and elastic strains develop differently for distinct components. During heat-up, the FA guide tubes (GTs) made of Zirconium alloy expand less than the reactor internals, which are usually made of stainless steel. This leads to a decrease of the HD force when compared to the CC. Moreover, the

Table 4.1: Processes over the reactor cycle (based on Salaün et al., 1993).

<div>Cycles</div> <div>Substeps</div>	Elements Phases	Nozzles	Guide tubes	Fuel rods	Spacer grids	Holddown device
	Water filling	Buoyancy force				
	Vessel closure	Structural constraints				Spring compression
	Start-up of pumps	Addition of hydrodynamic forces				
	Transition to hot condition	Thermal expansion Variation in the mechanical properties				
	Irradiation		Creep Growth		Relaxation Growth	Relaxation
	Return to cold condition	Thermal contraction Variation in the mechanical properties				
	Stopping of pumps	Elimination of hydrodynamic forces				
	Vessel opening	Remove constraints				Spring decompression

modulus of elasticity of the materials decreases, thus decreasing the stiffness of the structural components. In the following step, the reactor is made critical and power operation starts. During normal operation, different irradiation-induced or irradiation-enhanced processes prevail for the different components. Creep is important for all structures in the active core region that are put under stress by external loads, that is, mostly the fuel rod (FR) cladding and the GTs. For the pre-stressed spring components, such as the HD springs and the spacer grid springs, stress relaxation plays an important role. Finally, structural growth is relevant for all structural components made of Zirconium alloys, namely GTs, FR cladding, and spacer grids. After operation, the reactor is stopped and transited to HC, thus terminating all flux-dependent processes. Then the reactor is gradually cooled down and depressurized into CC. Before finally opening the reactor vessel, the pumps are shut down, thus removing the hydraulic loads from the FAs. After reshuffling the FAs in the core, the same procedure is repeated in the next cycle.

4.1.2 Load steps and BCs for reactor cycle runs

Based on the different reactor states presented in the previous section, the BCs representing the different physical fields and constraints acting on the FAs must be defined. For this purpose, we distinguish between operation, HC, and CC for the in-core condition. In addition, one ex-core condition is defined which considers hanging FAs after being lifted out of the core. Table 4.2 summarizes the FA BCs used for the different simulation steps. The gravitational load is always imposed on the FA structure and is not mentioned separately in the description. For all in-reactor simulations, the buoyancy force due to the surrounding coolant after the insertion of the FAs into the reactor is accounted for. It is described in appendix D along with the modeling of the axial hydraulic forces. The start-up steps in Table 4.1 do not have a significant influence on the final result if the core only consists of initially straight FAs. In this case, the start-up steps are omitted and the in-reactor FA analysis over one cycle starts immediately with a reactor under operation. During operation, all DOFs at the FA head and foot are fixed, except for the axial and rotational

Table 4.2: Constraints and loads for different simulation steps.

Condition	Constraints						Loads			Result step #
	FA foot			FA head			Temp	Flux	Hydraulic	
	u_x	u_z	θ_y	u_x	u_z	θ_y				
In-core, Initial step at BOC	0	0	0	0	$f(k_{\text{HD}}, T, BU)$		$T(\mathbf{x})$	0	$\mathbf{f}(\mathbf{x})$	0,24
In-core, Operation	0	0	0	0	$f(k_{\text{HD}}, T, BU)$		$T(\mathbf{x})$	$\phi(\mathbf{x})$	$\mathbf{f}(\mathbf{x})$	1-16
In-core, Hot condition (HC)	0	0	0	0	$f(k_{\text{HD}}, T, BU)$		300 °C	0	0	17,23
In-core, Cold condition (CC)	0	0	0	0	$f(k_{\text{HD}}, T, BU)$		50 °C	0	0	18,22
Ex-core, Hanging FAs	0	0	-	0	W_{FA}	-	50 °C	0	0	19-21

displacement DOFs at the FA head. These result implicitly from the connection of the FA head with the HD spring by means of the HD device with HD spring stiffness k_{HD} , see section 3.2.7. The axial compression of the HD springs due to the core plate is additionally influenced by the differential axial expansion of the FAs and core structures as a function of temperature T and the HD spring relaxation over burnup (BU), described in section 4.5.2. Before activating the creep and growth calculations during operation, one initial load step is simulated at the beginning of cycle (BOC). This load step sets up an initial thermoelastic equilibrium under reactor operating conditions. The same thermal and hydraulic loads as under operation are applied. That is, they are imposed as a function of the lateral and axial position, $T(x, z)$ and $\mathbf{f}(x, z)$, according to the axial and lateral profiles determined in section 4.4 and chapter 5. Based on the thermoelastic equilibrium obtained from this initial step, the operation load step is started. This load step includes creep and growth calculations depending on the lateral and axial distribution of the fast neutron flux $\phi(x, z)$ and extends over the entire cycle from BOC to end of cycle (EOC) over 330 full-power days or 7920 hours. For simulations without two-way fluid-structure interaction (FSI), the operation step is performed in one single load step, that is, $\Delta t_{load} = 7920$ h. This load step is divided into several time steps or substeps, in which equilibrium iterations are performed to obtain a converged solution after each substep. Details about the applied creep algorithm and time-step procedure are given in section 2.2.3.1. The total number of substeps depends on the time step size of the single steps. Usually automatic time stepping is used, applying an initial time step of $\Delta t_{sub} = 0.1$ h and limiting the time step size to a maximum of $\Delta t_{sub, max} = 100$ h. The final operation state gives the deformation state at EOC under operating conditions, that is, including all reactor operation loads.

After the operation cycle, different shut-down load steps can be performed in order to finally obtain the free FA deformation without external loads or constraints. In the simulations, these steps represent an attempt to illustrate the effect of the different loads on the deformation and do not necessarily correlate exactly to the conditions in the reactor. Therefore, the hydraulic loads are already withdrawn entirely in the course of the transition to HC, which represents the first load step after reactor operation. In this manner, we can appreciate the mechanical equilibrium based on the plastic deformation of the FAs without the influence of external hydraulic loads and temperature gradients. During the following transition to CC, the temperature is decreased to 50 °C, resulting in different thermal strains and a different modulus of elasticity of the materials. The ex-core BC represents the last load step of the analysis over one cycle. It simulates isolated hanging FAs to obtain the unconstrained FA deformation, which is measurable during the outage. Mechanically speaking, the FAs are laterally decoupled from each other and all rotational and HD constraints modeling the effect of the core plates are removed, thus creating a statically determinate system

without external loading. When the FA is lifted out of the core, its weight is supported from the FA top instead of from the FA bottom. To account for the resulting tensioning effect in the FA, an upward force about equal to the FA weight force W_{FA} is imposed on the top of the FA.

Figure 4.1 gives a flow chart of the general FA bow calculation procedure. For all runs, a script is initially executed which controls the calculation procedure. After defining the respective BC from Table 4.2 and the load step time as input arguments, the ANSYS Mechanical APDL code is started. In the initial run, the material models, nodes, and elements must be defined in the ANSYS preprocessor */PREP7*. The applied loads and solution parameters are defined in the ANSYS solution processor */SOLU*, which is started for all runs. After the solution process, the ANSYS time-stepping postprocessor */POST26* is started to print the output variables of interest. Then, ANSYS is stopped and the control is given back to the master process. If further load steps are required, ANSYS is restarted from the previous load step, usually using different BCs. Otherwise, the procedure is stopped.

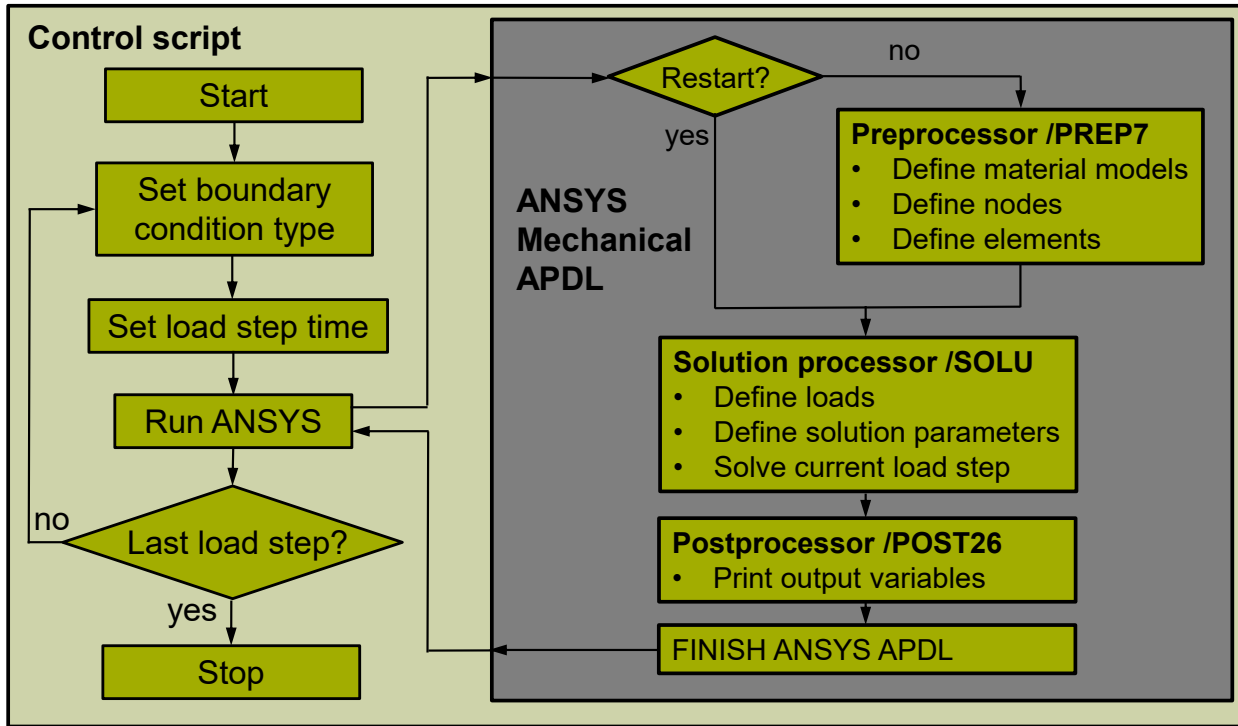


Figure 4.1: Flow chart of the FA bow calculation procedure.

4.2 Creep of structures

Two different generations of Zirconium alloys for FR cladding and GT materials are investigated in the framework of this thesis; first, Zircaloy-4 (Zry-4), which has been the conventional material in pressurized water reactors (PWRs) for several decades; second, advanced Zirconium alloys with Niobium content, which have become the standard in most Western PWRs in recent years. As for Zry-4, no difference will be made between the conventional Zry-4 and other further developments, such as low-tin Zry-4. As for the advanced alloys, different alloys with several particularities in the alloy composition have been developed by different fuel vendors. Since the availability of data for this type of alloys is limited and the different

alloys are all reported to exhibit an optimized performance, no difference will be made between the different types of advanced alloys with Niobium content. This facilitates deriving correlations from experimental and performance data since a larger database is available.

Furthermore, it is important to distinguish between GT and FR materials. The operating conditions are very different for GTs and FRs, concerning the stress and temperature range, as well as the loading state. When compared to GTs, FRs must resist higher stresses and temperatures. Moreover, FRs are loaded in a biaxial stress state with hoop and axial stresses while GTs mostly sustain only axial stresses due to compression, traction, or bending. To optimize their use for the respective applications, GTs and FRs rely on different fabrication processes. An important feature is the final heat treatment. Zry-4 GTs are usually deployed in a recrystallization-annealed (RXA) state whereas stress-relieved annealed (SRA) Zry-4 is used for the FR cladding. As for the advanced alloys, the differences in fabrication depend on the specific alloy. For example, ZIRLO GTs are delivered in a recrystallized condition (King et al., 2002) and exhibit hence a reduced creep rate compared to partially recrystallization-annealed (pRXA) or SRA ZIRLO FRs, see Figure 4.2.

It is hence important to distinguish between GT and FR materials and use dedicated GT and FR creep tests as a basis for the creep laws used for the FA structural model. In the next sections, first GT creep data and the derived laws will be discussed. As an elementary part of the FA structure, the GT creep is expected to have the largest influence on the FA deformations. Then, FR creep data are analyzed and corresponding creep correlations are deduced.

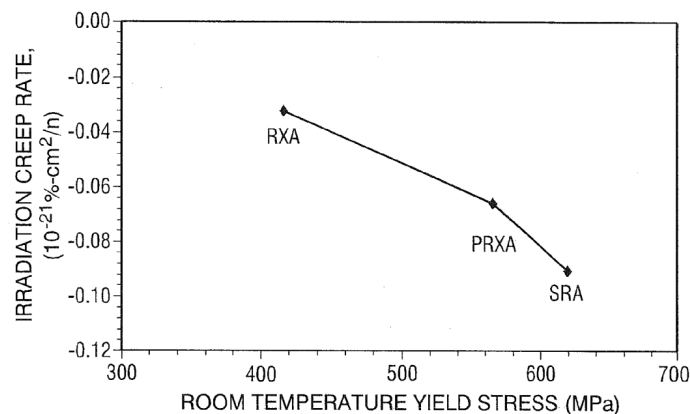


Figure 4.2: Irradiation creep rates for ZIRLO depending on the final heat treatment (Foster et al., 2015).

4.2.1 GT creep

4.2.1.1 RXA Zircaloy-4 GTs

The creep of GTs is usually considered less critical for reactor applications than that of the FR cladding. While the latter may be at the origin of serious performance problems like FR failure, the consideration of GT creep only has become more important after the occurrence of strong FA bow. Correspondingly the creep database in open literature about the in-reactor creep of FR claddings is significantly larger than that of GT materials under their typical operating conditions. As a result of the research related to the FA bow problem, a few publications with such experimental data have become available, which as a total, can serve to define a creep law which represents the typical creep behavior of RXA Zry-4. One set of experimental

data of Zry-4 GT creep was published by Yvon et al. (1998) in combination with a creep law derived from those data. In the experiments different samples of fully recrystallized Zirconium alloys in the α -phase were submitted to uniaxial stresses from 76 MPa to 102 MPa at temperatures from 297 °C to 315 °C and fast neutron fluxes between $1 \times 10^{14} \text{ n cm}^{-2} \text{ s}^{-1}$ and $2 \times 10^{14} \text{ n cm}^{-2} \text{ s}^{-1}$. From the obtained data, a creep correlation of the Norton-Bailey type, equation 2.142, was derived.

$$\varepsilon^{\text{cr}} = C_{\text{cr}} \sigma^{n_{\sigma}} e^{\frac{-Q_T}{T}} \Phi^{n_{\Phi}} \quad (4.1)$$

The coefficients of equation 4.1 resulting from the data analysis are given in Table 4.3. The unit of C_{cr} is such that the creep strain ε^{cr} is dimensionless. In the experimental tests, no specific influence of the neutron flux level was observed; hence, the neutron flux exponent n_{Φ} appearing in the differentiated form, equation 2.143, equals unity.

Table 4.3: Coefficients for the GT creep law by Yvon et al. (1998).

C_{cr}	n_{σ}	Q_T	n_{Φ}
1.5×10^{-24}	1.0	4700 K	0.8

The creep tests by Yvon et al. (1998) were executed with uniaxial tensile stress which is uniform over the tube cross-section. For the analysis of FA deformations, however, the effect of bending moments on the creep deformation is of particular interest to predict the FA bow. When FAs undergo lateral loads, the cross-sectionally uniform axial stresses due to axial loads are superposed by axial bending stresses, which have a non-uniform distribution over the GT cross-section. For this purpose, bending creep tests can be performed. These tests necessitate, however, a more elaborate experimental set-up and are hence not performed as frequently as simple compressive or tensile tests. One such bending test with RXA Zry-4 GTs was described by Pettersson (2002). This test has been performed under pure bending with a maximum stress in the outer fibre of about 70 MPa and a temperature of 317 °C. Further sets of data were published by McGrath and Yagnik (2011) and Seibold et al. (2000). McGrath and Yagnik (2011) investigated the in-reactor creep of axially compressed and preirradiated ($\Phi = 1 \times 10^{22} \text{ n cm}^{-2}$) GT specimens with different tin and initial hydrogen contents. Seibold et al. (2000) published data for the long-term irradiation up to $\Phi = 4.7 \times 10^{21} \text{ n cm}^{-2}$ of low-tin Zry-4 under the for GTs typical low axial compressive stresses between 7 MPa and 20 MPa.

All discussed data are summarized in Figure 4.3. Since Yvon et al. (1998) is the only publication to provide a creep law correlated to the experimental data, the validity of this law for the other experiments is investigated. For this purpose, equation 4.1 is evaluated for the respective test conditions and compared with the measured creep data. Figure 4.3 displays the resulting curves in the same color as the corresponding experimental data. For Yvon's data, evidently a good agreement exists between model and experiment since these data, amongst others, form the basis for the creep law. Figure 4.3 demonstrates as well that Yvon's creep law predicts Pettersson's results very well despite the fact that the deformation mode was different: axial traction for Yvon's data and bending for Pettersson's data. The applicability of Yvon's law for bending problems such as FA bow has hence been proved. The experimental creep data obtained by McGrath and Yagnik (2011) are somewhat overpredicted by Yvon's correlation. Besides the possible effects of the slightly different alloying configurations and fabrication processes, this might be linked to the pre-irradiation of the samples and the associated hardening effects. On the other hand, Yvon's creep law somewhat underpredicts Seibold

et al.'s results. An explanation for this could be the limitation of Yvon's creep data base to a maximum fluence of $\Phi = 2 \times 10^{21} \text{ n cm}^{-2}$. Irradiation creep laws of the Norton-Bailey type tend to underpredict the creep strain for fluences above the validated domain since the calculated creep rate decreases continuously over time due to the negative time exponent. For high fluences, however, the transient components are mostly saturated and pure steady-state irradiation creep with a linear dependence on time is present. For better predicting creep strain for high fluences, a linear dependence on fluence might be more appropriate. Besides, the fact that Seibold's values were obtained at a relatively low temperature of 290 °C might be the reason for the underprediction since the activation temperature further decreases for temperatures below 300 °C, see section 2.4.6. Still, it is demonstrated that Yvon's creep law is valid with a reasonable error also for a stress level well below the tested one between 76 MPa and 102 MPa.

We can conclude that a good agreement of Yvon's creep response predictions exists with experimental data for traction, compression, and bending problems of RXA Zry-4 for a wide range of stresses from 7 MPa to 102 MPa and the temperatures of interest. Yvon's law can hence be used to model the creep response of Zry-4 GTs in the context of FA bow problems.

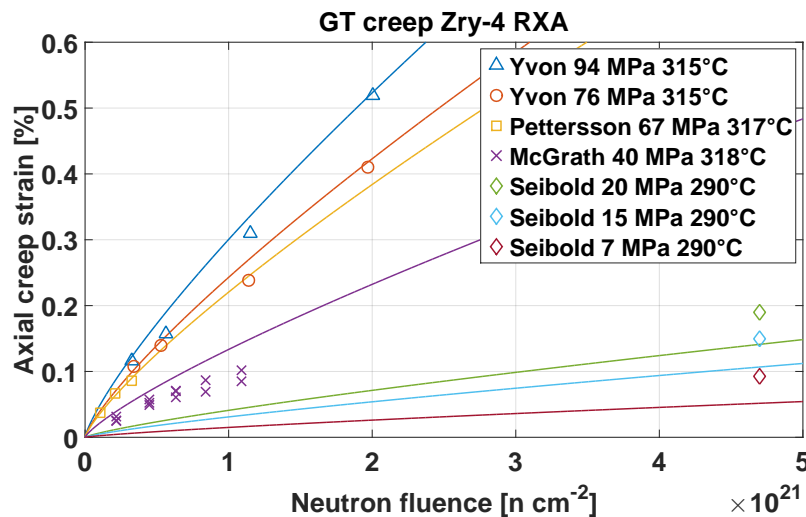


Figure 4.3: GT axial creep strain as a function of fluence for conventional or low-tin RXA Zry-4 for different experimental data by Yvon et al. (1998), Pettersson (2002), McGrath and Yagnik (2011), and Seibold et al. (2000).

4.2.1.2 Advanced-Alloy GTs

Analogously to Pettersson's tests with Zry-4, bending tests financed by SKI and the Swedish nuclear industry research co-operation (BFUK) were performed with two widely used GT materials. The experiments investigated GTs in two different material conditions, fresh material (FM) and pre-irradiated material (IM) up to about $\Phi = 1 \times 10^{21} \text{ n cm}^{-2}$, both in pile (IP) and out of pile (OP), see Figure 4.4. For the fresh material condition, both alloys exhibit similar creep strains. Considering, however, the pre-irradiated samples, the creep response is opposite between the two materials. For GTs made from alloy 1, the pre-irradiated sample exhibits less creep strain than the fresh sample whereas the pre-irradiated alloy 2 GT material exhibits a significantly higher creep than the fresh material. It is difficult to draw conclusions about the root of the different creep strains of the pre-irradiated material without a detailed microstructural investigation. The

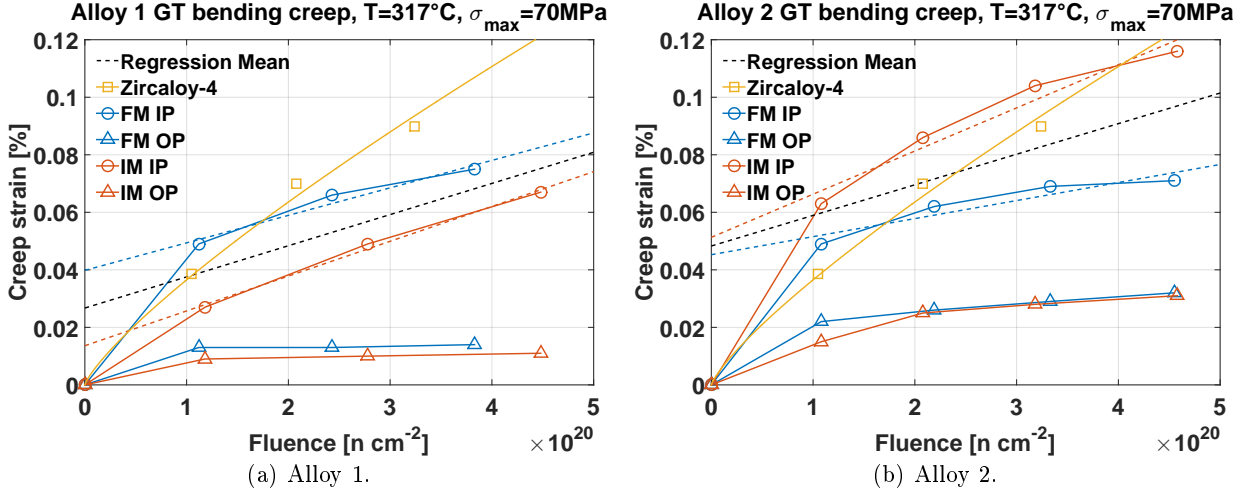


Figure 4.4: Axial creep strain as a function of fluence obtained from bending creep tests with two widely used GT alloys in fresh material (FM) and pre-irradiated material (IM) condition tested in pile (IP) and out of pile (OP). Data kindly provided by Vattenfall originating from bending tests financed by SKI and the Swedish nuclear industry research co-operation (BFUK).

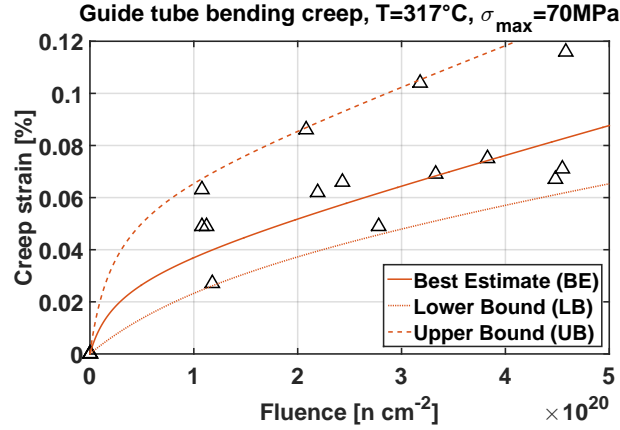


Figure 4.5: Best estimate (BE) creep curve with lower and upper bounds developed based on the GT bending creep test data given in Figure 4.4.

pre-irradiation fluence is not particularly high so that the difference may at least partially be a result of experimental scatter.

To use the presented data in the FA structural model, a creep law must be derived. Due to the limited scope of the data which were only obtained for a single specimen, a unique temperature and stress, as well as a up to a maximum fluence of $5 \times 10^{20} \text{ n cm}^{-2}$, several assumptions must be made. The first issue to be addressed is up to which fluence the transient creep delivers a relevant contribution to the total creep rate. In biaxial creep tests, Foster and McGrath (2007) observed that transient creep terminates after several hundred hours in a flux of about $\phi = 3 \times 10^{13} \text{ n cm}^{-2} \text{ s}^{-1}$, which corresponds to a saturated fluence of $\Phi_{\text{pri,sat}} = 4 \times 10^{19} \text{ n cm}^{-2}$. The corresponding transient strain is in the order of magnitude of 10^{-4} . These observations suggest that the transient creep is saturated at the fluence of $\Phi = 1 \times 10^{20} \text{ n cm}^{-2}$, at which the

first data points were obtained in the bending creep tests. Transient creep being mostly linked to thermal creep, this assumption is corroborated by the fact that the OP thermal creep rate strongly decreases after this lapse of time. All data points are hence assumed to lie in the secondary creep regime so that a steady-state creep rate can be obtained by performing a linear regression. The intersection of the linear curve with the y-axis then represents the saturated primary creep strain. In this manner a combined primary and secondary creep law, presented in equation 4.2, can be obtained, summing up the influences of both contributions. The time dependence of the primary creep is represented with a rational polynomial, see also equation 2.37.

$$\varepsilon^{\text{cr}} = \left(C_{\text{cr,pri}} \frac{p_{\text{cr}} t}{1 + p_{\text{cr}} t} + C_{\text{cr,sec}} \phi^{n_\phi} t \right) \sigma^{n_\sigma} e^{\frac{-Q_T}{T}} \quad (4.2)$$

Since the rational polynomial function converges slowly, a value of 90% is considered sufficient for primary creep to be considered saturated, yielding the following value for the exhaustion rate:

$$p_{\text{cr}} = \frac{9}{t_{\text{sat}}} = \frac{9\phi}{\Phi_{\text{pri,sat}}} \quad (4.3)$$

The linear regressions obtained for the different material conditions are represented by dashed lines in Figure 4.4. Table 4.4 lists the values obtained for the creep coefficients in equation 4.2 for the different materials and material conditions. Since no clear tendency was recognized between the different material conditions, an average regression is also represented for both materials. This regression mean of fresh and pre-irradiated materials yields similar values for the secondary creep rate of both alloys. As an approximation, the total mean is hence suited for representing the typical creep response for advanced-alloy GTs and will be used as a BE law for the subsequent analyses. The different creep rate levels can serve as a reference for a sensitivity analysis. The correlation obtained for the pre-irradiated alloy 2 can be considered as an upper bound (UB) for GT creep. As the lower bound (LB), the correlation obtained for fresh alloy 2 material can be used. Figure 4.5 shows the final curves obtained for the BE advanced-alloy GT creep law and the upper and lower bounds along with the underlying data. To reach a better fit and comprise all data points, $\Phi_{\text{pri,sat}}$ was increased to $1.5 \times 10^{21} \text{ n cm}^{-2}$ for the LB law and to $2 \times 10^{20} \text{ n cm}^{-2}$ for the UB law. Moreover, $C_{\text{cr,pri}}$ was increased by 20% for the UB law. As for the stress and temperature dependency, the values from Yvon's creep law are assumed. That is, a linear stress dependence and an activation temperature of $Q_T = 4700 \text{ K}$ are applied. Table 4.5 finally summarizes the parameters other than the creep coefficients of the advanced-alloy GT creep law.

Table 4.4: Creep coefficients for equation 4.2 derived from linear regression.

	Alloy 1			Alloy 2			Total
	FM	IM	mean	FM	IM	mean	mean
$C_{\text{cr,pri}} \times 10^8$	1.64	0.56	1.10	1.86	2.11	1.98	1.54
$C_{\text{cr,sec}} \times 10^{29}$	3.93	4.97	4.45	2.58	6.16	4.37	4.41

Table 4.5: Parameters for the advanced-alloy GT creep law in equation 4.2.

n_σ	Q_T	p_{cr}	$\Phi_{\text{pri,sat}}$	$\Phi_{\text{pri,sat,LB}}$	$\Phi_{\text{pri,sat,UB}}$
1.0	4700 K	$9\phi/\Phi_{\text{sat,pri}}$	$4 \times 10^{19} \text{ n cm}^{-2}$	$1.5 \times 10^{21} \text{ n cm}^{-2}$	$2 \times 10^{20} \text{ n cm}^{-2}$

4.2.2 FR creep

In reactor analysis, FR creep mostly plays a role for the analysis of FR diameter creep-down to ensure the integrity of the fuel. Hence, FR creep data are usually obtained in a biaxial creep state as a relationship between hoop stress and diametral creep strain. In contrast, for the present structural model only the effect of axial strain on the structure is of interest because the impact of creep-down has been taken into account in the grid spring relaxation model. The effect of the FR axial deformation and bending may play an important role during the first reactor cycle before the grid springs relax. Due to the restricted availability of axial creep data, the FR axial creep response must be derived from diametral creep data despite the limited knowledge about Hill's anisotropy coefficients. For the modeling of the FR cladding creep due to pure axial stress, the hoop-stress creep laws need to be corrected for the influence of the biaxial stress state. This correction term is derived in appendix B. For a linear stress dependence, equation B.11 stipulates that

$$C_{cr,z} = C_{cr,biax} \frac{(F + H)}{r_\sigma(2G + F)}, \quad (4.4)$$

where $C_{cr,biax}$ is the creep coefficient for the diametral creep under a biaxial stress state and $C_{cr,z}$ the coefficient for axial creep due to axial or bending stresses. For the time being, we use as an approximation the correction factor for an isotropic material and zero BU, that is, $F = G = H = 0.5$ and $r_\sigma = 0.4$.

4.2.2.1 SRA Zircaloy-4 FRs

A well-known and accepted model for the diametral creep of SRA Zry-4 was published by Limbäck and Andersson (1996), relying on an extensive creep measurement database. The model takes into account separately the different components of primary creep, secondary irradiation creep, and secondary thermal creep with an irradiation hardening term. The elaborate structure of this model requires, however, a complex implementation using subroutines, which exhibits numerical difficulties in the solution process. For this reason, the SRA Zry-4 FR creep model used in this work is based on data for low-tin SRA Zry-4 published

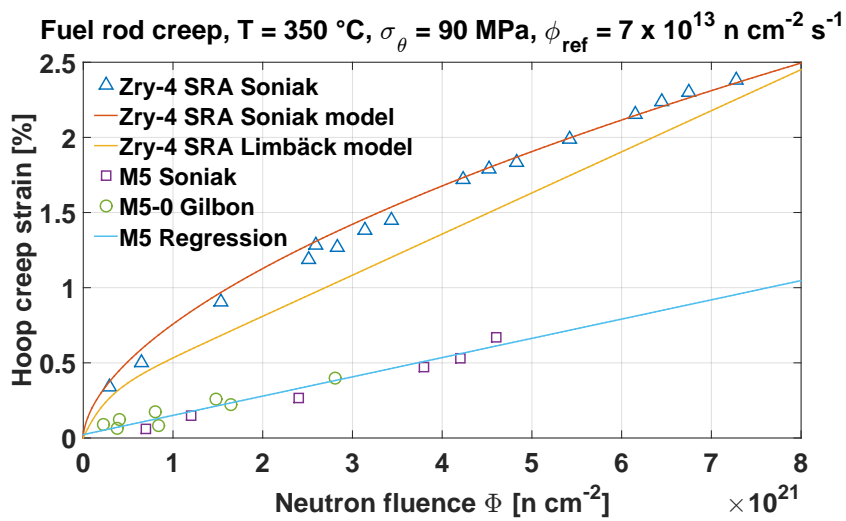


Figure 4.6: FR cladding hoop creep strain as a function of fluence for low-tin SRA Zry-4 and new Zirconium alloys with Niobium content.

by Soniak et al. (2002). This publication contains a relatively wide array of data and derived easy-to-implement dependencies on stress, temperature and fluence for the use in a Norton-Bailey creep law, see equation 2.142. Compared to the model by Limbäck and Andersson (1996), this allows a more straightforward implementation into the structural model and proved, as a result, a higher numerical stability. A further advantage is that Soniak et al. (2002) tested an optimized low-tin SRA Zry-4, which was fabricated using upgraded manufacturing and inspection processes whereas the irradiation creep model by Limbäck and Andersson (1996) is based on older experiments with standard Zry-4 summarized by Franklin et al. (1983). The results with the model based on Soniak et al.'s data are compared with those from Limbäck and Andersson's model to ensure a good performance despite the lower complexity of the model. Figure 4.6 gives the evolution of hoop creep strain of a pressurized SRA Zry-4 pressure tube under typical PWR operating conditions ($\sigma = 90$ MPa, $T = 350$ °C, and $\phi = 7 \times 10^{13}$ n cm⁻² s⁻¹) based on Soniak et al.'s experimental data. Since these measurements exhibit a clear dependence of the creep rate on the neutron flux level at which the material is irradiated, the data were normalized to the neutron flux level of $\phi = 7 \times 10^{13}$ n cm⁻² s⁻¹ by introducing a flux exponent with the widely used value of $n_\phi = 0.85$, see also section 2.4.6. The model predictions by both Limbäck and Andersson (1996) and Soniak et al. (2002) lie close together and predict the experimental data with a reasonable error. We can hence use the model based on Soniak et al.'s data for modeling the creep of SRA Zry-4 FRs. Table 4.6 summarizes the corresponding coefficients for the SRA Zry-4 FR creep law referring to the differentiated Norton-Bailey equation 2.143. Compared to the values proposed by Soniak et al., some minor modifications are applied. In particular, the generally agreed-upon linear dependence on stress is used instead of the published stress exponent of $n_\sigma = 1.61$.

Table 4.6: Parameters for the SRA Zry-4 FR creep law based on Soniak et al. (2002).

C_{cr}	n_t	n_σ	Q_T	n_ϕ
3.14×10^{-12}	0.573	1.0	9313 K	0.85

4.2.2.2 Advanced-Alloy FRs

As for advanced Zirconium alloy cladding, such as M5, ZIRLO, or MDA, Soniak et al. (2002), Gilbon et al. (2000), and Kido et al. (2002) confirm an increased creep and growth resistance when compared to conventional SRA Zry-4. For comparison, creep test data for M5 and its experimental precursor M5-0, which were irradiated under the same condition as the SRA Zry-4, are shown in Figure 4.6. The data demonstrate that particularly the primary creep strain is strongly reduced for the advanced alloys and that it saturates at a very early irradiation stage, exhibiting values in the order of 10^{-4} . To obtain a creep correlation from these data, we can use the same approach as in section 4.2.1.2, that is, by deriving a linear regression curve from all data points to obtain a secondary creep law. The primary creep law is then based on the resulting saturated primary creep in conjunction with a saturating time function. In this manner a creep law of the type of equation 4.2 is obtained. Table 4.7 summarizes the coefficients of the M5 FR creep law obtained by linear regression as well as the other relevant parameters. This creep law will be used representatively for all advanced alloys. The unit of the creep coefficients is such that a strain rate of 1/h is obtained. For the dependence on stress, neutron flux level, and temperature only insufficient data are available and assumptions are made. In agreement with the standard behavior of Zirconium alloys under the considered conditions, a linear stress dependence is assumed. Based on the detected flux dependence

in Soniak et al.'s tests, a flux exponent of $n_\phi = 0.85$ is applied. As for the temperature, the fact that the primary creep strain is small suggests a small contribution of thermal creep and hence a weak temperature dependency. This is, for example, confirmed by the data published by Gilbon et al. (2000), who did not detect a significant temperature dependence for the M5-0 alloy. The fact that the advanced alloys are deployed in recrystallized or partially recrystallized condition supports the supposition that the transition temperature to a strong temperature dependence is above the temperatures encountered in normal PWR operation. Hence, the mean value of the activation temperature range for a weak temperature dependence indicated in section 2.4.6 is used: $Q_T = 3500$ K.

Table 4.7: Parameters for the M5 FR creep law representative for all advanced alloys.

$C_{cr,pri}$	$C_{cr,sec}$	n_σ	Q_T	n_ϕ	p_{cr}	$\Phi_{pri,sat}$
4.74×10^{-9}	1.59×10^{-27}	1.0	3500 K	0.85	$9\phi/\Phi_{pri,sat}$	$4 \times 10^{19} \text{ n cm}^{-2}$

4.3 Growth of Structures

The in-reactor growth of Zirconium alloys depends strongly on the alloying composition and heat treatment. Moreover, depending on if GT or FR operating conditions are considered, different growth mechanisms are relevant leading to variable results, see section 2.4.5. With the use of advanced alloys, irradiation growth can be reduced compared to the performance of conventional alloys. It is hence necessary to distinguish between GT and FR growth models, as well as between conventional and advanced alloys.

4.3.1 FA or GT growth

The GT growth model is based on performance data published by Wikmark et al. (2009), which had in part been published before by King et al. (2002). The data are represented in Figure 4.7. GTs being recrystallized

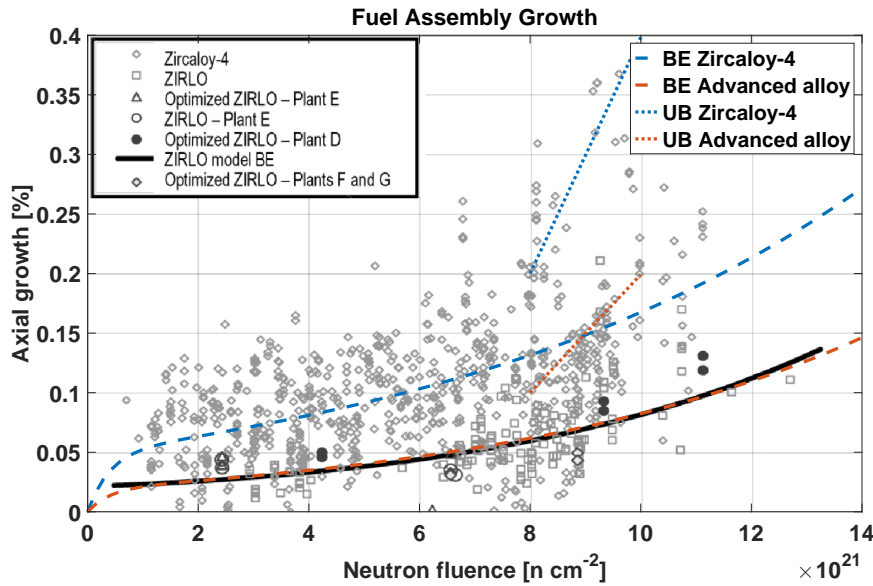


Figure 4.7: Derived laws for the modeling of best estimate (BE) and upper bound (UB) GT growth of Zircaloy-4 and advanced alloys with underlying FA growth performance data by Wikmark et al. (2009).

material, the three-stage process of irradiation growth is well perceptible from the presented data. Equation 4.5 is proposed to reproduce this behavior.

$$\varepsilon^{\text{gr}} = \varepsilon^{\text{gr},\text{ini}} \left(e^{-\frac{\Phi}{\tau_{\text{gr}}}} + e^{C_{\text{gr}}\Phi} \right) \quad (4.5)$$

The first exponential function represents the saturating growth in the initial stage expressed by an exponentially decreasing growth rate. This growth rate component appears to saturate at a fluence of about $\Phi = 2 \times 10^{21} \text{ n cm}^{-2}$. According to the rule of thumb that the exponential decay is nearly terminated after five times the exponential time constant τ_{gr} , we obtain:

$$\tau_{\text{gr}} = \frac{2 \times 10^{21} \text{ cm}^2}{5} \frac{1}{\text{n}} \quad (4.6)$$

The second exponential function in equation 4.5 represents the gradually increasing growth rate in the second stage and produces very low growth rates in the initial phase that are increasing steadily for higher BUs or fluences. Again, the exponential coefficient C_{gr} must be based on experimental data. The transition between the first and second growth stages is marked by the “saturated growth” strain $\varepsilon^{\text{gr},\text{ini}}$ of the initial stage. The scattering of growth performance data is relatively high, which is evident from Figure 4.7. For Zry-4, an average value of $\varepsilon^{\text{gr},\text{ini}} = 0.05\%$ can be estimated from this data, which is in agreement with other less extensive data published by Gilbon et al. (2000) and Garzarolli et al. (1996). As a simple means to obtain a correlation, Garzarolli’s data for RXA Zry-4 in Figure 2.18 are used to define an exponential curve $f = \varepsilon^{\text{gr},\text{ini}} \exp(C_{\text{gr}}\Phi)$ by means of regression analysis. Using $\varepsilon^{\text{gr},\text{ini}} = 0.05\%$, the blue dashed curve in Figure 4.7 is created, which represents a good estimation of the average growth of Zry-4 over the entire fluence range when compared with the underlying data.

For advanced-alloy GTs, Mardon et al. (2005) published data for M5 and Wikmark et al. (2009) for standard and optimized ZIRLO. The latter are more extensive and will hence be used as reference. Wikmark et al. (2009) also provided a BE curve for the growth of standard ZIRLO in Figure 4.7, which can be used to generate a curve $f = \varepsilon^{\text{gr},\text{ini}} \exp(C_{\text{gr}}\Phi)$ by means of regression analysis. The red dashed curve in Figure 4.7 shows the curve created with the obtained parameters. This curve also represents well the order of magnitude of the values published by Mardon et al. (2005) for the assembly growth of M5.

Due to the high scattering of measurement data, the sensitivity and uncertainty analysis of the influence of growth on the structural FA behavior plays an important role in the framework of this thesis. Particularly for high BUs, large differences in growth performance are detected depending on when breakaway growth with increased constant growth rates sets in. This sudden increase in growth rate is not covered by the model based on equation 4.5. To test the influence of the UB growth strains on the structural model, a linear UB growth law is also implemented for the use with high-BU FAs. McGrath and Yagnik (2011) measured a growth rate of $\dot{\varepsilon}^{\text{gr},\text{UB}} = 1.22 \times 10^{-24} \text{ cm}^2 \text{ n}^{-1}$ for a Zry-4 GT specimen pre-irradiated up to $\Phi = 10 \times 10^{22} \text{ n cm}^{-2}$ under average PWR coolant temperature conditions ($T = 307^\circ\text{C}$). The high growth rate is reported to be mainly a result of the hydrogen uptake during pre-irradiation. For illustration, the blue dotted curve in Figure 4.7 represents growth at this rate. This curve is in good agreement with other underlying Zry-4 high-BU data in Figure 4.7, which are also reported to have undergone accelerated growth due to high hydrogen uptake (King et al., 2002).

For advanced alloys, the rate increase towards end of life is usually not as fast as for conventional materials.

A representative UB linear growth rate half of that of Zry-4 is assumed, which is in good agreement with the maximum measurement data for ZIRLO in Figure 4.7. The finally used parameters for both conventional and advanced alloys for BE and UB growth are summarized in Table 4.8.

Table 4.8: Parameters defined for the BE GT growth model based on equation 4.5 and for the linear UB growth.

Parameter	Unit	Zry-4	Advanced alloy
$\varepsilon_{gr,ini}$	%	0.019	0.05
C_{gr}	$\frac{cm^2}{n}$	1.210×10^{-22}	1.434×10^{-22}
τ_{gr}	$\frac{cm^2}{n}$	4×10^{20}	4×10^{20}
$\dot{\varepsilon}_{gr,UB}$	$\frac{cm^2}{n}$	1.22×10^{-24}	0.61×10^{-24}

4.3.2 FR growth

Performance data of the growth of both the conventional FR cladding material SRA Zry-4 and advanced cladding alloys have been published by Gilbon et al. (2000) and Mardon et al. (2005) for M5, Wikmark et al. (2009) for different ZIRLOs, and Nakano et al. (2008) for MDA. SRA Zry-4 is observed to exhibit a relatively constant growth rate over BU with a typical average growth rate of $\dot{\varepsilon}_{gr,SRA\ Zry-4} = 1 \times 10^{-24} cm^2 n^{-1}$ (Mardon et al., 2005), that is 1 % after a fluence of $\Phi = 1 \times 10^{22} n cm^{-2}$. From the different data published for advanced alloys, it can be concluded that for low fluences up to about $\Phi = 3 \times 10^{21} n cm^{-2}$ the growth strain rate appears to be roughly constant with only a slightly lower average strain rate than that of SRA Zry-4. For this phase, a value of $\dot{\varepsilon}_{gr,advanced} = 0.75 \times 10^{-24} cm^2 n^{-1}$ is estimated. For higher fluences, the growth rate decreases gradually while that of SRA Zry-4 remains roughly constant, see Figure 4.8. Since the effects of FR growth are only transmitted to the FA structure for low fluences when the grid springs are not yet relaxed, a linear growth law with the cited constant growth rates is implemented for both conventional and advanced cladding materials.

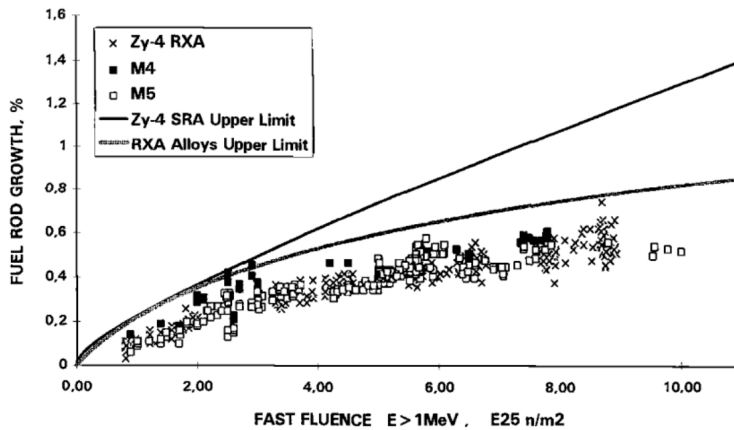


Figure 4.8: FR growth for different cladding materials (Gilbon et al., 2000).

4.4 Reactor operating conditions

Table 4.9 defines the operating conditions and other characteristic parameters of the considered reactor. Based on these parameters, we derive the structural temperatures and the fast neutron flux in this section and the hydraulic loads in chapter 5.

Table 4.9: Reference reactor data.

Variable	Symbol	Value
Mass flow in core for heat transfer	\dot{m}_{core}	18 000 kg/s
FA pitch	p_{FA}	230 mm
Number of FA in core	n_{FA}	193
Operating pressure	p_{sys}	15.8 MPa
Thermal power	$Q_{\text{th,core}}$	3900 MW
Core inlet temperature	T_{in}	292 °C
Core outlet temperature	T_{out}	326 °C
Axial pressure drop in core	Δp_{core}	0.188 MPa

4.4.1 Power distribution

For an ideal cylindrical, homogeneous, and unreflected reactor core, the power distribution can be calculated analytically. The solution is given by a Bessel function of order zero in radial direction and a cosine distribution in axial direction. In practice, reactor operation is limited by maximum permissible values for power density to avoid a boiling crisis and to eliminate the conditions which could cause fuel pellet melt. For an efficient use of the fuel, operators are also interested in a BU of fuel elements which is as uniform as possible. By partial refueling and charging fuel of different enrichments and poison concentrations to different zones in the reactor, it is possible to flatten the power distribution to a more uniform profile. More recent strategies seek for cores with low neutron leakage to increase fuel efficiency and to reduce neutron flux at the RPV wall to mitigate neutron embrittlement. To optimize this so-called fuel management, operators calculate the power density distribution in the core by reactor simulation codes. Figure 4.9 depicts the typical radial power distribution in an operating KWU-type PWR calculated by such a code. There is a high radial power gradient over the first two or three FAs at the core periphery and a slight depression in the core center. An as uniform as possible profile is also sought in axial direction. These calculations result in a specific core loading pattern defining the positions of all involved FAs for the following cycle. Figure 4.10 gives an example of such a FA loading arrangement in the reactor core. Based on this characteristic power distribution and core loading pattern, we define a typical 2D power profile and FA BU profile in one of the central FA rows. The local linear power density $q'(x, z)$ within the FA row is determined by the core-averaged linear power density q'_{ave} times a radial factor $a_r(x)$ and an axial factor $a_z(z)$, which are independent of each other:

$$q'(x, z) = a_r(x)a_z(z)q'_{\text{ave}} \quad (4.7)$$

In the framework of this thesis, we consider no evolution of the power density as a function of BU or due to changes in the inter-assembly water gaps. Moreover, no gradients over single FRs are assumed. The core-averaged linear power density is calculated from the thermal power of the core $Q_{\text{th,core}}$ and the heat

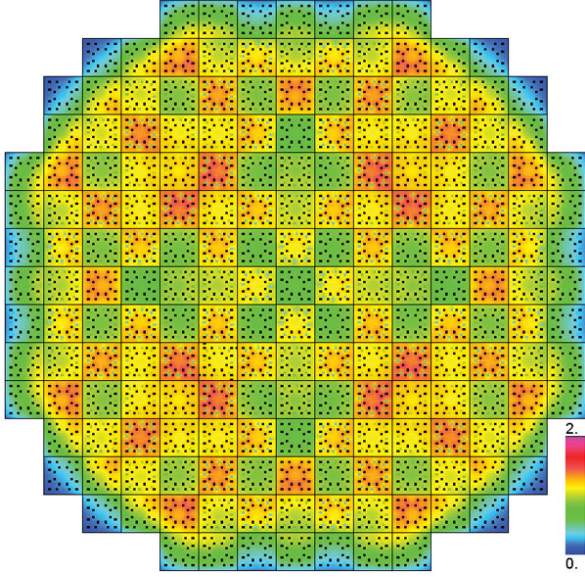


Figure 4.9: Typical power distribution in an operating KWU-type PWR (Fabry, 2014).

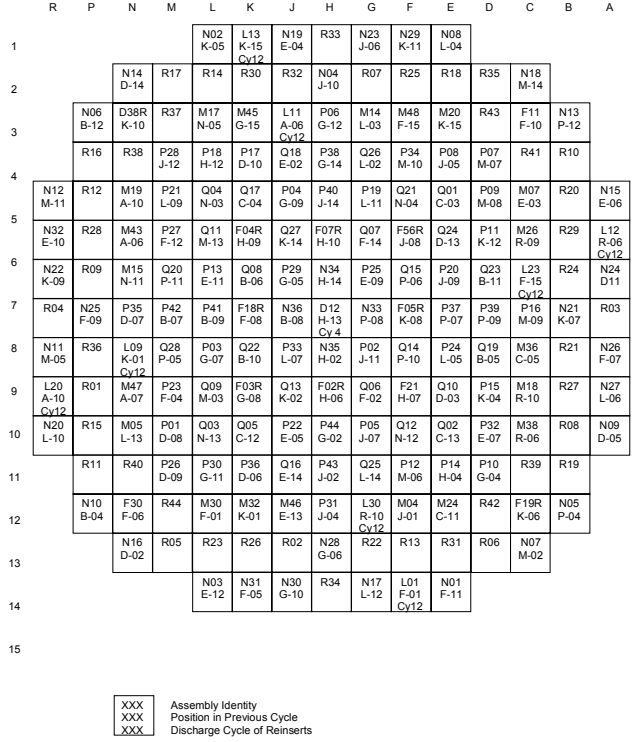


Figure 4.10: Example of a FA core loading plan (US-NRC, 2012).

deposition factor in the FR $\gamma_{\text{heat}} = 0.974$ (Todreas and Kazimi, 2012):

$$q'_{\text{ave}} = \frac{\gamma_{\text{heat}} Q_{\text{th,core}}}{n_{\text{FA}} n_{\text{FR}} l_{\text{active}}} \quad (4.8)$$

The radial factor $a_r(x)$ is the sum of two components; first, the averaged radial power factor of the respective FA $a_{r,i}$ defined by its position i in the FA row; second, the local power distribution inside the respective FA defined by the linearized lateral gradient, $g_{\text{lat},i}$. The resultant radial factor is then a function of the local cross-sectional coordinate x_i of the considered FA with origin in the FA central axis.

$$a_r(x) = a_{r,i_{\text{FA}}} + g_{\text{lat},i_{\text{FA}}} x_{i_{\text{FA}}} \quad (4.9)$$

By averaging over a large set of power distribution data, the typical radial and axial power profiles are determined. Figure 4.11a gives the defined lateral power profile over the FA row used for the analyses in the present work. When no gradients are assumed, we have $g_{\text{lat},i} = 0$. Figure 4.11b gives the defined axial power profile composed of piecewise linear functions between the spacer grid nodes.

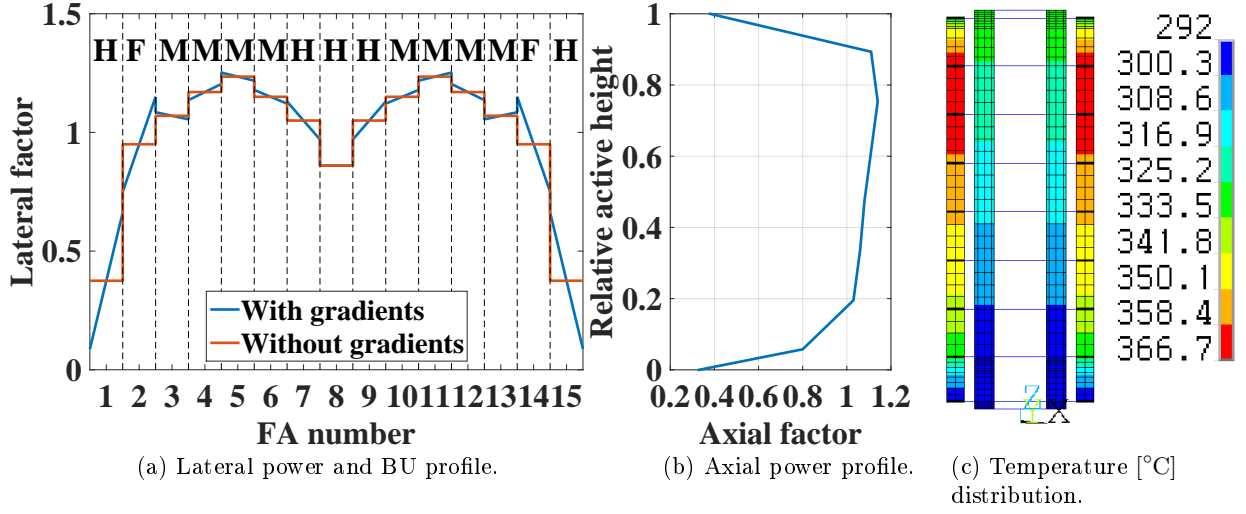


Figure 4.11: Lateral and axial distribution of the boundary conditions.

4.4.2 Burnup (BU) pattern

Over the FA row a heterogeneous BU configuration is implemented according to a typical loading pattern in the central core row. For this purpose, three different FA BU conditions are defined for the simulations: fresh (F), medium BU (M), and high BU (H). Table 4.10 gives the initial conditions for the different BU cases. For the high-BU FAs, additionally a case with UB growth is considered to account for the high scattering of FA growth at high fluences, see section 4.3.1. The table indicates the initial parameter values, which form the starting values for the different material evolution laws. The effective growth describes the combined effect of the accumulated growth reduced by the HD spring relaxation. The grid spring relaxation and gap size values indicate which grid spring state is considered according to section 4.5.1. The evolution of a decreasing grid spring force is only taken into account for fresh FAs. For FAs with higher BU, the grid spring state is assumed constant since no major influence on the FA stiffness is observed, see section 6.1.3. The BU condition used at the respective position is marked in Figure 4.11a.

Table 4.10: Initial Parameters for different BU conditions.

Case	BU [GWd/t _{HM}]	Effective growth			Grid relaxation		
		Zry-4	Advanced Alloy	law	Zr-alloy	Inconel	Evolution
Fresh (F)	0	0 mm		BE	0%	0%	decreasing
Medium(M)	15-40	0 mm		BE	99%	25%	constant
High (H)	> 40	5 mm	2.5 mm	BE	99%	25%	constant
		10 mm	5 mm	UB	99%	25%	constant

For the use in the present model, some data must be converted from BU-dependent data into time-dependent or fluence-dependent data. For this purpose, the linear heat rate q' is related to the linear mass density of heavy metal m'_{HM} in one FR:

$$BU = \frac{q'}{m'_{\text{HM}}} t = \frac{1}{c_{\phi} m'_{\text{HM}}} \Phi \quad (4.10)$$

Equation 4.11 derives m'_{HM} from equation 3.1, using the mass enrichment e_{mass} and the masses of the oxygen molecule and the Uranium isotopes. c_ϕ is defined in section 4.4.4.

$$m'_{\text{HM}} = \frac{m_{\text{fuel,column}}}{l_{\text{active}}} \frac{m_{\text{U}_{235}} e_{\text{mass}} + m_{\text{U}_{238}} (1 - e_{\text{mass}})}{m_{\text{O}_2} + m_{\text{U}_{235}} e_{\text{mass}} + m_{\text{U}_{238}} (1 - e_{\text{mass}})} \quad (4.11)$$

4.4.3 Temperature distribution in structures

FA skeleton and core structures For any structures except for the FR cladding, we can assume that the temperature is equal to that of the surrounding coolant, T_{coolant} . Heat transfer from these structures to the coolant is hence assumed to be sufficiently efficient to neglect the heat transfer to these structures from the FR cladding by conduction or radiation and the heat deposition in these structures by gamma heating and neutron scattering. To obtain the temperature in the concerned structures, the axial and radial coolant temperature profile needs to be determined. Assuming a constant specific heat capacity c_p , the axial coolant temperature profile has a sigmoidal shape in a homogeneous reactor. For a more realistic, nearly uniform power distribution, the profile approaches a linearly increasing curve. For the sake simplicity, it is assumed in this context that the mass flow rate is distributed uniformly over the core and that the coolant is heated equally in all FA radial positions. Under these conditions, it is reasonable to linearly interpolate between the core inlet and outlet temperatures T_{in} and T_{out} from the bottom to the top of the active region at the coordinates $z_{\text{active,bot}}$ and $z_{\text{active,top}}$. The following temperature conditions hold for the coolant and the FA skeleton and other core structures.

$$T_{\text{coolant}}(z) = T_{\text{in}} \text{ for } z < z_{\text{active,bot}} \quad (4.12)$$

$$T_{\text{coolant}}(z) = T_{\text{in}} + \frac{(z - z_{\text{active,bot}})(T_{\text{out}} - T_{\text{in}})}{z_{\text{active,top}} - z_{\text{active,bot}}} \text{ for } z_{\text{active,bot}} \leq z \leq z_{\text{active,top}} \quad (4.13)$$

$$T_{\text{coolant}}(z) = T_{\text{out}} \text{ for } z > z_{\text{active,top}} \quad (4.14)$$

The inner tubes in Figure 4.11c give the corresponding temperature distribution in the GTs for the coolant inlet and outlet temperatures given in Table 4.9.

FR cladding The FR cladding temperature is usually calculated based on the one-dimensional radial heat equation, neglecting the axial heat conduction (Todreas and Kazimi, 2012). To solve for the FR cladding outer temperature $T_{\text{FR,o}}$, we use the heat transfer from the FR cladding outer surface to the coolant with the heat transfer coefficient h_{th} as a Robin BC:

$$T_{\text{FR,o}}(z) = T_{\text{coolant}}(z) + \frac{q'(z)}{\pi d_{\text{FR,o}} h_{\text{th}}(z)} \quad (4.15)$$

The presence of an oxide layer at the outer surface is neglected. For the temperature at the cladding inner surface facing the fuel pellet, $T_{\text{FR,i}}$, we use the local linear heat generation rate $q'(z)$ as a Neumann BC, under the assumption that all heat is released inside the pellet:

$$T_{\text{FR,i}}(z) = T_{\text{FR,o}}(z) + \frac{q'(z)}{2\pi k_{\text{th}}(T_{\text{FR,o}}(z))} \ln \left(\frac{d_{\text{FR,o}}}{d_{\text{FR,i}}} \right) \quad (4.16)$$

To avoid the need for iterative solutions, $T_{\text{FR},o}$ is chosen as the reference temperature to determine the thermal conductivity $k_{\text{th}}(T)$ inside the cladding. Due to the good heat conductivity of Zirconium, the resulting error for the conduction term is well below 1 %. Based on equations 4.15 and 4.16, we calculate finally the approximate FR cladding average temperature $T_{\text{FR,ave}}$.

$$T_{\text{FR,ave}}(z) = \frac{T_{\text{FR,i}}(z) + T_{\text{FR,o}}(z)}{2} \quad (4.17)$$

Prior to solving equation 4.15, the heat transfer coefficient $h_{\text{th}}(z)$ must be determined. A typical procedure for this is described by Todreas and Kazimi (2012) and shortly presented here. The heat transfer coefficient is based on the Nusselt number of the bulk for fully developed flow Nu_{∞} , which in turn can be written as a function of the Reynolds and Prandtl numbers, Re and Pr . For the conditions encountered in a nuclear reactor, the well-known Dittus-Boelter correlation can be used. To account for the different geometry in rod bundles, a correction factor Ψ for square-array lattices is used. The heat transfer coefficient then reads as follows:

$$h_{\text{th}}(z) = \frac{\Psi Nu_{\infty} k_{\text{th}}}{d_{\text{hyd}}} = \frac{\Psi 0.023 Re^{0.8} Pr^{0.4} k_{\text{th}}}{d_{\text{hyd}}} \quad (4.18)$$

The outer tubes in Figure 4.11c give the calculated temperature distribution in the FR cladding for the core-averaged heat generation rate.

4.4.4 Fast neutron flux

Creep and growth experimental data are generally indicated as a function of fast reactor flux or fluence with neutron energies E_n above 1 MeV. To calculate the creep and growth rate of the different structures, the fast flux values $\phi = \phi(E_n > 1 \text{ MeV})$ must be known for the different positions in the core. Based on the fact that every fission produces an average amount of fast neutrons, we assume that the fast flux of neutrons is proportional to the power generation under steady-state conditions, using a conversion factor c_{ϕ} as proportionality constant:

$$\phi(E_n > 1 \text{ MeV}) = c_{\phi} q', \text{ with } c_{\phi} = 3 \times 10^{13} \frac{\frac{\text{n}}{\text{m}^2\text{s}}}{\frac{\text{W}}{\text{m}}} \quad (4.19)$$

The specified value of c_{ϕ} is a typical value used for fuel performance analyses, see Hales et al. (2013), for example. No decrease of the fast flux is assumed at the GT positions, which can be justified by the fact that the mean free path of a fast neutron is approximately equal to the FR pitch.

4.5 Spring relaxation models

4.5.1 Grid spring relaxation

Billerey (2005) presented calculation results for the spring force evolution at mid-grid level over BU, Figure 4.12a, which were validated by experimental measurements of the residual grid spring force, Figure 4.12b. The results were obtained taking into account three effects; first, the relaxation of the grid spring due to creep; second, the diametral creep-down of the FR cladding as a result of the pressure difference between coolant and the FR filling gas; and third, the increase of the grid strap width due to grid growth as a result

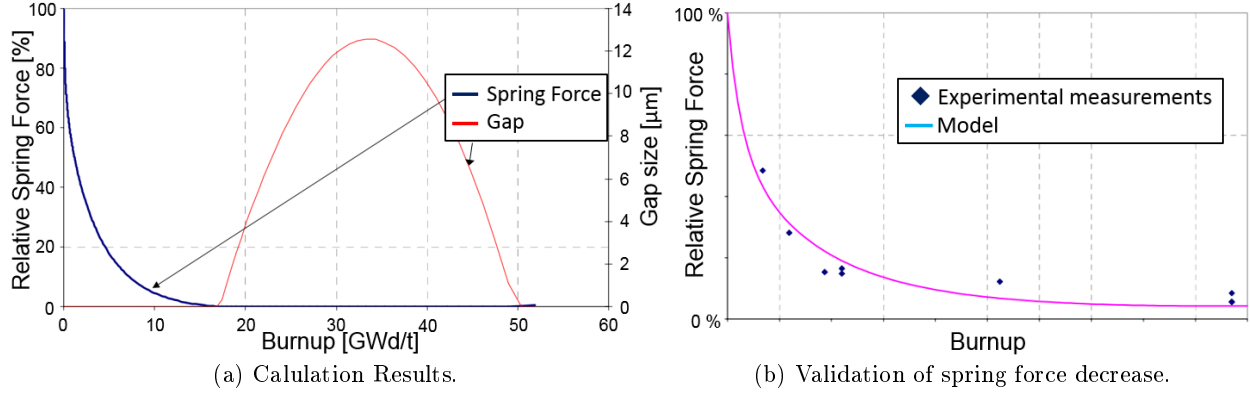


Figure 4.12: Relaxation of mid-grid spring (Billerey, 2005).

of hydrogen uptake. According to the results, the spring force relaxes after about the first cycle of operation, see the blue curve. If only creep relaxation were present, the spring force would decrease asymptotically towards zero because the relaxation rate decreases with decreasing spring force, see equation 2.51. Due to the additional effect of cladding creep-down and grid growth, a gap opens between the cladding and the grid spring, see the red curve. With increasing BU, the creep-down rate decreases because the fission gas release elevates the FR internal pressure. The maximum gap size is usually in the range of 10 μm to 20 μm . For high BUs, the gap size may decrease and finally close again due to the further increasing rod internal pressure and the swelling of the fuel, which may invert the direction of the diametral creep.

The validated model data given in Figure 4.12 are taken as a basis for the grid relaxation model in this work. For this purpose, a thorough analysis of the contribution of the different effects to the total grid spring relaxation has been made within the present project, presented by Alós Díez (2015). It was concluded that for the grid spring force decrease, the creep relaxation is the dominant process at the beginning. Only for reduced grid spring forces and relaxation rates, the relative contribution of creep-down becomes more important. The least contribution can be attributed to grid growth. Therefore, it is appropriate to represent the initial force decrease in Figure 4.12a by a creep relaxation law. In this manner, the decrease can be generalized and applied to various positions depending on local fluence and temperature. For this purpose, first the creep law representing the best fit for the model must be found. Assuming a linear relationship between BU and fluence according to equation 4.10, an irradiation creep law of the Norton-bailey type is sought for, equation 2.142. The strategy for modeling the grid spring relaxation is to decrease the compression u_{grid} of the grid springs and dimples from the initial value u_{ini} as a function of fluence. The elastic spring force data published by Billerey can be represented by a relaxation function depending on BU, $f(\text{BU})$, and the initial grid spring force $F_{\text{ini}} = k_{\text{s,n}} u_{\text{ini}}$:

$$F_{\text{grid}} = k_{\text{s,n}} u_{\text{grid}} = f(\text{BU}) F_{\text{ini}} \quad (4.20)$$

In analogy to equation 2.53, the relaxation function is given as:

$$f(\text{BU}) = y = e^{a \text{BU}^b} \quad (4.21)$$

with the two fitting parameters a and b . Since no original data could be obtained, data points were retrieved from the graph with a certain interval using graphical grabbing, see Figure 4.13. The fitting method used is a linear least-squares regression (Chapra, 2012) of equation 4.22, which represents the linearized form of equation 4.21.

$$\log_{10}(\ln(y)) = b \log_{10}(BU) + \log_{10}(a) = \beta \xi + \alpha \quad (4.22)$$

Figure 4.13 demonstrates the good fit between the obtained model function with coefficients $a = -0.64$ and $b = 0.68$ and the originally grabbed data points. The root mean square (RMS) error is given as 2.16%. In fact, the calculated exponent b lies within the value range from other RXA Zry-4 creep laws, such as those by Yvon et al. (1998) and Soniak et al. (2002).

To account for the different temperatures at the different axial grid levels, an Arrhenius term with the activation temperature obtained by Yvon et al. (1998) for Zry-4 GTs is applied, see also section 4.2.1. This is reasonable because the alloys and heat treatments used for the spacer grids in the active region are similar to those for the GTs. In accordance with section 4.4.3, the spacer grid temperature is assumed equal to the coolant temperature at the respective level, neglecting heat conduction through the contact surface between the cladding and the spring or dimples. Since the derived correlation is valid for the mid-grid position, the coolant average temperature T_{ave} is used as the reference temperature. As for the flux distribution, the axial and radial factors $a_z(z)$ and $a_{r,i}$ in equations 4.7 and 4.9 are accounted for by the model. However, only lateral variations between the different FAs are considered, that is, $g_{lat,i} = 0$. The relaxation law used in the model can hence be generalized to the following form:

$$f(BU) = e^{-C_{cr} E e^{\frac{-4700 \text{ K}}{T}} \Phi^b} \text{ with } C_{cr} = \frac{a}{E e^{\frac{-4700 \text{ K}}{T_{ave}}} (c_\phi m'_{HM})^b} \quad (4.23)$$

C_{cr} is the creep coefficient for the corresponding creep law in the form of equation 2.142.

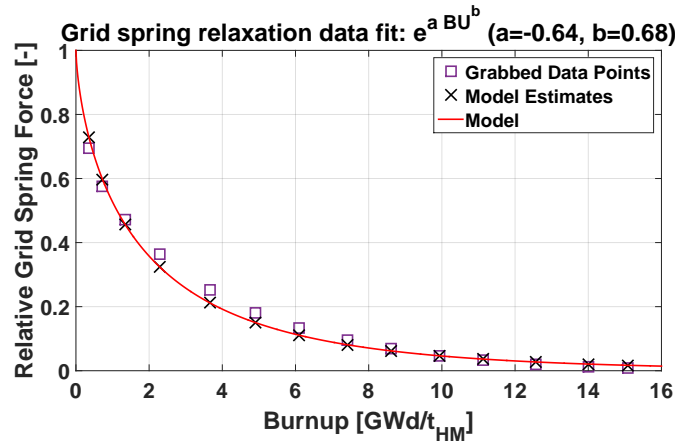


Figure 4.13: Linear least-squares regression to define creep relaxation law.

4.5.2 Holddown (HD) spring compression and relaxation

After the vessel closure in CC, the HD springs are loaded by imposing an initial downward spring displacement $\Delta u_{HD,CC,ini}$ determined by the FA height and the reactor internals geometry. In the model, $\Delta u_{HD,CC,ini}$

is chosen such that an initial HD force of about $F_{\text{HD,CC,ini}} = 7500 \text{ N}$ is generated at BOC 1 in CC. The modeling of the axial thermal expansion from cold to hot or operating conditions is treated separately for the FAs and the core structures. The evolution of the thermal strains ε^{th} of the FA structure is included in the structural solver solution. The thermal expansion of the core structures $\Delta u_{\text{th,core}}$ is calculated separately using equation 2.7. To account for the differential expansion of FA and core structure, $\Delta u_{\text{th,core}}$ is subtracted from $\Delta u_{\text{HD,CC,ini}}$, which gives the modified downward axial displacement $\Delta u_{\text{HD,ini}}$ applied on the HD device for hot or operating conditions.

$$\Delta u_{\text{HD,ini}} = \Delta u_{\text{HD,CC,ini}} - \Delta u_{\text{th,core}} \quad (4.24)$$

The HD springs are located within a certain distance outside the active core region. Therefore, the neutron fluence load is substantially decreased in comparison to other core components closer to or within the active region. Still, high-energy neutrons are able to travel far so that creep relaxation of the HD springs must be considered in the FA design to guarantee sufficient margin against FA lift-off. Therefore, highly creep-resistant alloys, such as Inconel X-750, are used, for which, however, in-reactor relaxation data are difficult to obtain. A conservative value for the estimation of the HD spring relaxation can be derived from Jeon et al. (2007), who published deterministic calculations of the minimum HD forces over three reactor cycles. The results indicate that at EOC 3 the minimum HD force is decreased by 10 %. Although the model by Jeon et al. accounts also for the minimum growth effects, it serves as a good estimate for the typical HD force decrease. Since the HD springs relax only up to about 20% during FA life, the relaxed spring compression $\Delta u_{\text{HD,relax}}$ can be approximated by a linear evolution as a function of BU and the initial HD spring displacement under operation $u_{\text{HD,ini}}$. The following relationship is assumed:

$$\Delta u_{\text{HD,relax}} = 0.1 \Delta u_{\text{HD,ini}} \frac{BU}{50 \text{ GWd}/t_{\text{HM}}} \quad (4.25)$$

The relaxation of the HD force during the calculation run is controlled based on the relaxed spring compression, that is, the relative displacement of spring nodes. To this end, the displacement constraint imposed by the upper core plate is corrected for the HD spring relaxation during the run:

$$\Delta u_{\text{HD}} = \Delta u_{\text{HD,ini}} - \Delta u_{\text{HD,relax}} \quad (4.26)$$

Chapter 5

Hydraulic Model

The flow of the coolant through the reactor core produces hydraulic pressure losses that are associated with a resistance force on the fluid due to the presence of the structure. The corresponding reaction forces generate hydraulic loads on the fuel assembly (FA) structure. Besides the principal axial flow component, also a lateral flow component exists in the reactor core due to cross-flow. Both axial and lateral hydraulic loads have a significant impact on the stress state in the FA structure and must be accounted for in the FA structural model. The calculation of the axial hydraulic forces in this work is based directly on pressure loss correlations for the axial coolant flow along the FA components. The different force terms are derived in appendix D. Unlike the axial forces, which can be derived by correlations only, the lateral forces are much more complex to determine and need to be calculated with numerical methods. Sections 1.3 and 1.4 provide a general discussion of the effects of lateral flow in the reactor core as well as a literature review over computational models designed for simulating the coolant flow distribution in the reactor. Within the present framework, the objective is not to predict the lateral hydraulic forces as accurately as possible, but to investigate the relative effect of parameter changes. Therefore, it is not necessary to create a highly detailed Computational Fluid Dynamics (CFD) model with resolved structures, but it is sufficient to design an approximate model to simulate the coolant flow path in the reactor core. To obtain an approximation of the flow field, we can resort to a porous medium approach, which has been introduced in section 2.3.3. With this approach, distributed negative momentum sources induce the pressure gradient due to the frictional and form drag effect of the structures. Consequently, the geometry of the structures does not need to be resolved anymore with a mesh so that the control volumes of the mesh can be sized much larger than when resolving the actual structure. In the present work, only a row of FAs is simulated. Therefore, we can use a structured 2D mesh composed of only rectangular cells, which further accelerates the code execution. To define the porous domain, the model must be provided with loss coefficients for the momentum sources. These coefficients must be determined previous to the model definition by means of experiments or resolved CFD simulations over the geometries of interest. For the present model, we rely on literature to obtain the necessary values.

5.1 Derivation of the loss coefficients for the porous model

For the present model, the axial and transverse loss coefficients for both rod bundle and spacer grid regions need to be determined, namely $K_{\parallel, \text{rods}}$, $K_{\parallel, \text{grid}}$, $K_{\perp, \text{rods}}$, and $K_{\perp, \text{grid}}$, which are represented schematically in Figure 5.1 with their corresponding porous rods and grid regions.

5.1.1 Axial loss coefficients

The axial loss coefficients are based on the correlations presented in appendix D. To derive the values of K_{\parallel} , we need to establish an equivalence between K_{\parallel} and the flow resistance coefficients and friction factors given in literature. Since the model is in superficial velocity formulation (see section 2.3.3), the reference velocity for K_{\parallel} is the superficial velocity whereas for the coefficients in literature the true velocity is the reference. The momentum in the streamwise direction parallel to the rod bundle axis is given based on equations 2.132 and 2.135:

$$S_{M, \parallel} = -K_{\parallel} \frac{\rho}{2} v_{\text{sup}}^2 \cos \theta \quad (5.1)$$

Integrating the distributed momentum loss $S_{M, \parallel}$ over the total area $A_{\text{total, FA}}$ and an arbitrary reference length l_{ref} gives the flow resistance force $F_{\text{res, } \parallel}$ exerted by the porous medium on the flow in this domain. Equation 5.2 stipulates that this force must equal the integrated pressure gradient $\frac{\partial p}{\partial z'}$ over the actual flow area $A_{\text{flow, FA}}$, which is derived from flow resistance coefficients given in literature. By virtue of equation 2.128, we then derive equation 5.3. Expanding equation 5.3 based on equations 5.1, 2.127, and 2.121 yields equation 5.4.

For nearly axial flow and small deformations, as they are present in nuclear reactors, we have $\cos \theta \approx 1$. $S_{M, \parallel}$ hence remains constant for the observed small variations in the angle of attack so that we can put $v_{\text{sup}} = \gamma v_{z'}$, which gives equation 5.5. Solving for K_{\parallel} yields finally equation 5.6, which describes the condition for the equivalence between the loss coefficient K_{\parallel} in superficial velocity formulation and any axial flow resistance coefficient ζ . For the case of friction, $\frac{\zeta}{l_{\text{ref}}} = \frac{f_D}{d_{\text{hyd}}}$.

$$F_{\text{res, } \parallel} = \int_{A_{\text{total, FA}}} S_{M, \parallel} l_{\text{ref}} dA \stackrel{!}{=} \int_{A_{\text{flow, FA}}} \frac{\partial p}{\partial z'} l_{\text{ref}} dA \quad (5.2)$$

$$S_{M, \parallel} = \gamma \frac{\partial p}{\partial z'} \quad (5.3)$$

$$K_{\parallel} \frac{\rho v_{\text{sup}}^2 \cos \theta}{2} = \gamma \frac{\zeta}{l_{\text{ref}}} \frac{\rho v_{z'}^2}{2} \quad (5.4)$$

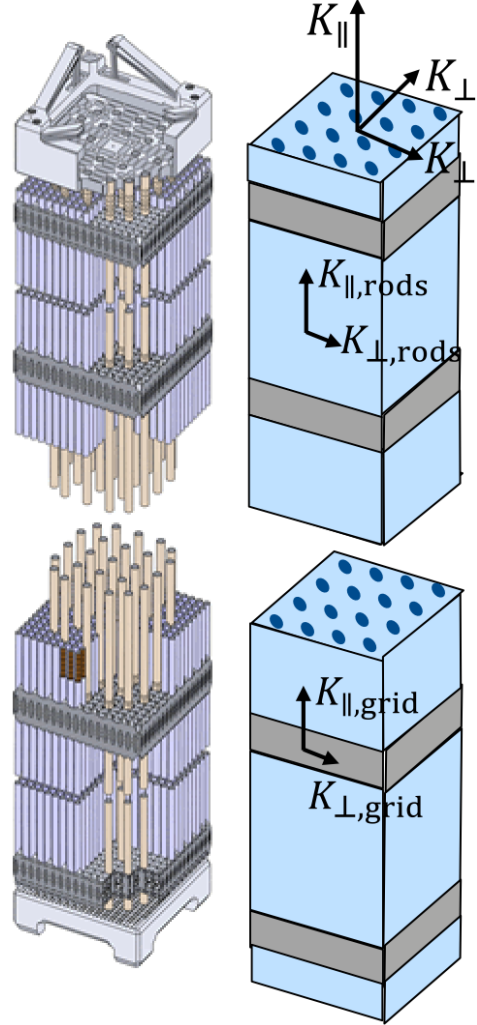


Figure 5.1: As-fabricated FA (MHI, 2016) and corresponding schematic of porous model regions with loss coefficients.

$$K_{\parallel} \frac{\rho v_{z'}^2 \gamma^2}{2} = \gamma \frac{\zeta}{l_{\text{ref}}} \frac{\rho v_{z'}^2}{2} \quad (5.5)$$

$$K_{\parallel} = \frac{1}{\gamma} \frac{\zeta}{l_{\text{ref}}} = \frac{1}{\gamma} \frac{f_D}{d_{\text{hyd}}} \quad (5.6)$$

Axial loss coefficient rods The loss coefficient due to friction of the axial flow along the rod bundle $K_{\parallel, \text{rods}}$ is calculated by inserting the McAdams correlation in equation D.7 into equation 5.6.

$$K_{\parallel, \text{rods}} = \frac{1}{\gamma} \frac{0.184 Re^{-0.20}}{d_{\text{hyd}}} \quad (5.7)$$

Axial loss coefficient grid To calculate the loss coefficient for axial flow along the grid, $K_{\parallel, \text{grid}}$, first the flow resistance coefficient per grid length, $\zeta_{\parallel, \text{grid}}/l_{\text{grid}}$, must be derived from the expression for the pressure drop over one grid in equation D.24:

$$\frac{\partial p}{\partial z'} = \frac{\Delta p_{\text{grid}}}{l_{\text{grid}}} = \frac{F_{z, \text{grid}}}{A_{\text{flow, FA}} l_{\text{grid}}} = \frac{\zeta_{\parallel, \text{grid}}}{l_{\text{grid}}} \frac{G^2}{2\rho} \quad (5.8)$$

Solving for $\zeta_{\parallel, \text{grid}}$ and inserting into equation 5.6, the loss coefficient $K_{\parallel, \text{grid}}$ for the porous model is obtained:

$$K_{\parallel, \text{grid}} = \frac{1}{\gamma} \frac{F_{z, \text{grid}}}{A_{\text{flow, FA}} l_{\text{grid}} \frac{G^2}{2\rho}} \quad (5.9)$$

Inserting the single force terms of equation D.23 we get:

$$K_{\parallel, \text{grid}} = \frac{1}{\gamma} \left(\frac{C_{\text{drag, grid}} \epsilon_{\text{grid}}}{(1 - \epsilon_{\text{grid}})^2} \frac{1}{l_{\text{grid}}} + \frac{C_{\text{drag, mv}} \epsilon_{\text{mv}}}{(1 - \epsilon_{\text{mv}})^2} \frac{1}{l_{\text{grid}}} + \frac{0.184 Re_{\text{grid}}^{-0.20}}{(1 - \epsilon_{\text{grid}})^2} \frac{1}{d_{\text{hyd}}} + \frac{C_{\text{fric, plate, turb}}}{(1 - \epsilon_{\text{grid}})^2} \frac{4n_{\text{pos}}^2 (p_{\text{FR}} - t_{\text{grid}})}{A_{\text{flow, FA}}} \right) \quad (5.10)$$

5.1.2 Lateral loss coefficients

Lateral loss coefficient rods Section 2.3.2 discussed the difficulties in establishing a reliable correlation for the resistance reduction ratio $\psi(\theta)$ to determine the loss coefficient for cross-flow in nuclear reactors. Peybernès (2005) published one of the only correlations available in literature which was specifically developed for pressurized water reactor (PWR) flow conditions and geometry. Similar to the experimental tests by Groehn (1982), Peybernès developed a correlation for the resistance reduction ratio ψ based on measurements of the pressure drop in unidirectional air flow over a PWR rod bundle in the so-called EOLE test section. The rod bundle in the test section can be inclined, thus creating unidirectional cross-flow with angles of attack from 30° to 90° . Figure 5.2 shows a picture of the EOLE test section. The particularity of Peybernès' correlation is that it has been validated with experimental tests inside a water flow loop with a FA mock-up and the possibility to inject cross-flow, the MISTRAL test section. This allows to verify the validity of the correlation in more realistic PWR flow conditions than with the EOLE test section because the flow in the MISTRAL test section features bidirectional flow and substantially smaller angles of attack, which are dominant in PWRs due to the strong axial component. In the following paragraphs, first the loss coefficient

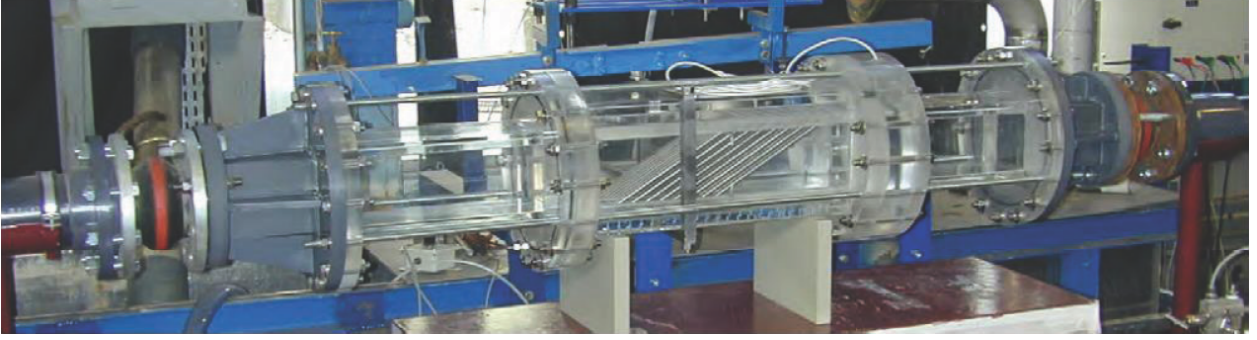


Figure 5.2: Picture of EOLE test section (Peybernès, 2005).

for the lateral flow in the porous medium model is derived from Peybernès' EOLE correlation. Then the validity of using the correlation in the framework of a porous medium model is tested by modeling the MISTRAL test section with a porous medium and comparing the simulation results with the experimental measurements. Finally, the applicability to real hot PWR operating conditions is discussed.

To establish the resistance reduction ratio $\psi(\theta)$, Peybernès defined a loss coefficient $\zeta(\theta)$ for the pressure drop over one row Δp_{row} in the test section:

$$\zeta(\theta) = \psi(\theta)\zeta_{90^\circ} = \frac{\Delta p_{\text{row}}}{\frac{1}{2}\rho v_{\text{ng}}^2} \quad (5.11)$$

with ζ_{90° being the flow resistance coefficient in cross-flow:

$$\zeta_{90^\circ} = 1.85 Re_{\text{ng}}^{-0.2} \quad (5.12)$$

Based on the measurements of the pressure drop over the rod bundle for narrow-gap Reynolds numbers Re_{ng} from 7000 to 37000 and different angles of attack in the EOLE test section, the following correlation was established for the resistance reduction ratio, henceforth called the EOLE correlation.

$$\psi(\theta) = \left(\frac{\sin \theta}{\cos \left(\frac{90^\circ - \theta}{2} \right)} \right)^{1.7} \quad (5.13)$$

The pressure gradient in the direction of the transversal flow component x' is then:

$$\frac{\partial p}{\partial x'} = -\frac{\Delta p_{\text{row}}}{p_{\text{FR}}} = -\frac{\psi(\theta)\zeta_{90^\circ}}{p_{\text{FR}}} \frac{\rho v_{\text{ng}}^2}{2} \quad (5.14)$$

Equating the transverse momentum loss term from equation 2.133 with the pressure gradient from equation 5.14, we can calculate the loss coefficient $K_{\text{rods},\perp}$ for the model input, see equations 5.15 to 5.18.

$$S_{M,\perp} \stackrel{!}{=} \frac{\partial p}{\partial x'} \quad (5.15)$$

$$-K_{\perp,\text{rods}} \frac{\rho |v_{\text{sup}}| v_{\text{sup},\perp}}{2} = -\frac{\psi(\theta)\zeta_{90^\circ}}{p_{\text{FR}}} \frac{\rho v_{\text{ng}}^2}{2} \quad (5.16)$$

$$K_{\perp,\text{rods}} \frac{\rho v_{\text{sup}}^2 \sin \theta}{2} = \frac{\psi(\theta)\zeta_{90^\circ}}{p_{\text{FR}}} \left(\frac{\delta}{\delta - 1} \right)^2 \frac{\rho v_{\text{sup}}^2}{2} \quad (5.17)$$

$$K_{\perp, \text{rods}} = \frac{\psi(\theta)\zeta_{90^\circ}}{\sin \theta p_{\text{FR}}} \left(\frac{\delta}{\delta - 1} \right)^2 \quad (5.18)$$

In equation 5.17, the velocity in the narrow gap was transformed into the superficial velocity by means of the pitch-to-diameter ratio $\delta = p_{\text{FR}}/d_{\text{FR},0}$:

$$v_{\text{ng}} = \frac{\delta}{\delta - 1} v_{\text{sup}} \quad (5.19)$$

To confirm the validity of the presented equation within the porous model environment, a model simulating the MISTRAL experimental set-up is to be created. Figure 5.3a shows the schematic set-up of the MISTRAL test section. The MISTRAL test section accommodates a FA mock-up with a 8×8 rod array. It is about 1.9 m in total height, simulating three PWR FA spans between four spacer grids, see Figure 5.3b. The generated mesh, Figure 5.3c, comprises the test section from the lower face of the bottom grid to the upper face of the top grid. The dimensions used for the mesh are summarized in Table 5.1. Since no explicit measures of the test section are given by Peybernès (2005), the typical dimensions of FAs as present in French PWRs were assumed as given, for example, in NEI (2012). To simulate the bidirectional flow in the MISTRAL test section in a porous medium environment, only a planar domain is necessary, covering the axial direction and the lateral direction in which the flow is injected. The third dimension is meshed one cell deep, thus creating a 2D model. At the bottom face of the mesh an inlet boundary condition (BC) is established based on the axial velocity values indicated by Peybernès. At the outlet a pressure BC with a static reference pressure of 0 bar is set. Over the entire left boundary of the second span, an inlet BC with a uniform normal velocity is set, representing the lateral flow injection. Over the entire right boundary of the second span, an outlet BC is set enforcing an extraction of that amount of flow that is injected laterally into the section. At all other domain boundaries, a no-slip wall BC is set up. Walls in the third dimension are represented by a symmetry BC. The reference thermodynamic state is set to ambient pressure and ambient temperature. The axial and lateral loss resistance coefficients for the rods and grid regions applied in the model are those derived in this and the previous section, equations 5.7, 5.10, 5.18, and 5.23.

Table 5.1: Geometric dimensions used for meshing the MISTRAL test section.

Geometric measure	Value
Rod outer diameter	9.5 mm
Rod pitch	12.6 mm
Section width	100.8 mm \times 100.8 mm
Grid height	40 mm
Span length	550 mm

The experimental tests in the MISTRAL test section were performed for different axial and cross-flow rates and are to be simulated with the generated porous model. The first test consists in measuring the lateral hydraulic force on the FA mock-up for different cross-flow rates, keeping the axial flow at a constant true inlet velocity of $v_{\text{ax}} = 5 \text{ m/s}$. The maximum injected cross-flow rate is $\dot{V}_{\text{lat}} = 40 \text{ m}^3/\text{h}$. In the model, this corresponds to a superficial cross-flow velocity of $v_{\text{lat},\text{sup}} = 0.2 \text{ m/s}$. For the measurements, the cross-flow injection was increased from zero to the maximum value in steps of $\dot{V}_{\text{lat}} = 5 \text{ m}^3/\text{h}$, that is, $v_{\text{lat},\text{sup}} = 0.025 \text{ m/s}$ in the model. The second test consists in measuring the lateral hydraulic force for different axial flow rates with a constant ratio between the axial flow rate and the cross-flow rate in the test section. Starting from

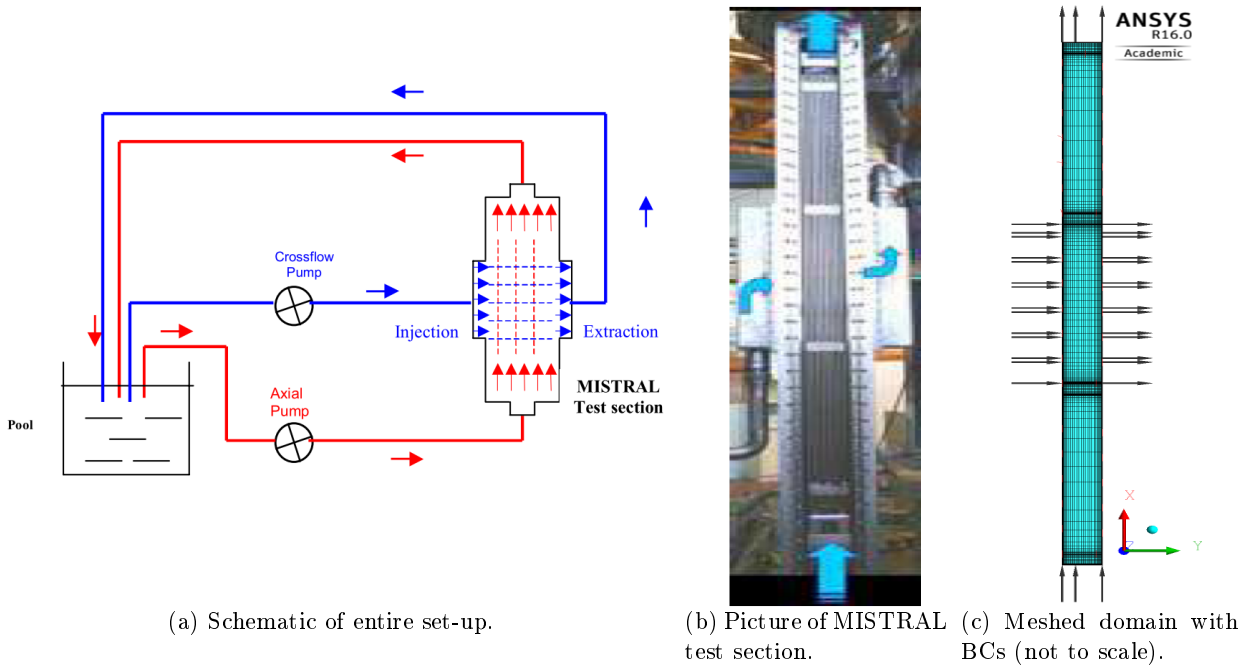


Figure 5.3: MISTRAL test section (Peybernès, 2005).

$v_{ax} = 5 \text{ m/s}$ and $v_{lat,sup} = 0.2 \text{ m/s}$, the axial and lateral inlet velocities are decreased stepwise by one fifth. Figure 5.4 compares the experimental results for the lateral hydraulic force on the FA mock-up obtained with the MISTRAL test section with the simulation results with ANSYS CFX using the EOLE correlation. Figure 5.4a gives the results for a constant axial flow rate of $125 \text{ m}^3/\text{h}$ and variable cross-flow rates. The results in Figure 5.4b are given for different axial flow rates with a constant ratio between the axial flow rate and the cross-flow rate and in the test section. The simulation results with the EOLE correlation are

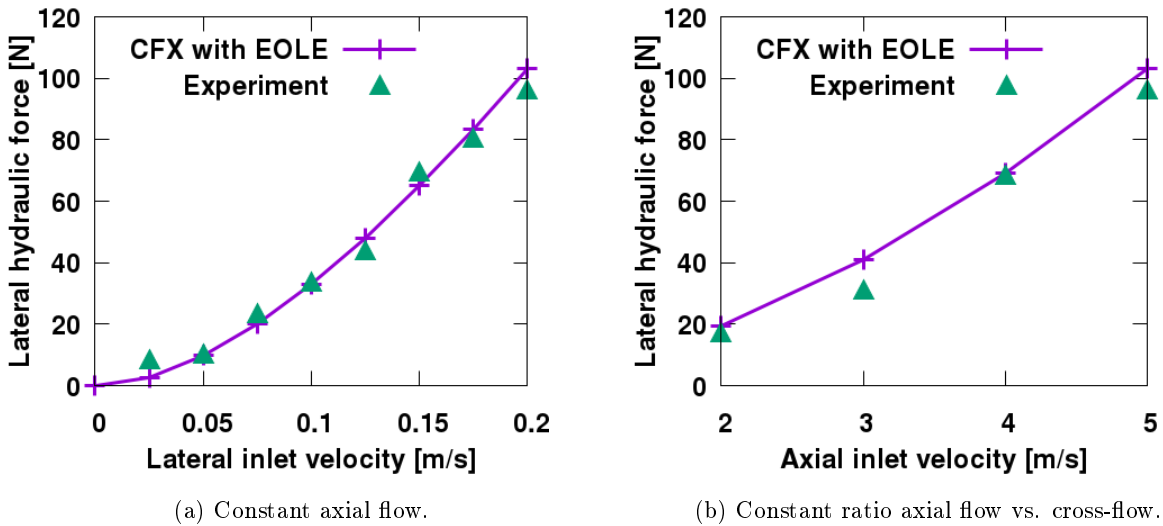


Figure 5.4: Comparison of CFX simulation results using the EOLE correlation with the experimental results with the MISTRAL test section.

in very good agreement with the experiment. This proves that the results obtained with the simple EOLE set-up, with air as medium and only one inlet and outlet, remain valid in the MISTRAL test section, which represents the flow in a PWR core much more realistically. The results demonstrate in particular that the correlation remains valid for small angles of attack. The good agreement may also be related to the fact that the flow conditions in the MISTRAL test section with a narrow-gap Reynolds number of about $Re_{ng} = 10^5$ differ not too strongly from those in the EOLE test section with Re_{ng} values up to 37 000. In PWR operating conditions, however, the narrow-gap Reynolds number may be more than one order of magnitude higher, potentially leading to diminished values of ψ according to the experimental observations of Groehn (1982). On the other hand, Bieder (2015) stated that, based on Large Eddy Simulation (LES) CFD analyses for PWR core conditions, the EOLE correlation underestimates the pressure drop by a factor of about six. This discrepancy is ascribed to the effect of the open unbounded flow in the core as opposed to the bounded flow in a test section channel. Despite these uncertainties, the EOLE correlation can be judged sufficiently reliable to provide a good estimation of the lateral pressure drop in PWR cross-flow within the present project.

Lateral loss coefficient grid LES analyses of the coolant flow through spacer grids performed by Bieder (2015) have shown that the flow leaves the spacer grid nearly vertically even if cross-flow was present when entering the spacer grid, see Figure 5.5. As an approximation, we can assume that the grid directs the flow completely into the axial direction after entering into the grid region with an arbitrary angle of attack θ . The resulting transverse force F_{\perp} is analogous to the force due to the impingement of a fluid beam on an inclined wall and corresponds to the inertial force of the fluid flow component in the direction perpendicular to the grid. Integrating the momentum equation in transverse direction, the following relation can be established for the transverse force F_{\perp} :

$$F_{\perp} = -\dot{m}v_{\perp} = -\rho|\mathbf{v}|A_{\text{beam}}v_{\perp} \quad (5.20)$$

The “beam” entering the grid cell has a cross-section of $A_{\text{beam}} = (p_{\text{FR}}^2 - \frac{d_{\text{FR},\text{o}}^2\pi}{4})\cos\theta$. Assuming that the transverse force is uniformly distributed over the volume of the grid cell in superficial formulation, $V = l_{\text{grid}}p_{\text{FR}}^2$, we can derive for the momentum source in transverse direction that:

$$S_{M,\perp} = -K_{\perp,\text{grid}}\frac{\rho}{2}|\mathbf{v}_{\text{sup}}|v_{\text{sup},\perp} = \frac{F_{\perp}}{l_{\text{grid}}p_{\text{FR}}^2} = -\frac{\rho|\mathbf{v}|v_{\perp}A_{\text{beam}}}{l_{\text{grid}}p_{\text{FR}}^2} \quad (5.21)$$

By virtue of equation 2.128 and assuming small angles, $\cos\theta \approx 1$, we have:

$$\frac{A_{\text{beam}}}{l_{\text{grid}}p_{\text{FR}}^2} = \frac{(p_{\text{FR}}^2 - \frac{d_{\text{FR},\text{o}}^2\pi}{4})\cos\theta}{l_{\text{grid}}p_{\text{FR}}^2} \approx \frac{A_{\text{flow,FA}}}{A_{\text{total,FA}}} = \gamma \quad (5.22)$$

Solving for $K_{\perp,\text{grid}}$ and applying equation 2.129, we obtain finally the following value for the transversal loss coefficient of the grid:

$$K_{\perp,\text{grid}} = \frac{1}{\gamma} \frac{2}{l_{\text{grid}}} \quad (5.23)$$

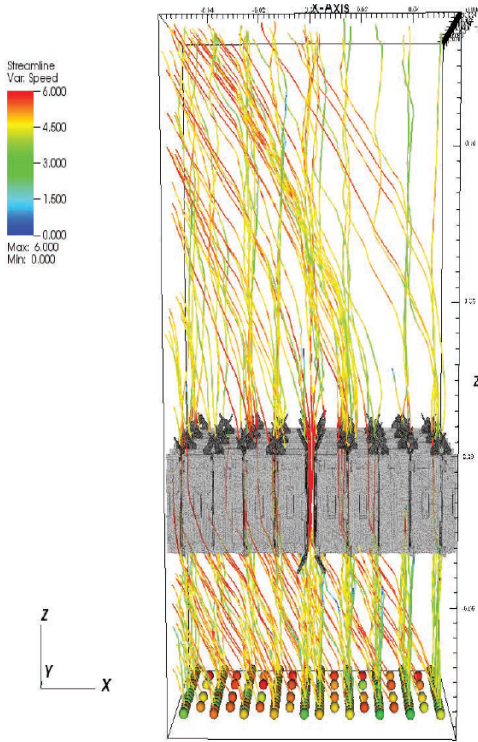


Figure 5.5: Streamlines for a LES analysis over a FA section (Bieder, 2015).

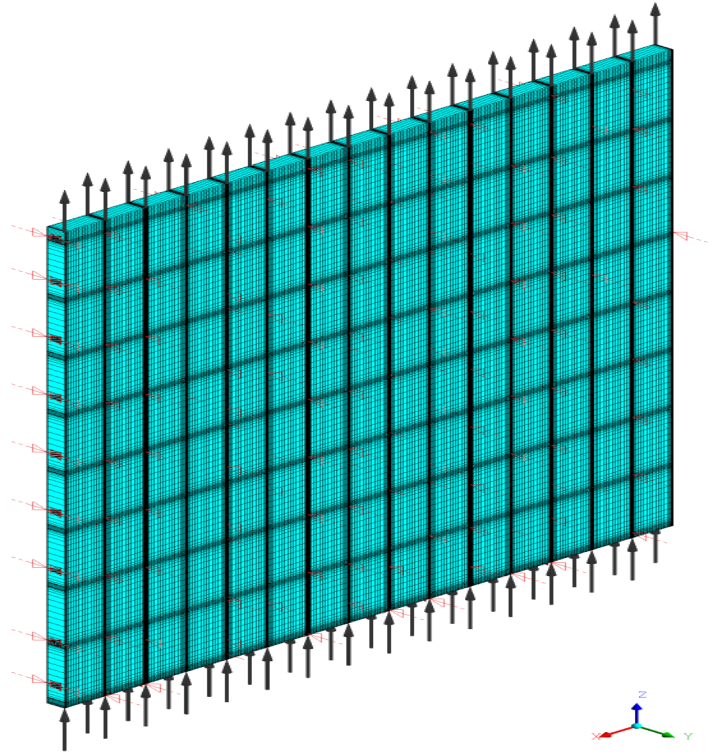


Figure 5.6: Isometric view of meshed domain. Black arrows indicate the mass flow inlet and outlet BCs and red arrows the symmetry BC.

5.2 Model pre- and postprocessing

5.2.1 Mesh and flow model

In the scope of this work, only a row of 15 FAs in the reactor core is modeled. A 2D model is hence sufficient to describe the approximate behavior of the flow over this row of FAs. Since ANSYS CFX is a 3D-only code, 2D conditions must be created artificially. To model a planar 2D geometry, a 3D mesh is created, which is only one element thick in the third direction. For the present mesh, the mesh depth is arbitrarily chosen to be 0.1 m in this direction. The entire meshed domain is based on individual meshes representing one FA each. One individual FA mesh has a width of $p_{FA} = 230$ mm. In its length, each FA mesh is composed of individual rectangular cuboids which represent either the grid region, reaching from the lower to the upper edge of one grid, or the rods region away from the grids, see also Figure 5.1.

To design the mesh, the knowledge about the expected flow conditions can be very helpful. Although the model is supposed to investigate the lateral flow inside the reactor core, we can expect the axial flow component to remain significantly larger than the lateral component due to the high mass flow rate through the PWR core. Since the main flow direction is well known, it is convenient to create a structured, hexagonal mesh to ensure that the faces of the mesh volumes are close to perpendicular to the principal flow direction, which improves the convergence behavior. This allows us to stretch the mesh volume cells along the axial

direction, that is, to create cells with a large axial-to-lateral ratio, known as aspect ratio. The overall number of cells can hence be reduced in favor of computational efficiency. Large aspect ratios also lead to a higher node density in the lateral direction, which is of specific interest for the present analysis. It is well known that meshes are to be refined in regions where large gradients are expected in order to improve accuracy. Velocity gradients are expected to be large close to the lateral and axial boundaries of the rods and grid regions. At the lateral boundaries, a region with low flow resistance will be created in order to model the influence of the inter-assembly gaps. At the axial boundaries, the flow transits from the rods region with moderate flow resistance to the grid region with comparably high flow resistance. Therefore, the mesh is gradually refined from the center of one region towards its boundaries. The final mesh describing the entire flow domain of the 15-FA row is created as a compound of 15 adjacent individual FA meshes in a row. Figure 5.6 gives an isometric view of the entire meshed domain.

The equations solved to simulate the modeled system are the Reynolds-averaged Navier-Stokes equations. The influence of turbulence is accounted for with the standard $k - \varepsilon$ model. It must be noted, however, that the additional turbulence induced by specific structural elements, such as the mixing vanes, is not modeled in the porous model. Simulation tests showed that the differences between isothermal simulations and simulations including the heat equation and a buoyancy term are sufficiently small to be neglected for the framework of this thesis. Therefore, isothermal conditions are used for all flow simulations, using the average coolant temperature T_{ave} which is defined as the arithmetic mean of the core inlet and outlet temperatures:

$$T_{\text{ave}} = \frac{T_{\text{in}} + T_{\text{out}}}{2} \quad (5.24)$$

5.2.2 Boundary conditions (BCs)

The meshed domain represented in Figure 5.6 is a cuboid with six faces, for which BCs must be applied. At the left and right faces of the domain a wall BC is applied, accounting for the fact that the FAs in the core are surrounded by the core baffle. This lateral vertical wall is set as a non-slip wall BC with smooth surface. The created mesh is, however, too coarse as to resolve the wall boundary layer so that ANSYS CFX will rely on the logarithmic wall function approximation to model the boundary layer. To create conditions equivalent to a 2D model, a symmetry BC must be applied to the front and back faces of the planar one-cell-deep mesh. Finally, the lower and upper faces serve as inlet and outlet for the coolant flow through the core. The inlet BC can be defined as normal speed BC or mass flow rate BC. When modeling also the heat generation by the FA, it is convenient to use the mass flow rate BC for both inlets and outlets which facilitates ensuring continuity. The turbulence intensity at the inlet is assumed to be 5%. For the outlet BC, a constant pressure BC is used when an open outlet is assumed. If, however, a nonuniform profile is to be imposed due to the assumed influence from the downstream flow, a nonuniform mass flow outlet BC is easier to handle than a nonuniform pressure BC. Specific nonuniform inlet and outlet BCs will be discussed in the next paragraphs.

Nonuniform core inlet profile As discussed in section 1.3, the hydraulic loads due to nonuniform core velocity inlet and outlet profiles are likely to be one of the drivers of FA bow. To simulate the cross-flow distribution in the core – and consequently obtain the lateral hydraulic forces on the FA structures – a core inlet and outlet profile must be assumed to create the associated lateral pressure gradients. A general

literature analysis about the in-reactor cross-flow and its modeling is given in section 1.4. Based hereupon, the flow profiles defined in the present section are based on the specific observations made in experimental tests and numerical simulations on the flow distribution in PWR reactor cores. Figure 5.7 gives different results for core inlet velocity profiles.

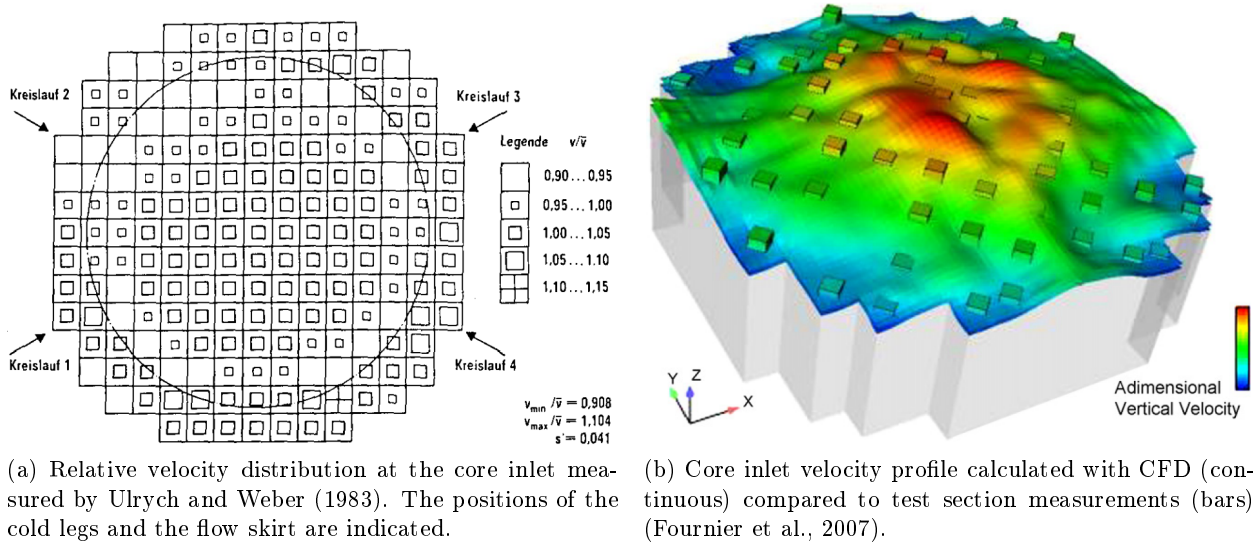


Figure 5.7: Different core inlet velocity profiles established by measurements or calculations.

Ulrych and Weber (1983) investigated experimentally the flow in Kraftwerk Union (KWU) PWRs. In their investigations, they measured the relative flow velocity at the entrance into the core after the lower core plate with a downscaled RPV mock-up which represents a KWU-type PWR with flow skirt in the lower plenum. Air was used as flow medium. Figure 5.7a shows the distribution of the inlet flow velocity. Depending on the FA position in the core, the flow inlet velocity varies $\pm 10\%$ around the mean value. In the center, a large region with inlet velocities above average develops, which is due to the flow inertia as described in the last paragraph of section 1.3. The influence of the flow skirt, which is marked by a circle in Figure 5.7a is clearly visible. In the core periphery, two regions can be distinguished: first, the region outside the flow skirt annulus, where the flow velocity is mostly above average; second, the region comprising the first FAs inside the flow skirt annulus, where the lowest velocities occur. From this region, the velocities increase gradually towards the core center. Finally, it can be observed that the flow distribution is not perfectly symmetric although all four loops are in full operation. This confirms that the distribution might depend on how the flow develops in the downcomer, which imposes an uncertainty on the flow distribution.

Fournier et al. (2007) calculated the flow in the lower core of a PWR using a CFD model with resolved structures. Figure 5.7b confirms a good agreement of the calculated core inlet profile with experimental values. The results corroborate the observations by Ulrych and Weber (1983) as for the general shape and the slight asymmetry of the flow profile. Only the flow distribution in the periphery is different from what was measured by Ulrych and Weber (1983) due to the different design of the lower plenum structures for this reactor type. Fournier et al. (2007) also state that a heterogeneous core configuration with modified flow resistance in some FAs has almost no influence on the flow under the lower core plates while it has a major influence on the lower core. This justifies using the same inlet flow profile without regard to the specific FA

designs used in the core. It is reasonable to assume that this assumption remains valid for the core outlet profile. Finally, Karoutas et al.'s (2010) CFD calculations over a quarter PWR core predict a reduction of axial velocity of approximately 15% between the core center and the periphery. This difference between the maximum and the minimum is in good agreement with what was measured by Ulrych and Weber (1983). From the results of the cited studies, a hypothetical symmetric inlet flow profile is defined for the porous medium model as a reference case, see Figure 5.8. Note that the mean value of the profile is not necessarily 1.0, which accounts for the fact that in the central row the inlet mass flow is higher than the core average. Additionally, also a possible asymmetric profile is defined. It is based on the symmetric profile, but the maximum is shifted a distance of two FA pitches. At the periphery, some adaptations are made to obtain the same mass flow as for the symmetric profile. The represented outlet profile is introduced in the next section.

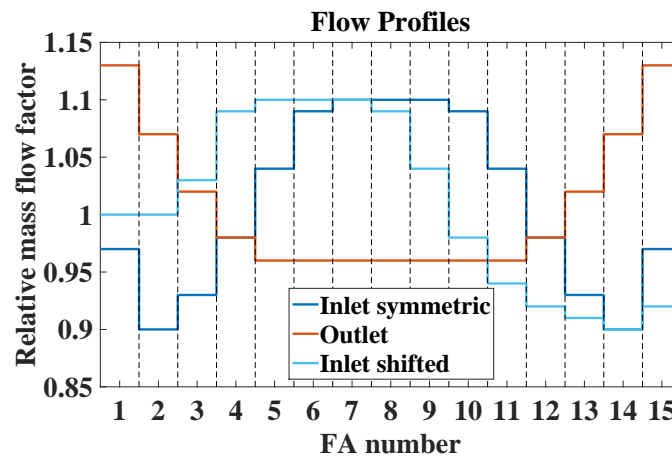


Figure 5.8: Defined relative mass flow profiles over one FA row at inlet and outlet.

Nonuniform core outlet profile As Xu et al. (2012) indicate in a CFD study about the flow in the upper plenum of an AP1000 reactor vessel, a sharp increase of lateral velocities is possible in the zone reaching from the top grid to the upper core plate due to the influence of the outlet nozzle on the upper plenum flow. At the mid-plane of the upper core plate, Xu et al.'s results, given in Figure 1.8b, show a decreasing pressure from the center of the core towards the periphery, with a minimum at the FA position closest to the outlet nozzle. An outlet flow profile is estimated based on these observations. It is evident that the flow redistribution initiated from the indicated pressure difference will lead to higher outlet flow at the periphery than in the core center. Since the results published by Xu et al. (2012) are not quantified, a similar ratio between the maximum and minimum flow as for the inlet is assumed. The influence on the axial flow profile of the support columns and the control rod channels is neglected. The flow profile assumed at the domain outlet is illustrated in Figure 5.8. The outlet mass flow is relatively uniform in the central core region but is assumed to increase gradually towards the core periphery.

5.2.3 Postprocessing

The CFD solver provides the solution for the distributed values of the unknown variables velocity and pressure. However, structural model requires as an input the distributed force on the structure. In the

porous medium model, the flow resistance imposed by the structure is modeled by defining a distributed body force on the fluid. The force on the structure is hence the corresponding reaction force. To extract the lateral forces on the FA from the porous medium model, several assumptions are made. The first assumption is that for any FA the force is uniformly distributed over the FA cross-section. For the forces on the tube bundle, this means that the load is equally distributed over all fuel rods (FRs) and guide tubes (GTs). For the grid forces, the entire flow force attacks in the grid center. The second assumption is that the force is uniformly distributed in axial direction over a rod bundle span and is a point force for the grid. Effectively, a uniformly distributed line force acts then on each FR and GT. The first assumption can easily be justified by the strong lateral coupling of the tubes at the grid levels which would, in any case, lead to a load distribution over the FA cross-section. The second assumption represents an approximation since a modification of the axial points of attack has an effect on the bending moment created in the FA tubes, but is justified by the nature of the results presented in section 5.3. These assumptions allow to extract the lateral force on the structure in a certain rods or grid region by integrating over lateral the body force $f_{B,x}(x, z)$ in this region given by the CFD model solution. In this manner, the lateral force on each defined region is obtained.

$$F_{x,i,k,\text{grid}} = \int_{V_{i,k,\text{grid}}} f_{B,x}(x, z) dV \quad (5.25)$$

Equation 5.25 calculates the force on the k -th grid of FA i and is directly applied on the corresponding central grid node in the structural model. In turn, the lateral loads in the rods region must be applied as a distributed line force on all FRs and GTs. According to the second assumption, this line force $f_{\text{lin},x,i,k,\text{rods}}$ is obtained by equally distributing the integrated force $F_{x,i,k,\text{rods}}$ over all n_{pos}^2 tube positions and the length l_k of the respective span minus the grid length l_{grid} .

$$f_{\text{lin},x,i,k,\text{rods}} = \frac{\int_{V_{i,k,\text{rods}}} f_{B,x}(x, z) dV}{n_{\text{pos}}^2(l_k - l_{\text{grid}})} \quad (5.26)$$

Below the first and above the ninth grid, only the GTs are accounted for since the FRs in the model are assumed to reach from the first to the last grid only.

To estimate the effect of the flow on the FA structure, the lateral hydraulic force is an inappropriate measure because the lateral FA deformation strongly depends on the point of attack. Forces which attack more centrally will induce higher bending moments, and therefore an increased deflection, than forces which attack closer to the extremities. To better estimate the effect on the FA deformation, the concept of the “equivalent force” is defined. For this purpose, we assume the FA as a simple Euler-Bernoulli beam clamped at its extremities, see Figure 5.9 (Wittenburg and Richard, 2012). Then, we consider the maximum deflection $u_{x,\text{max}}$ caused by the force F applied at a distance a from the further extremity and a distance b from the closer extremity with $b = l - a$:

$$u_{x,\text{max}} = \frac{2}{3} \frac{F a^3 b^2}{EI l^2} \left(\frac{1}{1 + \frac{2a}{l}} \right)^2 \quad (5.27)$$

Finally, we calculate the centrally applied equivalent force which is necessary to obtain the same deflection:

$$F_{\text{eq}} = \frac{192EI u_{x,\text{max}}}{l^3} = \frac{128F a^3 b^2}{l^5} \left(\frac{1}{1 + \frac{2a}{l}} \right)^2 \quad (5.28)$$

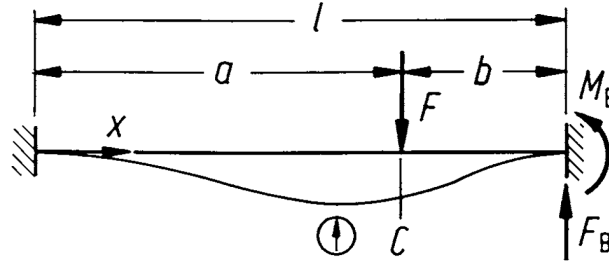


Figure 5.9: Schematic of the loading of a doubly-clamped beam with a force F (Wittenburg and Richard, 2012).

The sum of lateral forces on all rods and grid regions of FA i results in the total lateral hydraulic force:

$$F_{x,i} = \sum_{k=1}^{n_{\text{grid}}} F_{x,i,k,\text{grid}} + \sum_{k=1}^{n_{\text{grid}}+1} F_{x,i,k,\text{rods}} \quad (5.29)$$

The total equivalent force is given as:

$$F_{\text{eq},i} = \sum_{k=1}^{n_{\text{grid}}} F_{\text{eq},i,k,\text{grid}} + \sum_{k=1}^{n_{\text{grid}}+1} F_{\text{eq},i,k,\text{rods}} \quad (5.30)$$

5.3 Analysis of model results

5.3.1 Uniform inlet and outlet profiles

First, the results with a uniform mass flow at the inlet and outlet are presented. The inlet mass flux is chosen equal to the average mass flux obtained with the inlet profiles presented in Figure 5.8 to create comparable conditions. The plot in Figure 5.10 shows that the axial velocity is roughly constant inside the FA bundles. In the gaps between the FAs, the flow is accelerated due to the lower flow resistance. Substantially higher than average velocities can be observed especially in the gaps between the spacer grids, where the red color indicates velocities between $v_z = 5.5$ m/s and the maximum of $v_z = 7.12$ m/s whereas the average velocity in the domain is about $v_z = 4.9$ m/s. The legend limits do not represent the minimum and maximum values but were defined for an optimal representation of the results. The flow redistribution towards the gaps can also be observed in the plot representing the lateral velocity in the calculated domain, Figure 5.11a. It is particularly visible from the bottom up to the second spacer grid. At the first spacer grid level, but also in the following span, a flow towards the closest gap is clearly noticeable in the fuel bundles. The same effect is visible close to the wall gaps and the outlet and, to a lesser extent, at all spacer grid gaps. Apart from these regions, the lateral velocity is zero since no other lateral gradients exist. Again, the minimum and the maximum of the legend were redefined for better clarity. The actual minimum and maximum

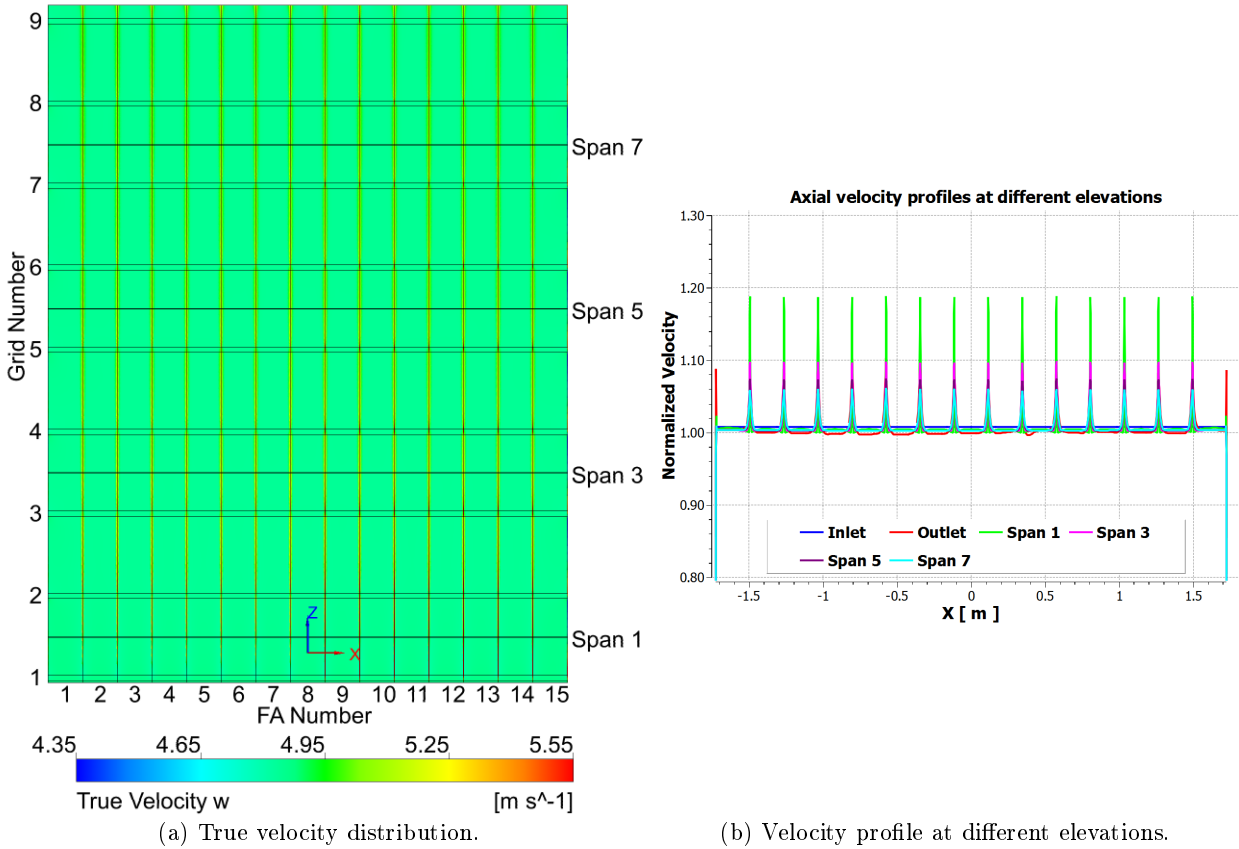


Figure 5.10: Axial velocity for uniform inlet and outlet profiles.

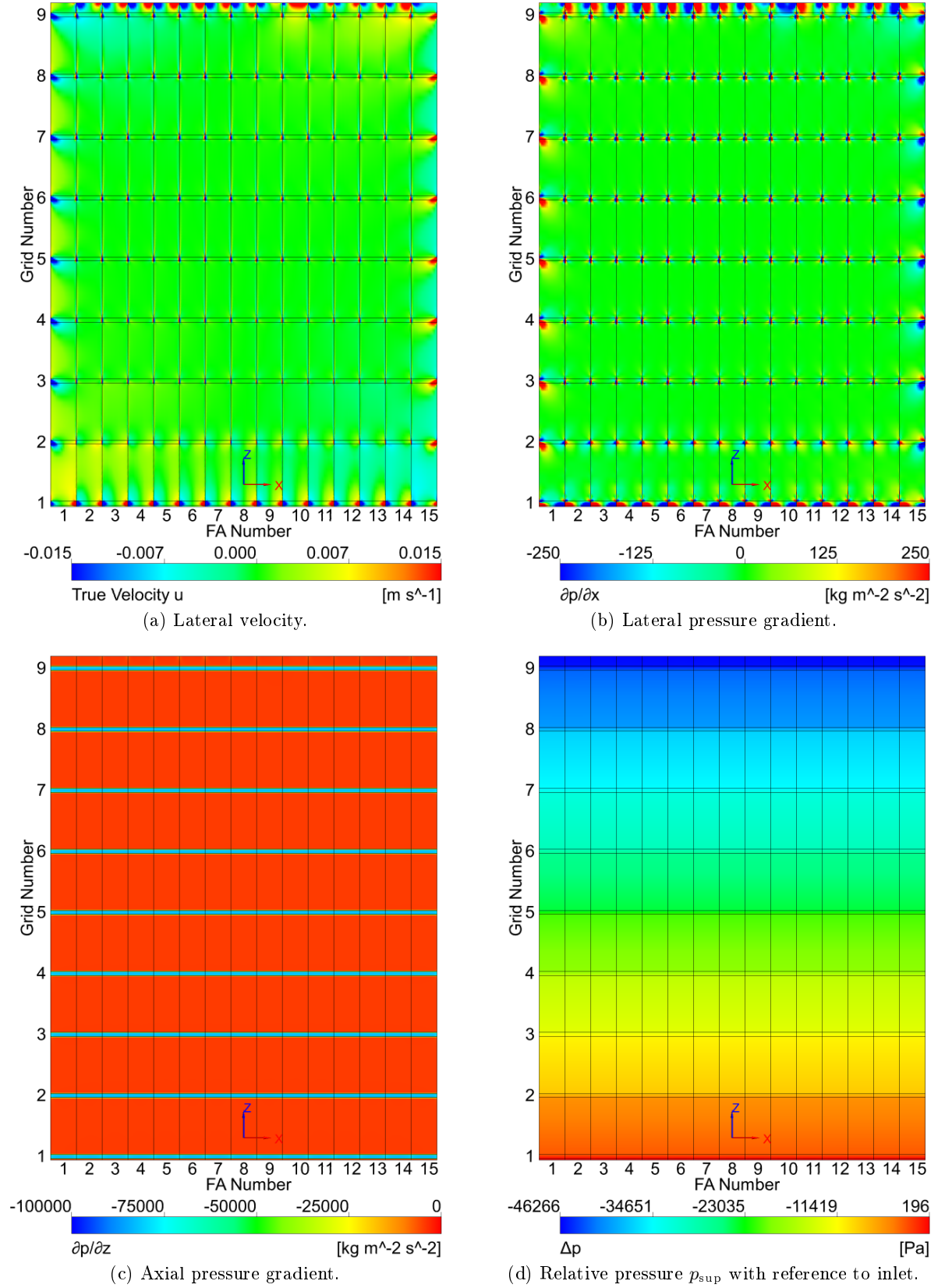


Figure 5.11: Pressure gradient plots for uniform inlet and outlet conditions.

is $v_x = \pm 0.076 \text{ m/s}$. The flow redistribution is the result of locally increased values of the lateral pressure gradient near the FA gaps, particularly at the grid levels, see Figure 5.11b. In Figure 5.11c the axial pressure gradient is plotted over the entire domain. In this plot, we see very well the higher flow resistance in the nine spacer grid regions, where the gradient is about $\partial p_{\text{sup}}/\partial z = -82\,500 \text{ Pa/m}$ whereas in the rods regions it is about $\partial p_{\text{sup}}/\partial z = -4500 \text{ Pa/m}$. Figure 5.11d shows additionally the pressure drop Δp_{sup} with reference to the domain inlet. Since the gravity term was omitted in the momentum equation, the hydrostatic pressure is not accounted for.

5.3.2 Symmetric inlet and outlet profiles

When using the symmetric inlet and outlet profiles presented in Figure 5.8 as BC, both pressure and velocity distributions in the entire domain change. As for the axial velocity in the domain, Figure 5.12, the initially marked profile becomes uniform towards the center of the core. Figure 5.12b shows the velocity profiles at the inlet and outlet as well as at different elevations. In the middle of the core, in the span between 5th and 6th spacer grid, the profile is practically uniform over the FA row cross-section. Somewhat upwards, the influence of the outlet becomes visible. We can derive that the inlet and outlet BC do not affect each other but can be seen as independent for the considered profiles. The redistribution of the flow in the core due to the influence of the outlet only starts at roughly the elevation of grid level 7. As a result of the non-uniform axial velocities, the pressure distribution in the entire domain will change. The first effect is

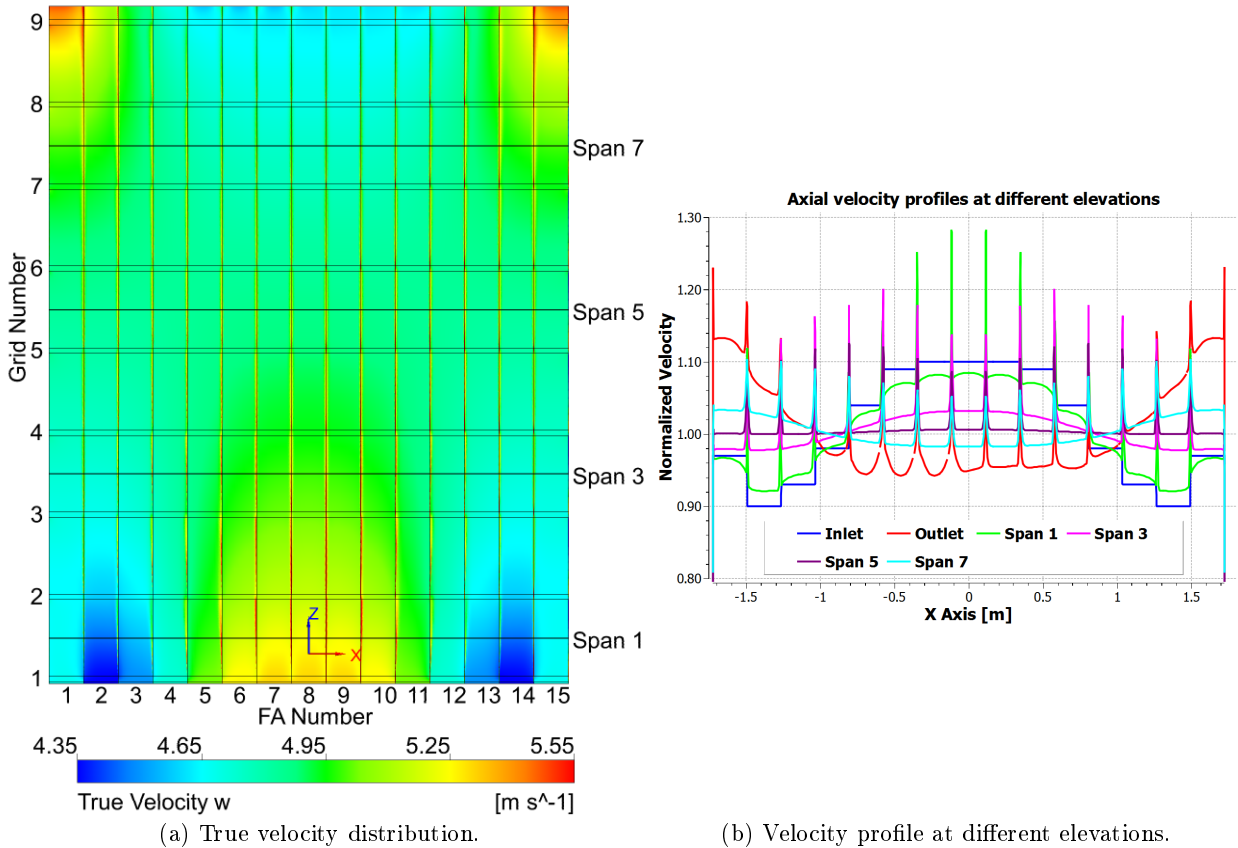


Figure 5.12: Axial velocity for non-uniform symmetric inlet and outlet profiles.

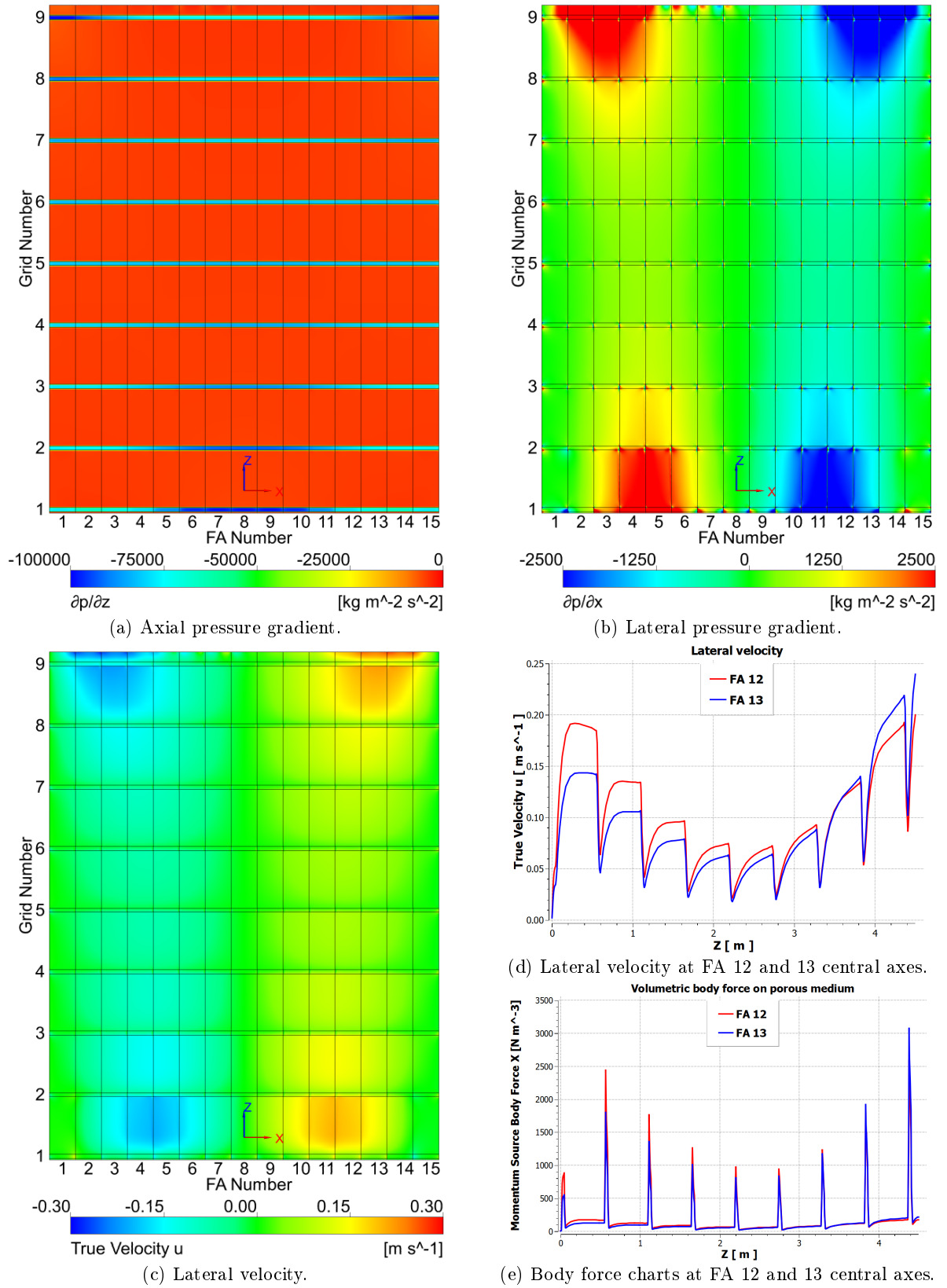
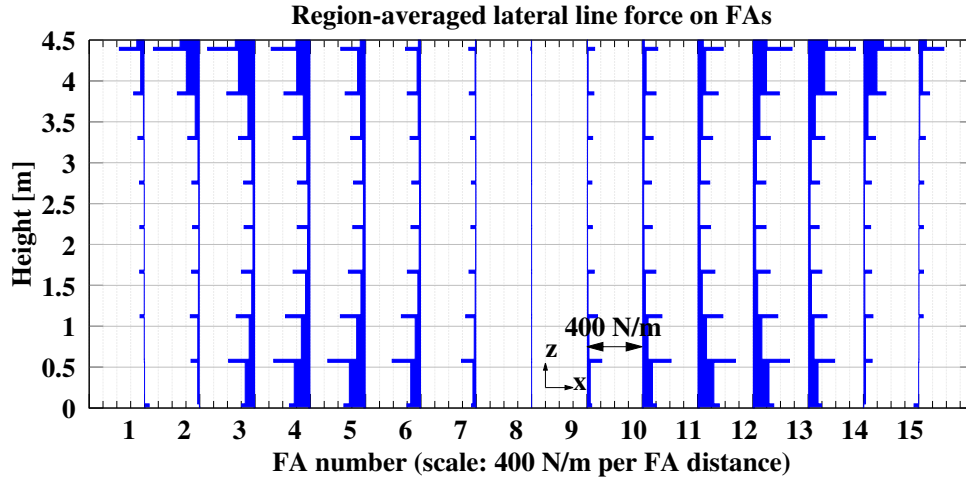
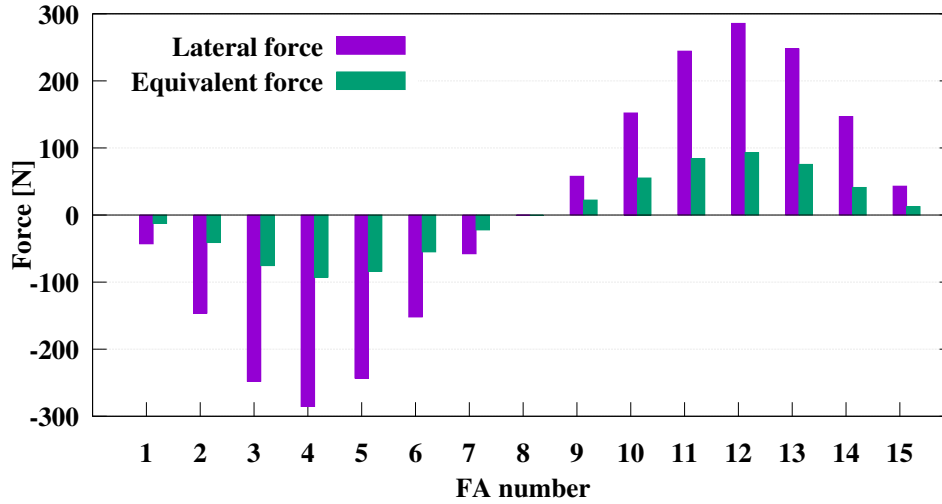


Figure 5.13: Flow solution for non-uniform symmetric inlet and outlet profiles.



(a) Distribution of region-averaged lateral line forces over the single FA spans and grids. The distance between two FAs in the plot corresponds to 400 N/m.



(b) Total force and equivalent force on each FA.

Figure 5.14: Hydraulic forces on FAs for non-uniform symmetric inlet and outlet profiles.

that the axial pressure gradient changes with the lateral position due to different velocity heads over the FA row, see Figure 5.13a. The second effect is the occurrence of significant lateral pressure gradients over several FAs, as opposed to local lateral pressure gradients in the proximity of the FA gaps, see Figure 5.13b. Note that the legend limits have been redefined compared to Figure 5.11b. It can be noticed that the lateral pressure gradients are maximum near the domain inlets and outlets at those positions at which also the mass flow gradient is highest. Then the lateral gradients decrease towards the core center. This is due to the redistribution of the flow as a result of the pressure gradient. The redistribution becomes apparent when considering the lateral velocity distribution in the domain, Figure 5.13c. The lateral velocity is highest where the highest lateral gradients occur; however, it decreases suddenly at the grid levels, where the lateral flow resistance is so high that the flow is redirected in axial direction. After the grid, the lateral flow redevelops from nearly zero until it reaches its maximum before the next grid level. This behavior is illustrated in Figure 5.13d, in which the lateral velocity along the central axes of FAs 12 and 13 is plotted. The absolute

maximum is somewhat above $v_x = 0.25$ m/s near the outlet. In the lower core, it reaches values of about $v_x = 0.20$ m/s.

For FAs 12 and 13, Figure 5.13e shows the lateral component of the user-implemented volumetric body force representing the porous medium. The force in the rods regions tends to be higher at the top of one span than at the bottom as a result of increased lateral flow at the top; however, the difference is small enough to assume a uniformly distributed force over each span. This facilitates extracting the force from the fluid model and imposing it on the structural model. Also, the assumption of a discrete point force at the grids is justified by the peaks at the grid levels. Figure 5.14a gives the corresponding distribution of line forces over each FA obtained from the postprocessing described in section 5.2.3. This distribution serves as the data source for the lateral hydraulic forces in the structural model. Figure 5.14b finally compares the total lateral force on each FA with the equivalent force. Due to the concentration of the line forces close to the FA extremities, the equivalent force is only less than half the total force for most FAs.

5.3.3 Asymmetric inlet and symmetric outlet profiles

Figure 6.20 gives, for comparison with the symmetric case, the solution of the flow field for the case with the shifted, asymmetric inlet profile and unmodified symmetric outlet profile. The axial velocity distribution and profiles in Figure 5.15a and 5.15b demonstrate that the symmetry is broken in the lower core due to the asymmetric inlet. Furthermore, the redistribution of the flow due to the inlet gradient has not finished before the influence of the outlet sets in at grid level 7 since the number of FAs over which the flow must be redistributed in one direction is increased. The resulting lateral pressure gradients are plotted in Figure 5.15c. Due to the shifted profile, the pressure gradient absolute values to the left of the profile maximum are significantly decreased while to the right higher values than before are observed. It can be noticed that the region with a lateral pressure gradient of -2500 Pa/m and below grew significantly, particularly towards the center of the core. In the lower core, the lateral velocity reaches values of about $v_x = 0.26$ m/s at the right and about $v_x = 0.10$ m/s at the left, see 5.15d. The flow conditions at the outlet are nearly unchanged. The lateral forces on the porous medium are represented in Figure 5.16. As opposed to the symmetric case, the symmetry is clearly broken. Since the redistribution of the flow has not terminated in the lower core, the forces in the center of the core are significantly higher, see Figure 5.16a. This increases both the total lateral forces and the ratio of equivalent force and total force at the right side of the domain while it decreases at the left, see Figure 5.16b. An increase in the amount of flow to be redistributed has hence a twofold detrimental effect on the FA structures at the right. Not only the total lateral force increases, but also the effect on the FA structure is increased more than linearly due to a redistribution of forces towards the axial center.

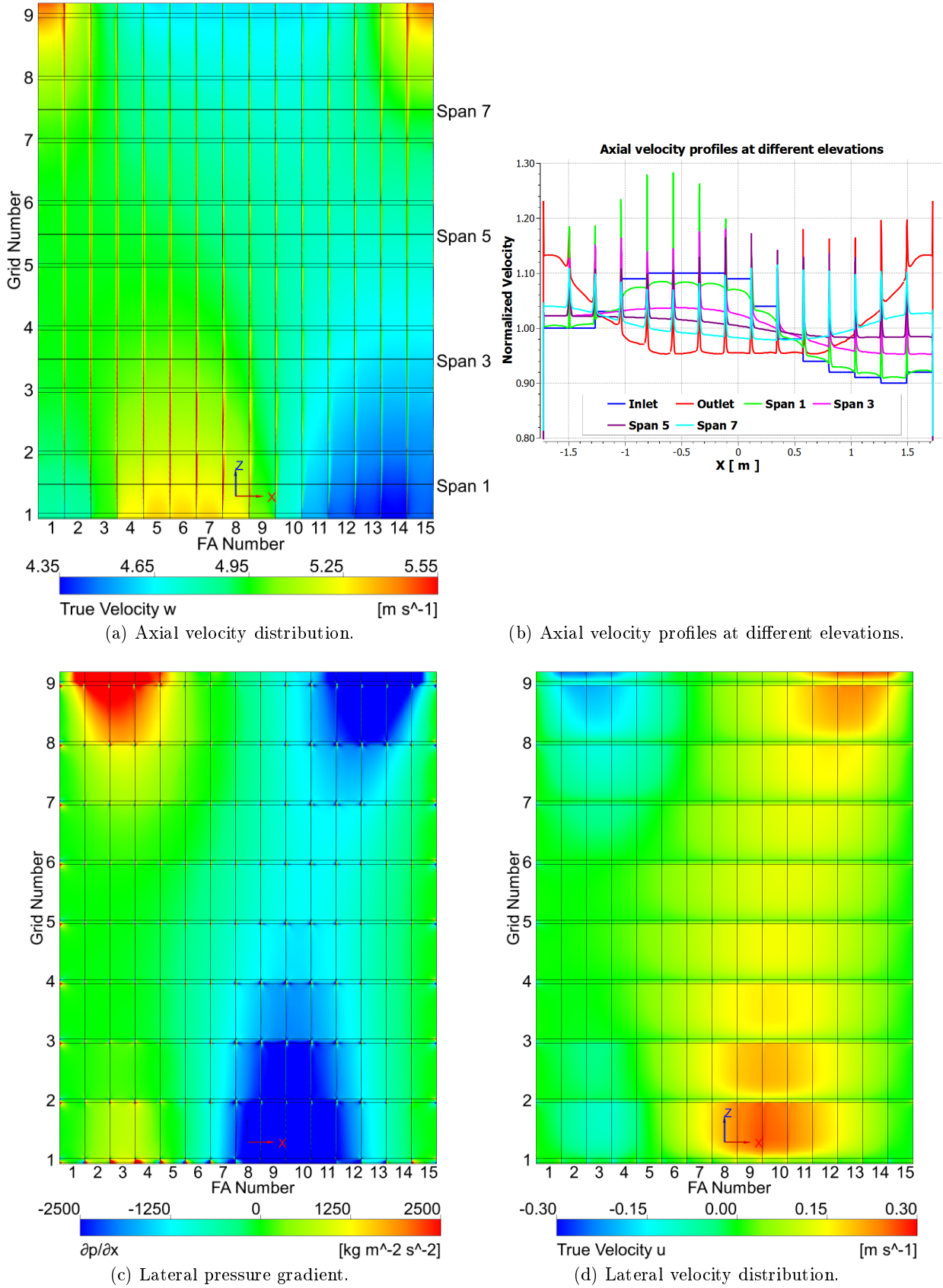
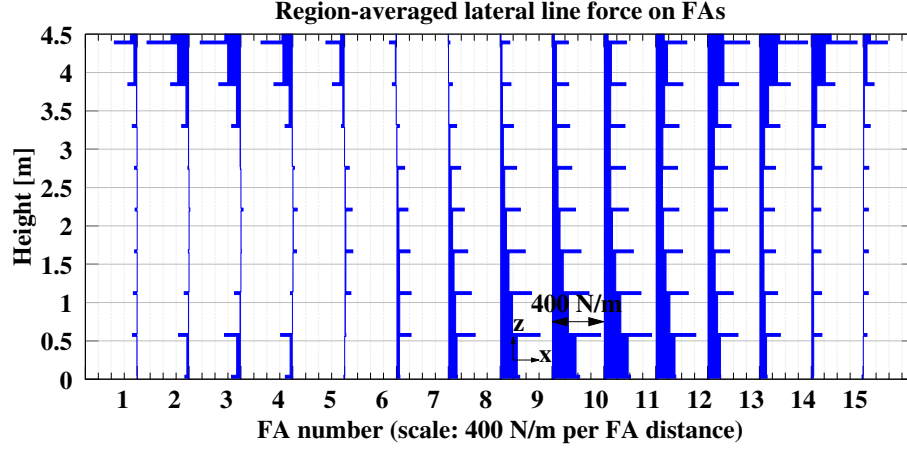
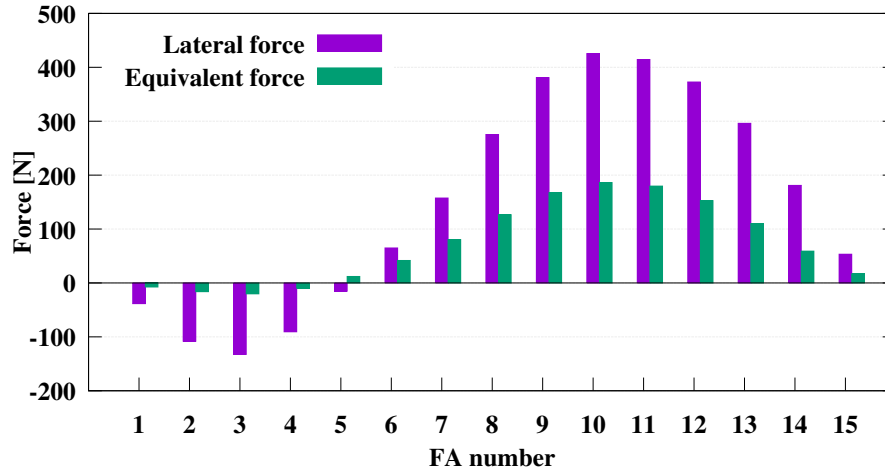


Figure 5.15: Flow solution for shifted, asymmetric inlet profile and symmetric outlet profile.



(a) Distribution of region-averaged lateral line forces over the single FA spans and grids. The distance between two FAs in the plot corresponds to 400 N/m.



(b) Total force and equivalent force on each FA.

Figure 5.16: Hydraulic forces on FAs for shifted, asymmetric inlet profile and symmetric outlet profile.

5.4 Fluid-structure interaction (FSI)

FSI effects in the reactor core have a non-negligible influence on the FA bow response, see section 1.4. Therefore, a two-way fluid-structure coupling has been established to account for the feedback of the FA structural deformation on the coolant flow. Figure 5.17 gives a flow chart of the implemented coupling procedure. Initially, in the zeroth load step at time $t_0 = 0$ h, the flow field is calculated with the hydraulic ANSYS CFX model based on the undeformed structure. Then, the structural calculations over the first load step are performed with ANSYS Mechanical APDL. Since no dynamic effects such as FA vibrations are considered, the FA structure deforms only slowly so that an explicit coupling approach is the most efficient. This means that the modified hydraulic loads are updated at the end of each structural solver load step at time t_n ; however, no iterations are performed to obtain a tight convergence between the flow field and the structural deformations. In contrast, an implicit coupling would provide a fully converged solution at time t_n (Benra et al., 2011; Busch, 2012). The load transfer from the fluid to the structure was described

in section 5.2.3. To obtain a two-way coupling, the displacement transfer from the structure to the fluid needs to be incorporated into the model as well. This is done by adapting over time the position and size of the gaps, grid and rods regions in the modeled domain according to the FA structural deformation. Ruiz Antón (2016) presented the details of the displacement transfer and first results. FA bow calculation results including the fluid-structure coupling are presented in section 6.3.6.

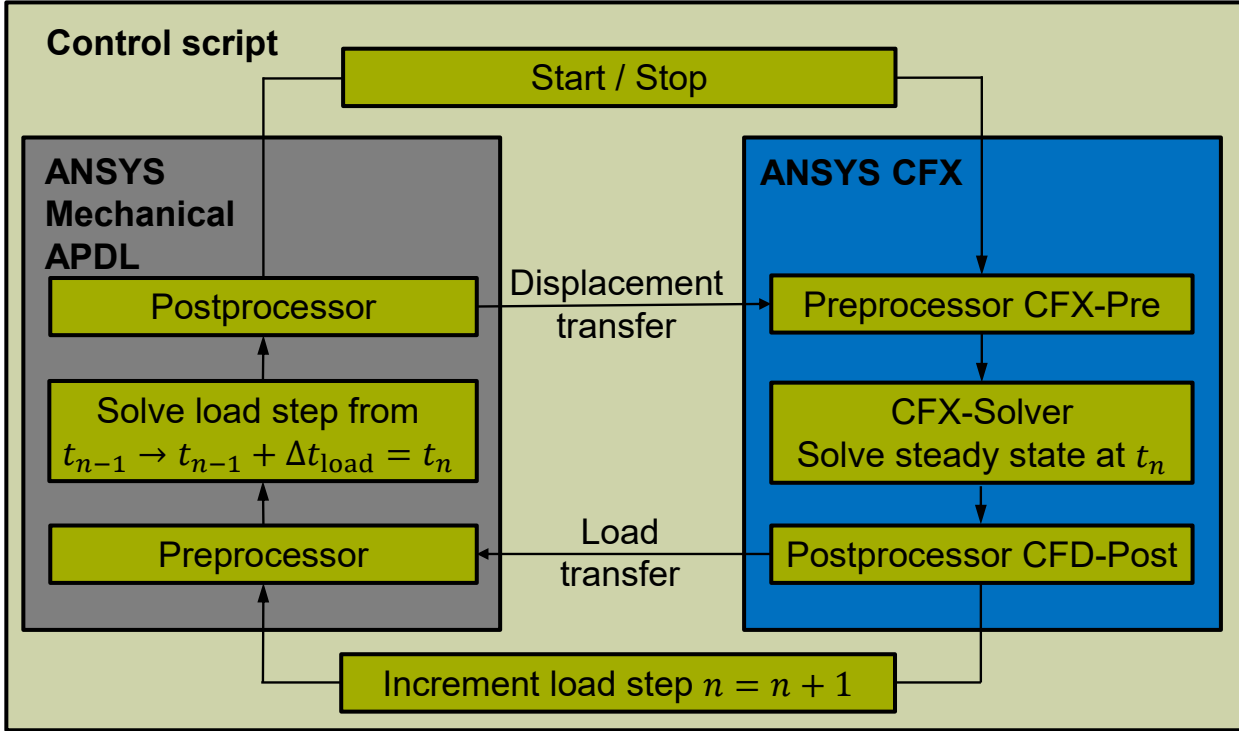


Figure 5.17: Flow chart of implemented explicit two-way fluid-structure coupling procedure.

Chapter 6

In-Reactor Simulation Results and Sensitivity Analyses

6.1 Single-FA deflection tests

The objective of this first analysis part is to focus on the effects of the reactor conditions and the irradiation environment on the fuel assembly (FA) structural behavior. This means that the corresponding hydraulic loads, thermal loads and the effects of neutron irradiation described in the two previous chapters 4 and 5 are imposed on the model. So far, no creep, relaxation, or growth calculations are performed, but the objective is to investigate the FA structural performance for different operation and burnup (BU) states.

As a first step, the axial stress state of the different FA components for different reactor conditions is investigated, in particular during start-up. Since the axial stresses can have an important influence on the FA stiffness due to the stress stiffening effect, this analysis facilitates the comprehension of the impact of the different operation states on lateral stiffness. Correspondingly, the second part of this section consists in predicting the lateral FA stiffness performance by means of the same lateral deflection test as described in section 3.5, but under reactor conditions. In the last part of the section, a screening sensitivity analysis as described in appendix E is performed, investigating the sensitivity of the FA stiffness to different FA structural parameters for different BUs and operating states.

6.1.1 Definition of operation and BU states

Six different simulation cases are established to define the underlying operation and BU states for the subsequent analyses, see Table 6.1. The first focus, cases 1 to 3, lies on the different start-up conditions that a fresh FA undergoes before reactor operation, which are described in section 4.1.1. Fresh FAs are those operating in their first cycle in the reactor at their beginning of life (BOL). For these FAs, the structural response in cold condition (CC), hot condition (HC), and under operation at beginning of cycle (BOC) 1 is investigated. To better appreciate the different contributing effects, the axial hydraulic flow forces are only accounted for in the operation state, but not in cold and hot conditions.

Table 6.1: Simulation cases with constant parameters for different BU conditions.

Case #	BU state	BU [GWd/t _{HM}]	Effective growth	Grid relaxation		Gap size	Axial flow
				Zr-alloy	Inconel		
1	BOL CC	0	0 mm	0	0	0 μ m	no
2	BOL HC	0	0 mm	0	0	0 μ m	no
3	BOL (BOC 1)	0	0 mm	0	0	0 μ m	yes
4	BOC 2 to EOC 3	15-40	0 mm	99%	25%	0 μ m	yes
5			0 mm	100%	25%	12 μ m	yes
6	EOL	> 40	15 mm	99%	50%	0 μ m	yes

The FAs represented by cases 4 and 5 exhibit medium BUs ranging from about 15 GWd/t_{HM} to 40 GWd/t_{HM}, that is, approximately from BOC 2 to end of cycle (EOC) 3. In this BU range, the effect of the neutron fluence on the FA structural stiffness is approximately constant. The grid springs are practically relaxed for all Zirconium alloy grid levels and the first growth stage has practically saturated so that only moderate changes in growth can be expected. The axial guide tube (GT) growth rate is approximately compensated for by the holddown (HD) spring relaxation rate. Hence, the effective growth rate is zero and no change in HD force is assumed. However, it is difficult to predict the grid spring state in this medium BU range. The fact if a small grid spring residual force remains or a gap opens depends mostly on the local creep-down of the fuel rod (FR) cladding, which is difficult to determine. To verify the sensitivity to a potential gap opening, two cases are tested: case 4, in which the grid spring relaxation for all Zr-alloy grids is 99%, and case 5 with only open gaps of 12 μ m.

Case 6 represents high-BU FAs approaching their end of life (EOL) with BUs greater than about 40 GWd/t_{HM}. For these FAs, growth rates gradually increase, which might have a non-negligible effect on FA stiffness by means of the HD force. In certain cases, breakaway growth with high linear growth rates is also observed, possibly giving rise to significant deformations due to the build-up of excessive of HD forces. To account for the combined effect of GT growth, HD spring relaxation, and the axial compressive creep of the GTs, an effective growth of 15 mm is assumed. This value is composed of an upper bound (UB) growth of Zry-4 at EOL of 20 mm, see Figure 4.7, and a HD spring relaxation and GT compressive creep of in total 5 mm. As for the grid spring, a residual force of 1% is assumed since for high BU it is likely that a possible FR-spring gap closes again due to the increasing FR internal pressure as a result of fission gas release.

6.1.2 Investigation of axial stress states

In this section the distribution of axial stresses in the GTs and FRs for different reactor conditions is investigated. For a better visualization only two GTs and two FRs are shown in the plots in Figure 6.1, one for each FA half. Since no lateral loads are imposed, the stress distribution is symmetric about the FA z-axis for the represented cases. The ratio between height and width is reduced by a factor of 4 and the GT and FR diameters are increased by a factor of 2. The spacer grids are marked by non-dimensional horizontal lines. Note that, as discussed in section 3.2.1, the axial stress due to the difference between FR internal and external pressure is not accounted for in the model.

Figure 6.1a gives the axial stress distribution in the GTs and FRs in CC due to the HD force of about 7500 N and without the effect of axial hydraulic forces. The spots with the maximum axial compressive stresses below -13 MPa are in the GTs below the 2nd spacer grid, where the dashpot region has ended, and above the

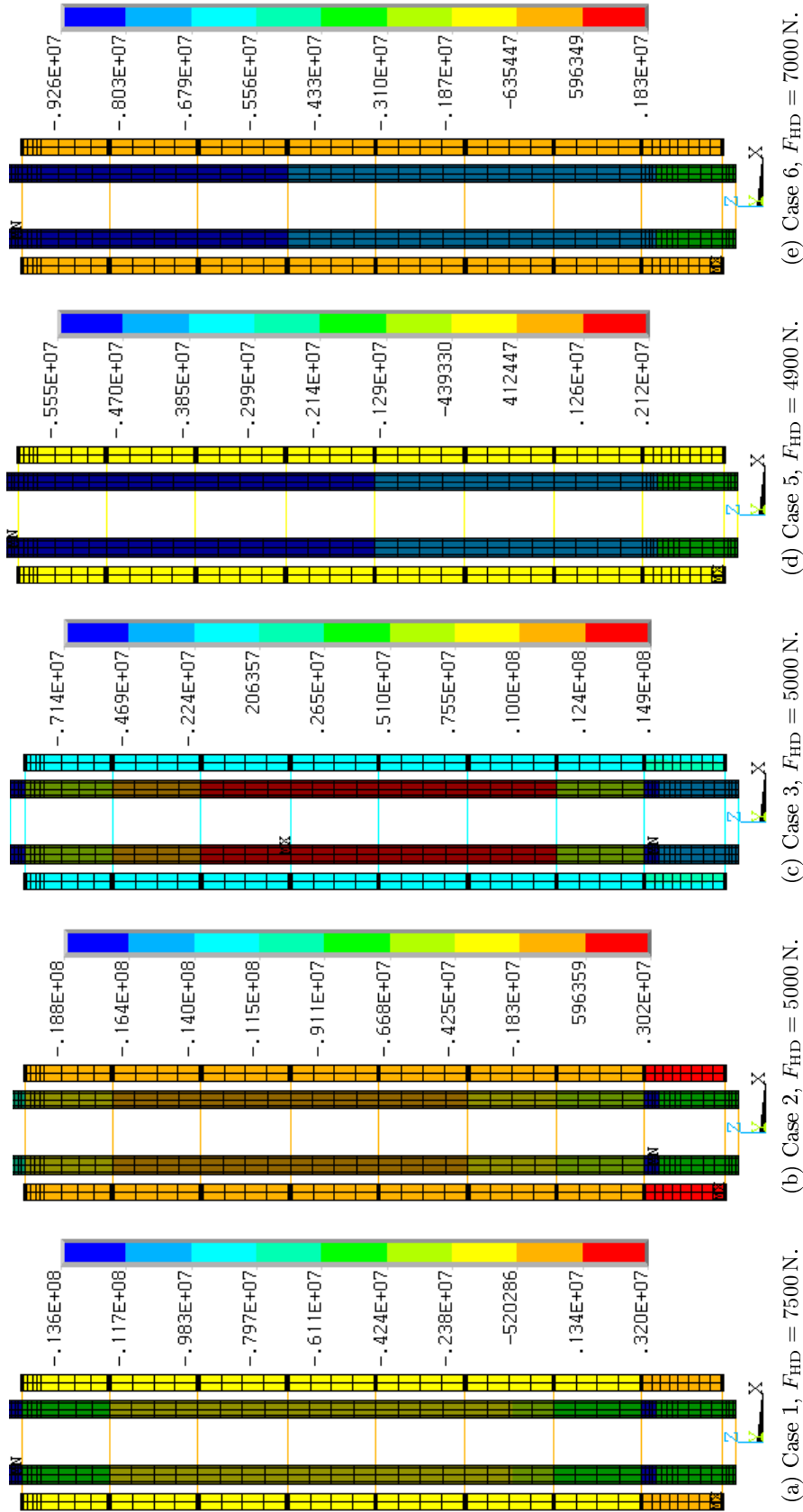


Figure 6.1: Axial stress σ_z [Pa] in GTs (inner tubes) and FRs (outer tubes).

9th grid. In the middle spans, the HD force is distributed over GTs and FRs through the grid-to-rod spring connections, thus reducing the load on the GTs. Towards the lower spans, the stress is increasing because of the partial redistribution of the loads from the FRs back to the GTs. The fuel weight has no major effect on the GTs outside the dashpot region since it is assumed to rest on the FR bottom end plugs. In the lower part of the GTs, the stress-reducing effect of the GT dashpots is well appreciable. Due to the more than doubled cross-section, the axial load is reduced by more than one half when compared to the portion after the dashpot ends. The FRs undergo only small compressive axial stresses of around -1 MPa due to the loading with the HD force and with their own weight. Note that because of the use of beam elements for the FRs, the model does not account for the elastic deformation due to the internal pressurization. If the pressurization was accounted for, the FRs would remain under tension.

After the transition to HC, case 2 given in Figure 6.1b, two major effects are important. First, the HD force decreases to about 5000 N due to the differential expansion between the Zirconium-alloy GTs and FRs and the stainless-steel core barrel. Second, the increased temperature in HC reduces the FA stiffness because the modulus of elasticity decreases. The decrease in the axial compressive load is more significant than the decrease in the modulus of elasticity of the FA structure. Therefore, the maximum compressive stress in the GT top decreases to -9.2 MPa. However, the decrease in the modulus of elasticity also reduces the grid spring forces and, as a result, less axial load is deviated through the grid springs into the FRs. Therefore, although the axial compressive load is decreased, the maximum compressive GT stress increases to -18.8 MPa just above the dashpot region. Again, it must be pointed out that the model does not account for the change in the FR axial deformation due to the transition from CC at ambient pressure to HC at $p_{\text{sys}} = 15.8$ MPa. If the pressurization was accounted for, the FRs would be contracted due to the resulting axial compressive stresses. This contraction would also be transmitted to the GTs, thus increasing the GT compressive stress in the middle spans.

When operating conditions at BOL are considered, case 3 given in Figure 6.1c, the thermal expansion of the GTs, and with it the HD force, remains nearly unchanged. Only the FRs expand strongly as a result of increased cladding temperatures due to the heat generation, see Figure 4.11c. As a result of this differential expansion, the GTs are put under tension with a maximum axial stress of 14 MPa due to the coupling through the grid-to-rod connection. In reality, this tensioning effect is somewhat weaker than represented due to the previously mentioned additional FR contraction.

Figures 6.1d and 6.1e finally give the axial stress distribution in operational states with practically no axial coupling between FRs and GTs. In this state, nearly the entire HD force rests on the GTs. As a result of the supporting effect of the upward axial hydraulic force, the compressive force on the GTs decreases from the top to the bottom. The maximum is hence found at the top with a compressive stress of -5.55 MPa for case 5 and -9.26 MPa for case 6. The increased compressive stress for the EOL case will have a detrimental effect on lateral stiffness, see the following section.

6.1.3 In-reactor lateral deflection tests

Figure 6.2a gives the results of the in-reactor deflection tests based on the test matrix in Table 6.1, which were first presented in Wanninger et al. (2016a,c). Case 1 is the result for a fresh FA in CC. Since no axial hydraulic forces are considered, it is very similar to the result of the in-laboratory axial deflection test. For case 2, the increased temperature in HC reduces the FA stiffness due to the decreased modulus of

elasticity. Since this causes a decrease in the grid spring forces, the transmitted moment at the grid level is reduced, as can be observed in Figure 6.2b. Under operating conditions at BOL, case 3, the FA lateral stiffness is slightly increased again. This is mainly a result of the stress stiffening of the FA structure due to the differential expansion of the FRs and GTs (see Figure 6.1c), which outweighs the further decrease of the modulus of elasticity as a result of the somewhat higher average structural temperatures. As a matter of fact, the moment transmitted at grid 3 is slightly reduced due to the in average somewhat lower grid spring compression. For BUs greater than zero, cases 4 to 6, irradiation effects decrease the FA stiffness. As the grid force decreases due to grid spring relaxation, the moment threshold values for the transition between the different phases presented in section 3.2.6 decrease. This is because the maximum dimple force before lifting off from the decompressed dimple and the maximum friction force decrease. The FA stiffness decreases accordingly, and the hysteresis loop narrows due to lower friction forces. For case 4 the spring force is close to zero and nearly no friction occurs. In this case the FRs lift off almost instantly from one dimple upon loading since the dimples are completely decompressed. The moment-deflection graph consists almost exclusively of phase 4, that is, the FR is supported by one spring and one dimple in normal direction. The force-deflection relationship of the FA nearly loses its hysteresis (for better clarity, the unloading phase is only shown for case 6) and becomes close to linear and elastic since there are practically no frictional or other nonlinear effects except for the Inconel grid. Still, the FRs stiffen the FA structure when compared to the force-deflection curve of the FA skeleton without FRs. For case 5 with open gaps, the grid-to-rod connection is only loaded after a certain threshold value, which corresponds to the rotation which is necessary for the FR to touch both the dimple and the spring at the same time. Due to the gap width of only $12\mu\text{m}$ there is only a minor effect of the gap on the FA stiffness. For case 6 the moments at the grids are similar to case 4 and hence not shown. The decrease in FA stiffness is entirely due to the higher compressive HD force. In conclusion, the in-reactor irradiation effects decrease FA stiffness almost by half when compared to BOL conditions in this model scenario.

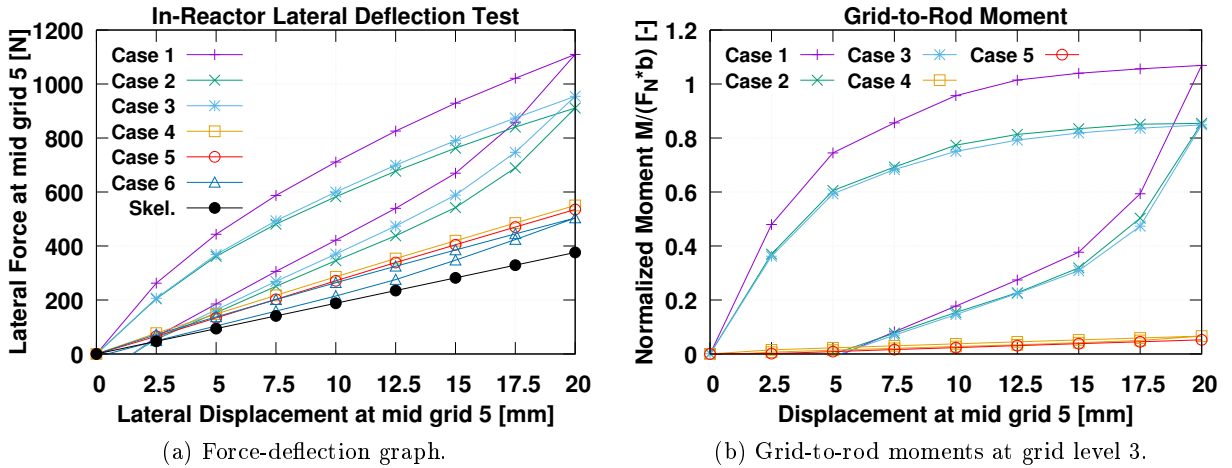


Figure 6.2: In-Reactor lateral deflection test for the cases in Table 6.1.

6.1.4 Sensitivity Analysis of FA lateral stiffness increase with structural parameters

The presented structural model already includes most of the optimized features with which fuel vendors have equipped their FAs to decrease FA deformation amplitudes, such as an increased GT outer diameter compared to earlier designs and a massive dashpot. The objective of this first sensitivity analysis, which was first published in Wanninger et al. (2016b), is to screen the FA design for stiffness parameter optimizations which can provide a further increase in stiffness. To this end, a screening sensitivity analysis is performed with the in-reactor FA lateral stiffness test from the previous section as test experiment. For this analysis, both BOL and EOL conditions, cases 3 and 6, are considered. The monitored output variable for the analysis is the lateral reaction force F_{lat} for the maximum deflection of $u_{\text{lat}} = 20$ mm. The input factors for the screening analysis are selected based on the principal structural parameters of the presented FA model in Tables 3.1 and 3.3. A crucial step for the analysis is the definition of the investigated range of values for the input parameters. For the purpose of this analysis the value range is extended in the direction for which an increase in overall FA lateral stiffness is expected. Table 6.2 presents the investigated sensitivity parameters and the chosen range of values, which are described in the following paragraph.

The geometric FA parameters, given in Table 3.1, represent the first class of parameters which are important for the FA stiffness. Modifications of the parameters related to FRs, such as the FR cross-section or pitch, would impair the fuel performance and are not considered. As for the GT geometry, sensitivity parameter 1 in Table 6.2, the potential for modifying the inner diameter $d_{\text{GT},i}$ is limited by the margin for a proper insertion of the control rods while the outer diameter $d_{\text{GT},o}$ is limited by the size of the grid cell. In the present model, $d_{\text{GT},o}$ is roughly equal to the pitch p_{FR} minus the grid strap thickness t_{grid} , limiting a further increase. Nevertheless, we assume a slight modification in the order of magnitude of the manufacturing tolerances. This may still have large effects on stiffness since the bending rigidity is a function of the 4th power of the diameters. Parameter 2 in Table 6.2 investigates the influence of a decrease of the GT dashpot inner diameter $d_{\text{GT},dp,i}$.

The next set of parameters capable of providing a FA stiffness increase are those linked to the grid connection stiffness, given in Table 3.3. The FR support model comprises several independent influential parameters. The first group of input parameters (4 to 6), are the normal and tangential stiffness of the springs and dimples. For these parameters, an increase of 20 % compared to the nominal values is chosen as a maximum for the analysis. Parameter 7, the distance between the dimples, provides a good potential for stiffness increase since it has a quadratic influence on $k_{\theta, \text{FR-grid}}$ according to equation 3.6. On the other hand, a modification of b is limited by the spacer grid design and height. An increase of 10 % compared to the nominal values is considered as a maximum. The maximum increase in the instantaneous rotational stiffness is hence 45.2 % ($1.2 \times 1.1^2 = 1.452$). For parameters 8 and 9, a maximum increase of 20 % is assumed. The margins against FR buckling due to axial forces are sufficiently high to accommodate such an increase. Analogously to $k_{\theta, \text{FR-grid}}$, the rotational connection stiffness between GTs and spacer grids, parameter 3, can be stiffened by increasing the vertical distance between the spot welds or by modifying the properties and number of spot welds. Altogether a similar increase as for the FR support is feasible, so that we assume an increase by 45.2 % as well. The last considered parameter is the initial axial HD force, parameter 10. A decrease in the order of 1000 N, or 20 %, is feasible if additional measures are taken to ensure the margin against a potential lift-off of the FA due to upward hydraulic forces.

Table 6.2: Sensitivity analysis input parameters for the FA stiffness test.

Param. #	Variable	Minimum multiplier	Maximum multiplier	Description
1	$d_{GT,i}$	1	0.995	Inner GT diameter
	$d_{GT,o}$	1	1.005	Outer GT diameter
2	C_{dp}	1	0.95	Factor for inner GT diameter in dashpot
3	$k_{\theta,GT-grid}$	1	1.452	Rotational stiffness of GT-grid connection
4	$k_{s,n}$	1	1.2	Zircaloy grid spring stiffness
5	$k_{d,n}$	1	1.2	Zircaloy grid dimple stiffness
6	k_t	1	1.2	Grid spring and dimple tangential stiffness
7	b	1	1.1	Vertical distance between grid dimples
8	F_N	1	1.2	Grid spring preload at BOL
9	μ	1	1.2	Friction coefficient
10	$F_{ax,BOL}$	1	0.8	Holddown force at BOL

Figure 6.3 gives Morris' sensitivity measures for the different input parameters in Table 6.2 for BOL and EOL conditions. The μ_i measures are about an order of magnitude higher than the σ_i measures. This means that the input parameters have a mostly linear effect on the output parameter F_{lat} of the simulation experiment. Despite the small input range, the GT diameter, parameter 1, plays an important role when it comes to optimizing FA stiffness. An increase of the dashpot wall thickness, parameter 2, would only have a minor influence on the FA stiffness. The influence of every individual grid cell stiffness input parameter (4 to 6) is comparatively small since each parameter accounts only for a part of the moment transmission in the grid cell. In contrast, parameter 7, which has a quadratic influence on $k_{\theta,FR-grid}$, is significantly more influential. The grid spring preload, parameter 8, has the largest influence on the solution of all parameters for BOL conditions. The preload determines both the maximum friction force and the maximum dimple moment whereas parameter 9 only accounts for the friction force and is hence less influential. Finally, the relative influence of a decrease of the HD force, parameter 10, is small for BOL conditions. For EOL conditions, Figure 6.3b, the absolute values of μ_i for the skeleton-related parameters 1 to 3 remain nearly constant; hence, their influence on the solution remains nearly the same. The grid-cell related parameters (4 to 9) show significant differences compared to the BOL condition. The parameters related to the nonlinear behavior of the FR cell and in particular to friction, parameters 6, 8, and 9, lose their influence on the solution. Also, parameters 4, 5, and 7, which account for the linear rotational stiffness of the FR support for EOL conditions, have become much less influential than for BOL conditions. The influence of the HD force remained nearly constant in absolute terms, but gained in relative importance, becoming the third-most influential parameter at EOL. In conclusion, considering both BOL and EOL conditions the skeleton-related parameters 1 and 3 offer the most potential for optimization. A decrease of the HD force also stiffens the FA, albeit to a minor extent. The grid-cell related parameters show a large dependence on BU. Modifications may stiffen the FA significantly initially. But during BU their influence on the FA stiffness decreases so that the overall potential for optimizations is small.

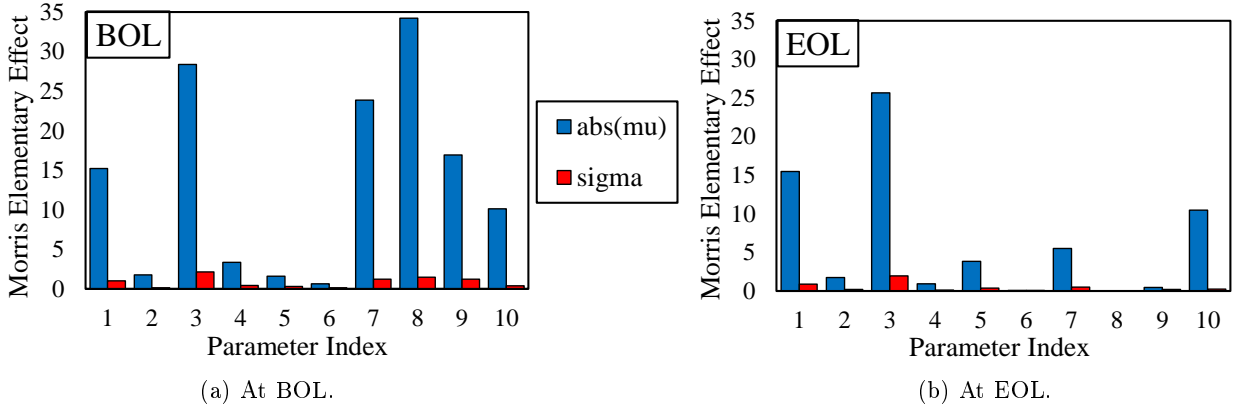


Figure 6.3: Morris' $|\mu|$ and σ measures for the input parameters in Table 6.2.

6.2 Single-FA creep deformation analysis

In this section, the deformation of a single FA after irradiation in the reactor core during one reactor cycle is analyzed. That is, the creep, growth, and relaxation models presented in chapter 4 are used to determine the permanent deformation after the cycle. For the time being, only the creep and growth models for conventional Zircaloy-4 (Zry-4) are applied for both GTs and FRs. The different solution load steps to obtain the final deformation state are described in section 4.1.2. The results are given in terms of result steps. The start-up load step is numbered 0. During the operation load step, intermediate results are written to the results file in an interval of approximately 500 h, producing $n = 16$ result steps for the reference cycle length of 7920 h. All indications of step numbers in this chapter refer to these result steps and not to the actual time steps used in the numeric simulation. Table 4.2 gives the operational states corresponding to each result step.

In the first analysis of this section, a FA undergoing lateral hydraulic forces in the reactor core is considered. The second analysis investigates the deformation of FAs at the core periphery due to differential creep and growth as a result of lateral power gradients, neglecting the effect of lateral hydraulic forces. Finally, we perform a systematic sensitivity analysis of the permanent FA deformation due to different influencing parameters.

6.2.1 Creep deformation due to lateral hydraulic forces

For this analysis, the hydraulic load boundary condition (BC) on the FA is based on the lateral hydraulic force distribution obtained with the non-uniform symmetric inlet flow profile, Figure 5.14. Specifically, the FA at position 12 is simulated since it undergoes high hydraulic loads and has a relatively high power level, see Figure 4.11a.

Operation Figure 6.4a gives the evolution of the lateral displacement at grid levels 5 and 6. Initially the maximum deflection occurs at the mid-grid level 5. During operation, the relaxation of the upper grids is faster than for the lower grids, see Figure 6.5; therefore, the position of maximum deflection shifts from the 5th to the 6th level. Figure 6.4b gives the lateral reaction forces and reaction moments on the FA constraints as a result of the external loading. The sum of the bottom and top lateral reaction force results in the total lateral hydraulic force of $F_{\text{lat}} = 286 \text{ N}$. Although the loading is roughly symmetric about the

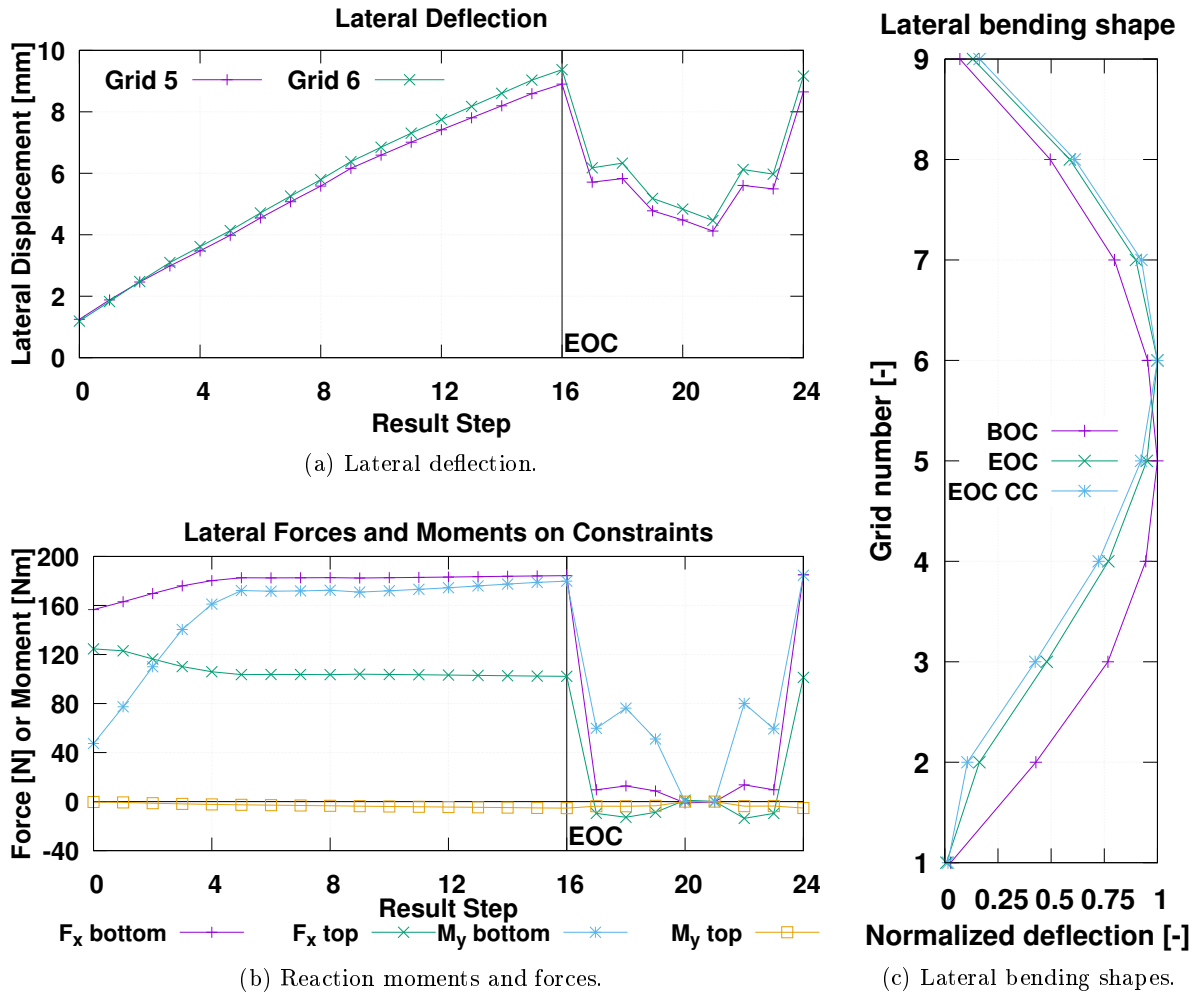


Figure 6.4: Single-FA creep test over one cycle with hydraulic load of FA 12 in Figure 5.14.

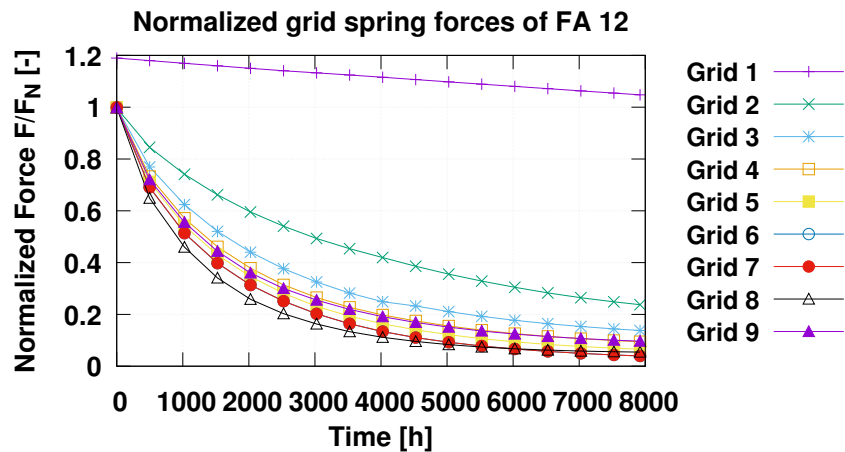


Figure 6.5: Normalized grid spring forces at the different grid levels over the reactor cycle during the single-FA creep test with FA 12.

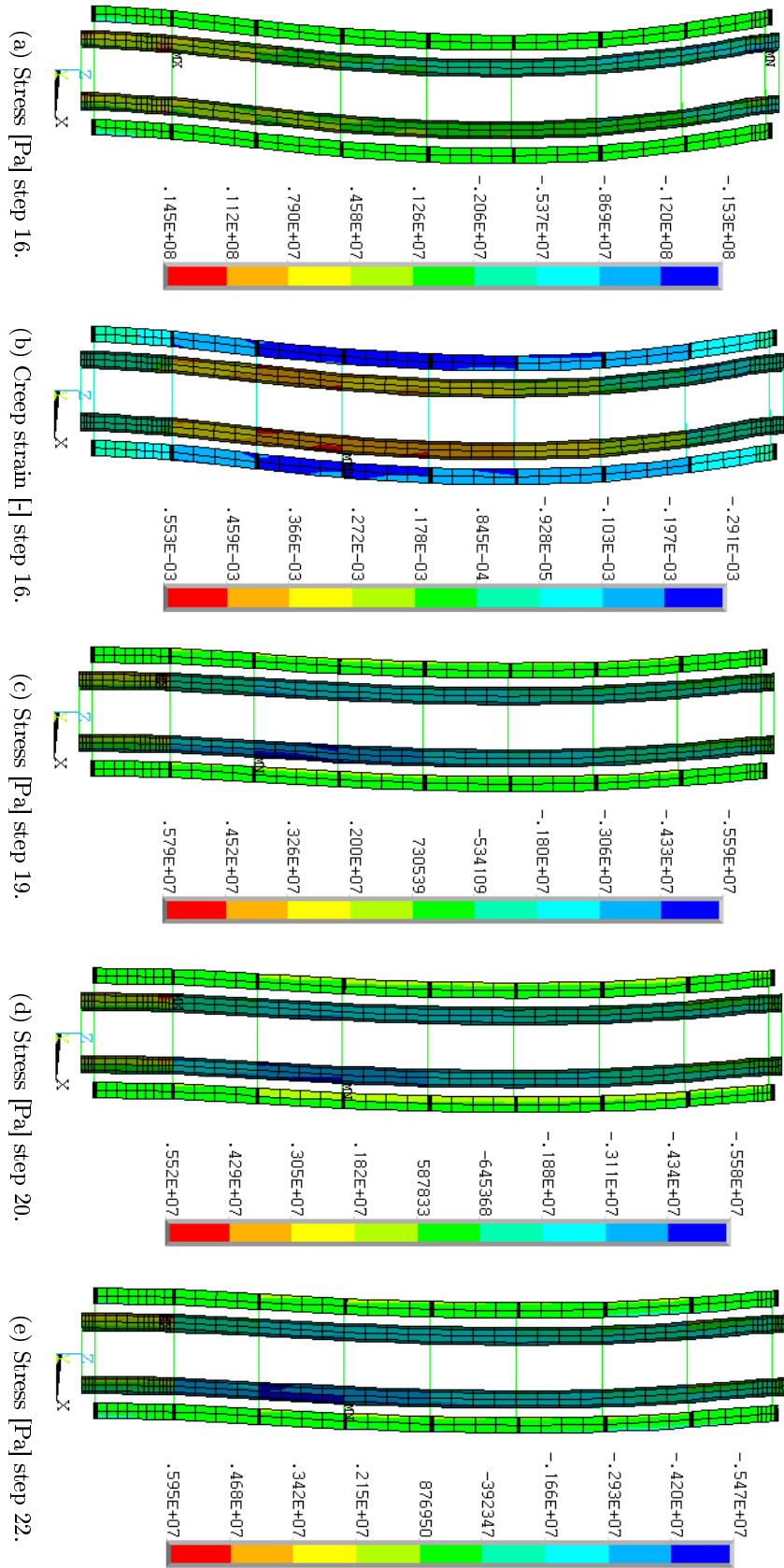


Figure 6.6: Distribution of selected distributed variables in selected GTs and FRs for the single-FA creep deflection test.

horizontal middle axis, the bottom constraint exhibits a higher reaction force. This is due to the higher stiffness of the lower part of the FA which can accommodate higher loads. As for the rotational constraints, a significant reaction moment only builds up at the bottom where a clamped condition is assumed whereas the rotational stiffness of the HD spring is relatively small in comparison, leading to a very reduced reaction moment. During operation, the moment at the bottom increases significantly in the first 2500 hours and the ratio between bottom and top lateral reaction force also increases further. This is because the upper half of the FA yields more during operation due to increased creep and relaxation rates as a result of higher temperatures. Afterwards, the reaction forces and moments remain roughly constant. Only the reaction moment at the top increases further since the increasing deflection leads to higher rotation angles θ_y of the top nozzle. The shift in the axial stiffness distribution is also well appreciable considering the lateral bending shapes in Figure 6.4c. At EOC the bending shape is clearly shifted upwards when compared to the elastic deformation at BOC. Since the Zirconium alloy grid springs are nearly relaxed, the relative influence of the GT dashpots is much more pronounced than at BOC. Figure 6.6a gives the distribution of the stress in selected GTs and FRs at EOC under operation or result step 16. The plot represents the deformed FA shape scaled by a multiplication factor of 5. As discussed in section 2.1.3.4, the stress at any point in the GT or FR is the result of the joint effect of the uniaxial stress at the neutral axis and the bending stress; hence, it is non-uniform over both the GT and FR cross-sections. Moreover, the stress plot illustrates different axial stress levels in the two depicted GTs as a result of the coupling at the spacer grid levels. Figure 6.6b gives the corresponding distribution of the creep strain. Since the creep strain derives from the stress distribution, it can also be decomposed into the sum of a uniaxial creep strain component, which is constant over the beam cross-section, and a bending creep strain component. The axial loading of the GTs and FRs, which is mostly tensile for GTs and compressive for FRs according to section 6.1.3, causes a uniaxial creep strain in the order of magnitude of 1×10^{-4} . The bending creep strain is one order of magnitude lower. This demonstrates that, despite the significant deflection of nearly 10 mm, the bending creep strain causing this deformation is in the order of only 1×10^{-5} after one reactor cycle. This is, for example, significantly smaller than the hoop strains expected for the FR cladding creep-down. The order of magnitude of the saturated primary strain being 1×10^{-4} , this demonstrates also that the primary strain is an important component for the calculation of the FA creep deformation which must be accounted for.

Shutdown After removing the hydraulic loads and transition to HC, result step 17, the deflection is reduced by more than 3 mm. As predicted in Figure 6.2a, the FA lateral stiffness decreases strongly due to the grid relaxation. Therefore, the elastic deflection has more than doubled when compared to the BOC condition. In CC, result step 18, the deflection increases somewhat due to the increased HD force and the related stress weakening effect. The following transition from the in-core to the ex-core condition is subdivided into three single steps in order to better distinguish the different effects. First, the HD force is released in step 19. That is, the axial displacement constraint is removed from the FA top. Although no external lateral loads are imposed anymore, the reaction forces and moments in this phase are non-zero. That is, the support reactions are associated with the internal stress state, which is given in Figure 6.6c for result step 19. To appreciate only internal stresses, the effect of gravity is turned off ($g = 0$) for this plot and the following plots in this paragraph. In step 20, the rotational constraints are also removed from the FA top and bottom. In this manner, the system is transformed into a statically determinate system releasing

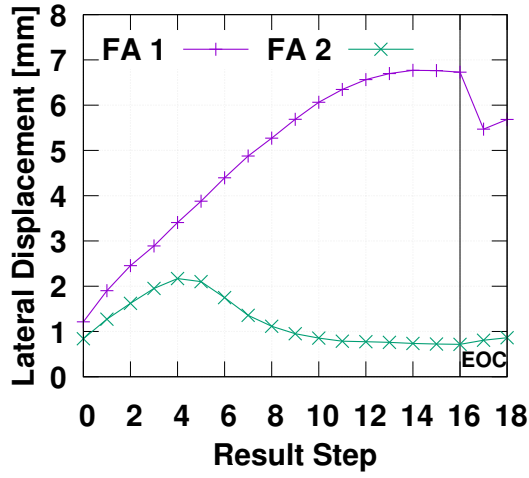
the internal stress in equilibrium with external reactions. As a result, only the residual stress due to the plastic creep deformation remains in the FA structure, see the stress plot in Figure 6.6d. This step leads to a further reduction of deflection amplitude. Finally in step 21, the FA is lifted out of the core by applying an upward force W_{FA} at the FA head. Due to the resulting stress stiffening, the amplitude is reduced further. This is the state in which the FA deflection is usually measured and can be validated.

Start-up of following cycle As the final part of the analysis, the FA is now re-inserted into the core to investigate possible structural effects happening between the transition from EOC n to BOC $n + 1$. When constraining the FA again in CC, step 22, a somewhat different equilibrium than at EOC is reached, see Figure 6.6e. The reaction forces and moments are somewhat increased and the maximum deflection in this state is reduced by 3.3%. This discrepancy persists also after transforming the FA again into HC and the operational state, steps 23 and 24. This means that the FA does not exhibit the same state that it had at the end of a specific cycle at the beginning of the following cycle, probably due to hysteresis effects. That is, the evolution path of the loads and the deformations has still an impact on the instantaneous FA stiffness although the Zirconium alloy grid springs are nearly relaxed.

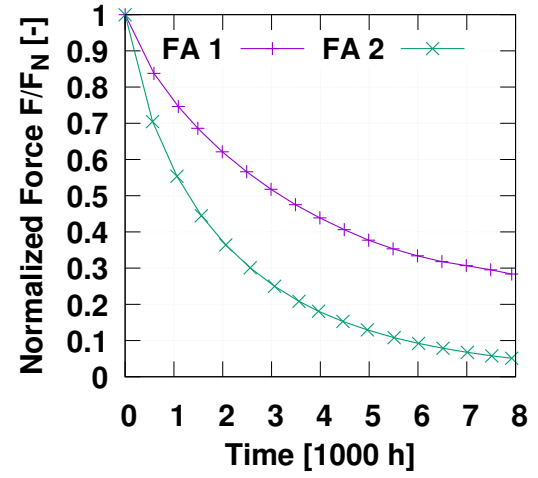
6.2.2 Deformation of peripheral FAs due to differential creep and growth

In this second analysis, the lateral response of the two peripheral FAs in Figure 4.11a, FAs 1 and 2, is simulated in their fresh state under the effect of the given power gradients and neglecting lateral hydraulic forces. Figure 6.7a gives the evolution of the lateral deflection of both FAs at grid level 6 where the maximum amplitude occurs. Result step 0 represents the initial thermoelastic equilibrium at BOC resulting in deflections of 1.21 mm and 0.84 mm. The bending of the FA structure can be explained by means of the total axial strain gradient $\Delta\epsilon_z^{\text{tot}}/\Delta x$ between the outer GTs in lateral x -direction. Figure 6.8 gives the evolution of the different strain gradient components over the reactor cycle for the GTs and FRs. For the BOC state, the GT total strain gradient results completely from a positive elastic strain gradient over the GTs, see Figure 6.8a and 6.8b. This is due to the differential thermal expansion of the FRs, see the chart of strain gradients over the FRs in 6.8c and 6.8d at BOC. This positive thermal gradient in the FRs is transmitted to the FA structure by the FR-to-grid connections leading to a positive stress gradient in the GTs, thus bending the FA structure in positive x -direction. Since the thermal gradient is somewhat higher for FA 1, it presents a higher deflection at BOC.

Under operation, result steps 1 to 16, the deflection amplitude increases in the direction of the increasing gradient due to the joint effect of creep and growth mechanisms. In the initial phase of the operation cycle, a positive GT growth strain gradient is the main contributor to the increasing total strain gradient, and hence the deflection amplitude, until the first-stage growth saturates according to the implemented GT growth law. Then, differential creep becomes more important. It is remarkable that the deflection of FA 1 increases during the entire cycle while FA 2 reaches its maximum after about 2000 hours of operation. This behavior can be explained by the relaxation of the grid spring force during the irradiation given by Figure 6.7b. Due to the low average neutron flux level, the coupling between the FRs and GTs is maintained significantly longer for FA 1 than for FA 2. This implies that in FA 2 the coupling forces between the FRs and the GTs decrease significantly in the first operation phase, thus decoupling the FA structure from the FRs. For FA 1, in turn, the relatively high differential FR growth, see Figure 6.8c, continues to be transmitted to the FA structure. This causes two effects. First, the GTs are bent by the coupling forces, leading to an increasing

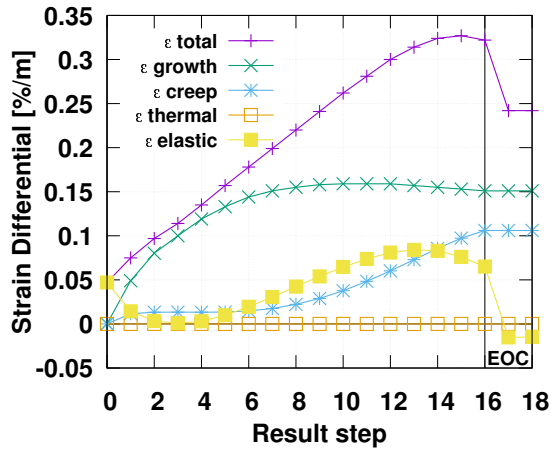


(a) Lateral deflection.

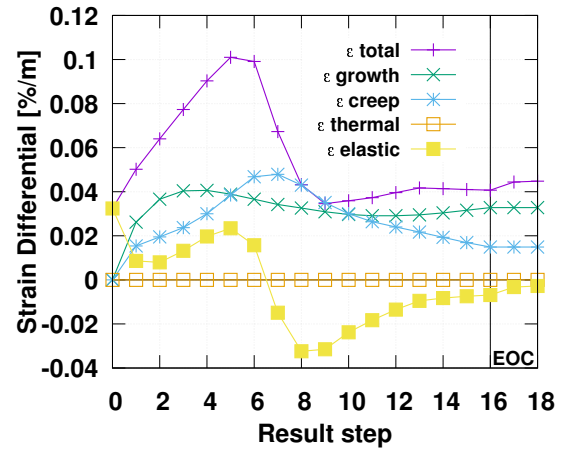


(b) Normalized grid spring force at grid 5.

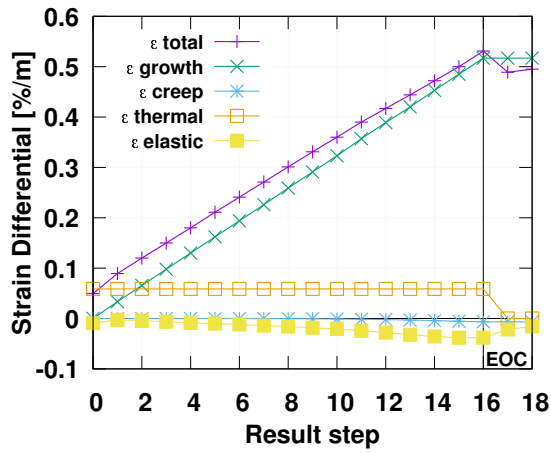
Figure 6.7: Single-FA creep test over one cycle of FA 1 and FA 2 in Figure 4.11a under the effect of power gradients without lateral hydraulic forces.



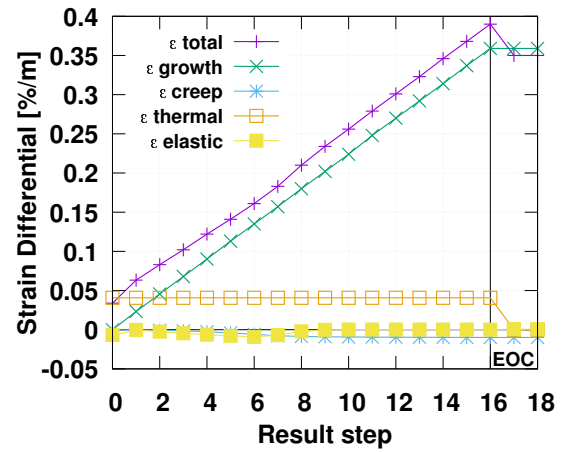
(a) Gradient over GTs in FA 1.



(b) Gradient over GTs in FA 2.



(c) Gradient over FRs in FA 1.



(d) Gradient over FRs in FA 2.

Figure 6.8: Lateral strain gradients $\Delta\epsilon/\Delta x$ at grid 5 over the peripheral FAs 1 and 2.

elastic strain gradient. Second, the GTs remain under tension over the entire cycle due to these coupling forces. Creep is always faster at the hotter side of the FAs so that under tension a positive creep strain gradient is present over the FA structure, promoting the deformation in the direction of the gradient. For FA 2, the compressive HD and weight forces on the GTs quickly exceed the tensile grid coupling forces. Under this compression, a negative creep strain rate gradient develops over the GTs so that the creep counteracts the initial deformation, causing a strong decrease of the amplitude. For FA 1, such an effect becomes only visible shortly before EOC. After transition to HC and CC, steps 17 and 18, the thermal gradient over the FRs disappears so that the deflection of FA 1 decreases. The deflection of FA 2 remains relatively constant because almost no coupling effect between the FRs and the FA structure is present anymore.

In conclusion, the permanent deformation of FAs under the effect of power gradients is often the result of several coupled mechanisms in the GTs, the FRs and the spacer grid structure. Which mechanism is dominant depends on several parameters, such as the value of the power gradient, the neutron flux level, and the relative importance of the creep, growth, and relaxation rates, and must be determined for the specific FA conditions. However, it is unlikely that the highly deformed cores observed in pressurized water reactors (PWRs) are only due to differential creep and growth because the FA deformations are limited to the peripheral regions with high gradients and the deformation amplitudes are relatively moderate compared to the potential deformation due to lateral hydraulic forces observed in the previous analysis.

6.2.3 Sensitivity analysis of FA creep deformation with uncertainty parameters

This analysis, which was first published in Wanninger et al. (2016b), investigates the sensitivity of the FA creep deformation to different influencing parameters over the entire FA life. For this reason, the previous deflection analysis of a single isolated FA over one reactor cycle is extended over the equivalent duration of four reactor cycles, corresponding to a BU of approximately 50 GWd/t_{HM}. The hydraulic loads and the heat generation are assumed constant over the FA lifetime for this simulation experiment and for the test a constant lateral force of $F_{\text{lat}} = 50 \text{ N}$ is applied at the FA mid grid. This discrete force is assumed to be representative of the effect of the distributed lateral hydraulic loads at a certain point in the reactor. The monitored output variable for the sensitivity analysis is the evolution of the FA lateral deflection u_{lat} at grid 5. Figure 6.9 gives the calculated evolution over BU of the lateral FA deflection u_{lat} for the simulation experiment with best estimate (BE) parameters.

In this second sensitivity analysis we set the potential stiffness increase obtained from the first analysis in section 6.1.4 in relation to other input parameters by means of the described FA creep deformation simulation experiment. These parameters are usually linked to relatively high uncertainties which must be assessed first. The first objective of this analysis is to investigate how efficient the deterministic potential stiffness increase is in view of the uncertainties of other influential parameters. At the same time, this analysis allows to evaluate the relative influence of the different uncertainty parameters on FA bow. Table 6.3 specifies the sensitivity input parameters for the FA creep deformation simulation experiment. The stiffness parameters of the previous analysis in Table 6.2 are grouped into one input factor, parameter 1, assuming that all proposed modifications can be implemented. The other input parameters can be divided into two groups: (1) boundary conditions (BCs), parameters 2 to 4, and (2) material evolution laws, parameters 5 to 7. The BC group comprises the lateral force representing the cross-flow, material temperatures and fast neutron flux.

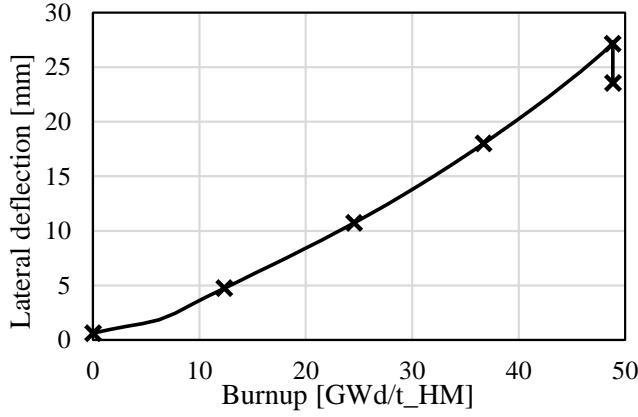


Figure 6.9: Evolution over BU of the monitored output variable (lateral FA deflection u_{lat}) for the simulation experiment with BE parameters.

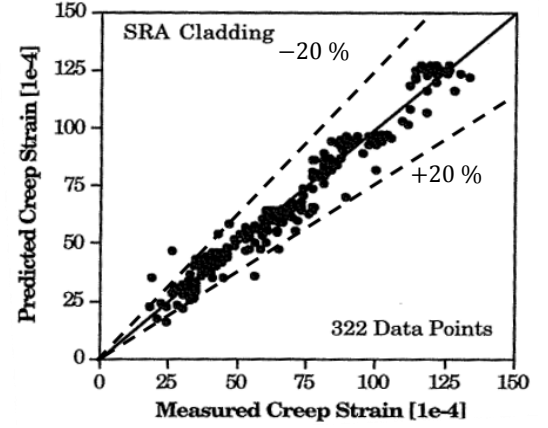


Figure 6.10: Example for predicted versus measured secondary creep strain (Limbäck and Andersson, 1996)

During reactor operation, the temperature and fast neutron flux are relatively well controlled. The input uncertainty for the fast neutron flux is assumed to be $\pm 3\%$ around the nominal value. The uncertainty about temperature is assumed to be approximately $\pm 3^\circ\text{C}$. For the lateral force, an uncertainty of $\pm 20\%$ around the nominal value is assumed as a first approach. The second group is associated to the material evolution laws due to creep and growth processes. Experimental measurements usually show a substantial spread for the creep and growth strains of Zirconium alloys under neutron irradiation. The best estimate (BE) models based hereupon are consequently linked to modeling uncertainties due to this spread. Figure 6.10 gives a comparison between the predictions of the steady-state creep model by Limbäck and Andersson (1996) and measurements of secondary creep strain of Zircaloy claddings under constant conditions. Based on these values, we estimate an uncertainty of $\pm 20\%$ about the BE Zry-4 creep constants, parameter 5, which are derived in section 4.2. Creep processes are also the main drivers of the grid spring relaxation and the opening of the grid-cladding gap, expressed jointly by parameter 6. Accordingly, we also assume an uncertainty of $\pm 20\%$ about the nominal value for the exponential grid spring relaxation constant, which

Table 6.3: Sensitivity analysis input parameters for the FA creep deformation test.

Param. #	Variable	Minimum multiplier	Maximum multiplier	Description
1	FA stiffness increase, see Table 6.2			
2	F_{lat}	0.8	1.2	Applied lateral force at mid grid
3	ϕ	0.97	1.03	Fast neutron flux (>1 MeV)
4	T	0.99	1.01	Temperature
5	C_{cr}	0.8	1.2	Constant for GT and FR creep
6	C_{grid}	0.8	1.2	Constant Zr-alloy grid spring relaxation
	d_{gap}	0	2	Gap size between Zr-alloy grid and cladding
7	$C_{gr,FA}$	0.25	2	Constant for FA growth
	$C_{gr,FR}$	0.8	1.2	Constant for FR growth
	C_{hd}	0.95	1.05	Factor for HD spring residual force

is derived in section 4.5.1. For the gap-opening behavior, we assume that for a slow grid spring relaxation the FR creep-down is completely accommodated during the grid spring relaxation and no gap opens. For a fast grid spring relaxation, the gap opens up to a maximum value of 20 μm . Both extremal cases are represented graphically in Figure 6.11. The evolution of the HD force, parameter 7, is mainly linked to the FA growth and the relaxation of the HD springs. The parameter range for $C_1^{\text{gr,FA}}$ is estimated based on the measurement data spread of Zry-4 FA growth in Figure 4.7. For FR growth, the same parameter spread as for creep is used because the data scattering appears not to be as high as for GT growth, see Figure 4.8. As for the HD spring, residual forces at EOL of $\pm 5\%$ around the nominal value defined by equation 4.25 are assumed.

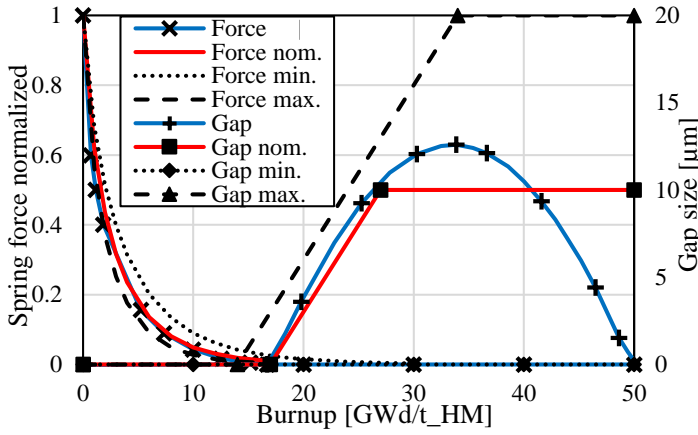


Figure 6.11: Literature values (Billerey, 2005, in blue) and deduced model nominal (nom.), minimum (min.) and maximum (max.) values for the normalized spring force and gap size of Zry-4 mid grids.

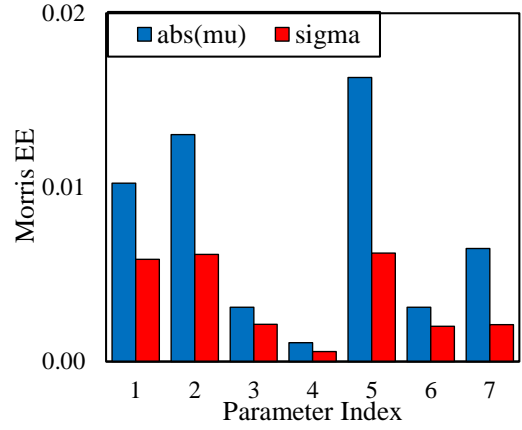


Figure 6.12: Morris' $|\mu|$ and σ measures for the last time step of the FA creep deformation simulation experiment for the input parameters in Table 6.3.

Figure 6.12 gives Morris' elementary effect measures for the last time step of the creep deformation simulation experiment. We can identify parameters 1, 2, and 5 as the predominant parameters for the selected input range. As for the linear effects, expressed by the measure μ_i , the largest influence on the solution can be attributed to the uncertainty about the GT and FR creep, parameter 5. This parameter even has a larger influence than the deflection-inducing lateral force, parameter 2. The third-most influential parameter is due to the proposed stiffness increase, parameter 1. Then parameters 7, 6, 3, and 4 follow, in the order of decreasing influence. The σ_i measures, that is, the nonlinear effects and the parameter interactions, play a more important role for the creep deformation than for the previous analysis, but are still inferior to the linear effects. For σ_i , parameters 1, 2, and 5 have similar magnitudes of importance. To better compare the relative influence of the different parameters between different BUs, the normalized measures $\mu'_i(BU)$ and $\sigma'_i(BU)$ are defined.

$$\mu'_i(BU) = \frac{\mu_i(BU)}{\sum_{i=1}^7 \mu_i(BU)} \quad (6.1)$$

$$\sigma'_i(BU) = \frac{\sigma_i(BU)}{\sum_{i=1}^7 \sigma_i(BU)} \quad (6.2)$$

Figures 6.13a and 6.13b give the BU-dependent evolution of these normalized measures. Both figures indicate that parameters 1 and 2, the stiffness increase and the applied lateral force, are the predominant factors for the BOL condition since no radiation effects are considered. During the first cycle, particularly parameters 5 and 6 become important while the relative contribution of 1 and 2 decreases. Parameter 6 is especially influential during the first cycle when the FR creep-down determines the grid spring relaxation. With higher BU, after about 2 cycles, parameter 7 outweighs parameter 6. This can be attributed to the fact that neutron-induced growth shows its effect particularly for high BUs. Similarly, parameter 5 becomes more important than parameters 1 and 2, making it the most influential parameter in this analysis. Most other parameters remain relatively constant after the first cycle. We conclude that for reducing the creep deformation an increase in FA stiffness plays an important role, but the uncertainties about the lateral force and the creep rate can outweigh the effect of an increased FA stiffness.

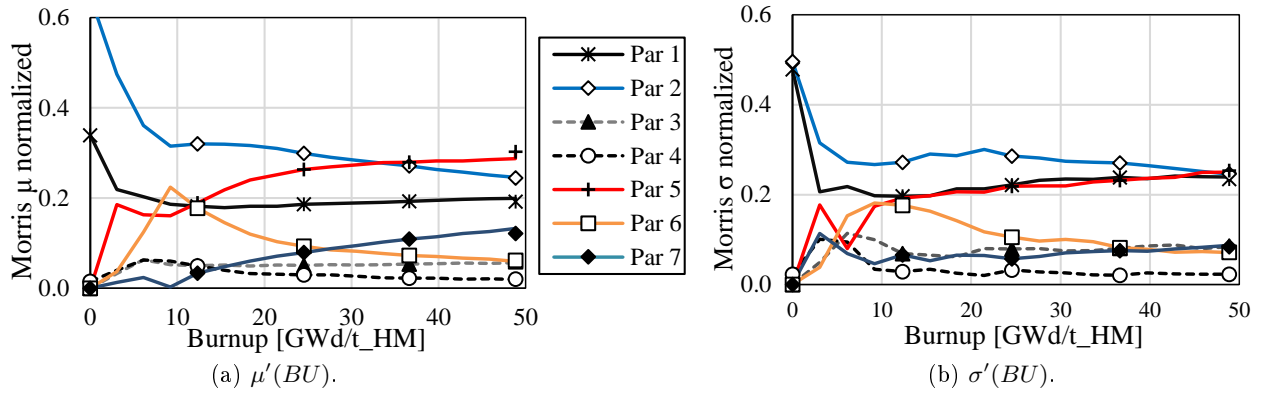
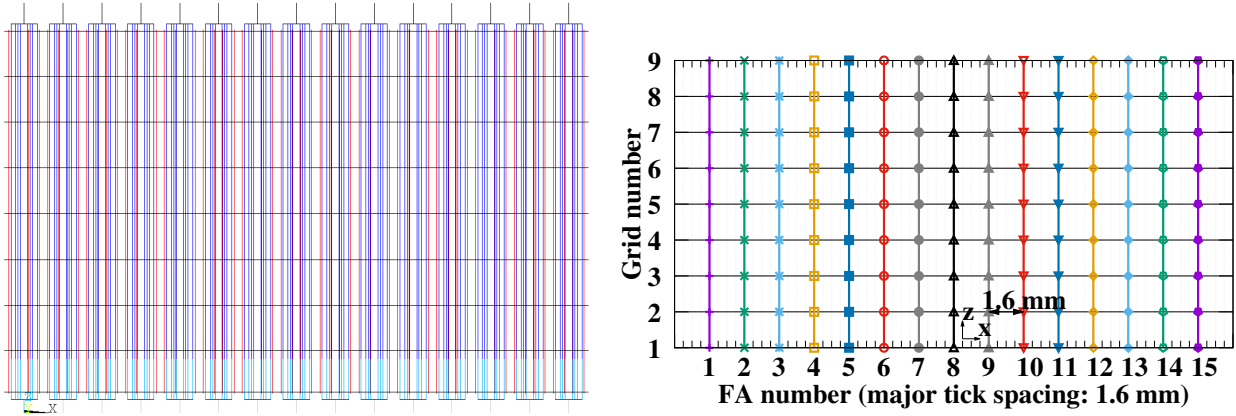


Figure 6.13: BU-dependent evolution of the normalized Morris measures for the input parameters in Table 6.3.

6.3 In-reactor creep deformation of FA rows over one cycle

In the previous sections, only one single isolated FA has been investigated, neglecting the coupling between neighboring FAs which occurs when the relative deformation is larger than the gap size. In this section, the investigation is extended to a row of 15 FAs in the reactor core, interconnected by structural gap elements as described in section 3.2.4. Figure 6.14a depicts the entire system as represented by the ANSYS Graphical User Interface (GUI). To better appreciate the FA deformations, the FAs in the result plots are reduced to a line defined by the displacements at the grid levels. Figure 6.14b gives the undeformed configuration of the FA row. For the in-core condition, the left and right borders of the plots mark the left and right reactor walls formed by the core baffle, which is assumed stiff. For the ex-core condition, the plot width is increased such that all FAs fit into the plot without overlapping. Each major tick corresponds to the initial gap size between undeformed hot FAs of 1.6 mm. The major ticks are subdivided into four minor ticks corresponding to a distance of 0.4 mm.

The objective of this section is to investigate the sensitivity of the considered mechanical system of one FA row to the different influencing mechanisms presented so far: thermal and flux gradients, the alloying condition, the hydraulic condition, the creep and growth processes, and the interaction with initially bowed FAs. We want to assess the influence of the uncertainty about the discussed parameters on both the bow



(a) FA row in the ANSYS GUI. FA height is reduced by factor 2. (b) Simplified representation of the undeformed FA row.

Figure 6.14: Considered system of a row of 15 FAs in the reactor core.

amplitudes and the bow patterns. Unlike for the case of a single FA, it is more difficult to judge the effect of a parameter change by monitoring a single output variable due to the large number of degrees of freedom (DOFs) in the FA row. The deformation state is not only characterized by the average magnitude of the deformation amplitudes, but also by their directions and the FA distortion. A deformed core may exhibit a very different deformation shape despite having the same nominal average deformation amplitude. Moreover, FA row creep calculations over one reactor cycle have a significantly increased computational cost compared to a single FA. For these reasons, a systematic sensitivity analysis as performed in sections 6.1.4 and 6.2.3 is not appropriate to investigate the sensitivities of the FA row. Instead, a more simplistic approach is chosen. Departing from a reference case, we introduce extremal parameter changes within the previously defined uncertainty bounds or parameter ranges. This reduces, on the one hand, the number of simulation runs to be executed. On the other hand, applying this strategy we can demonstrate the possible effect of uncertainties on the final bow pattern, rather than concentrating on the deformation amplitude only. The considered uncertainty parameters can be limited to those that have proved to be the most influential in the previous sensitivity analysis over a single FA. The outcome of this analysis shows that it is essential to consider possible uncertainties about the evolution of the structural creep and the distribution of the hydraulic forces. Both parameters exhibit an important influence on the solution over the entire operational life of the FAs, see Figure 6.13a. Besides, two other parameters proved to have a non-negligible influence for certain BU conditions. First, uncertainties about the grid relaxation rate should be considered in the simulation of FAs in the first operation cycle, that is, for initially fresh FAs. Second, uncertainties about the FA growth should be considered for high-BU FAs. This concerns not only the evolution of the HD force but also the differential growth. Therefore, a preliminary analysis is first performed without hydraulic forces to investigate the effect of the breakaway growth on the FA deformation due to flux gradients, see section 6.3.1. Then, the actual reference analysis is performed in section 6.3.2, including BE creep, growth, and relaxation laws, as well as a symmetric hydraulic condition. Starting from this reference case, the sensitivity of the simulation results to different parameter changes is investigated. First, the hydraulic condition is switched from the symmetric distribution in Figure 5.14 to the asymmetric distribution in Figure 5.16, see section 6.3.3.

Then, the uncertainties about the creep, growth, and relaxation models are included in section 6.3.4. In addition, the effect of initially bowed elements on the FA row will be investigated in section 6.3.5. Finally, we perform simulation runs including a two-way fluid-structure interaction (FSI) between the coolant and the FA structure in order to investigate the effect of the backcoupling of the deformed structure on the flow, see section 6.3.6.

Due to their symmetric configuration, we can use the first two cases to verify the sensitivity of the system to the alloying condition. For this purpose, the FAs to the left (1 to 7) are defined to be made of conventional Zry-4 whereas the FAs to the right (8 to 15) are made of advanced alloys for these symmetric cases. For all following calculations with asymmetries, only FAs with advanced-alloy GT and FR materials are modeled because they have become the standard in most Western PWRs. First results of the analyses over a FA row have been published in Wanninger et al. (2017, 2018).

6.3.1 Preliminary analysis: effect of thermal and neutron flux gradients without hydraulic forces

The single-FA analysis performed in section 6.2.2 demonstrated that a certain amount of the FA deformation can be explained by differential creep and growth particularly in regions with high gradients. To illustrate the effect of these gradients, a run without lateral hydraulic lateral forces is done using the lateral power and BU profiles presented in Figure 4.11a. Figure 6.15a gives the thermoelastic equilibrium at BOC. Since the highest gradients are found at the core extremities, larger effects can only be appreciated near the core baffle. The FAs bend in the direction of increasing thermal gradients at the outer FA positions. A clear difference between the fresh FAs and the high-BU FAs becomes visible although a similar thermal gradient is present over the two outer FAs. The bending is much stronger for the fresh FAs since the FRs are still tightly coupled to the FA structure while for the high-BU FAs the Zr-alloy grid springs are nearly relaxed and transmit hardly any coupling forces on the structure. At EOC, Figure 6.15b, a permanent FA bow in the direction of increasing gradients is appreciable. This is due to the differential GT growth causing a positive total strain gradient in the direction of increasing flux, see Figure 6.16a, which gives the lateral strain gradients over the GTs at grid 5 for FA 1 with BE growth. Still, only relatively small bow amplitudes below 1 mm are observed. This is because during operation the differential growth is compensated for by the differential creep of the compressed GTs. The total strain gradient takes consequently relatively low values. Figure 6.15c gives the results after one cycle of operation for the case with UB growth rates. The FAs exhibit a significantly stronger permanent deformation at EOC when compared to the BE case. This is due to the high differential growth as a result of the accelerated growth rate, which exceeds significantly the differential creep in the opposite direction, see Figure 6.16b. In addition, the deflection amplitudes are promoted by the decreased stiffness of the FAs as a result of quickly increasing HD forces due to the accelerated axial growth, but only to a minor extent. For the conventional-alloy FAs at the left, the maximum deflection reached under operation is of about 5.6 mm for FA 1, for the advanced-alloy FAs with roughly half the growth rate the maximum deflection is somewhat over 3.3 mm for FA 15. Figure 6.15d illustrates additionally the deformation shapes obtained for the high-growth case in the hanging ex-core condition, that is, after releasing the FAs from all mechanical constraints and lifting the FAs out of the core. In the ex-core condition, the maximum bow amplitude, FA 1, increases to 5.92 mm since the lateral support provided previously by the neighboring FAs is released. On the other hand, the deflection of FAs 2 to 4, 6, and 14 decreases since

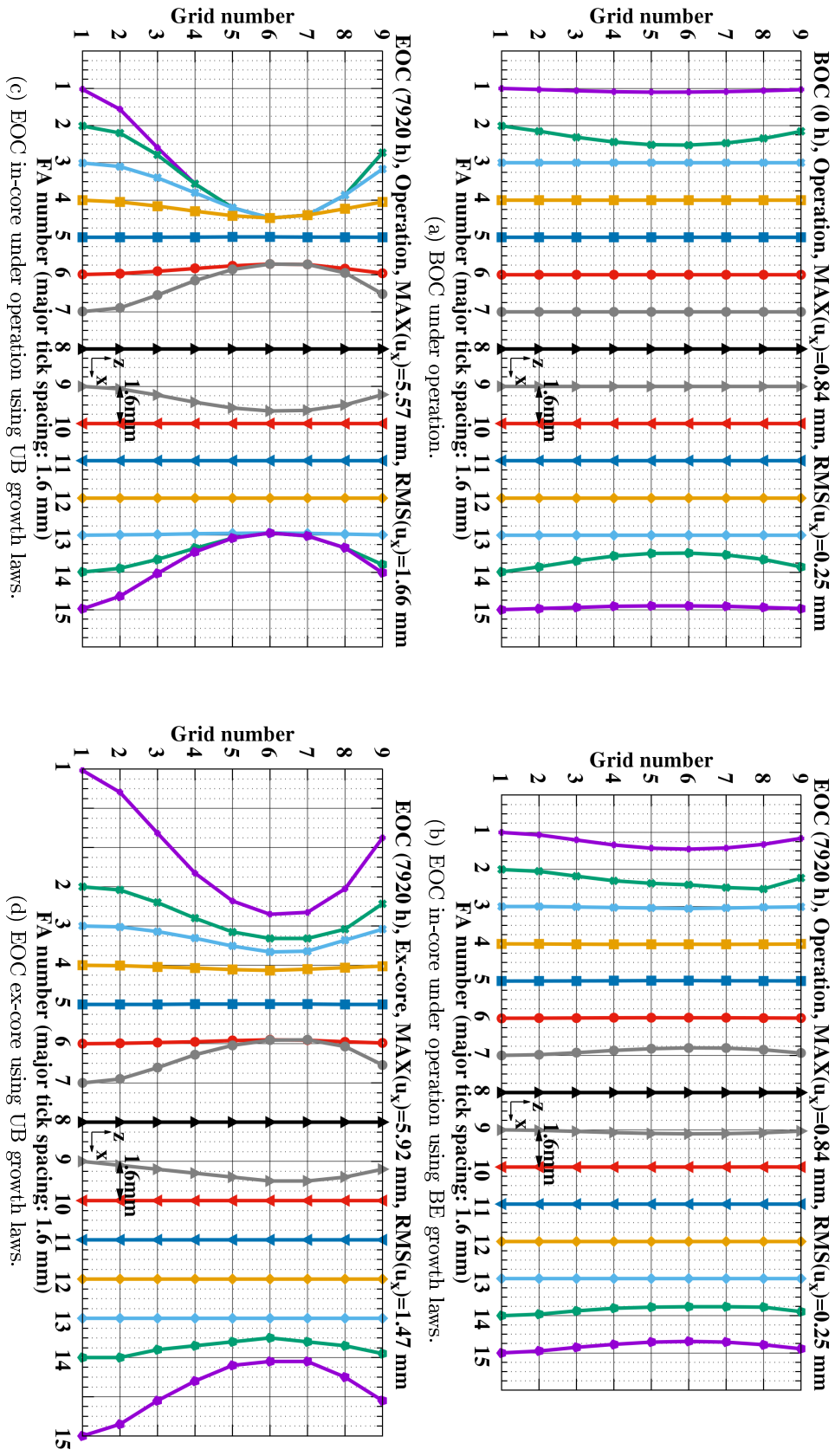


Figure 6.15: FA deformations for different operation states under the effect of thermal and flux gradients without hydraulic forces. FAs 1 to 8 consist of Zry-4 materials and FAs 9 to 15 of advanced Zirconium alloys.

their deformation resulted mostly due to the mechanical coupling with a neighboring FA. Furthermore, the stress stiffening effect contributes to the amplitude decrease. This is because after removing the HD force and lifting the FAs, tensile stresses are present in the GTs. Therefore, also the deflection of FA 9 is reduced although it has not been in contact with neighboring FAs. In conclusion, UB differential growth can cause significant FA bow amplitudes at FA positions with high flux gradients. The overall effect on the remaining FAs in the core is, however, rather small.

Comparing the conventional-alloys FAs at the left with the advanced-alloy FAs at the right, it can be concluded that the deflection can be reduced by half using FAs with advanced alloys. This demonstrates the importance of the alloying condition for the bow problem. Moreover, the results illustrate the significance of uncertainty analysis for bow problems. When using BE laws, only moderate bow is observed for both Zry-4 and advanced materials. Using UB laws, the deformation amplitudes increase significantly due to high differential growth in regions with high flux gradients.

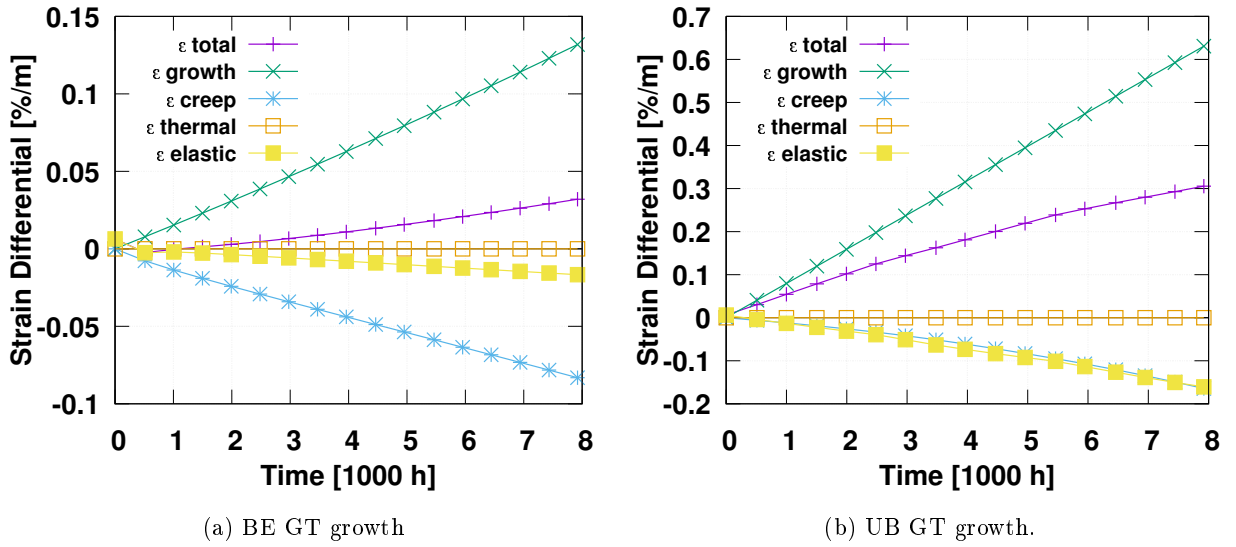


Figure 6.16: Lateral strain gradients $\Delta\epsilon/\Delta x$ at grid 5 over the GTs of FA 1 for BE and UB GT growth.

6.3.2 Reference case: symmetric hydraulic forces with best estimate (BE) creep and growth

To create the reference case, the symmetric hydraulic load distribution from Figure 5.14 is imposed on the FAs additionally to the thermal and flux gradients and BE creep and growth laws are used for the simulation. Figure 6.17a depicts the thermoelastic equilibrium in the FA row at BOC. While the medium-BU and high-BU FAs are clearly deformed in the direction of the hydraulic force, the fresh FAs exhibit only little deformation. Although these FAs undergo an important outwards-directed hydraulic load, both directly due to the applied hydraulic forces and indirectly due to the contact forces from the two neighboring FAs, the inward thermal bending nearly cancels out this effect since the thermal gradient acts in the opposite direction of the hydraulic load. As operation advances and the stiffening effect due to the grid-to-rod coupling diminishes in the fresh FAs, more and more contacts are gradually closed between the outer FAs, forming a cluster of mechanically coupled FAs. This cluster of FAs moves slowly towards the core baffle. At middle of

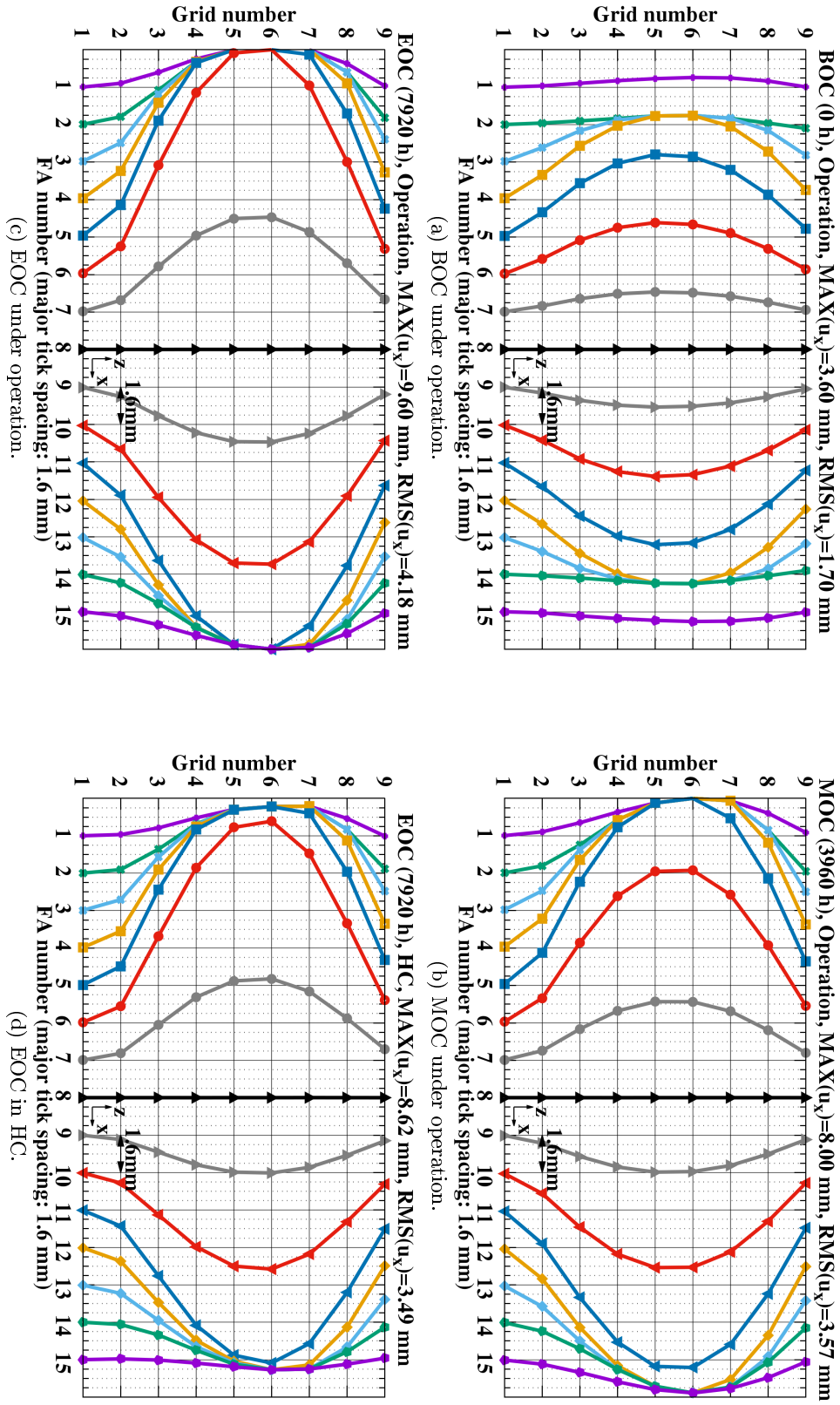


Figure 6.17: FA deformations for different operation states with symmetric hydraulic forces. FAs 1 to 8 consist of Zry-4 materials and FAs 9 to 15 of advanced Zirconium alloys.

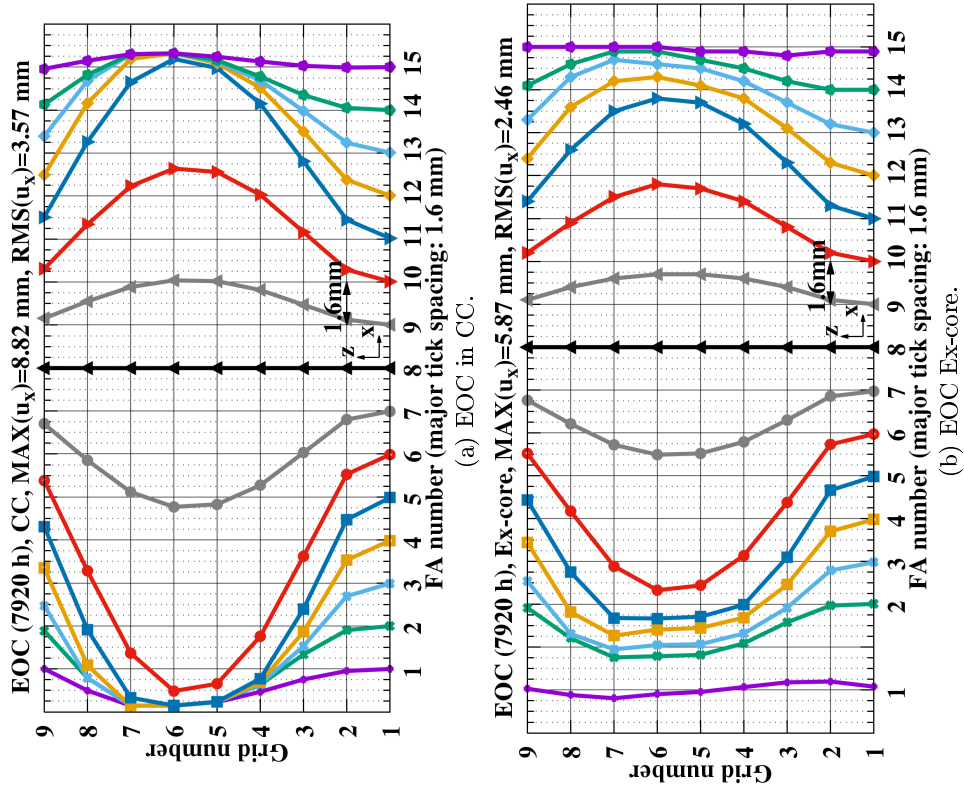


Figure 6.18: FA deformations for different cold EOC states after operation with symmetric hydraulic forces. FAs 1 to 8 consist of Zry-4 materials and FAs 9 to 15 of advanced Zirconium alloys.

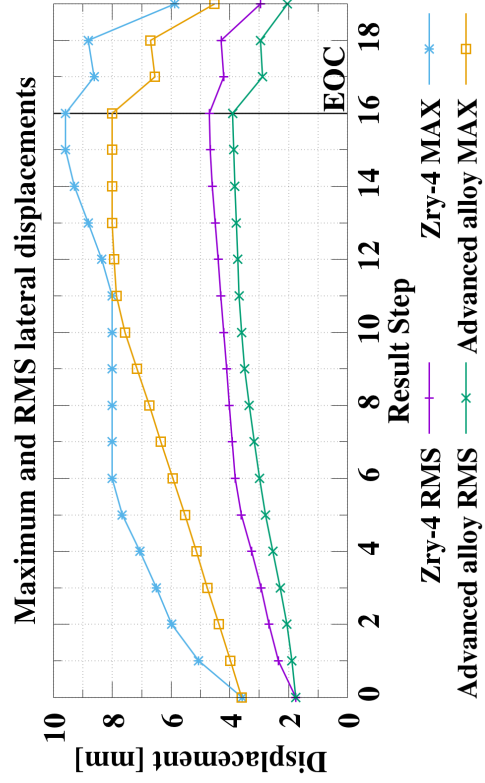


Figure 6.19: Evolution of maximum and RMS displacements for the reference case.

cycle (MOC), Figure 6.17b, the contact with the core baffle is closed for the conventional-alloy FAs and is about to close for the advanced-alloy FAs. At EOC, Figure 6.17c, the six outer FAs and the core baffle are coupled when using the conventional-alloy FAs. For the advanced-alloy FAs, the deformation rate is only about half as fast. After releasing the hydraulic forces and transition to HC, Figure 6.17d, only a minor change in amplitude is appreciated for FAs 2 to 5. This means the hydraulic lateral load was finally mainly supported by the core baffle and the outer FA and not by the elastic straining of the FAs. After transition to CC, Figure 6.18a, the deformation increases somewhat due to the increased HD forces. Figure 6.18b finally gives the ex-core condition. It becomes clear that before opening the gaps, the outer FAs have supported the inner FAs since the deflection of the outer FAs 1 and 15 decreases while that of the neighboring FAs increases. The FA deflection amplitudes generally decrease compared to the in-core CC due to the stress stiffening effect when lifting the FAs. FA 6 undergoes the largest deflection of nearly 6 mm or more than three times the initial FA gap size.

To summarize, Figure 6.19 gives the evolution of the maximum and root mean square (RMS) displacements over the entire cycle including the reactor shutdown steps depending on the used alloy. During operation, a stepwise increase is observed for the maximum amplitudes due to the nonlinear effects introduced by the gaps. The RMS amplitudes increase continuously with a decreasing deformation rate because the core baffle places a strong constraint on the total FA deformation. After the transition to HC following the final operation step 16, the deflection of the FAs decreases because the hydraulic forces are removed. With temperature decrease to CC, step 18, the deformation increases somewhat because of increased HD forces in this state. In the ex-core condition, the FA amplitudes finally decrease due to the stress stiffening effect when lifting the FAs. It can be concluded that the use of advanced alloys has the potential to reduce the maximum and average deformations by about one quarter to one third.

6.3.3 First parameter change: asymmetric hydraulic forces with BE creep and growth

For the symmetric cases, the deflection amplitudes are limited by the symmetry BC in the middle of the row. Under perfect symmetry the deflection is limited to a value equivalent to seven gap sizes, that is 11.2 mm in the present case. In reality, asymmetric bow patterns and bow amplitudes up to more than 20 mm have been observed. This indicates that the hydraulic driving force might also exhibit an asymmetric distribution in the core. Accordingly, a asymmetric flow profile has been assumed at the core inlet by shifting to the left the maximum in the middle of the symmetric profile by a distance of two FA pitches, see section 5.2.2. Due to the asymmetric force distribution as a result of the shifted inlet profile, the maxima for the elastic deflection occur for the FAs at the right, see Figure 6.20a. Due the increased forces and due to the fact that the forces attack more centrally, the elastic deflections are higher than for the symmetric case with a maximum of 7.61 mm for FA 10. The plot shows also the importance of the concept of the equivalent force introduced in section 5.2.3. Although FA 6 undergoes a clearly smaller total lateral force than FA 4 according to Figure 5.14b, its maximum deflection is larger. This is linked to the fact that the equivalent force, which is larger for FA 6, is more relevant for an estimation of the maximum deflection. Due to the higher elastic deformation and the inherently higher stresses, also creep will be faster than for the symmetric case. At EOC under operation, Figure 6.20b, at least one contact is closed from FA 9 to 15. Due to the unilateral force on most FAs, mostly C-shapes are created. Only the FA 5 undergoes forces in opposite

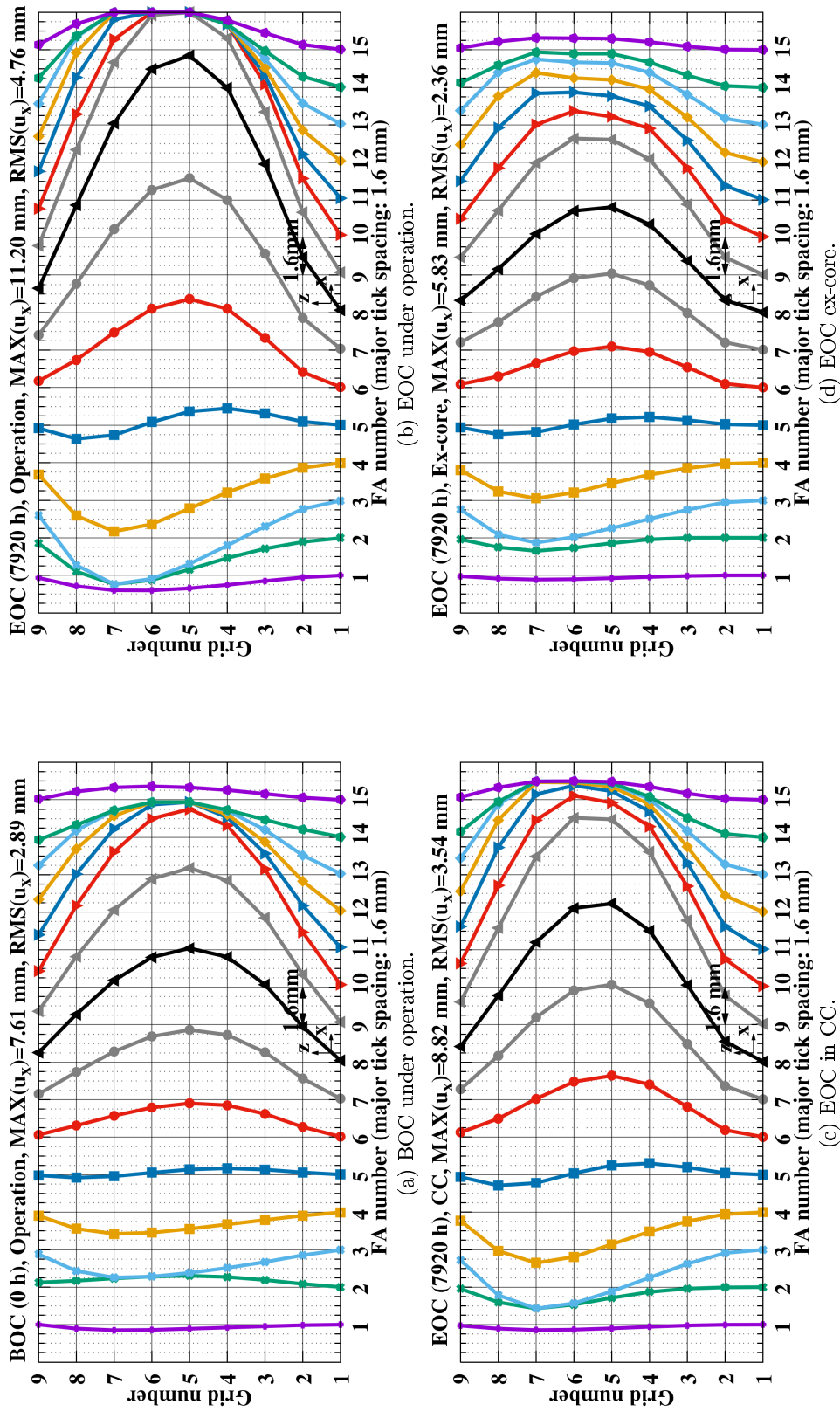


Figure 6.20: FA deformations for different operation states with asymmetric hydraulic forces using advanced Zirconium alloys.

direction at the bottom and the top and exhibits consequently a S-shape. Figures 6.20c and 6.20d finally give the deformation states at EOC in CC and ex-core.

6.3.4 Second parameter change: creep and growth uncertainties

With the second parameter change, we account additionally for the effect of the uncertainty in the creep and growth models. To assess the variability of the solution due to the uncertainty about the creep and growth, two extremal cases are defined which create maximum and minimum deformations in the core. That is, we seek to create one simulation with maximum positive (+) amplitudes and one with maximum negative (−) amplitudes, only by modifying the creep and growth rates within the uncertainty bounds defined in sections 4.2.1 and 4.3.1 and without changing the hydraulic condition. As flow BCs, the asymmetric hydraulic condition due to the shifted inlet flow profile is chosen. That is, the results in Figure 6.20 represent the BE case.

Table 6.4: Creep and growth models used for the different FAs in the core row for the two extremal cases: lower bound (LB), best estimate (BE), or upper bound (UB).

Case	FA #:	1	2	3	4	5	6	7	8	9	10	11	12	13	14	15
(−)	Creep	UB				BE	LB									
	Growth	BE						UB	BE							UB
(+))	Creep	LB				BE	UB									
	Growth	UB	BE						UB	BE						

Table 6.4 summarizes the creep (including creep relaxation) and growth conditions assumed for the different FAs to generate the different bow patterns. As for the growth, only UB and BE conditions are distinguished to differentiate between FAs which undergo or not breakaway growth. The UB conditions are assumed for those high-BU FAs that will bend in the respective direction due to differential growth. As for the creep, UB conditions are assumed for the FAs with prevailing lateral force in the respective direction and lower bound (LB) creep in the opposite direction, see the force histogram in Figure 5.16b. For FA 5, which is loaded similarly in both directions, BE conditions are assumed.

Figure 6.21 gives the different results. Important differences exist between the (−) case and the (+) case, regarding both the FA deformation amplitude and pattern. For the FA exhibiting the maximum bow amplitude, at grid level 6 of FA 9, a variation of approximately $\pm 25\%$ about the value obtained for BE creep and growth can be observed. That is, the maximum amplitude may be increased by almost 50% merely due to the uncertainty about the creep law. As for the deformation pattern, a particularly strong effect becomes evident for the peripheral FAs undergoing UB growth. The inward bow due to the accelerated differential growth significantly outweighs the bow due to creep as a result of the outward hydraulic forces. The deformation amplitude and shape of the concerned FAs change strongly when compared to the BE case. That is, there is a high uncertainty about the final deformation pattern for the high-BU FAs placed at positions with high flux gradients.

Figure 6.22 gives the total deviation of the lateral displacements u_x due to the joint effect of both parameter changes. That is, it compares the results of the reference case with symmetric hydraulic forces with the results of the extremal case with a shifted coolant inlet velocity profile and UB creep for the FAs at the right. In this extremal case, there is a maximum deviation in deflection amplitudes of 6.88 mm while the maximum displacement in the reference case was 4.52 mm. The RMS variability of the displacements is

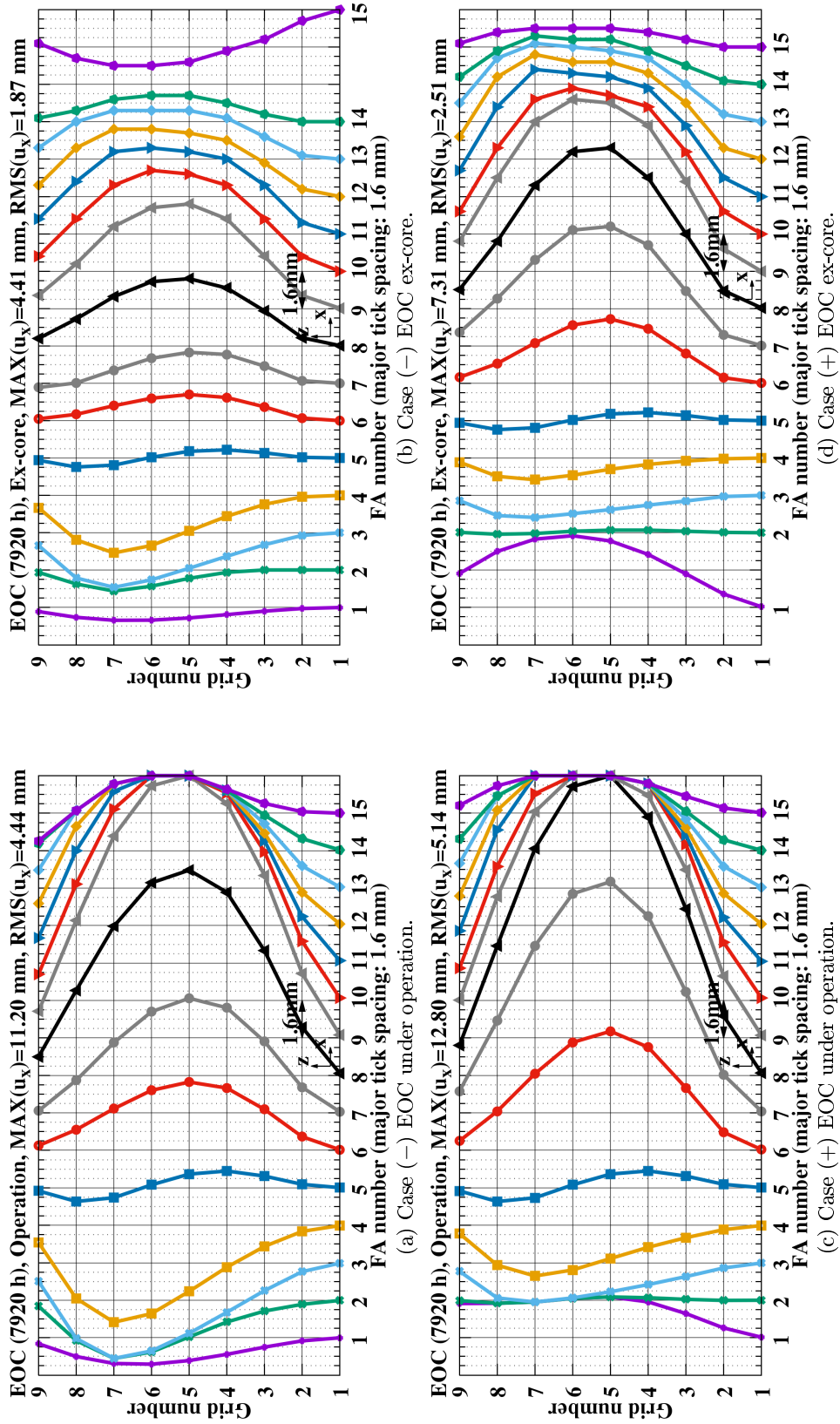


Figure 6.21: FA deformations for the two extremal cases defined in Table 6.4 with asymmetric hydraulic forces using advanced Zirconium alloys.

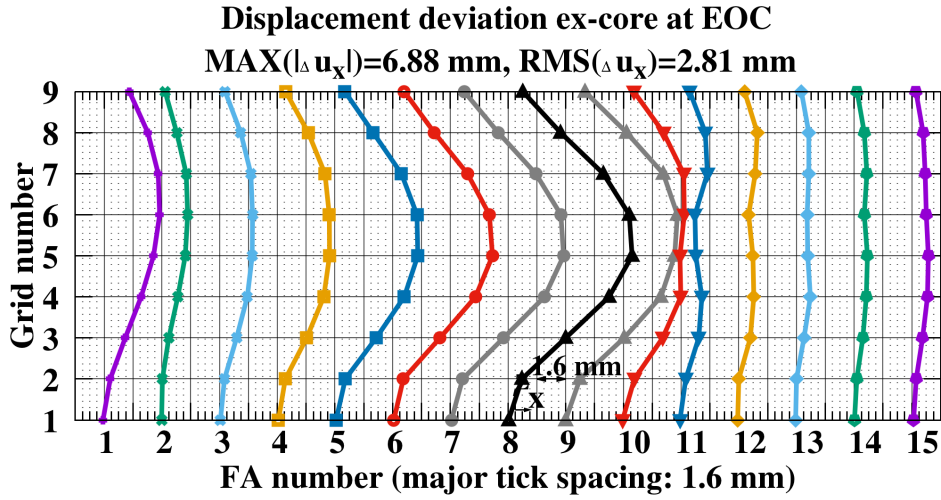


Figure 6.22: Deviation of ex-core lateral displacements u_x at EOC between the reference case and the case with extremal parameter changes.

2.81 mm while the RMS of displacements of the reference is 2.04 mm. The variability of the results due to the uncertainties in the modeling are hence of the same order of magnitude as the deformations themselves. That is, the bow pattern may be modified fundamentally under unfavorable circumstances. Certainly, the given results represent an extremal case; but they demonstrate that a good knowledge of the specific creep behavior and the core hydraulic condition is crucial for making reliable predictions.

6.3.5 Analysis with initially bowed elements

The objective of this analysis is to investigate the effect of initially bowed elements on the FA row as compared to the system under the same conditions without initial bow. It is important to analyze this effect in order to estimate how influential the initial deformation state at BOC is on the outcome of the bow pattern at EOC. This provides, for example, an idea to which degree highly precise measurement techniques for measuring the FA bow are necessary and how much effort needs to be invested in the accurate prediction of the in-core FA deformation at BOC. The evident effect of setting bowed FAs next to straight FAs is that contact with the neighboring FAs is established at least at the grid level with maximum amplitude if the bow amplitude is larger than the gap size. The bowed FAs then exert lateral loads on the neighboring FAs, thus modifying the strain distribution and consequently the creep rate and direction. It is expected that, if no other lateral loads are present, the initially straight FAs will be permanently deformed according to the shape of the neighboring initially bowed FA. Inversely, the bow amplitude of the initially bowed FA itself will be reduced due to the reaction force as a result of the contact with its neighbors.

The analysis consists of two reactor cycles. In the first cycle, initial plastic bow shapes are imposed on three FAs. The bow shapes and amplitudes to be created are defined according to the typical observations in PWRs with deformed cores, namely:

- one FA with an S-shape, placed at position 5;
- one FA with a C-shape and high deformation, placed at position 11; and

- one FA with a C-shape with reduced deformation, placed at position 14.

For sake of simplicity, discrete lateral forces are applied at those grid levels which are to exhibit the maximum amplitude. For the C-shape, the force is exerted at grid level 5; for the S-shape, forces are applied in opposite directions at grid levels 3 and 7. To obtain an S-shape with similar amplitudes at the top and bottom, the absolute value of the force at grid level 3 is chosen twice as high than at grid level 7 to account for the fact that the FA stiffness is higher in the lower part of the FA and the creep is increased in the upper part. In this first cycle, no contact between neighboring FAs is considered. That is, the initial gap size is chosen large enough so that no contact between the FAs occurs. The unloaded – and not to be bowed – FAs form already part of this cycle, but no creep and growth calculations are performed. In the following second cycle, contact is established between the pre-bowed FAs and the straight FAs and creep and growth is activated for all FAs.

Figure 6.23a depicts the elastic deformation of the initially considered FAs as a result of the applied forces. All FAs are assumed to be medium-BU FAs with an average fluence of $\Phi = 4 \times 10^{21} \text{ n cm}^{-2}$. The resulting ex-core bow shapes after one cycle are given in 6.23b. Figure 6.23c gives the equilibrium in CC at the beginning of the following cycle once the pre-bowed FAs are coupled to the other straight FAs. The initially bowed FAs are restrained by their neighboring FAs, thus inducing lateral reaction forces at the contact levels. Due to the structural support by the neighboring FAs, the deflection amplitude of the pre-bowed FAs decreases. This effect is most pronounced for FA 11, for which the deflection is reduced by more than one third. Due to the coupling, nearly the entire FA row is deformed previous to operation of cycle 2. In this second cycle two cases are analyzed. The first case considers no lateral hydraulic forces. That is, a uniform core inlet and outlet velocity profile is assumed. In this manner, the effect of the initially bowed FAs can be analyzed as an isolated phenomenon. In the second case, hydraulic forces from the symmetric profile are imposed during the second cycle, resulting in the deformation state depicted in Figure 6.23d at BOC 2.

For the first case, no major movements are detected during the reactor cycle due to the lack of additional forces, see Figure 6.24a, which gives the deformation state at EOC 2. Due to the constant deformation state, a typical relaxation process progresses during operation. The elastic strain is gradually converted into plastic creep strain while the total strain remains nearly constant. Figure 6.24b gives the final ex-core deformation shapes. Due to the mechanical coupling between the FAs, the deflection amplitude of the FAs with initial bow is reduced, up to nearly one half for FA 11. On the other hand, the FAs neighboring the pre-bowed assemblies remain permanently deformed due to the interaction.

For the second case, the deformation during operation is dominated by the hydraulic forces; however, the pre-bowed FAs introduce additional perturbations and modify the bow pattern. Figure 6.24c shows the final operation state at EOC. As for FAs 3 and 14, the hydraulic loads appear to outweigh the pre-bow effect. For FA 11, the deformation shape is still strongly influenced by the initial bow. The final ex-core deformation can be appreciated in Figure 6.24d. Due to the effect of the unilateral hydraulic forces, the S-shape of FA 3 has transformed into a C-shape with a maximum in the lower portion of the FA. FA 11 forms now a W-shape and the amplitude is reduced to less than a quarter of the original value whereas the initial bow direction of FA 14 has been inversed by the creep deformation due to the hydraulic loads. Altogether, a clear difference in the final bow pattern can be observed when comparing the deformation to the reference state with only initially straight advanced-alloy FAs in the right half of Figure 6.18b. This confirms a strong effect of the initial bow on the final bow patterns.

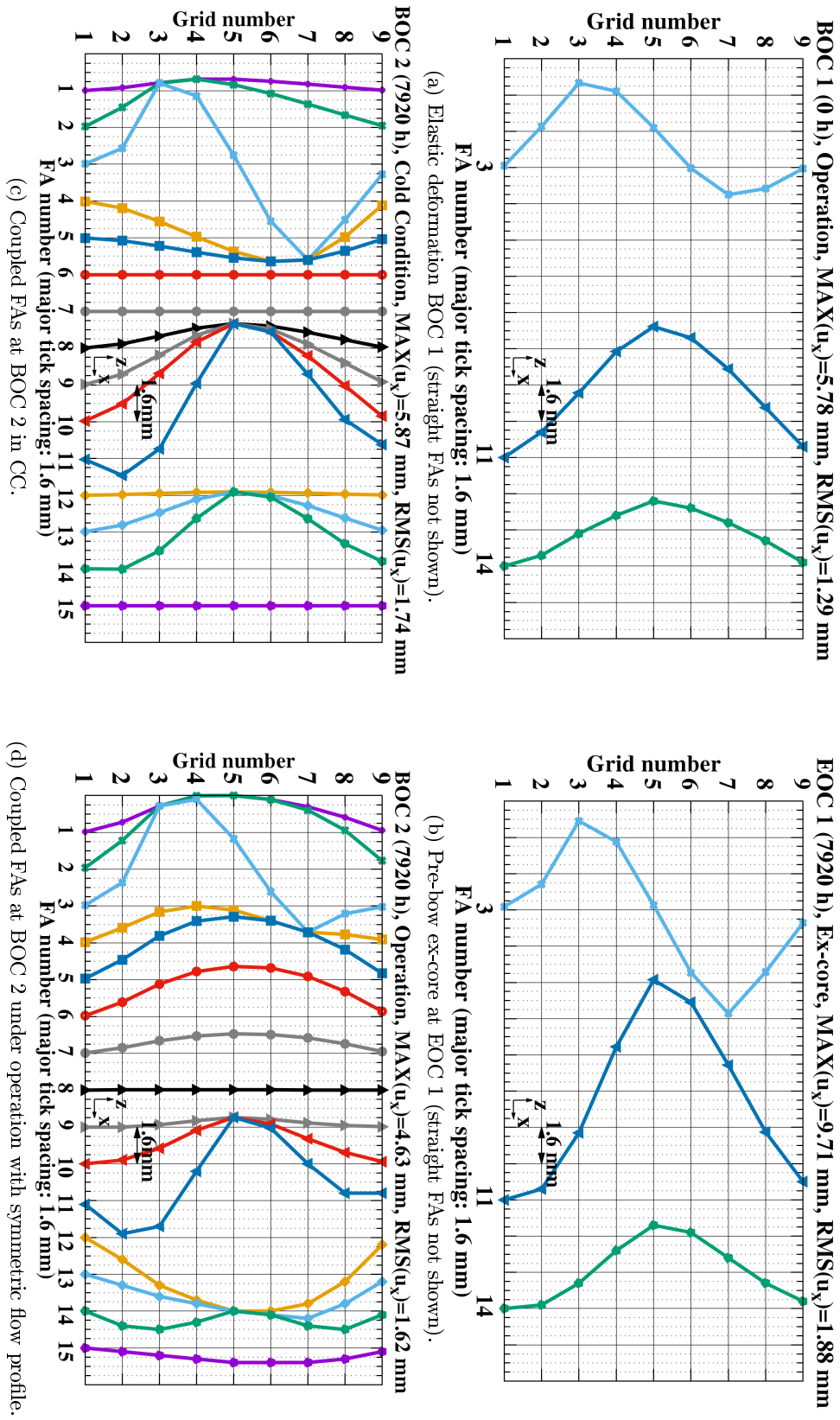


Figure 6.23: Preparation runs to create a core configuration consisting of both undeformed FAs and FAs presenting initial bow.

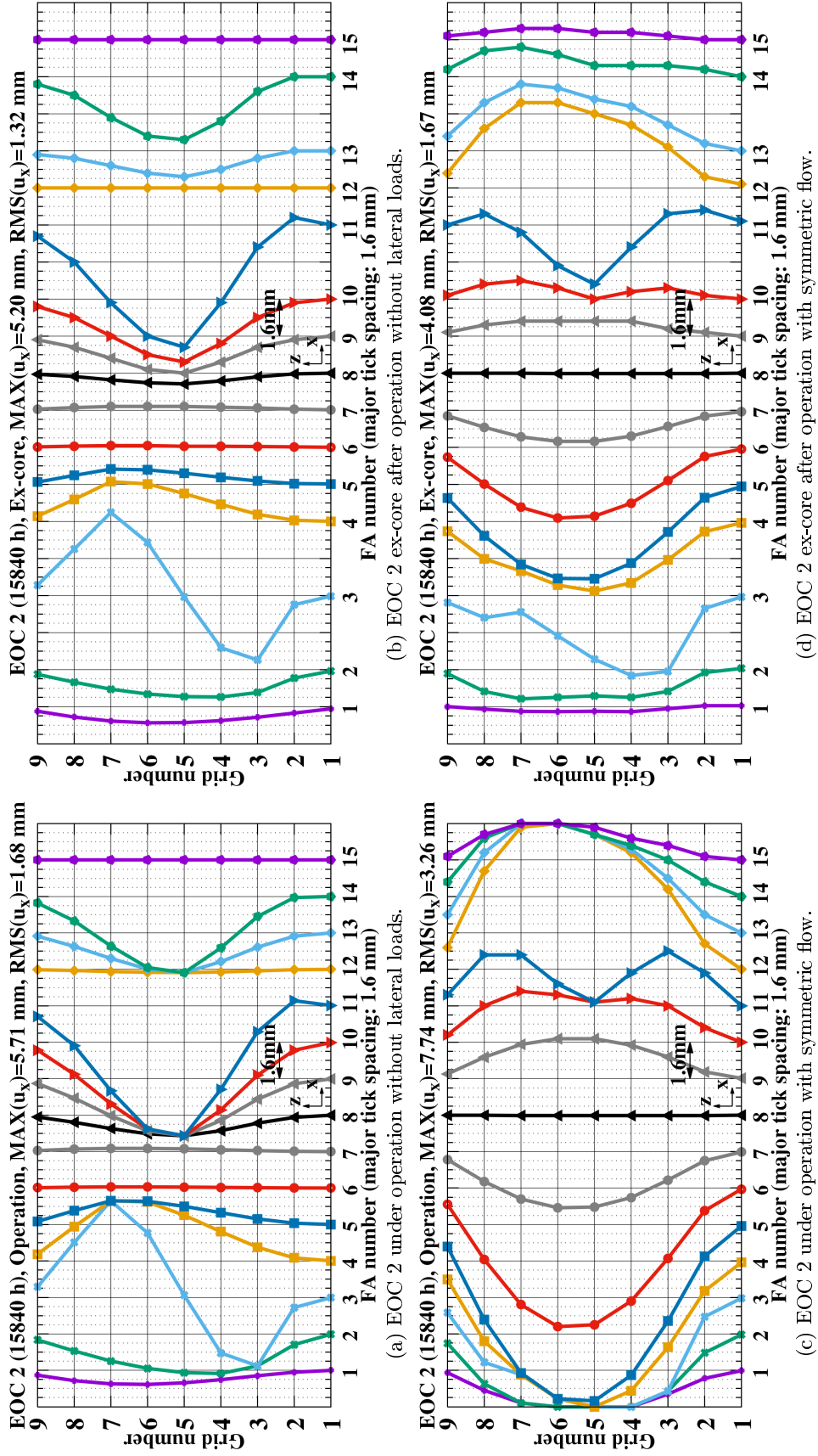


Figure 6.24: FA deformations when introducing FAs with initial bow.

6.3.6 The effect of fluid-structure interaction (FSI)

So far, only a one-way coupling from the fluid to the structure has been considered. That is, the coolant flow acts on the FA structure by means of a hydraulic force distribution but not vice versa. An additional effect is added when considering a two-way FSI between the coolant and the FA structure. That is, the feedback of the deformed structure on the flow is accounted for. Due to the bowed FAs, the gap sizes between the FAs are modified. This can lead to a redistribution of the flow in the core and therefore to a modified lateral force distribution on the FAs. Details about the applied FSI modeling method are given in section 5.4 and by Ruiz Antón (2016).

The reference case chosen for this simulation is the first run case described in section 6.3.5 which includes initially bowed FAs but no lateral hydraulic forces. In this manner, we can investigate the isolated effect of the lateral hydraulic forces resulting from the flow redistribution due to the deformed core. The initial configuration for the FSI calculation is hence the one given in Figure 6.23c, in which the deformation of the core is plotted after coupling the initially straight FAs and the FAs with initial bow. This deformation state represents the initial condition for the porous-medium CFD calculation. Figure 6.25a gives the resulting flow forces on the deformed FAs due to flow redistribution in the core. The flow forces are maximum over the most deformed FAs and their orientation indicates that the flow is pushed away from closing gaps towards their neighboring gaps that are opening up. Figure 6.25b gives the resulting thermoelastic equilibrium at BOC 2 accounting for the hydraulic forces due to the deformed core. The arrows emphasize schematically the path of the flow redistribution causing the hydraulic forces in Figure 6.25a. However, the predicted forces due to FSI are about one order of magnitude smaller than the hydraulic forces due to the non-uniform flow profiles at the inlet and outlet. Note that, for example, a scale of 400 N/m per FA distance is used in Figure 5.14 while in 6.25a it is 100 N/m per FA distance. Therefore, only minor deformations are induced due to the flow redistribution. Due to the small feedback of the structural deformation on the flow field, a large load step size of $\Delta t_{\text{load}} = 1000$ h can be used for the operation load steps. Figure 6.25c gives the final ex-core deformation of the FAs after performing eight load steps according to the coupling scheme in Figure 5.17. Only small changes can be appreciated when comparing the bow shapes with those obtained without FSI in Figure 6.24b. To highlight the effect of FSI, Figure 6.25d gives the displacement deviation Δu_x between the cases with and without FSI. Although the absolute effect on the final deformation is rather small, it can be appreciated that FA 3 has been pushed somewhat to the left because of the outward cross-flow over the central FA section. For the same reason, FAs 11 and 14 have been pushed somewhat to the right. The outward flow forces on the two outer FAs induce additional outward bow. These hydraulic loads are, however, a result of the boundary effect of the flow at the core baffle and not due to the flow redistribution. In conclusion, the FSI has only a minor effect on the final bow shapes. Due to the flow redistribution, both loads counteracting the initial deformation are generated, mostly in the lower part of the domain, and loads enhancing the initial deformation, mostly close to the outlet. Due to the coolant advection, the former loads attack more centrally and, consequently, outweigh the effect of the latter. Consequently, FSI with deformed FAs tends to decrease the bow amplitudes of strongly deformed FAs.

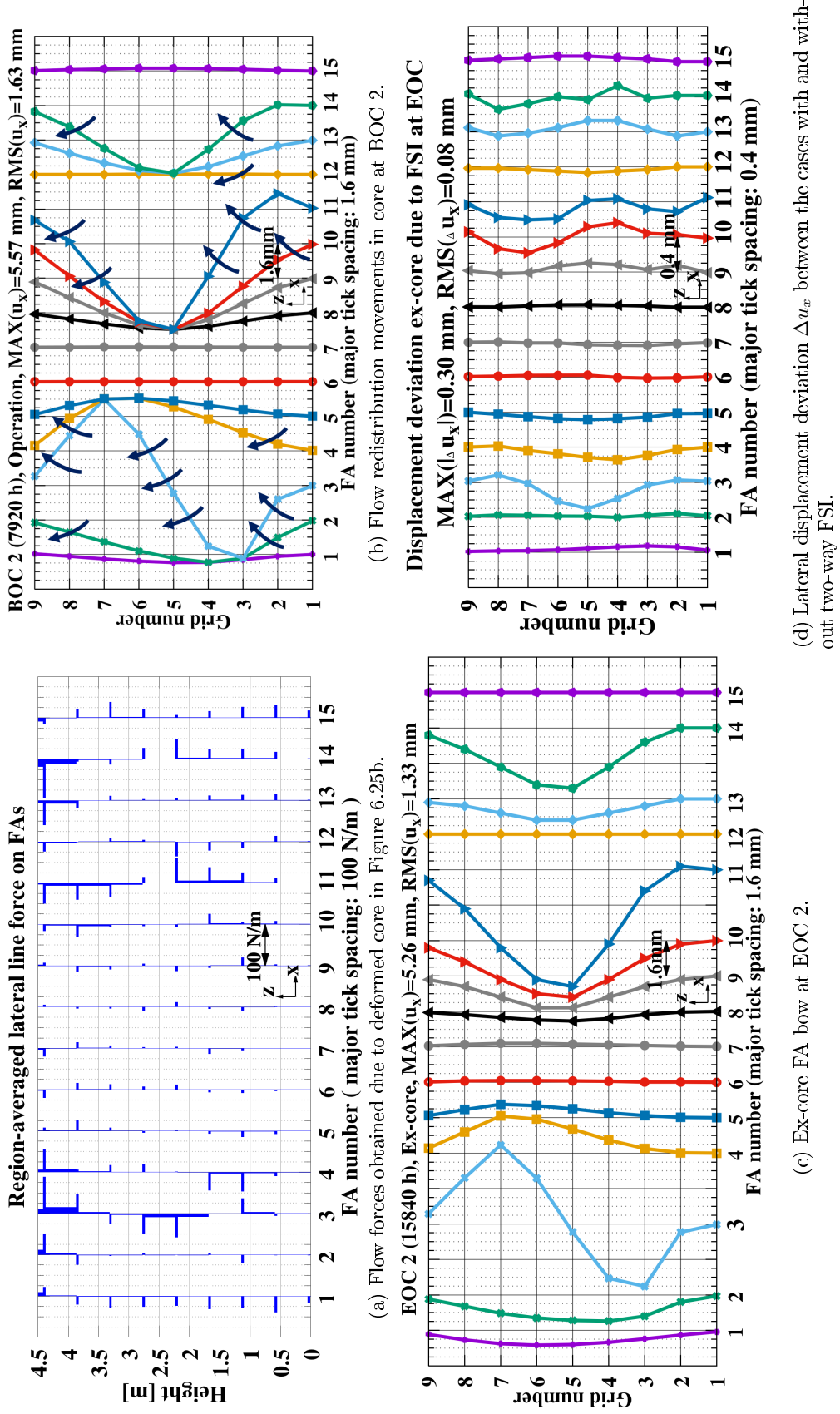


Figure 6.25: Flow forces and FA deformations accounting for two-way FSI with uniform core inlet and outlet profiles.

Chapter 7

Conclusions and Outlook

This final chapter summarizes and discusses the particularities of the developed FA bow model, the obtained analysis results, and the conclusions that can be drawn. In this context, an outlook on possible future work is also given with the objective to further develop the FA bow model.

7.1 Summary of achievements

7.1.1 Development of a computational FA bow model

FA structural model The first major step in this work was the set-up of a structural model of a generic PWR FA with the FEM code ANSYS Mechanical APDL, described in chapter 3. The most important model features can be summarized as follows:

- The FA structural model has been designed as a full 3D model, taking into account that the deformations in the cross-sectional directions are not independent of each other due to the nonlinearities in the fuel rod (FR) support and the creep laws. Common 2D-only FA structural models neglect these nonlinearities and calculate separately the deformation of each FA row in each lateral direction of the reactor core.
- A model reduction method was developed, which decreases the run time and memory expenses by more than two third for the 3D model and more than 80% if only two dimensions are considered, see section 3.4.
- The axial and lateral out of pile (OP) structural response of the generic FA model used in this work has been validated qualitatively with deflection tests of fresh fuel assemblies (FAs), see section 3.5.
- The generic FA structural model can be adapted flexibly to any common PWR FA design of interest by modifying the concerned structural parameters. As an example, a model parameter calibration procedure was presented in section 3.6. With this method, a very good fit to OP deflection test data of a specific FA design could be obtained.

- Based on the validated OP structural model, the in-core FA response can be predicted by applying creep, growth, and relaxation models.
- By laterally coupling the FAs with gap-contact elements at the grid levels, a FA row model can be created, which may also be extended to a 3D full-core model.

Several in-reactor simulation test cases demonstrated the capabilities of the model and served as best estimate (BE) simulation experiments for the sensitivity and uncertainty analyses, whose results are summarized in the following section 7.1.2. The observed in-reactor FA model response is in good agreement with what is observed for reactor FAs:

- A majority of C-shapes was detected for the permanent bow after one reactor cycle in the FA row calculations in section 6.3, but also S- and W-shapes were observed.
- A collective movement of the FAs in the simulated FA row was observed under the effect of the lateral hydraulic forces, creating characteristic bow patterns after one cycle which depend on the specific hydraulic force distribution, see sections 6.3.2 and 6.3.3. This is very similar to the collective bow patterns observed in real reactor cores, see Figures 1.4a or 1.9a, for example.
- The model also demonstrates a good performance concerning the prediction of the stress stiffening effect. As observed for FAs in the reactor core, a significantly lower stiffness is obtained under a compressive holddown (HD) force than under a tensile lifting force when unloading the core.

Creep, growth, and relaxation models An extensive literature analysis for available creep, growth and relaxation data has been performed in the context of the definition of the in-reactor model parameters in chapter 4. Both experimental data obtained from irradiated specimens and performance data of real FAs deployed in a reactor core were used. Based hereupon, existing material model laws were examined for their performance and new laws were developed for the description of the in-reactor evolution of creep, growth and relaxation processes. Moreover, characteristic uncertainty bounds were defined for the different model laws based on this data analysis.

Reactor core hydraulic model A hydraulic model based on a porous-medium approach was developed with the CFD code ANSYS CFX to estimate the distribution of lateral hydraulic forces on the FAs in the reactor core, see chapter 5. In this context, different core inlet and outlet velocity profiles were discussed as boundary condition (BC) to demonstrate the uncertainty in the prediction of FA bow.

7.1.2 Analysis of the FA bow model sensitivities and uncertainties

Different sensitivity and uncertainty analyses were performed to investigate the sensitivity of the model to different influencing mechanisms based on the assumed uncertainty range for the concerned model parameters. This section is subdivided according to the most important influencing mechanisms on FA bow, which have been determined in the results section of this thesis.

FA stiffness The first sensitivity analysis in section 6.1.4 screened the FA design for stiffness parameter optimizations which can provide an increase in the lateral FA stiffness. After performing the analysis for

both beginning of life (BOL) and end of life (EOL) conditions, it was shown that the highest overall potential for a FA lateral stiffness increase lies in the modification of skeleton-related stiffness parameters. The largest potential for a FA stiffness increase was attributed to the rotational stiffening of the connection between guide tubes (GTs) and the spacer grid. In addition, even small increases of the GT diameter can significantly increase the FA lateral stiffness at all burnups (BUs).

HD force and FA growth It is well known that increased HD forces decrease the FA lateral stiffness as a result of increased compressive stresses. The occurrence of FA bow has often been ascribed to excessive HD forces due to accelerated FA growth. In the single-FA sensitivity analysis it was found that the sensitivity of the final bow amplitude to increased growth rates, by means of the HD force, is relatively low compared to the influence of lateral hydraulic forces and the creep rates, see section 6.2.3. That is, smaller modifications in the core hydraulics or the use of somewhat different materials causing a potentially higher creep rate are much more likely to cause increased FA bow. This was confirmed in the calculations over one FA row, section 6.3, in which the uncertainty about the hydraulic and creep conditions resulted to have a much higher impact on the solution than the uncertainty about FA growth. A very significant effect of growth on the bow amplitude can only be expected when accelerated FA growth occurs in high-BU FAs at positions with high neutron flux gradients, see section 6.3.1. However, since this effect can be limited to a very reduced number of FAs in the reactor core, the impact on the remaining FAs is rather small.

Creep The sensitivity analysis performed with the single-FA creep deformation test showed that the uncertainties about the creep rate have a significant impact on the final bow amplitude. The FA row structural analysis demonstrated that under unfavorable conditions a variation of approximately $\pm 25\%$ about the BE simulation results can be expected, mostly due to the uncertainty about creep.

In addition, the sensitivity of the solution to the creep resistance of different materials was demonstrated. We observed an important beneficial effect on the FA bow amplitudes when updating the GT materials from conventional Zirconium alloys, such as Zircaloy-4, to more advanced alloys with Niobium content. The use of these advanced alloys in recent years might be one of the reasons that bow amplitudes have become more moderate and excessively bowed cores are only rarely observed anymore. However, this does not eradicate the direct causes for the bow, which is probably due to increased lateral hydraulic forces as a result of a different hydraulic design.

Hydraulic Forces The lateral hydraulic forces appear to be the principal driving force of FA bow. In the sensitivity analyses, the uncertainties about the lateral hydraulic force were shown to account for a large part of the solution variability for both a single FA and the FA row. In addition, the hydraulic forces control for the most part the final bow pattern in the FA row. As a bow-driving mechanism, the differences in the hydraulic loads do not only act on the deformation rate by means of the magnitude of the loads, but also on the bow direction by means of the load distribution. Therefore, changes in the hydraulic condition may fundamentally modify the bow pattern and it is important to further develop the hydraulic model in order to predict the flow as accurately as possible.

Fluid-structure interaction (FSI) Only minor changes have been observed between calculations with two-way FSI and calculations with only a one-way coupling from the fluid to the structure, see section 6.3.6.

The trend of the results, indicating that FA bow amplitudes decrease when applying two-way FSI, is in agreement with the results by Horvath and Dressel (2013) who simulated the FSI between FAs and the coolant flow with a more detailed flow model. However, their calculations predict a substantially higher impact of FSI on the bow amplitude than observed with the present porous-medium model. Experiments by Stabel et al. (2011) also predict a more significant impact of the two-way FSI. Therefore, a further refinement of the present model should be considered to verify the reliability of the model results. Recommendations are given in the last paragraph of section 7.2.

Initial bow Section 6.3.5 presented simulation runs over two reactor cycles, in which only certain FAs were deformed in the first cycle and then coupled to the other straight FAs in the second cycle of the same run. This illustrated how bow patterns can propagate over several cycles. It indicates, furthermore, that if the bow shapes are not measured after each cycle, the initial bow imposes another source of uncertainty for the predictions.

7.1.3 Final conclusions

This thesis demonstrates the important challenges in FA bow modeling. The variability of the results due to the uncertainties in the modeling is of the same order of magnitude as the deformations themselves. That is, under unfavorable circumstances the bow patterns observed in the reactor may differ fundamentally from the bow patterns predicted with BE modeling methods. For a full-core 3D system, that will be implemented in the future, it can be expected that the variance of the bow patterns increases further due to the higher number of degrees of freedom (DOFs). Given the limited knowledge about the processes and the BCs inside an operating core, it appears to be a challenge to predict a specific unique bow pattern. Instead, it is more realistic to determine a distribution of potential bow patterns. To characterize the spread of the model predictions, statistical measures can be introduced in the future to quantify more accurately the expected deviations and their probability of occurrence.

In conclusion, it is recommended that bow calculations be always accompanied by an uncertainty analysis to estimate the variability of the model predictions. Provided that the uncertainties are accounted for, FA bow prediction models may offer in the future important support to operators about the expected bow patterns for a specific core loading plan. For this purpose, the next section proposes new further developments of the presented bow model. In this context, additional measurement data must be acquired for model validation. Moreover, any further development needs to be combined with a continuous effort to decrease the uncertainty range for the mentioned BCs and model parameters. To reach these goals, a joint effort of reactor operators, fuel suppliers, and academic institutions is required.

7.2 Towards a validated full-core FA bow model

There is a continuously strong interest by reactor operators for tools offering a reliable prediction of the FA bow. Specific fields of interest are, for example:

- the estimation of the impact of future hardware changes. The analysis of these effects can help to avoid strongly deformed cores in the future or even to further reduce FA bow amplitudes.
- the prediction of the water gap distribution in the operating core. The FA bypass water gaps are an im-

portant input parameter for reactor neutronics codes to predict modifications in the power distribution due to opened or closed inter-FA gaps.

It is therefore of great interest to further develop the present bow model to provide an accurate prediction of the bow amplitudes. For this purpose, a larger focus needs to be set on the model validation. That is, the generic model results need to be validated quantitatively with in-reactor measurements to verify the performance of the predictions. The following paragraphs present a possible roadmap for the development of a validated tool for FA bow predictions. A stepwise validation and calibration strategy is offered, making it possible to gradually extend the functionality of the model by adding new model features and simultaneously adjusting the model performance to provide more and more realistic simulation results. The steps are arranged in the order of increasing complexity, both regarding the implementation of new features and the effort necessary for the validation or calibration. This roadmap represents one of many ways of proceeding and has the necessary condition that the mentioned validation data are available.

Adaption to a specific FA design To provide reliable results, the first step is to adapt the FA model to the FA design of interest by modifying the number of FRs and GTs, the geometric dimensions, and all available stiffness parameters. Specific design features, such as the material models and the details of the FR support, should also match the considered FA type. Finally, the good fit of the model results to experimental data of OP deflection tests is to be verified and, if necessary, a calibration is to be performed. Section 3.6 presents an example of such a calibration procedure.

FA EOL lateral stiffness In addition to the deflection tests of fresh FAs, FA lateral deflection tests at EOL are sometimes performed to assess the stiffness decrease of the FA during the residence time in the reactor. Such measurements can confirm that the grid-spring relaxation and gap-opening model offers a good prediction of the FA stiffness decrease during BU. Calculation results of this type are given in section 6.1.3. Such a validation would be the first step to gain more confidence in the bow calculations because prediction errors of the lateral FA stiffness act directly on the stress distribution in the FA and therefore on the creep rate.

Creating bow shapes as initial condition As a preliminary step to any validation based on initially bowed FAs, a methodology must be developed to create permanently bowed FAs with similar deformations to the measured ones. This is because the deformation must not be due to external loads but due to plastic creep and growth strains. That is, the elastic stresses in the structure must be converted into creep strains over several irradiation time steps so that the desired geometric shape is “burnt” in. A similar procedure was applied in section 6.3.5 where a configuration of lateral forces has been estimated to create FAs with initial bow.

Transition ex-core to in-core Since most bow measurements are performed ex-core, the transition from the ex-core bow to the in-core bow is one of the crucial steps in bow modeling and remains one of the large unknowns. This relates to the change in bow shape and amplitude between the completely unconstrained state ex-core and the strong constraints inside the reactor, that is, the axial HD constraint, the lateral and rotational constraints at the FA bottom and top, as well as the inter-FA contacts. The HD constraint acts on

the FA lateral stiffness by means of the stress stiffening effect. Confirming the good prediction of the stress stiffening behavior of the FA represents therefore a first important step towards validating the transition between the in-core and ex-core condition. For bowed FAs after irradiation, the stress stiffening causes, for example, a decrease of the bow amplitude between the unconstrained FA standing in the core at end of cycle (EOC) and the hanging state after the FA has been lifted out of the core, see the transition from step 20 to step 21 in Figure 6.4a. Based on FA bow measurements performed in both standing and hanging conditions, we can validate that the code predicts reliably the effect of the HD force on the FA bow amplitude and the FA stiffness.

In few cases, measurements are also performed for certain FAs at EOC both in-core in cold condition (CC) and ex-core. With this data, the full effect of releasing the structural constraints on the FAs in the reactor core can be validated. That is, we can assess how well the code predicts the displacement decrease due to the release of the in-reactor rotational constraints and the HD forces, which corresponds to the transition from step 18 to step 21 in Figure 6.4a. However, in a strongly deformed core, the inter-FA forces acting on the FAs in-core at EOC could significantly modify the in-core deformation. That is, the row model, or potentially a full-core model, would need to be used for the validation and the measurements would need to be done at least over one FA row in the core.

Full-core water gaps at BOC or EOC Once a good performance for the transition between the ex-core and in-core conditions has been confirmed for single FAs, we can proceed to the next validation step, namely the prediction of the water gaps between the FAs in the core at beginning of cycle (BOC) and EOC. Increased water gaps in some regions, and decreased gaps in others, potentially increase the quadrant power and neutron flux tilt in nuclear reactors (Andersson et al., 2005). Since the in-reactor neutron flux is measurable online during operation, such changes might be detectable. If the predicted power tilt agrees with the measured values, this confirms that the water gaps have been indicated accurately. By this means, an indirect validation of the accurate prediction of the in-core deformation state might be possible.

A full-core model, which is discussed in the next paragraph, is necessary in most cases to predict the water gaps. At BOC, high inter-assembly coupling forces are likely to occur between the FAs since after the reshuffling FAs with different bow amplitudes and directions are placed next to each other. At EOC, in turn, the bow shapes usually roughly fit together so that the coupling forces should be significantly lower and might even be negligible. Moreover, the simulation results presented in this thesis suggest that we cannot generally neglect the elastic deformation due to lateral hydraulic forces, neither at BOC nor at EOC. This is illustrated, for example, in Figure 6.17 for the EOC case and in Figure 6.23 for the BOC case. This potentially complicates the predictions of both BOC and EOC water gaps because we would always need the information about the hydraulic forces to make a reliable prediction.

Full-core calculations from BOC to EOC Once the calculations of the two previous steps perform satisfactorily, the final objective in bow modeling can be tackled: the prediction and validation of the full-core bow development from BOC to EOC. For the validation of such calculations, a larger database exists because many bow measurement data have been collected for the ex-core FA deformation since the first occurrence of FA bow. The implemented FA structural model has already been designed as a full 3D model accounting for deformations in both cross-sectional dimensions. To obtain a full-core configuration, we must only define additional FA nodes and elements at the different FA positions. However, this substantial

amplification of the model size also implies a strong increase in computational expense and will require new solutions to enhance performance. To determine the full-core water gap distributions at BOC, the current shared-memory parallel processing on four central processing units (CPUs) may be sufficient because only the elastostatic equilibrium without creep needs to be calculated. However, for full-core creep calculations from BOC to EOC, it is recommended that distributed parallel processing with an increased number of CPUs is implemented since the required memory and run time would increase strongly. In addition to a full-core structural model, a powerful full-core hydraulic model is required. Recommendations for a further development of the present hydraulic model are given in the last paragraph of this section.

FA reshuffling When bow calculations over one single cycle deliver accurate results, there is a strong interest in performing also the bow calculations for the following cycle based on these results. To be able to perform such calculations with the present model, an efficient FA reshuffling functionality needs to be implemented. For this purpose, the bow state from previous cycles obtained from previous calculation runs must be transferred to the next one-cycle run. The final bow deformation is the result of the structural equilibrium between the elastic, thermal, creep, and growth strain and the external constraints. In particular, internal stresses form as a result of the plastic deformation processes, that is, creep, growth, and frictional sliding. To reproduce accurately the initial bow from previous cycles, exactly this internal stress and strain state must be imposed as an initial condition for the following one-cycle run. In addition, grid growth should be accounted for by modifying the initial gap size of the contact elements as a function of the fluence and temperature. In this manner, the propagation of bow patterns can be simulated flexibly for any FA reshuffling plan.

Refined full-core hydraulic model The 2D porous-medium flow model for a FA row that was used in the present work can be extended to a full-core 3D model by expanding the mesh over the entire reactor core. Due to this expansion, the number of mesh cells would be roughly squared so that more powerful computational methods must be applied to cope with this increase. For the full-core 3D model, a refined modeling of the flow resistances might be necessary to better track the flow redistribution in the 3D space, where the flow has more DOFs. The FSI calculations with the current model appear to underestimate the impact of the deformed FA structure on the distribution of the hydraulic loads. The currently used EOLE correlation accounts only for the drag inside the rod bundle, neglecting flow resistance effects at the entrance and exit of the bundle. Therefore, the observed discrepancy might originate from a not sufficiently detailed description of the entrance and exit effects when the flow passes from the FA bypass gaps to the FA interior and back. In two-way FSI calculations, the local pressure increases in regions where a gap closes between two FAs whereas in regions with opening gaps a lower local pressure is expected. An increased flow resistance between the bypass and the FA interior leads therefore to higher local pressure gradients; that is, a higher impact of the structural feedback on the hydraulic loads can be expected.

It is therefore recommended to refine the porous medium hydraulic model by using dedicated flow coefficients in regions where these entrance and exit effects occur. However, hardly any experimental data are available in literature for the estimation of the entrance and exit effects for different angles of attack. One opportunity to obtain such data could be to perform resolved CFD calculations on a local scale. These local domains could, for example, cover two FA halves over the length of one grid span, similar to the calculation domain depicted in Figure 5.5. The flow resistance at the entrance and exit can be determined by imposing flow

at different angles of attack over the domain and calculating the pressure drop. To account for structural deformation, the relative angle between the tube bundle axes of the two FA halves can be modified. In this manner, the flow resistance of a closing gap can be simulated. The same exercise can be repeated for the spacer grid region. This might lead to important improvements since the lateral loss coefficient of the spacer grid used in this present work is based on a relatively simplistic approach.

Appendix A

Derivation of the Euler-Bernoulli beam equations

We depart from the assumption of an arbitrarily supported beam with an axially uniform and homogeneous cross-section, see Figure 2.4, which is only loaded only within the x - z plane. For this case of uniaxial beam bending, the strains in the perpendicular y -direction are exclusively due to the Poisson effect of transverse dilation or constriction and can be neglected. Discarding the perpendicular component of the displacement vector leaves us with the axial component u_x and the transverse component u_z . The resulting strains according to equation 2.2 are:

$$\varepsilon_x = \frac{\partial u_x}{\partial x}, \varepsilon_{xz} = \varepsilon_{zx} = \frac{1}{2} \left(\frac{\partial u_x}{\partial z} + \frac{\partial u_z}{\partial x} \right), \varepsilon_z = \frac{\partial u_z}{\partial z} \quad (\text{A.1})$$

Let us consider an undeformed infinitesimal beam element of length dx with central axis at $z = 0$, which is set under pure bending by a bending moment M , see Figure A.1. The Euler-Bernoulli beam theory is based on the assumption of small displacements and rotations and small strains. Therefore, no normal strain in transverse direction is expected and the slopes of the cross-section and the neutral axis are equal to the rotation angles ψ and θ :

$$\frac{\partial u_z}{\partial z} = 0, \frac{\partial u_x}{\partial z} = \psi, \frac{\partial u_z}{\partial x} = -\theta \quad (\text{A.2})$$

The Euler-Bernoulli theory requires that the beam cross-section remains planar ($\psi = \text{constant}$) and perpendicular to the slope of the neutral axis at any time during the deformation, see Figure A.2. This normality assumption can be expressed by equation A.3.

$$\frac{\partial u_z}{\partial x} = -\frac{\partial u_x}{\partial z} \text{ or } \theta = \psi \quad (\text{A.3})$$

With the normality principle, the deformed section becomes a circular arc with constant angle $d\psi$ over the cross-section. Considering only small deformations, the element length remains approximately constant at

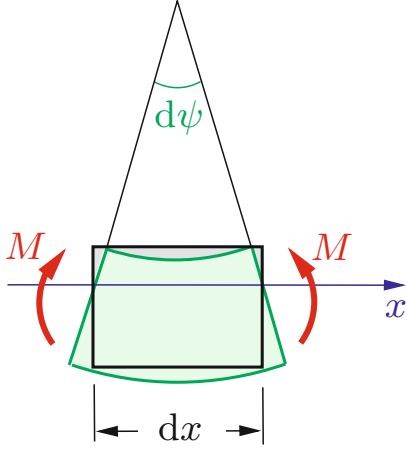


Figure A.1: Infinitesimal beam cross-section forming circular arc with opening angle $d\psi$ (Gross et al., 2012).

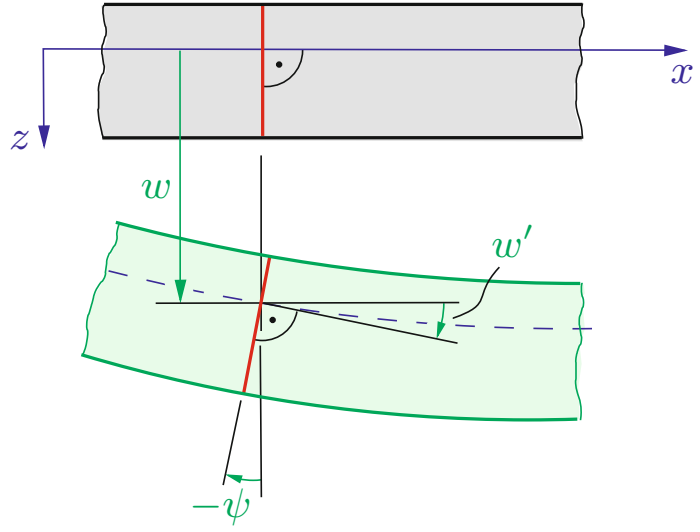


Figure A.2: Schematic of Bernoulli's normality assumption (Gross et al., 2012). $w = u_z$ stands for the beam deflection and $w' = \frac{\partial u_z}{\partial x} = -\theta$ stands for the slope of the bending curve.

the neutral axis. Away from the neutral axis, the infinitesimal displacement is $du_x = z d\psi$. The axial strain is then:

$$\varepsilon_x = z \frac{d\psi}{dx} = -z \frac{d^2 u_z}{dx^2} \quad (\text{A.4})$$

With the simplified Hooke's law, we obtain the bending stress σ_x :

$$\sigma_x = E \varepsilon_x = -E z \frac{d^2 u_z}{dx^2} \quad (\text{A.5})$$

The bending stress at the surface dA (see Figure 2.4b) creates an infinitesimal bending moment $dM = z \sigma_x dA = z dF_x$ about the neutral axis, with dF_x being the infinitesimal axial force associated with the bending stress. By integrating dM over the cross-sectional surface A , we find the bending moment M over the entire beam section:

$$M = \int_A dM = \int_A z dF_x = \int_A z \sigma_x dA = -E \frac{d^2 u_z}{dx^2} \int_A z^2 dA \quad (\text{A.6})$$

The remaining integral term is defined as the second moment of area I :

$$I = \int_A z^2 dA \quad (\text{A.7})$$

The bending moment becomes:

$$M = -EI \frac{d^2 u_z}{dx^2} \quad (\text{A.8})$$

Inversely, the bending stress σ_x results from the moment by the following equation:

$$\sigma_x = \frac{M}{I}z \quad (\text{A.9})$$

So far only the axial equilibrium originating from a hypothetical moment applied at the cross-section has been considered. In many applications, a transverse linear load $q = \int_A f_{B,z} dA$ is applied. Figure A.3a gives the force and moment equilibrium over an infinitesimal beam element, where Q is the transverse cutting force in the beam resulting from the integrated shear stress (see also Figure A.3b):

$$dQ = \int_A \frac{\partial \tau_{xz}}{\partial x} dx dA \quad (\text{A.10})$$

Equation A.11 expresses then the force equilibrium over the beam cross-section in transverse direction.

$$dQ = -q dx \quad (\text{A.11})$$

The transverse force Q exerts a moment dM on the opposite face of the infinitesimal element, resulting in the following moment equilibrium:

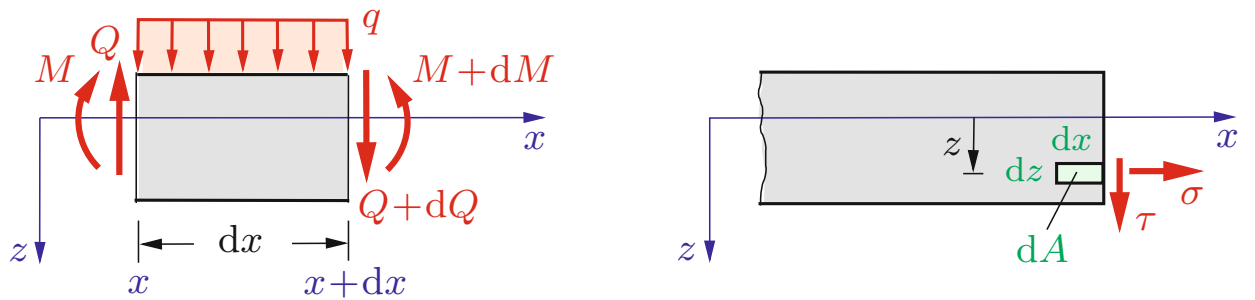
$$dM = Q dx \quad (\text{A.12})$$

Combining equations A.6, A.11, and A.12, we obtain the fundamental equilibrium equation of the Euler-Bernoulli beam theory, from which the bending curve $u_z(x)$ along the beam can be calculated for an axially uniform beam cross-section.

$$EI \frac{d^4 u_z}{dx^4} = q \quad (\text{A.13})$$

If the beam is also loaded by a uniform axial load F_x , the normal cutting force N appears in x -direction.

$$N = \int_A \sigma_x dA = F_x \quad (\text{A.14})$$



(a) Force and moment equilibrium of an infinitesimal beam cross-section.

(b) Infinitesimal volume element in beam.

Figure A.3: Infinitesimal beam elements (Gross et al., 2012).

Due to the integration $\int_A z dA = 0$, this term does not contribute to the bending moment based on equation A.6. The deflection equation A.13 is hence fully decoupled from the axial state. If the equilibrium equations are, however, established considering a deformed beam element, Figure A.4, the normal cutting force induces an additional moment about the bending axis. In the equilibrium equations of the Euler-Bernoulli beam theory, these moments are neglected since only small deformations occur. However, if the magnitude of the axial loads is much higher than that of the transverse load, an additional term must be added to equation A.11:

$$dQ = -qdx + Nd\psi \quad (\text{A.15})$$

Inserting equation A.15 into equation A.12, the new differential equation for the bending curve becomes:

$$EI \frac{d^4 u_z}{dx^4} - \frac{d}{dx} \left(N \frac{du_z}{dx} \right) = q \quad (\text{A.16})$$

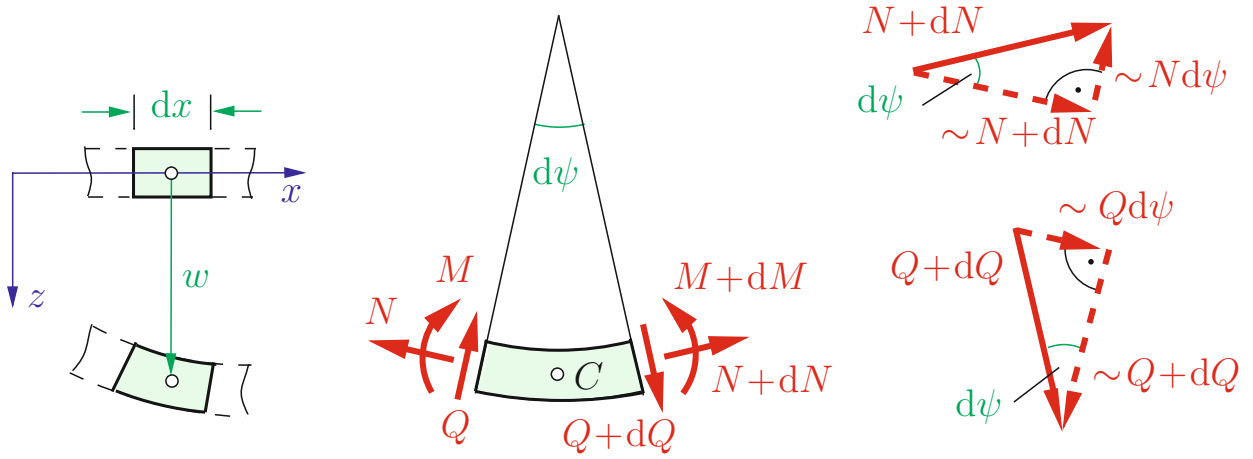


Figure A.4: Deformed infinitesimal beam element with cutting forces (Gross et al., 2012).

Appendix B

Modeling of the anisotropic creep of Zirconium alloy fuel rods (FRs)

Due to the internal pressurization of FRs, the FR cladding exhibits a biaxial stress state with hoop and axial stresses, see section 2.1.3.3, leading to multiaxial creep. Due to the material anisotropy of Zirconium alloys, Hill's anisotropy factors F , G , and H in equation 2.45 need to be determined for the modeling of multiaxial creep. Ideally, creep tests in all three principal directions are to be performed. In practice, researchers mostly use a combination of uniaxial creep tests in longitudinal direction and biaxial creep tests by internally pressurizing the tube. Due to the large scope of necessary irradiation samples, only very few experimental investigations have been published for Zirconium alloys, from which F, G , and H can be completely determined. Examples are those by Ross-Ross et al. (1972), Hunt (1975), Ibrahim and Holt (1980) and Erbacher et al. (1982). Table B.1 summarizes their results based on the notation used in equation 2.45. Since the anisotropy factors always appear as ratios in any mechanical test, an additional condition is required. Based on the approach by Ross-Ross et al. (1972), the condition $F + G + H = 1.5$ was chosen to calculate the values in Table B.1. Unlike these multiaxial tests, most creep tests for FR cladding materials

Table B.1: Anisotropy Factors F , G , and H for cold-worked Zircaloy-2 (Zry-2) or Zircaloy-4 (Zry-4) in α -phase published by different authors.

Hill's factor	Isotropy	Ross-Ross et al. Zry-2	Hunt ^a Zry-4	Ibrahim and Holt ^a Zry-4	Erbacher et al. Zry-4
F	0.5	0.50	0.408	0.665	0.304
G	0.5	0.25	0.221	0.111	0.240
H	0.5	0.75	0.871	0.723	0.956
$\frac{F+H}{2G+F}$	0.67	1.25	1.50	1.51	1.61

^a The factors were averaged from a matrix of values.

are performed only under a single loading condition, which is normally generated by internally pressurizing tube specimens. The magnitude of creep is mostly established by measuring the diameter change of the investigated tube as a function of the hoop stress σ_θ . The derived FR creep models relate the hoop creep

strain rate $\dot{\epsilon}_\theta$ to the hoop stress σ_θ :

$$\dot{\epsilon}_\theta = B_{\text{biax}} \sigma_\theta^{n_\sigma} \quad (\text{B.1})$$

In its generalized form a creep law relates the effective strain to the effective stress.

$$\dot{\epsilon}_{\text{eff}} = B_{\text{eff}} \sigma_{\text{eff}}^{n_\sigma} \quad (\text{B.2})$$

Inserting the stresses for a thick-walled pressurized tube in equations 2.68 to 2.70 into equation 2.45, we obtain:

$$\sigma_{\text{eff}} = |\sigma_\theta - \sigma_z| \sqrt{F + 4G + H} = |\sigma_B| \sqrt{F + 4G + H} \quad (\text{B.3})$$

Introducing equations B.2 and B.3 into 2.47, the hoop creep strain is related to the hoop stress σ_θ as follows:

$$\dot{\epsilon}_\theta = B_{\text{eff}} (F + 4G + H)^{\frac{n_\sigma - 1}{2}} (2G + F) r_\sigma^{n_\sigma} \sigma_\theta^{n_\sigma}, \quad (\text{B.4})$$

where r_σ is the stress ratio:

$$r_\sigma = \frac{\sigma_\theta - \sigma_z}{\sigma_\theta} = \frac{\sigma_B}{\sigma_A + \sigma_B} \quad (\text{B.5})$$

For a fresh PWR FR under operating conditions, r_σ is about 0.4. This value decreases slowly as the pressure difference diminishes as a result of the fission gas release. Under the approximation of a thin-walled pressure tube, r_σ has a constant value of 0.5. From equations B.1 and B.4, we deduce that:

$$B_{\text{biax}} = B_{\text{eff}} (F + 4G + H)^{\frac{n_\sigma - 1}{2}} (2G + F) r_\sigma^{n_\sigma} \quad (\text{B.6})$$

Based on Table B.1, the term $(2G + F)$ yields a value close to 1 for Zry-4 according to most authors. For the common case of $n = 1$, B_{biax} is hence about 40% of B_{eff} . Section 2.1.3.4 points out that the axial stress in the FR can be represented as the sum of several components: the axial stress due to the biaxial stress state as a result of pressurization $\sigma_{z,\text{biax}}$ in equation 2.79, the axial stress as a result of bending moments $\sigma_{z,\text{bend}}$ in equation 2.78, and the uniaxial stress $\sigma_{z,\text{uniax}}$ in equation 2.77. For solving the structural behavior of the fuel assembly (FA), the last two axial stress components are of specific interest. Let us assume for the moment that the magnitude of the additional axial stresses due to external FR loads, $\sigma_{z,\text{bend}}$ and $\sigma_{z,\text{uniax}}$, does not significantly modify the effective stress σ_{eff} due to the biaxial stress state. In other words, equation B.3 remains valid regardless of the additional axial stress. Applying the approximations for a thick-walled pressure tube, the axial creep strain rate from equation 2.48 becomes:

$$\begin{aligned} \dot{\epsilon}_z &= B_{\text{eff}} \sigma_{\text{eff}}^{n_\sigma - 1} [F(\sigma_z - \sigma_\theta) - H(\sigma_r - \sigma_z)] = \\ &= \frac{\dot{\epsilon}_{\text{eff}}}{\sigma_{\text{eff}}} [(H - F)(\sigma_\theta - \sigma_{z,\text{biax}}) + (F + H)(\sigma_{z,\text{uniax}} + \sigma_{z,\text{bend}})] \end{aligned} \quad (\text{B.7})$$

The axial anisotropy factor $(H - F)$ due the biaxial stress is zero for isotropic creep and usually provides relatively small contributions to the total axial strain for anisotropic creep of Zirconium alloys. The orientation depends on the microstructural texture of the cladding material. Figure B.1 shows experimental

data for the axial creep strain component in a biaxial stress state for different materials. For pressurized

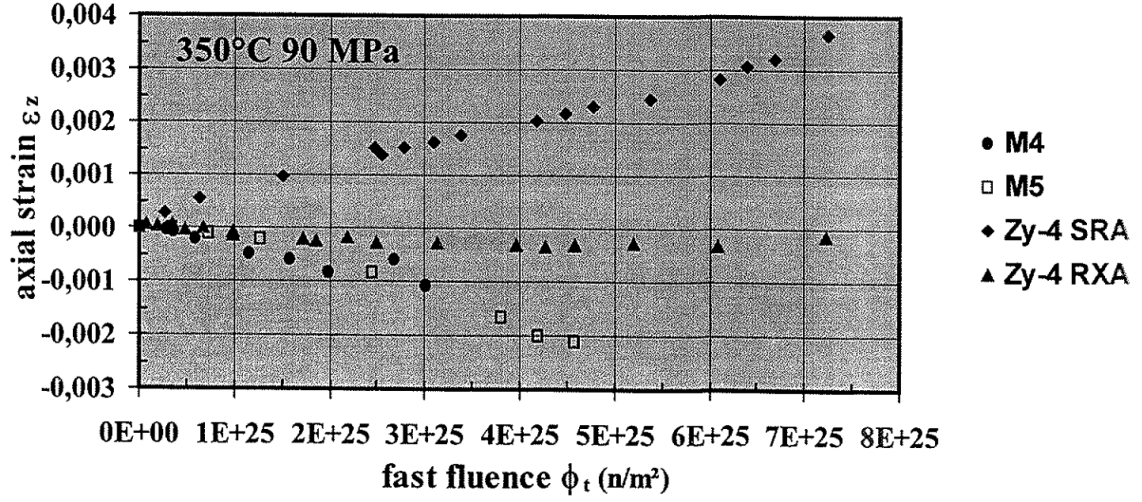


Figure B.1: Axial strain as a result of anisotropic creep of Zirconium alloys under a biaxial stress state (Soniak et al., 2002).

tubes, its effect cannot be separated from that of irradiation growth. Therefore, its magnitude is usually included in the FR growth measurement data and the derived models, see section 4.3. This term can hence be neglected for the present creep calculations, reducing the creep law to the second term only. However, the biaxial stress still appears in the effective stress term σ_{eff} :

$$\dot{\epsilon}_z = B_{\text{eff}} \sigma_{\text{eff}}^{n_{\sigma}-1} (F + H) (\sigma_{z,\text{uniax}} + \sigma_{z,\text{bend}}) \quad (\text{B.8})$$

Inserting equation B.3 yields:

$$\dot{\epsilon}_z = B_{\text{eff}} (F + 4G + H)^{\frac{n_{\sigma}-1}{2}} |\sigma_B|^{n_{\sigma}-1} (F + H) (\sigma_{z,\text{uniax}} + \sigma_{z,\text{bend}}) \quad (\text{B.9})$$

Applying equation B.6 to equation B.9, a creep law for $\dot{\epsilon}_z$ depending on B_{biax} is obtained:

$$\dot{\epsilon}_z = B_{\text{biax}} |\sigma_B|^{n_{\sigma}-1} \frac{F + H}{r_{\sigma}(2G + F)} (\sigma_{z,\text{uniax}} + \sigma_{z,\text{bend}}) \quad (\text{B.10})$$

Different values for $\frac{F+H}{2G+F}$ depending on the author are tabulated in Table B.1. If, finally, the creep law is linear in its dependence on stress, that is, $n = 1$, then the relationship between axial stress and axial creep strain becomes independent of the biaxial stress state:

$$\dot{\epsilon}_z = B_{\text{biax}} \frac{(F + H)}{r_{\sigma}(2G + F)} \sigma_z \quad (\text{B.11})$$

Equation B.11 hence represents the creep law to use for modeling the bow deformation of the FRs based on creep laws from biaxial creep tests.

Appendix C

Equivalence of the fuel rod (FR) internal energy for the full and reduced models

This section derives the conditions for the positioning of the equivalent rods in order to obtain an equivalent FR internal strain energy for the full and reduced models. To calculate the strain energy of a single FR, the distribution of stresses σ and strains ε needs to be analyzed. For Euler-Bernoulli beams under the given conditions, only stresses and strains in axial beam direction need to be considered, $\sigma = \sigma_z$ and $\varepsilon = \varepsilon_z^{\text{tot}}$. Note that against the general convention in beam theory, the beam axis in the present model is aligned with the z -direction of the coordinate system and not with the x -direction. The internal strain energy of a single fuel rod U_{FR} reads then as:

$$U_{\text{FR}} = \frac{1}{2} \int_V \boldsymbol{\sigma} \boldsymbol{\varepsilon} \, dV = \frac{1}{2} \int_V \sigma_z \varepsilon_z^{\text{tot}} \, dA dz \quad (\text{C.1})$$

According to equation 2.104, we have $\varepsilon_z^{\text{tot}} = \varepsilon_z^{\text{el}} + \varepsilon_z^{\text{th}} + \varepsilon_z^{\text{cr}} + \varepsilon_z^{\text{gr}}$, where $\varepsilon_z^{\text{el}} = \sigma_z/E$. As a next step, the distribution of the thermal, creep, and growth strain is to be determined. Section 4.4.1 defines a linear power profile over each FA, on the basis of which the temperature T and the fast neutron flux ϕ are calculated. The thermal, creep, and growth strains are dependent on these two field variables by means of different models introduced in chapter 2. If we assume additionally that the lateral differences in T and ϕ over a single FA are sufficiently small, we can also linearize the physical models on which they are based over the lateral coordinate. Equations C.2 and C.3 represent the linearized formulations for the thermal and growth strain with the average value ε_{avg} and the lateral gradient g_{lat} for a certain FA inside the reactor core at a certain point of time and axial height z .

$$\varepsilon^{\text{th}} = \varepsilon_{\text{avg}}^{\text{th}} + g_{\text{lat}}^{\text{th}} x_i \quad (\text{C.2})$$

$$\varepsilon^{\text{gr}} = \varepsilon_{\text{avg}}^{\text{gr}} + g_{\text{lat}}^{\text{gr}} x_i \quad (\text{C.3})$$

For the creep strain, we need to account additionally for the effect of the linear dependence of the creep on stress according to section 2.4.6.

$$\varepsilon^{\text{cr}} = (a_{\text{avg}}^{\text{cr}} + g_{\text{lat}}^{\text{cr}} x_i) \sigma \quad (\text{C.4})$$

The creep and growth strain in equations C.4 and C.3 are a linear combination of the integrations of the creep and growth rate over each time step, thus maintaining the linearity of the model. With the assumptions from equations C.2 to C.4, equation C.1 becomes:

$$U_{\text{FR},i} = \frac{1}{2} \int_V \frac{1}{E} \sigma_z^2 + \sigma_z (\varepsilon_z^{\text{th}} + \varepsilon_z^{\text{cr}} + \varepsilon_z^{\text{gr}}) \, dAdz \quad (\text{C.5})$$

$$= \frac{1}{2} \int_V \sigma_z^2 \left(\frac{1}{E} + a_{\text{avg}}^{\text{cr}} + g_{\text{lat}}^{\text{cr}} x_i \right) + \sigma_z (\varepsilon_{\text{avg}}^{\text{th}} + \varepsilon_{\text{avg}}^{\text{gr}} + (g_{\text{lat}}^{\text{th}} + g_{\text{lat}}^{\text{gr}}) x_i) \, dAdz \quad (\text{C.6})$$

Since the axial configuration remains the same for the reduced model, it is more convenient to use the linear internal strain energy $U_{\text{FR},\text{lin},i}$ as the criterion, which must be fulfilled for any z . The axial stress σ_z in the FRs can be expressed by means of the normal cutting force $N(x_i)$ and the bending moment M_{bend} , see also section 2.1.3.4. It follows:

$$U_{\text{FR},\text{lin},i} = \frac{\partial U_{\text{FR},i}}{\partial z} = \left(\frac{1}{E} + a_{\text{avg}}^{\text{cr}} + g_{\text{lat}}^{\text{cr}} x_i \right) \int_A \left(\frac{N(x_i)}{A} \right)^2 + \frac{2N(x_i) M_{\text{bend}}}{AI} \hat{x}_i + \left(\frac{M_{\text{bend}}}{I} \hat{x}_i \right)^2 \, d\hat{x}_i + \\ + (\varepsilon_{\text{avg}}^{\text{th}} + \varepsilon_{\text{avg}}^{\text{gr}} + (g_{\text{lat}}^{\text{th}} + g_{\text{lat}}^{\text{gr}}) x_i) \int_A \left(\frac{N(x_i)}{A} + \frac{M_{\text{bend}}}{I} \hat{x}_i \right) \, d\hat{x}_i \quad (\text{C.7})$$

After solving the integrals, all terms linear in \hat{x}_i disappear, keeping in mind that $\int_A d\hat{x}_i = A$, $\int_A \hat{x}_i d\hat{x}_i = 0$, and $\int_A \hat{x}_i^2 d\hat{x}_i = I$:

$$U_{\text{FR},\text{lin},i} = \left(\frac{1}{E} + a_{\text{avg}}^{\text{cr}} + g_{\text{lat}}^{\text{cr}} x_i \right) \left(\frac{N(x_i)^2}{A} + \frac{M_{\text{bend}}^2}{I} \right) + (\varepsilon_{\text{avg}}^{\text{th}} + \varepsilon_{\text{avg}}^{\text{gr}} + (g_{\text{lat}}^{\text{th}} + g_{\text{lat}}^{\text{gr}}) x_i) N(x_i) \quad (\text{C.8})$$

After expanding $N(x_i)$ according to equation 2.77, equation C.9 shows that the strain energy is a polynomial of third degree in x_i .

$$U_{\text{FR},\text{lin},i} = \left(\frac{1}{E} + a_{\text{avg}}^{\text{cr}} + g_{\text{lat}}^{\text{cr}} x_i \right) \left(\frac{N_{\text{unif}}^2}{A} + \frac{M_{\text{bend}}^2}{I} + \frac{2N_{\text{unif}} N_{\text{cpl,ref}}}{x_{\text{ref}}} x_i + \frac{N_{\text{cpl,ref}}^2}{x_{\text{ref}}^2} x_i^2 \right) + \\ + (\varepsilon_{\text{avg}}^{\text{th}} + \varepsilon_{\text{avg}}^{\text{gr}} + (g_{\text{lat}}^{\text{th}} + g_{\text{lat}}^{\text{gr}}) x_i) \left(N_{\text{unif}} + \frac{N_{\text{cpl,ref}}}{x_{\text{ref}}} x_i \right) \quad (\text{C.9})$$

That is, to fulfill the energy criterion in equation 3.22, the conditions in equations 3.20 and 3.21 must be complemented with a third condition for the equivalence of the sum of cubes of x_i , equation 3.23.

Appendix D

Pressure drop correlations to determine axial hydraulic forces

The calculation of the axial hydraulic forces in this work is based on the axial pressure losses along the coolant flow path in the reactor core obtained from correlations given in literature. The total axial pressure drop across the core, given in Table 4.9, can be decomposed into the gravitational pressure drop and the irrecoverable form and friction losses along the flow path.

$$\Delta p_{\text{core}} = \Delta p_{\text{grav,FA}} + \Delta p_{\text{loss,FA}} = \rho(T_{\text{ave}}) g l_{\text{FA}} + \Delta p_{\text{form}} + \Delta p_{\text{fric}} \quad (\text{D.1})$$

The axial hydraulic force on the fuel assembly (FA) is proportional to the irrecoverable pressure loss. With $A_{\text{total,FA}} = p_{\text{FA}}^2$ being the flow area away from the FR bundle, the total axial hydraulic force on the FA is:

$$F_{z,\text{hyd}} = \Delta p_{\text{loss,FA}} A_{\text{total,FA}} = (\Delta p_{\text{core}} - \Delta p_{\text{grav,FA}}) A_{\text{total,FA}} \quad (\text{D.2})$$

The single terms of the axial hydraulic force are estimated based on the theory about internal channel flow in section 2.3.2 using correlations given in literature. First, some fundamental reference values need to be introduced. Equation D.3 gives the mass flux G in the FA subchannel with flow area $A_{\text{flow,FA}}$, which is defined in equation D.4. To calculate $A_{\text{flow,FA}}$, it is assumed that the flow inside of the guide tubes (GTs) is negligible.

$$G = \frac{\dot{m}_{\text{core}}}{n_{\text{FA}} A_{\text{flow,FA}}} \quad (\text{D.3})$$

$$A_{\text{flow,FA}} = p_{\text{FA}}^2 - n_{\text{FR}} \frac{d_{\text{FR,o}}^2}{4} \pi - n_{\text{GT}} \frac{d_{\text{GT,o}}^2}{4} \pi \quad (\text{D.4})$$

The Reynolds number in the fuel bundle, equation D.5, is determined by means of the mass flux G and the hydraulic diameter d_{hyd} , which is defined in equation D.6. For d_{hyd} and all other geometry-related

thermohydraulic parameters in this section, it is assumed that all GTs have the same outer diameter as the fuel rods (FRs), $d_{\text{FR},o}$.

$$Re = \frac{G d_{\text{hyd}}}{\mu} \quad (\text{D.5})$$

$$d_{\text{hyd}} = \frac{4p_{\text{FR}}^2 - d_{\text{FR},o}^2 \pi}{d_{\text{FR},o} \pi} \quad (\text{D.6})$$

Friction forces on GTs and FRs The Darcy friction factor f_D can be determined based on the Reynolds number and the FR cladding surface roughness. The surface roughness λ of conventional Zircaloy cladding tubes is between $0.3 \mu\text{m}$ and $0.5 \mu\text{m}$, resulting in a relative roughness of $\lambda/d_{\text{FR},o} < 5 \times 10^{-5}$. The Moody (1944) chart shows that for the considered Reynolds number, the tubes with such roughness can be approximated as smooth. Since the Reynolds number Re is within the range from 3×10^4 to 1×10^6 , the McAdams relation can be used to approximate the Darcy friction factor (Todreas and Kazimi, 2012):

$$f_{D,\text{FR}} = 0.184 Re^{-0.20} \quad (\text{D.7})$$

Correction factors for diabatic flow, flow in rod bundles, and due to initially developing flow only slightly affect the friction factor for the considered conditions and are therefore neglected. The resulting terms for the pressure loss due to friction is:

$$\Delta p_{\text{fric},\text{FR}} = 0.184 Re^{-0.20} \frac{l_{\text{FR}}}{d_{\text{hyd}}} \frac{G^2}{2\rho} \quad (\text{D.8})$$

Based hereupon, the following linear tangential force is applied on the GTs and FRs in the structural model:

$$f_{\text{lin},z,\text{fric}} = \frac{0.184 Re^{-0.20}}{4} d_{\text{FR},o} \pi \frac{G^2}{2\rho} \quad (\text{D.9})$$

Force on spacer grids The pressure drop over the spacer grids is one of the largest contributors to the overall pressure drop in the core. The flow constriction in the spacer grid region is the main contributor to this pressure drop. Due to the complex geometry, accurate predictions of pressure drop call for experimental tests in flow loops using the specific spacer grid design of interest. Still, several authors developed general correlations to estimate the approximate pressure drop over the spacer grids. In particular, In et al. (2002) developed a relatively elaborate model which estimates the force on the spacer grid $F_{z,\text{grid}}$ as the sum of four terms: the form drag forces on the grid and the mixing vanes, $F_{\text{form},\text{grid}}$ and $F_{\text{form},\text{mv}}$, and the frictional drag forces on the grid straps and the FRs in the spacer region, $F_{\text{fric},\text{strap}}$ and $F_{\text{fric},\text{FR}}$. To calculate these forces, equation D.10 defines the mass flux in the grid region G_{grid} based on the relative plugging factor of the flow cross-section due to the presence of the grid ϵ_{grid} , given in equation D.11. The projected grid cross-section area A_{grid} was defined previously in equation 3.2.

$$G_{\text{grid}} = G \frac{A_{\text{flow,FA}}}{A_{\text{flow,FA}} - A_{\text{grid}}} = G \frac{1}{1 - \epsilon_{\text{grid}}} \quad (\text{D.10})$$

$$\epsilon_{\text{grid}} = \frac{A_{\text{grid}}}{A_{\text{flow,FA}}} \quad (\text{D.11})$$

In et al. (2002) use the drag coefficient $C_{\text{drag,grid}}$ to estimate the hydraulic drag force due to form pressure loss in the flow over the grid:

$$F_{\text{form,grid}} = C_{\text{drag,grid}} \frac{G_{\text{grid}}^2}{2\rho} A_{\text{grid}} \quad (\text{D.12})$$

The drag coefficient at the grid is correlated to experimental measurements and is given as:

$$C_{\text{drag,grid}} = 2.75 - 0.27 \log_{10}(Re) \quad (\text{D.13})$$

To obtain the drag force term as expressed in equation 2.122, the reference reference velocity and area must be modified using equation D.11 and D.10:

$$F_{\text{form,grid}} = \zeta_{\text{drag,grid}} A_{\text{flow,FA}} \frac{G^2}{2\rho} = C_{\text{drag,grid}} \frac{\epsilon_{\text{grid}}}{(1 - \epsilon_{\text{grid}})^2} A_{\text{flow,FA}} \frac{G^2}{2\rho} \quad (\text{D.14})$$

The hydraulic drag force due to the mixing vanes is calculated in a similar manner, using the plugging factor for the mixing vanes ϵ_{mv} and the drag coefficient of the mixing vanes $C_{\text{drag,mv}}$:

$$F_{\text{form,mv}} = C_{\text{drag,mv}} \frac{\epsilon_{\text{mv}}}{(1 - \epsilon_{\text{mv}})^2} A_{\text{flow,FA}} \frac{G^2}{2\rho} \quad (\text{D.15})$$

Based on experimental tests, In et al. (2002) recommend a constant value for the drag coefficient, $C_{\text{drag,mv}} = 0.72$. The value of ϵ_{mv} depends on the specific design of the mixing vanes. In et al. (2001) indicate a value of $\epsilon_{\text{mv}} = 0.22$ for a spacer grid design similar to that of the reference FA.

Finally, the friction losses along the grid remain to be determined. In et al. (2002) distinguish between the developed flow along the FRs and the developing flow at the grid straps to calculate $F_{\text{fric,FR}}$ and $F_{\text{fric,strap}}$. Both values are determined based on frictional drag coefficients C_{fric} and the corresponding surface friction area A_{fric} , see equation 2.120. For the developed flow along the FRs, the frictional drag coefficient $C_{\text{fric,FR}}$ equals one quarter of Darcy's friction factor f_{D} . Again, f_{D} is determined with the McAdams correlation, but is based on the Reynolds number in the grid region Re_{grid} in the present case. The frictional drag coefficient for the FR then becomes:

$$C_{\text{fric,FR}} = \frac{f_{\text{D}}}{4} = \frac{0.184}{4} Re_{\text{grid}}^{-0.20} \quad (\text{D.16})$$

with

$$Re_{\text{grid}} = \frac{G_{\text{grid}} d_{\text{hyd,grid}}}{\mu} \quad (\text{D.17})$$

and

$$d_{\text{hyd,grid}} = \frac{4(p_{\text{FR}} - t_{\text{grid}})^2 - d_{\text{FR,o}}^2 \pi}{d_{\text{FR,o}} \pi + 4(p_{\text{FR}} - t_{\text{grid}})} \quad (\text{D.18})$$

The total friction force on all FRs in the grid region is then:

$$F_{\text{fric,FR}} = n_{\text{pos}}^2 C_{\text{fric,FR}} d_{\text{FR},0} \pi l_{\text{grid}} \frac{G_{\text{grid}}^2}{2\rho} \quad (\text{D.19})$$

The frictional drag coefficient on the grid strap $C_{\text{fric,strap}}$ is derived from the correlations for a developing boundary layer on a flat plate, consisting of one laminar coefficient for the boundary layer before the transition to turbulent flow and one turbulent coefficient for the flow after the transition. Since the transition length as proposed by In et al. (2002) is much smaller than the grid length, $l_{\text{trans}} = 3 \times 10^4 \mu G_{\text{grid}} \ll l_{\text{grid}}$, we can approximate the frictional drag coefficient with the turbulent coefficient only:

$$C_{\text{fric,strap}} = C_{\text{fric,plate,turb}} = \frac{0.523}{\ln^2 0.06 Re_L} \quad (\text{D.20})$$

with Re_L being the Reynolds number based on the turbulent length $L = l_{\text{grid}} - l_{\text{trans}} \approx l_{\text{grid}}$:

$$Re_L = \frac{G_{\text{grid}} l_{\text{grid}}}{\mu} \quad (\text{D.21})$$

The total friction force on all grid straps in the grid region becomes:

$$F_{\text{fric,strap}} = n_{\text{pos}}^2 C_{\text{fric,strap}} 4(p_{\text{FR}} - t_{\text{grid}}) l_{\text{grid}} \frac{G_{\text{grid}}^2}{2\rho} \quad (\text{D.22})$$

Altogether, the hydraulic force on one spacer grid resolves to the sum of the four presented terms.

$$F_{z,\text{grid}} = F_{\text{form,grid}} + F_{\text{form,mv}} + F_{\text{fric,FR}} + F_{\text{fric,strap}} \quad (\text{D.23})$$

The value of $F_{z,\text{grid}}$ is applied on each spacer grid central node as axial force boundary condition (BC). Based on an equilibrium of forces over one grid, we can derive the following equation for the associated pressure loss.

$$\Delta p_{\text{grid}} = \frac{F_{z,\text{grid}}}{A_{\text{flow,FA}}} \quad (\text{D.24})$$

Other axial hydraulic force terms Since all spacer grids are assumed to induce the same pressure loss, the total pressure loss over the FR bundle is:

$$\Delta p_{\text{FR}} = \Delta p_{\text{loss,FR}} + \Delta p_{\text{grav,FR}} = \Delta p_{\text{in}} + \Delta p_{\text{out}} + n_{\text{grid}} \Delta p_{\text{grid}} + \Delta p_{\text{fric}} + \Delta p_{\text{grav,FR}} \quad (\text{D.25})$$

where Δp_{in} and Δp_{out} are the pressure losses at the FR bundle inlet and outlet. These loss terms can be approximated by the loss coefficients for a sudden sharp contraction or expansion in a pipe given by Idel'čik (1994). At the inlet, the pressure loss is

$$\Delta p_{\text{in}} = 0.5 \epsilon_{\text{FR}} \frac{G^2}{2\rho_{\text{in}}} \quad (\text{D.26})$$

while at the outlet it is

$$\Delta p_{\text{out}} = \epsilon_{\text{FR}}^2 \frac{G^2}{2\rho_{\text{out}}} \quad (\text{D.27})$$

with

$$\epsilon_{\text{FR}} = \frac{d_{\text{FR},o}^2 \pi}{4\rho_{\text{FR}}^2} \quad (\text{D.28})$$

being the relative plugging of the flow inside the core due the presence of the FR bundle. Due to the pressure drop along the FR bundle, there is a pressure difference between the FR top and bottom faces, leading to the following resultant axial force $F_{z,\text{FR},\text{face}}$ on the FR faces:

$$F_{z,\text{FR},\text{face}} = (\Delta p_{\text{loss,FR}} + \Delta p_{\text{grav,FR}}) \frac{d_{\text{FR},o}^2 \pi}{4} = \Delta p_{\text{loss,FR}} \frac{d_{\text{FR},o}^2 \pi}{4} + \rho g l_{\text{FR}} \frac{d_{\text{FR},o}^2 \pi}{4} \quad (\text{D.29})$$

This upward axial force is imposed on every FR bottom node in the model. The second term in equation D.29 represents the buoyancy force on the FRs in the coolant. The buoyancy forces on the other structural elements are calculated accordingly by multiplying the volume of the displaced coolant with the average coolant density and are applied at the bottom nodes of the respective elements.

The axial hydraulic force on the FA head and foot is finally deduced from the difference between the total pressure loss across the core and the pressure loss over the FR bundle. For both head and foot, an equal pressure loss is assumed.

$$F_{z,\text{nozzle}} = \frac{\Delta p_{\text{loss,FA}} - \Delta p_{\text{loss,FR}}}{2} A_{\text{total,FA}} \quad (\text{D.30})$$

For sake of simplicity, all axial hydraulic forces are calculated assuming constant core-averaged thermodynamic state variables. This reference state is defined by the system pressure p_{sys} and the core average temperature T_{ave} . That is, the buoyancy force and hydraulic loads are not modified as a function of temperature but are always based on the density at the coolant average temperature under operation $\rho(T_{\text{ave}})$. This is reasonable since, on the one hand, it will not introduce a considerable error for the buoyancy forces and, on the other hand, the reactor state in cold condition with running pumps is not of specific interest for the present analyses.

Appendix E

Screening sensitivity analysis

Screening sensitivity analysis is the identification of the few most influential model input parameters from numerous potential contributors to the model outcome variability. This method is also useful to gain knowledge on the type of relation existing between the input and the output. One possible design of screening analysis is that of the one-at-a-time experiments, in which the impact of changing each input factor included in the sensitivity analysis is evaluated. Based on a control scenario with nominal values for each parameter, two extreme boundaries are proposed to represent the range of likely values. The sample size is in the order of the number of input parameters k . The low computational cost is hence one of the main advantages of the one-at-a-time design. It is ideal for a first approach before performing more extensive quantitative sensitivity and uncertainty analyses. Morris' elementary effects method, described by Saltelli et al. (2000), is a one-at-a-time design widely used for screening analysis and helps to determine which factors have negligible effects, linear and additive effects, or nonlinear and interaction effects. This method is based on the definition of trajectories with $k + 1$ points, for which the value of only one input factor is modified between subsequent points and each factor is only changed once. A common approach is the use of $r = 8$ trajectories. Equations E.1 to E.3 show the statistical measures proposed by Morris and the measures derived thereof.

$$EE_{i,j} = \frac{Y(x_{i,j} + \Delta_{i,j}) - Y(x_{i,j})}{\Delta_{i,j}} \quad (\text{E.1})$$

$$\mu_i = \frac{1}{r} \sum_{j=1}^r EE_{i,j} \quad (\text{E.2})$$

$$\sigma_i = \left(\frac{1}{r} \sum_{j=1}^r (EE_{i,j} - \mu_i)^2 \right)^{\frac{1}{2}} \quad (\text{E.3})$$

In equation E.1, $EE_{i,j}$ denotes the elementary effect and Y the monitored output parameter. $x_{i,j}$ is the value of the i -th input factor out of k for the trajectory with index j . $\Delta_{i,j}$ denotes a perturbation of the

input value $x_{i,j}$ within the defined input range. In equation E.2, μ_i denotes the mean value of the elementary effect for a given input factor i . It accounts for the linear effect of the associated input factor. In equation E.3, σ_i denotes the standard deviation of the elementary effect for a given input factor i , thus accounting for nonlinear effects and/or interactions between model input factors. For a normalized input space, the dimension of the elementary effects is the dimension of the monitored output Y . This implies that the statistical measures increase as a result of the increase of the underlying output parameter.

Bibliography

- Y. Aleshin, M. A. Chaves, and S.-Y. Jeon. Methodology to Assess Fuel Assembly Dimension Stability on Design Stage. In *Water Reactor Fuel Performance Meeting 2009 : WRFPM Top Fuel 2009*, volume 2, pages 715–720, Paris, France, 6-10 September 2009. SFEN.
- A. Alós Díez. Structural Analysis of the Irradiation-Induced Behavior of the Fuel-Rod Support of a PWR Fuel Assembly using the Finite Element Method. Master’s thesis, Technical University of Munich, Department of Mechanical Engineering, Chair of Nuclear Technology, Garching, May 2015.
- T. Andersson, J. Almberger, and L. Björnkvist. A Decade of Assembly Bow Management at Ringhals. In *IAEA-TECDOC-1454 Structural Behaviour of Fuel Assemblies for Water Cooled Reactors*, pages 129–136, Vienna, Austria, July 2005. IAEA.
- ANSYS. *ANSYS® CFX Documentation, Release 15.0*. ANSYS, Inc., 2013a.
- ANSYS. *ANSYS® Mechanical APDL Documentation, Release 15.0*. ANSYS, Inc., 2013b.
- M. Aulló and W. D. Rabenstein. European Fuel Group Experience on Control Rod Insertion and Grid To Rod Fretting. In *IAEA-TECDOC-1454 Structural Behaviour of Fuel Assemblies for Water Cooled Reactors*, pages 147–163, Vienna, Austria, July 2005. IAEA.
- M. Aulló, Y. Aleshin, and J. Messier. Reduction of Fuel Assembly Bow with the RFA Fuel. In *Transactions of TopFuel 2012*, pages 155–160, Manchester, UK, September 2-6 2012. European Nuclear Society (ENS).
- R. W. Bailey. The Utilization of Creep Test Data in Engineering Design. *Proceedings of the Institution of Mechanical Engineers*, 131(1):131–349, 1935.
- L. Barinka. Nonlinear Deflection Analysis for Coupled Tubular Structures. *Journal of Engineering for Industry*, 93(4):1255–1260, 1971.
- F.-K. Benra, H. J. Dohmen, J. Pei, S. Schuster, and B. Wan. A Comparison of One-Way and Two-Way Coupling Methods for Numerical Analysis of Fluid-Structure Interactions. *Journal of Applied Mathematics*, 2011:1–16, 2011.
- P. Berglund. Fuel Assembly for a Nuclear Reactor, November 1995. US Patent 5,465,282.
- U. Bieder. CFD Analysis of Non-Axial Flow in Fuel Assemblies. In *16th International Meeting on Nuclear Reactor Thermal Hydraulics (NURETH-16)*, pages 2611–2623, Chicago, IL, USA, August 30 - September 4 2015.
- A. Billerey. Evolution of Fuel Rod Support under Irradiation - Impact on the Mechanical Behaviour of Fuel

- Assemblies. In *IAEA-TECDOC-1454 Structural Behaviour of Fuel Assemblies for Water Cooled Reactors*, pages 101–111, Vienna, Austria, July 2005. IAEA.
- M. K. Booker. Mathematical Analysis of the Elevated-Temperature Creep Behavior of Type 304 Stainless Steel. Technical Report ORNL/TM-6110, Oak Ridge National Laboratory, Oak Ridge, Tennessee, USA, December 1977.
- J. Boyle and J. Spence. *Stress Analysis for Creep*. Butterworths, London, UK, 1983.
- M. Busch. *Zur effizienten Kopplung von Simulationsprogrammen*. Phd thesis, Universität Kassel, 2012.
- B. Chalmers. *Physical Metallurgy*. Wiley, New York, NY, 1959.
- S. C. Chapra. *Applied Numerical Methods with MATLAB for Engineers and Scientists*. McGraw-Hill, New York, NY, USA, 3rd edition, 2012.
- J. Davis, editor. *ASM Specialty Handbook: Stainless Steels*. ASM International, Materials Park, OH, USA, 1994.
- F. J. Erbacher, H. J. Neitzel, H. Rosinger, H. Schmidt, and K. Wiehr. Burst Criterion of Zircaloy Fuel Claddings in a Loss-of-Coolant Accident. In D. Franklin, editor, *Zirconium in the nuclear industry, Fifth Conference, ASTM STP 754*, pages 271–283. American Society for Testing and Materials, 1982.
- I. Fabry. The Biblis Activity Atlas. *Nuclear Engineering International*, pages 13–15, May 2014.
- V. Fidleris. The Irradiation Creep and Growth Phenomena. *Journal of Nuclear Materials*, 159:22–42, 1988.
- J. Foster and M. McGrath. In-Reactor Creep Behavior of Zircaloy-2. Technical Report IFE/HR/E-2007/035, IFE, Halden, Norway, 2007.
- J. P. Foster, R. J. Comstock, A. Atwood, G. Pan, A. Garde, M. Dahlback, J. P. Mundorff, and A. J. Mueller. Zirconium Alloys with Improved Corrosion/Creep Resistance due to Final Heat Treatments, November 2015. US Patent App. 14/745,792.
- Y. Fournier, C. Vurpillot, and C. Béchaud. Evaluation of Fluid Flow in the Lower Core of a PWR with Code Saturne. *Nuclear Engineering and Design*, 237:1729–1744, 2007.
- D. G. Franklin, G. E. Lucas, and A. L. Bement. *Creep of Zirconium alloys in nuclear reactors*. ASTM STP 815. ASTM, Philadelphia, PA, USA, 1983.
- F. Garzarolli, H. Stehle, and E. Steinberg. Behavior and Properties of Zircalloys in Power Reactors: A Short Review of Pertinent Aspects in LWR Fuel. In E. R. Bradley and G. P. Sabol, editors, *Zirconium in the Nuclear Industry: Eleventh International Symposium, ASTM STP 1295*, pages 12–32. American Society for Testing and Materials, 1996.
- F. Garzarolli, I. Pohlmeyer, T. Grimmelsmann, and A. Schaa. Pressurized Water Reactor Fuel Assembly with a Guide Tube and Method for Producing the Guide Tube, December 2000. US Patent 6,167,104.
- G. Gentet, C. Hintergräber, P. Louf, N. Teboul, and C. Wiltz. Areva Product Experience in Support of EPR Fuel Design. In *Transactions of TopFuel 2012*, pages 64–72, Manchester, UK, September 2-6 2012. European Nuclear Society (ENS).
- D. Gilbon, A. Soniak, S. Doriot, and J. P. Mardon. Irradiation Creep and Growth Behavior, and Microstructural Evolution of Advanced Zr-Base Alloys. In G. Sabol and G. Moan, editors, *Zirconium in the Nuclear*

- Industry: Twelfth International Symposium, ASTM STP 1354*, pages 51–73, West Conshohocken, PA, 2000. American Society for Testing and Materials.
- H. G. Groehn. Influence of the Yaw Angle on Heat Transfer and Pressure Drop of Tube Bundle Heat Exchangers. In U. Grigull, E. Hahne, K. Stephan, and J. Straub, editors, *Heat transfer 1982: Proceedings of The Seventh International Heat Transfer Conference*, volume 6, pages 203–208. Hemisphere Publishing Corporation, 1982.
- H. G. Groehn. Influence of the Yaw Angle on Heat Transfer and Pressure Drop of Helical Type Heat Exchangers. In *Technology of steam generators for gas-cooled reactors: Proceedings of a specialists' meeting*, pages 182–188. International Atomic Energy Agency, 1988.
- D. Gross, W. Hauger, J. Schröder, and W. A. Wall. *Technische Mechanik 2*. Springer, Heidelberg, 11th edition, 2012. In German.
- H. Hadžić and B. Dressel. CFD Applications for Nuclear Reactor Fuel Assembly Design. In *STAR Global Conference 2016*, Prague, CZ, March 7-9 2016.
- J. D. Hales, S. R. Novascone, G. Pastore, D. M. Perez, B. W. Spencer, and R. L. Williamson. *BISON Theory Manual*. Idaho National Laboratory, Idaho Falls, ID, USA, October 2013.
- R. Hill. A Theory of the Yielding and Plastic Flow of Anisotropic Metals. *Proceedings of the Royal Society of London A*, 193(1033):281–297, May 1948.
- R. Hill. *The mathematical theory of plasticity*. Clarendon Pr., Oxford, UK, 1983.
- R. A. Holt. Mechanisms of Irradiation Growth of Alpha-Zirconium Alloys. *Journal of Nuclear Materials*, 159:310–338, 1988.
- R. A. Holt, A. R. Causey, N. Christodoulou, M. Griffiths, E. T. C. Ho, and C. H. Woo. Non-Linear Irradiation Growth of Cold-Worked Zircaloy-2. In E. Bradley and G. P. Sabol, editors, *Zirconium in the Nuclear Industry: Eleventh International Symposium, ASTM STP 1295*, pages 448–468. American Society for Testing and Materials, 1996.
- N. E. Hoppe. Engineering Model for Zircaloy Creep and Growth. In *Fuel for the 90's: International Topical Meeting on LWR Fuel Performance Proceedings*, volume 1, pages 201–209, Avignon, France, April 21-24 1991.
- A. Horvath and B. Dressel. On Numerical Simulation of Fuel Assembly Bow in Pressurized Water Reactors. *Nuclear Engineering and Design*, 265:814–825, 2013.
- C. Hunt. Anisotropic Theory and the Measurement and Use of the Anisotropic Factors for Zircaloy-4 Fuel Sheaths. In *Third International Conference on Structural Mechanics in Reactor Technology (SMiRT 3)*, London, UK, September 1-5 1975.
- E. Ibrahim and R. Holt. Anisotropy of Irradiation Creep and Growth of Zirconium Alloy Pressure Tubes. *Journal of Nuclear Materials*, 91:311–321, 1980.
- I. Idel'čik. *Handbook of Hydraulic Resistance*. CRC Press, Boca Raton, USA, 3rd edition, 1994.
- W. K. In, D. S. Oh, and T. H. Chun. Pressure Drop Correlation for a PWR Fuel Assembly with Mixing Vane. In *Proceedings of the Korean Nuclear Society Spring Meeting*, Cheju, Korea, May 2001.

- W. K. In, D. S. Oh, and T. H. Chun. Empirical and Computational Pressure Drop Correlations for Pressurized Water Reactor Fuel Spacer Grids. *Nuclear Technology*, 139(1):72–79, July 2002.
- S. Y. Jeon, N. K. Park, K. S. Lee, and H. K. Kim. A Hold-down Margin Assessment using Statistical Method for the PWR Fuel Assembly. In *Transactions of the Korean Nuclear Society Autumn Meeting*, pages 273–274, Pyeongchang, Korea, October 2007.
- Z. Karoutas, K. Lang, and P. Joffre. Evaluating PWR Fuel Performance Using Vessel CFD Analysis. In *Proceedings of 2010 LWR Fuel Performance/TopFuel/WRFPFPM*, pages 681–688, Orlando, FL, USA, September 26-29 2010.
- W. Kast and H. Nirschl. *VDI-Wärmeatlas*, chapter L1, pages 1221–1283. Springer-Verlag, Berlin, 11th edition, 2013.
- T. Kido, Y. Senda, Y. Tukuta, H. Hayashi, and K. Murai. Quantitative assessment of irradiation effect on creep and corrosion properties of Zr-base alloys. In G. Moan and P. Rudling, editors, *Zirconium in the Nuclear Industry: Thirteenth International Symposium, June 10-14, 2001, Annecy, France, ASTM STP 1423*, pages 780–795, West Conshohocken, PA, 2002. American Society for Testing and Materials.
- I.-K. Kim. A Study on the Fuel Assembly Stress Analysis for Seismic and Blowdown Events. *Journal of the Korean Nuclear Society*, 25(4):552–559, December 1993.
- Y.-E. Kim, J.-W. Park, and J. Cleveland. Thermophysical properties database of materials for light water reactors and heavy water reactors. Final report of a coordinated research project 1999-2005 IAEA-TECDOC-1496, IAEA International Atomic Energy Agency, Vienna, Austria, June 2006.
- S. J. King, R. L. Kesterson, K. H. Yueh, R. J. Comstock, W. M. Herwig, and S. D. Ferguson. Impact of Hydrogen on Dimensional Stability of ZIRLO Fuel Assemblies. In G. Moan and P. Rudling, editors, *Zirconium in the Nuclear Industry: Thirteenth International Symposium, June 10-14, 2001, Annecy, France, ASTM STP 1423*, pages 471–489, West Conshohocken, PA, 2002. American Society for Testing and Materials.
- M. Kojić and K.-J. Bathe. *Inelastic Analysis of Solids and Structures*. Springer, Berlin, 2005.
- C. Lascar, J. Champigny, A. Chatelain, B. Chazot, N. Goreaud, E. M. D. Montigny, J. Pacull, and H. Salaün. Advanced Predictive Tool for Fuel Assembly Bow based on a 3D Coupled FSI Approach. In *TopFuel 2015 Conference Proceedings Part II*, Zurich, Switzerland, September 13-17 2015.
- H. Lee. Dynamic Characteristics of Fuel Rods. *Journal of the Korean Nuclear Society*, 12(4):255–266, December 1980.
- Y. H. Lee, K. H. Lee, J. Y. Kim, K. H. Yoon, H. K. Kim, C. H. Shin, D. S. Oh, W. K. In, T. H. Chun, and K. W. Song. Unit Spacer Grid Strap, Unit Spacer Grid, and Spacer Grid for Nuclear Fuel Rods, April 2014. US Patent 8,693,612.
- J. Lemaitre and J.-L. Chaboche. *Mechanics of Solid Materials*. Cambridge University Press, Cambridge, 1990.
- B. Levasseur, G. Chaigne, and R. Fernandes. 3-D Modeling of Fuel Assembly Bow for EDF PWRs. In *Water Reactor Fuel Performance Meeting 2009 : WRFPFPM TopFuel 2009*, volume 2, pages 679–686, Paris, France, September 6-10 2009. SFEN.

- M. Limbäck and T. Andersson. A Model for Analysis of the Effect of Final Annealing on the In- and Out-of-Reactor Creep Behavior of Zircaloy Cladding. In E. Bradley and G. P. Sabol, editors, *Zirconium in the Nuclear Industry: Eleventh International Symposium, ASTM STP 1295*, pages 448–468. American Society for Testing and Materials, 1996.
- G. E. Lucas and R. M. N. Pelloux. Some Observations on Time-Hardening and Strain-Hardening Rules for Creep in Zircaloy-2. *Nuclear Technology*, 53(1):46–57, April 1981.
- V. Makarov, A. Afanasiev, I. Matvienko, Y. Drozdov, and V. Puchkov. A Study of the Friction and Wear Processes of the Structural Components of Fuel Assemblies for Water-Cooled and Water Moderated Power Reactors. In *2011 Water Reactor Fuel Performance Meeting*, Chengdu, China, September 11-14 2011.
- J. Mardon, P. Hoffmann, and G. Garner. High Burnup Behavior and Licensing of Alloy M5. In *Proceedings of the 2005 International Meeting on LWR Fuel Performance*, pages 288–294, Kyoto, Japan, October 2-6 2005.
- J. Marin, M. Aullo, and E. Gutierrez. Fuel Assemblies Mechanical Behaviour Improvements Based on Design Changes and Loading Patterns Computational Analyses. In *ICONE 9: Ninth International Conference on Nuclear Engineering*, Nice, France, April 8-12 2001. SFEN.
- C. F. Mattos Schettino, G. Pennachin Sakamiti, and J. C. Aguiar Gaspar Júnior. Stiffness Evaluation of the Welded Connection between Guide Thimbles and the Spacer Grids for 16 x 16 Fuel Assemblies Types, Using the Finite Element Method. *Journal of Energy and Power Engineering*, 8:1583–1589, 2014.
- M. A. McGrath and S. Yagnik. Experimental Investigation of Irradiation Creep and Growth of Recrystallized Zircaloy-4 Guide Tubes Pre-Irradiated in PWR. *Journal of ASTM International*, 8(3):875–898, 2011.
- C.-H. Menq, J. Bielak, and J. H. Griffin. The Influence of Microslip on Vibratory Response, Part I: A New Microslip Model. *Journal of Sound and Vibration*, 107(2):279–283, 1986.
- M. Merkel and A. Öchsner. *Eindimensionale Finite Elemente*. Springer, Heidelberg, 2010. In German.
- J. G. Merkle. An Engineering Approach to Multiaxial Plasticity. Technical Report ORNL-4138, Oak Ridge National Laboratory, Oak Ridge, TN, USA, July 1967.
- MHI. Core and Fuel, 2016. URL <https://www.mhi-global.com>. Mitsubishi Heavy Industries, Ltd.
- L. F. Moody. Friction Factors for Pipe Flow. *Transactions of ASME*, 66(8):678–684, November 1944.
- M. Morales, A. Cerracín, Y. Aleshin, and J.-H. Kim. SAVAN3D: Improving Simulation Capabilities of the SAVAN Technology. In *2012 Water Reactor Fuel Performance Meeting*, pages 686–694, Manchester, UK, September 2-6 2012.
- A. Mubeen. *Mechanics of Solids*. Pearson Education, Noida, India, 2nd edition, 2002.
- K. Murty, editor. *Materials’ Ageing and Degradation in Light Water Reactors*. Woodhead Publishing, Cambridge, 2013.
- K. L. Murty and I. Charit. Texture Development and Anisotropic Deformation of Zircaloys. *Progress in Nuclear Energy*, 48:325–359, September 2006.
- T. Nakano, H. Fujii, and J. Shimizu. Mitsubishi PWR Fuel Experience and Reliability. In *Proceedings of 2008 Water Reactor Fuel Performance Meeting*, Seoul, Korea, October 19-23 2008.

- K. Naumenko and H. Altenbach. *Modeling of Creep for Structural Analysis*. Foundations of Engineering Mechanics. Springer, Berlin, 2007.
- NEI. Fuel Design Data. *Nuclear Engineering International (NEI)*, pages 42–51, September 2012.
- F. H. Norton. *The Creep of Steel at High Temperatures*. McGraw-Hill, New York, 1929.
- K.-J. Park, B.-S. Kang, K.-N. Song, and G.-J. Park. Design of a Spacer Grid Using Axiomatic Design. *Journal of Nuclear Science and Technology*, 40(12):989–997, December 2003.
- R. Penny and D. Marriott. *Design for Creep*. Chapman & Hall, London, UK, 2nd edition, 1995.
- K. Pettersson. Evaluation of Results from an In-pile Creep Test in the Studsvik R2 Reactor. Technical Report 02:48, SKI, January 2002.
- J. Peybernès. Evaluation of the Forces Generated by Cross-Flow on PWR Fuel Assembly. In *IAEA-TECDOC-1454 Structural Behaviour of Fuel Assemblies for Water Cooled Reactors*, IAEA-TECDOC-1454, pages 13–21, Vienna, Austria, July 2005. IAEA.
- P. Ross-Ross, V. Fidleris, and D. Fraser. Anisotropic Creep Behaviour of Zirconium Alloys in a Fast Neutron Flux. *Canadian Metallurgical Quarterly*, 11(1):101–111, 1972.
- S. Roudier and R. Béraha. Nuclear Fuel in France: an ever changing world - most recent safety concerns of DSIN. In *Specialist Meeting on Nuclear Fuel and Control Rods: Operating Experience, Design Evolution and Safety Aspects*, pages 63–77, Madrid, Spain, November 5-7 1996. OECD-NEA.
- RSK. Verformungen von Brennelementen in deutschen Druckwasserreaktoren (DWR). RSK-Stellungnahme (474. Sitzung der Reaktor-Sicherheitskommission (RSK) am 18.03.2015), RSK, 2015.
- J. Ruiz Antón. Set up of a Fluid Structure Coupling Interface (FSI) between PWR Fuel Assemblies and the Reactor Coolant, based on a Porous Medium Approach. Master’s thesis, Technical University of Munich, Department of Mechanical Engineering, Chair of Nuclear Technology, Garching, August 2016.
- W. Rust. *Nichtlineare Finite-Elemente-Berechnungen*. Vieweg+Teubner Verlag, Wiesbaden, 2nd edition, 2011. In German.
- H. Salaün, C. Callens, S. D. Perthuis, and J. C. Leroux. CASI: Prediction of Fuel Assembly Axial Behaviour under Irradiation. In *Transactions of the 12th International Conference on Structural Mechanics in Reactor Technology (SMiRT-12)*, Stuttgart, August 15-20 1993.
- H. Salaün, J. Baleon, and E. Francillon. Analytical approach to PWR fuel assembly distortions. In *Transactions of the 14th International Conference on Structural Mechanics in Reactor Technology (SMiRT-14)*, Lyon, France, August 17-22 1997.
- A. Saltelli, K. Chan, and E. M. Scott. *Sensitivity Analysis*. Wiley, Chichester, UK, 2000.
- A. Seibold, F. Garzarolli, and R. Manzel. Material Development for Siemens Fuel Elements. In *International Topical Meeting on Light Water Reactor Fuel Performance*, Park City, Utah, USA, April 10-13 2000. American Nuclear Society.
- A. Soniak, N. L’Hullier, J. Mardon, V. Rebeyrolle, P. Bouffieux, and C. Bernaudat. Irradiation Creep Behavior of Zr-Base Alloys. In G. Moan and P. Rudling, editors, *Zirconium in the Nuclear Industry: Thirteenth International Symposium, June 10-14, 2001, Annecy, France, ASTM STP 1423*, pages 837–862, West Conshohocken, PA, 2002. American Society for Testing and Materials.

- G. Spykman and J. Pattberg. PWR Fuel Assembly Bow. In *Proceedings of the 45th Annual Meeting on Nuclear Technology (AMNT 2014)*, Frankfurt, Germany, May 6-8 2014.
- J. Stabel and H.-P. Hübsch. Fuel assembly bow: Analytical modeling and resulting design improvements. In *Transactions of the 13th International Conference on Structural Mechanics in Reactor Technology (SMiRT-13)*, Porto Alegre, Brazil, August 13-18 1995.
- J. Stabel, B. Dressel, V. Marx, C. Muench, A. Horvath, C. Brun, E. M. de Montigny, and C. Song. Advanced Methodology to Predict In-Reactor Bow of PWR Fuel Assemblies for Efficient Design Optimization: Background, Validation, Examples. In *2011 Water Reactor Fuel Performance Meeting*, Chengdu, China, September 11-14 2011.
- H. Stehle, H. Assmann, and F. Wunderlich. Uranium Dioxide Properties for LWR Fuel Rods. *Nuclear Engineering and Design*, 33(2):230–260, 1975.
- A. Steinke. Spring Element for Holding Down Nuclear Reactor Fuel Assembly, July 1981. US Patent 4,278,501.
- B. Szabó and I. Babuška. *Introduction to Finite Element Analysis: Formulation, Verification and Validation*. Wiley Series in Computational Mechanics. Wiley, Chichester, UK, 1st edition, 2011.
- N. E. Todreas and M. S. Kazimi. *Nuclear Systems*, volume I: Thermal Hydraulic Fundamentals. CRC Press, Boca Raton, USA, 2nd edition, 2012.
- G. Ulrych and E. Weber. Neuere Ergebnisse zur Kühlmittelströmung in Druckwasserreaktoren. *Atomkernenergie, Kerntechnik*, 42(4):217–223, 1983.
- USNRC. *Westinghouse Technology Systems Manual*. USNRC Human Resources Training & Development, 2012.
- R. von Mises. Mechanik der festen Körper im plastisch-deformablen Zustand. *Nachrichten von der Gesellschaft der Wissenschaften zu Göttingen, Mathematisch-Physikalische Klasse*, pages 582–592, 1913.
- A. Wanninger, M. Seidl, and R. Macián-Juan. Development of Computational Methods to Describe the Mechanical Behavior of PWR Fuel Assemblies. In *Proceedings of the 47th Annual Meeting on Nuclear Technology (AMNT 2016)*, Hamburg, Germany, May 10-12 2016a.
- A. Wanninger, M. Seidl, and R. Macián-Juan. Screening Sensitivity Analysis of a PWR Fuel Assembly FEM Structural Model. In *TopFuel 2016 Conference Proceedings*, Boise, USA, September 11-16 2016b.
- A. Wanninger, M. Seidl, and R. Macián-Juan. Development of Computational Methods to Describe the Mechanical Behavior of PWR Fuel Assemblies. *atw - International Journal for Nuclear Power*, 61(10): 612–616, 2016c.
- A. Wanninger, M. Seidl, and R. Macián-Juan. Mechanical Analysis of the Creep Deformation of a Row of Fuel Assemblies in a PWR Core. In *2017 Water Reactor Fuel Performance Meeting (WRFPM 2017)*, Jeju, Korea, September 10-14 2017.
- A. Wanninger, M. Seidl, and R. Macián-Juan. Mechanical Analysis of the Bow Deformation of a Row of Fuel Assemblies in a PWR Core. *Nuclear Engineering and Technology*, 2018. In Press.
- G. S. Was. *Fundamentals of Radiation Materials Science*. Springer, Berlin, 2007.

- W. B. Weihermiller and G. Allison. LWR Nuclear Fuel Bundle Data for Use in Fuel Bundle Handling. Topical Report PNL-2575, Battelle Pacific Northwest Laboratory, Richland, WA, USA, September 1979.
- C. Whitmarsh. Review of Zircaloy-2 and Zircaloy-4 Properties Relevant to N.S. Savannah Reactor Design. Technical Report ORNL-3281, Oak Ridge National Laboratory, Oak Ridge, TN, USA, 1962.
- G. Wikmark, L. Hallstadius, and K. Yueh. Cladding to Sustain Corrosion, Creep and Growth at High Burn-Ups. *Nuclear Engineering and Technology*, 41:143–148, 2009.
- J. Wittenburg and H. Richard. *Hütte - Das Ingenieurwissen*, chapter E, pages E1 – E225. Springer Vieweg, Berlin, 34th edition, 2012. In German.
- D. Wood. Dose Dependence of Irradiation Creep of Zircaloy-2. In *Properties of Reactor Structural Alloys After Neutron or Particle Irradiation*, ASTM STP 570, pages 207–217, 1975.
- Y. Xu, M. Conner, K. Yuan, M. B. Dzodzo, Z. Karoutas, S. A. Beltz, S. Ray, T. A. Bissett, C.-C. Chieng, M.-T. Kao, and C.-Y. Wu. Study of Impact of the AP1000 ® Reactor Vessel Upper Internals Design on Fuel Performance. *Nuclear Engineering and Design*, 252:128–134, 2012.
- K.-H. Yoon, H.-K. Kim, and T.-H. Chun. Impact Analysis for the Lateral Impact Characteristics of a 16 by 16 type PWR Fuel Assembly using FE Method. In *Transactions of the Korean Nuclear Society Autumn Meeting*, Gyeongju, Korea, November 2-3 2006.
- K.-H. Yoon, H.-K. Kim, and T.-H. Chun. Lateral Bending Characteristic Analysis of a 16 by 16 type PWR Fuel Assembly using Test Method. In *Transactions of the Korean Nuclear Society Spring Meeting*, Jeju, Korea, May 10-11 2007.
- P. Yvon, J. Diz, and N. Ligneau. Irradiation Creep and Growth of Guide Thimble Alloys. In *Proceedings of the International Symposium Fontevraud IV*, volume 2, pages 1241–1252, 1998.
- A. Ziegler. *Lehrbuch der Reaktortechnik*, volume 2: Reaktortechnik. Springer-Verlag, Berlin, 2nd edition, 1984. In German.